HELSINKI INSTITUTE OF PHYSICS INTERNAL REPORT SERIES

Measurement of the inclusive jet cross section in $p\bar{p}$ collisions at $\sqrt{s} = 1.96$ TeV

Mikko Voutilainen

Helsinki Institute of Physics
P.O.Box 64, FI-00014 University of Helsinki, Finland

Dissertation for the degree of Doctor of Science in Technology to be presented with due permission of the Faculty of Information and Natural Sciences, Helsinki University of Technology, for public examination and debate in Auditorium Ko216 at Helsinki University of Technology (Espoo, Finland) on the 1st of July, 2008, at 12 o'clock noon.

ISBN 978-952-10-3722-1 (printed)
ISNB 978-952-10-3723-8 (PDF)
ISSN 1455-0563
Helsinki 2008
Yliopistopaino

Acknowledgements

This thesis is based on research work carried out as a member of the DØ Collaboration, as a Visiting Scholar at the University of Nebraska in Lincoln and as an Adjoint Scientist to the Helsinki Institute of Physics. This thesis is also part of a joint degree between Helsinki University of Technology and Universite de Paris-Sud 11 (Orsay), initiated by collaboration with the high-energy physics group of CEA Saclay.

I am very grateful for my professors Greg Snow and Jorma Tuominiemi for the opportunity to come and work at Fermilab in the DØ Collaboration, and for the great work they did with the initial research plan. It has been a unique experience. I have learned a great deal from my advisor Christophe Royon, who has guided me throughout the thesis work, and from my colleague Alexander Kupčo, whose work I continued in my analysis. We have shared the labor in the Jet Energy Scale group and the consequent successes in the analysis, and I also thank them for the many memorable times at Fermilab.

A large portion of the work required for this thesis has been done in the context of the Jet Energy Scale group. Initially assembled by Christophe and then spear-headed by Aurelio Juste, our "dream team" managed to push the limits of precision in jet energy calibration at hadron colliders. We owe much of this to Aurelio's almost inexhaustible energy and determination to always improve. I would also like to say thanks and wish all the best for my JES colleagues Jiří Kvita, Zdeněk Hubáček, Jeroen Hegeman, Andrés Tanasijczuk, David Lam, Jochen Cammin, Dag Gillberg and Zhiyi Liu.

During my stay I had a rare opportunity for a graduate student to be a co-convener in the JetID group. I would like to thank the ex-convener Amnon Harel and my co-convener Bernard Andrieu for teaching me and helping out in the beginning and along the way. Big thanks also to Murilo Rangel, who did most of the work during the important JetID certification phase.

Much credit for the final analysis goes to Markus Wobisch, who currently convenes the QCD group and provided all the NLO theory calculations as

well as important insights for the error treatment and statistical analysis. I would like to thank Don Lincoln and Michael Begel, from whom I've had many useful insights to the analysis. My favorite reading on the subject has been the Run I thesis of UNL-alumnus and Run I QCD convener John Krane, whom I would like to thank for his comments out of "retirement" on the thesis manuscript. The final work has benefited much from the comments of Heidi Schellman, who chaired the editorial board for the analysis and provided the detailed measurement of the shape of the interaction region used in the analysis.

This thesis will be defended twice, in Espoo on July 1 and in Paris on July 4. I would like to thank the referees Kenneth Österberg, Martine Bosman and Joël Feltesse for reading the thesis and providing useful comments to improve the manuscript. Thanks to Rainer Salomaa for making ends meet in this somewhat complicated co-leadership project and being the supervisor after the passing away of my long-time supervisor Martti M. Salomaa. Thanks also to the other members of the French jury, Etienne Augé, Alan D. Martin and John Womersley, and to my opponent in Finland, Günther Dissertori.

During my three and a half years at Fermilab I have much enjoyed the great athmosphere in the Fermilab volleyball community. I would like to thank all of you with whom I have had the pleasure to play with, and in particular my multiple season teammates Leah Welty-Rieger, Jason Rieger, Len Christofek, Adam Yurkewicz and Sergey Los, who has recently also organized the volleyball league.

Finally, and most importantly, I want to thank Tuula for her love, support and encouragement, and for all the adventures we have had.

Mikko Voutilainen

Abstract

This thesis studies the high-energy collisions of protons and antiprotons. The data used in the measurement were collected during 2004–2005 with the DØ detector at the Tevatron Collider of the Fermi National Accelerator Laboratory and correspond to 0.7 fb^{-1} of integrated luminosity. High energy hadron collisions usually produce collimated sprays of particles called jets. The energy of the jets is measured using a liquid Argon-Uranium calorimeter and the production angle is determined with the help of silicon microstrip and scintillating fiber trackers. The inclusive jet cross section in proton-antiproton collisions is measured as a function of jet transverse momentum p_T in six bins of jet rapidity at the center-of-mass energy $\sqrt{s} = 1.96$ TeV. The measurement covers jet transerve momenta from 50 GeV up to 600 GeV and jet rapidities up to $|y| = 2.4$.

The data are collected using a set of seven single jet triggers. Event and jet cuts are applied to remove non-physical backgrounds and cosmic-ray interactions. The data are corrected for jet energy calibration, cut and trigger efficiencies and finite jet p_T resolution. The corrections are determined from data and the methods are tested with Monte Carlo simulation. The main experimental challenges in the measurement are the calibration of jet energies and the determination of the jet p_T resolution. New methods are developed for the jet energy calibration that take into account physical differences between the γ+jet and dijet calibration samples arising from quark and gluon jet differences. The uncertainty correlations are studied and provided as a set of uncertainty sources.

The production of particle jets in hadron collisions is described by the theory of quantum chromodynamics (QCD). When the transverse jet momentum is large, the contributions from long-distance physics processes are small and the production rates of jets can be predicted by perturbative QCD. The inclusive jet cross section in $p\bar{p}$ collisions at large p_T is directly sensitive to the strong coupling constant (α_s) and the parton distribution functions (PDFs) of the proton. This measurement can be used to constrain the PDFs, in particular the gluon PDF at high proton momentum fraction x, and to look for quark substructure at the TeV scale. The data are compared to the theory predictions with perturbative QCD in the next-to-leading order precision and a good agreement between data and theory is observed.

Tiivistelmä

Tässä työssä tutkitaan protonien ja antiprotonien törmäyksiä korkealla energialla. Mittauksessa käytetty data on kerätty vuosina 2004–2005 DØ ilmaisimella Yhdysvaltain Fermilab-kiihdytinlaboratorion Tevatron-törmäyttimellä ja vastaa 0.7 fb^{-1} yhteenlaskettua luminositeettia. Suurenergisten hadronien törmäyksissä syntyy yleensä yhdensuuntaisia hiukkasryöppyjä, jettejä. Jettien energia mitataan nestemäistä argonia ja uraania sisältävällä kalorimetrilla ja niiden suunnan mittaamiseen käytetään apuna piimikronauha- ja tuikekuitu-jälki-ilmaisimia. Jettien tuotanto eli hadroninen kokonaisvuorovaikutusala mitataan poikittaisen liikemäärän p_T funktiona kuudessa rapiditeettialueessa massakeskipiste-energialla $\sqrt{s} = 1.96$ TeV. Mittaus kattaa poikittaisen liikemäärän 50 GeV:istä 600 GeV:iin saakka ja rapiditeetin $|y| = 2.4$ saakka.

Mittausdata on kerätty käyttäen seitsemää jettiliipaisua. Epäfysikaalinen tausta ja kosmisten säteiden aiheuttamat signaalit poistetaan eventti- ja jettileikkauksilla. Jettien energia kalibroidaan ja dataa korjataan leikkausten ja liipaisinten tehokkuudella sekä $p_T : n$ mittauksen epätarkkuudesta. Korjaukset määritetään käyttäen dataa ja menetelmät testataan Monte Carlo-simuloinnilla. Mittauksen haasteena on jettien energian kalibrointi sekä p_T-resoluution määritys. Energian kalibrointiin kehitetään uusia menetelmiä, jotka huomioivat kvarkki- ja gluonijettien eroista johtuvat erot γ+jetti ja kahden jetin tapausten välillä. Epävarmuustekijöiden korrelaatiota tutkitaan, ja niistä muodostetaan joukko virhelähteitä.

Jettien tuotantoa hadronitörmäyksissä kuvataan kvanttikromodynamiikalla (QCD). Kun jettien poikittainen liikemäärä on suuri, pitkän matkan vuorovaikutukset ovat pieniä ja jettien tuotantoa voidaan ennustaa häiriöteorian avulla. Hadroninen kokonaisvuorovaikutusala $p\bar{p}$-törmäyksissä korkealla p_T:llä on suoraan riippuvainen vahvasta kytkentävakiosta (α_s) sekä protonin partonidistribuutiofunktioista (PDFs). Tätä mittausta voidaan käyttää rajoittamaan erityisesti gluonien PDF-jakaumaa korkealla osalla x protonin liikemäärästä sekä etsimään kvarkkien alirakennetta TeV-energiaskaalassa. Mittausta verrataan teorian ennustuksiin, jotka on laskettu käyttäen pQCD:tä toisen kertaluvun tarkkuudessa, ja nämä ovat hyvässä sopusoinnussa mittausten kanssa.

Selected publications by the author

D0 Collaboration: V. M. Abazov, *et al.*,
"Measurement of the inclusive jet cross section in $p\bar{p}$ collisions at $\sqrt{s}$ = 1.96 TeV", FERMILAB-PUB-08-034-E, submitted to Phys. Rev. Lett (2008) [arXiv:0802.2400].

M. Voutilainen, in
"Deep Inelastic Scattering, Proceedings of the 14th International Workshop", ed. by M. Kuze, K. Nagano and K. Tokushuku, World Scientific (2006) [arXiv:hep-ex/0609026].

JES Group,
"Jet Energy Scale Determination at DØ Run II (final p17 version)",
DØ Note 5382 (2007). *Results to be published as a NIM paper.*

M. Voutilainen, JES Group,
"Jet Four-vector Scale Determination for Dijets in DØ Run IIa (final p17 version)", DØ Note 5550 (2007).

M. Voutilainen,
"Jet p_T resolution for Run IIa final JES (v7.2) with dijet J4S jet corrections",
DØ Note 5499 (2007).

A. Harel, H. Nogima, M. Rangel, M. Voutilainen,
"Combined JetID efficiency for p17", DØ Note 5218 (2006).

M. Voutilainen,
"Single jet trigger efficiencies in Run IIa", DØ Note 5549 (2007).

The author has been a member of DØ since August 2004 and an author for DØ publications since September 2005. He has been one of the leading authors for the preliminary Run IIa (2005) Jet Energy Scale (JES) and for the final Run IIa JES (2007). His main contributions to JES are the η-dependent corrections, the explicit handling of γ+jet and dijet sample differences arising

from differences in quark and gluon initiated jets, combining the energy, p_T and rapidity corrections into a cohesive dijet four-vector correction for QCD samples and the closure test for the dijet sample η-dependence. He has written and maintained a large portion of the JES correction package (jetcorr). He has also been alone responsible for the jet p_T resolution measurement and the development of new methods to account for the non-Gaussian tails.

The author was co-convener of the JetID group in 2006–2007 and lead the determination of the jet identification efficiencies. He produced and released the final JetID corrections to the collaboration in the jetid_eff package. He pioneered the use of the trigeff_cafe package to measure the single jet trigger efficiencies Run IIa and updated the caf_trigger package to implement the efficiency corrections.

The author has written and maintained the jet analysis package qcd_jet_caf. He has been the principal author for two updates of the inclusive jet cross section measurement including the final one, and participated in one earlier update. He has implemented the programs to handle a large amount of uncertainty sources and to do a global fit to data and theory with associated uncertainties.

Abbreviations and acronyms

CC	Central calorimeter
ICR	Intercryostat region
EC	Endcap calorimeter
SMT	Silicon microstrip tracker
CFT	Central fiber tracker
EM	Electromagnetic
EMF	Electromagnetic fraction
CHF	Coarse hadronic fraction
JES	Jet energy scale
JER	Jet energy resolution
MC	Monte Carlo (simulation)
MPF	Missing-E_T projection fraction
ZB	Zero bias (trigger)
MB	Minimum bias (trigger)
L1,L2,L3	Level 1,2,3 (trigger)
ID	Identification
CAF	Common analysis format
QED	Quantum electrodynamics
QCD	Quantum chromodynamics
pQCD	Perturbative quantum chromodynamics
LO	Leading order
NLO	Next-to-leading order
PYTHIA	Event generator
HERWIG	Event generator
PDF	Parton distribution function
DIS	Deep inelastic scattering
CTEQ	Coordinated Theoretical-Experimental Project on QCD
MRST	Martin-Roberts-Stirling-Thorne

CDF	Collider Detector at Fermilab
CERN	Conceil Europeen pour la Recherche Nucleaire
LHC	Large Hadron Collider
DESY	Deutches Elektronen-Synchrotron
HERA	Hadron Electron Ring Accelerator
H1	Particle detector at HERA
ZEUS	Particle detector at HERA
BCDMS	Bologna - CERN - Dubna - Munich - Saclay Collaboration
NMC	New Muon Collaboration
CCFR	Chicago - Columbia - Fermilab - Rochester Collaboration

Common variables and units

The DØ experiment uses a right-handed coordinate system where positive x points to the middle of the accelerator ring, positive y points vertically up and positive z points along the proton beam direction.

ϕ	azimuth angle, $\phi = \arctan\left(\frac{y}{x}\right)$
θ	polar angle, $\theta = \arctan\left(\frac{\sqrt{x^2+y^2}}{z}\right)$
η	pseudorapidity, $\eta = -\ln\left(\tan\left(\frac{\theta}{2}\right)\right)$

The jet is characterized by a four-vector (E, p_x, p_y, p_z).

E	energy of the jet
p_T	transverse momentum of the jet, $p_T = \sqrt{p_x^2 + p_y^2}$
y	rapidity, $y = \frac{1}{2}\ln\left(\frac{E+p_z}{E-p_z}\right)$
E_T	transverse energy of the jet, $E_T = E/\cosh(\eta)$; NB: used in Run I when massless jets had $E_T = p_T$ and $\eta = y$
$\Delta\phi$	distance in ϕ, $\Delta\phi = \min(\lvert\phi_2 - \phi_1\rvert, 2\pi - \lvert\phi_2 - \phi_1\rvert)$ $(0 \leq \Delta\phi < \pi)$
ΔR	distance in y-ϕ-space, $\Delta R = \sqrt{(y_2 - y_1)^2 + (\Delta\phi)^2}$

The parton distribution functions are usually measured as a function of the proton momentum fraction x.

$\sqrt{s}$	center-of-mass energy of the proton-antiproton system
x	fraction of proton momentum carried by the interacting parton, $x = E/\sqrt{s}$

The following numbers are extracted from the *Review of Particle Physics*, W-M. Yao *et al.*, Journal of Physics G **33**, 1 (2006).

c	speed of light in vacuum, $c = 299792458 \frac{\mathrm{m}}{\mathrm{s}^2}$
M_Z	Z boson mass, $M_Z = 91.1876(21)$ GeV/c^2
α_s	strong coupling constant, $\alpha_s(M_Z) = 0.1176(20)$
eV	unit of energy, kinetic energy of an electron accelerated by a 1 volt potential difference, electron-volt, eV $= 1.60217653(14) \times 10^{-19}$ J
GeV	gigaelectron-volt, GeV $= 10^9$ eV
TeV	teraelectron-volt, TeV $= 10^{12}$ eV
barn	unit of cross section (area), barn $= 10^{-28}$ m^2
pb^{-1}	inverse picobarn, pb$^{-1} = 10^{40}$ m^{-2}
fb^{-1}	inverse femtobarn, fb$^{-1} = 10^{43}$ m^{-2}

It is common to use the convention $c = 1$ and omit c in units of momentum (GeV/c) and mass (GeV/c^2).

Contents

List of Tables

List of Figures

Chapter 1

Introduction

1.1 Zeitgeist

High energy physics is the study of the smallest elements of the universe, the subatomic particles that live within the atomic nuclei and come into brief existence in collisions of high energy. The particles and fields that describe these collisions are also needed to understand the earliest times of the universe, the era after the hot Big Bang when all the matter we see today came into existence.

The theories of particle physics, jointly known as the "Standard Model", have withstood testing against mountains of data during the past fifty years with only minor modifications to the parameters of the model. Yet the theory is incomplete: there is no universally accepted and experimentally tested extension that would combine the Standard Model with the other grand theory of physics, Albert Einstein's General[1] Relativity, the theory of gravity. The description of gravity is simply omitted in the Standard Model, its effect imperceptible in the energy range being accessible to colliders today.

Many experimental observations also support the notion that as thoroughly tested as the Standard Model is, it is still incomplete. The universally accepted model of cosmology, the "ΛCDM" model [1, 2], asserts that the universe is composed of 74% "dark energy" (Λ, Lambda) and 22% "cold dark matter" (CDM), neither of which is described by or known to the Standard Model. A mere 4% of the universe is visible in stars, galaxies and gas clouds and described by the Standard Model. The cosmological model is supported

[1]The other famous theory of Einstein's on the interconnectedness of time and space (producing $E = mc^2$), the Special Relativity, is part and parcel of the Standard Model.

by a wealth of data from the cosmic microwave background (afterglow of the Big Bang), measurements of the expansion speed of the universe using distant quasars, models of the structure formation in the universe and the measurements of gravitating matter (both visible and dark) using gravitational lensing.

The Standard Model still lacks the experimental observation of the last key element, the Higgs boson, which is the quantum of the scalar field that creates the mass of elementary particles. The Standard Model predicts one Higgs boson; The minimal supersymmetric extension of the Standard Model predicts five Higgs bosons and in addition a heavier superpartner for every known elementary particle. The increasingly popular string theory suggests supersymmetry and extra dimensions beyond the familiar time and three spatial dimensions. If large extra dimensions existed in sufficiently low number, high energy collisions could produce instantly vaporizing mini black holes at the Large Hadron Collider (LHC), due to start in 2008. Many experimentalists think and hope that the theorists have missed something, and the nature will bring another surprise.

In anticipation of the LHC the stage is set to do precision measurements of the Standard Model and pave the way for future measurements of the new physics that is expected in the TeV energy scale. The Tevatron is already probing the lower end of the TeV scale and, with luck, could get the first glimpse of the new discoveries to come.

The status of the current theoretical predictions is discussed in Chapter 3.

1.2 Inclusive jet cross section

The inclusive jet cross section measured in this thesis is first and foremost a test of perturbative quantum chromodynamics (pQCD) and a measurement of the structure of the proton. Quantum chromodynamics is an important part of the Standard Model that describes the interactions of quarks and gluons. Together these form the protons and neutrons of the atomic nuclei. Understanding the composition of the protons is important in order to precisely describe the collision of protons with antiprotons and protons. Only then the relatively weak effects of new physics become observable.

The distributions of quark and gluon momenta inside the proton are reasonably well known from measurements of electron-proton collisions and from fixed target experiments. However, there is significant freedom in the gluon distribution at a high fraction of the proton momentum. This feeds into a

large uncertainty in the tests of new physics at the LHC, in particular for searches of extra dimensions at high energy [3].

The inclusive jet cross section is sensitive to the parton (quark and gluon) distributions over a wide angular range, but new physics (non-QCD) processes would contribute most in the direction transverse to the beam direction. By measuring the cross section over a wide range of jet momenta and scattering angles it is possible to simultaneously constrain both the parton distribution functions (PDFs) and the new physics processes such as quark compositeness, or substructure.

The inclusive jet cross section measurement is not alone in constraining the structure and testing the validity of pQCD. Related measurements are reviewed in Ch. 2.

1.3 Collider and detector

The proton-antiproton collisions measured in this thesis were produced at the Fermilab Tevatron Collider at a center-of-mass energy of 1.96 TeV. Fermi National Accelerator Laboratory (Fermilab) is a busy particle physics hub in the United States located in Illinois about 50 km west of Chicago. The laboratory employs about 2000 scientists and engineers and about 1,200 physicists collaborate in its two main experiments, DØ and CDF.

The laboratory produces a constant supply of antiprotons by bombarding a target with a high energy beam of protons. The protons themselves have been pre-accelerated with a chain of accelerators. The antiprotons are stored in a recycler ring, bunched together, accelerated in the Tevatron ring and collided with the protons at the sites of the two detectors, DØ and CDF.

The DØ detector is a three-story tall detector made out of tons of Uranium, liquid Argon, steel, plastic scintillator and silicon. Like most particle detectors, its composed of an onion-like structure with concentric cylindrical layers of silicon tracking, scintillating fibre tracking, Uranium-liquid Argon electromagnetic and hadron calorimetry and an outer layer of muon scintillators and chambers. The detector has a 2T solenoid magnet wedged between the tracker and the calorimeter for bending charged particle tracks and producing an enhanced momentum measurement.

The collider and detector systems are discussed in more detail in Chapter 4.

1.4 Experimental challenges

The DØ experiment records collisions at a rate of 2.5 million per second, selects the most interesting events with a chain of dedicated electronics and a farm of a few hundred commodity CPUs and stores about fifty events per second on tapes housed at the Feynman Computing Center. The amount of data collected in Run II of the Tevatron between 2002 and 2005 is about 1 PetaBytes or equivalent to a 150 m stack of dual-side DVDs.

The data collected at a high energy collider undergoes a long chain of processing before being published. The raw data is reconstructed to find objects such as particle tracks and calorimeter energy clusters. These are grouped into physical objects such as interaction vertices and jets, collimated sprays of particles.

The experimental challenges lie in the careful cleaning and calibration of the data. The time periods with detector problems are removed and real events are separated from cosmic-ray background. Jets and vertices are selected with object identification (ID) cuts that remove spurious detector noise, additional soft collisions and events that are hard to calibrate. The remaining good events are calibrated to measure the average jet energies, angles, energy resolution and angular resolution. The final analysis corrects the measurement for selection efficiencies, unfolds the resolutions and normalizes the result to the total inelastic cross section.

The processing and reconstruction of the data is discussed in Chapter 5, the energy and angular calibration in Chapter 6 and the resolutions in Chapter 7. The analysis and final results are detailed in Chapter 8.

Chapter 2

Review of previous measurements

To understand the impact of the DØ Run IIa inclusive jet cross section measurement in high-energy physics, it is important to review what other related measurements have contributed. This chapter will outline measurements performed at HERA, fixed target experiments and the Fermilab Tevatron Collider that have contributed to our understanding of the parton distributions functions (PDFs), the validity of theoretical perturbative quantum chromodynamics (pQCD) predictions and Monte Carlo models, and the possibility of new physics at high energies. These measurements span almost two decades in time starting from Tevatron Run I (1992–1996), through HERA (1992–2007) to the latest Tevatron Run IIa (2002–2006) results published in 2007.

2.1 HERA measurements

The Hadron Electron Ring Accelerator (HERA), operated at the Deutches Elektronen-Synchrotron (DESY) in Hamburg, Germany, between 1992 and 2007, was the first and so far the only electron-proton collider in the world. The 27.5 GeV electrons and positrons collided on 920 GeV protons were measured by four particle detectors, H1, ZEUS, HERMES and Hera-B. The two largest experiments, H1 and ZEUS, took data between 1992 and 2007. Colliding electrons and positrons on protons allowed for very detailed studies of the proton structure functions through neutral and charged current deep-inelastic scattering (DIS). The very extensive and precise DIS measurements from HERA form the backbone of the parton distribution analysis, along

with fixed-target data[1] from BCDMS [26, 27], NMC [28] and CCFR [29].

The H1 collaboration has presented results on the measurement of the proton structure functions[2] $F_2(x, Q^2)$ shown in Fig. 2.1(a), $F_L(x, Q^2)$ and xF_3 [30]. These measurements have constrained the quark and gluon PDFs and tested the Q^2 evolution of the structure functions as predicted by the DGLAP evolution equation in the framework of next-to-leading order perturbative QCD. These theoretical concepts will be discussed in more detail in Ch. 3. The ZEUS collaboration has a similarly strong set of measurements of $F_2(x, Q^2)$ shown in Fig. 2.1(b), $F_L(x, Q^2)$, xF_3 and DGLAP evolution [31]. Together these experiments have laid strong constraints on the quark and low-x ($x < 0.01$) gluon PDFs. They have also observed the running of the strong coupling constant α_s with Q^2 and tested QCD in jet and particle production [32].

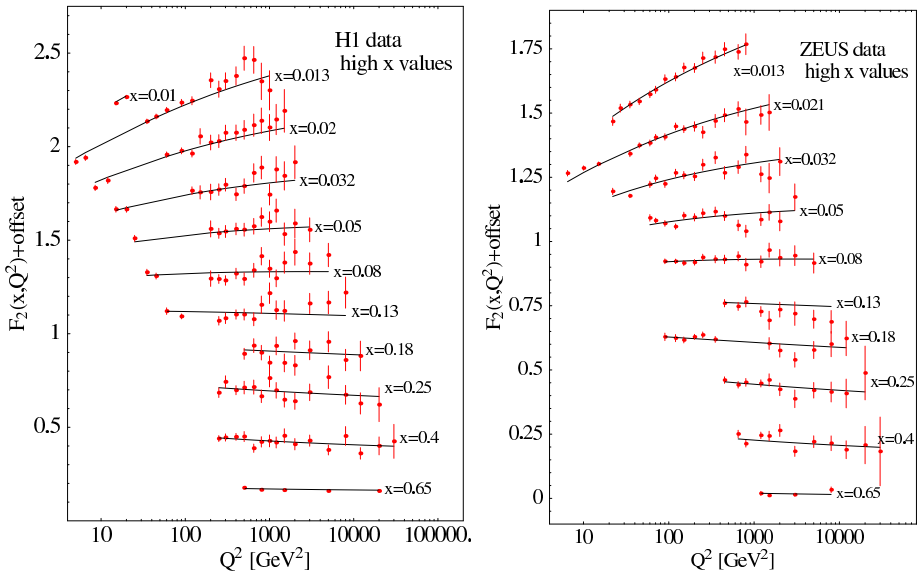

Figure 2.1: (a) H1 [30] and (b) ZEUS [31] high-x ($x > 0.01$) data compared to CTEQ6M PDF fits. The values on the vertical axis are offset to separate the curves for readability. The data points include the estimated corrections for systematic errors as needed by the PDF fits. Error bars show the statistical uncertainty only.

[1] The older fixed target experiments are not covered in this thesis, but the interested reader is invited to follow the references provided herein.

[2] $F_L(x, Q^2)$ has been measured only indirectly, but a direct measurement is being done.

2.2 Tevatron Run I measurements

Fermilab's Tevatron collided proton-antiproton beams at a center-of-mass energy of $\sqrt{s} = 1.8$ TeV during Run I. Although the center-of-mass energy was comparable to what it is at the Tevatron today, the beam intensity was considerably lower. The integrated luminosity collected during Run I was about 100 pb^{-1}, about one tenth of the present Run IIa data set and one fiftieth of the projected Run IIb data set by 2009.

Tevatron's Run I had on its side a cleaner collision environment caused by the lower luminosities and longer signal integration times, but also lacked the more accurate tracking we have available today. Nevertheless, the Run I measurements set the standard for high energy QCD measurements to which today's Run II measurements are compared. Reference [4] provides a good summary of the DØ high-p_T jet measurements in Run I. Another useful review article on inclusive jet and dijet production is [5], covering both DØ and CDF experiments in Run I.

2.2.1 DØ inclusive jet cross section

The Run I inclusive jet cross section measurement [6] is a direct predecessor of the inclusive jet cross section measurement presented in this thesis. Most of the techniques used are the same as today. The cone size for jets was the same $R_{\text{cone}} = 0.7$ as in this thesis, but the actual jet algorithm, DØ Run I cone [4], was different. The data set contained 95 pb^{-1} of luminosity collected at a center-of-mass energy of 1800 GeV. The measurement was later extended to include pseudorapidity bins $0.5 < |\eta| < 1.0$, $1.0 < |\eta| < 1.5$, $1.5 < |\eta| < 2.0$ and $2.0 < |\eta| < 3.0$ [7], shown in Fig. 2.2(a) along with theoretical predictions for CTEQ4M PDF. The central $|\eta| < 0.5$ measurement was also repeated using the k_T jet algorithm [106] with parameter $D = 1.0$, where the next-to-leading order (NLO) pQCD prediction is essentially identical to the cone algorithm with $R_{\text{cone}} = 0.5$ [8].

The uncertainty of the measurement for $|\eta| < 0.5$ is shown in Fig. 2.2(b). The total uncertainty and its main components are plotted versus jet E_T. The perturbative QCD next-to-leading order predictions using PDFs available at the time, CTEQ3M, CTEQ4M and MRST [9, 10, 11], were in agreement with data. The level of agreement with theory and the size of uncertainties, shown in Fig. 2.3, is comparable to the results presented in this thesis. The interesting region of the inclusive jet cross section measurement is at high

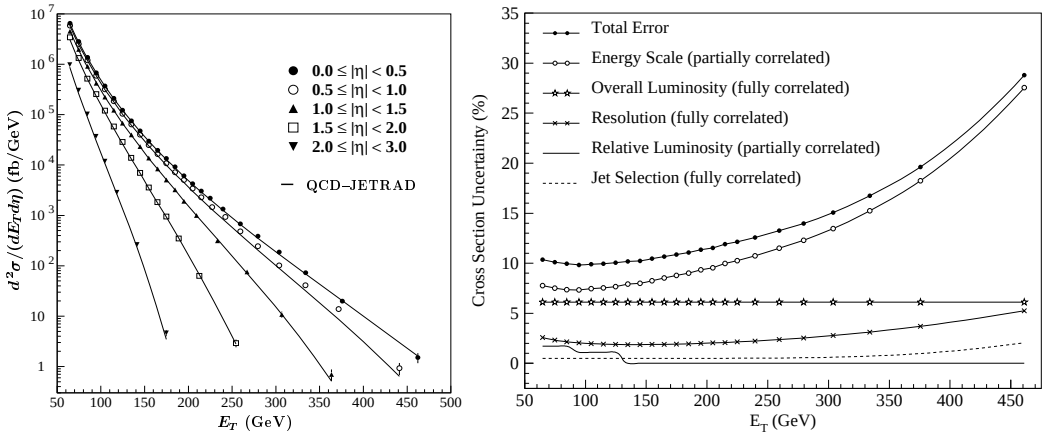

(a) (b)

Figure 2.2: (a) Inclusive jet production cross section in DØ Run I in five rapidity intervals, showing only statistical uncertainties [7]. Solid lines show the theoretical prediction using CTEQ4M PDF. (b) Contributions to the $|\eta| < 0.5$ cross section uncertainty plotted by component [6].

p_T, where the present measurement benefits from more luminosity, higher $\sqrt{s}$ and smaller systematics.

2.2.2 DØ 1800 GeV versus 630 GeV

At the end of Tevatron's Run I, special data was taken at a lower center-of-mass energy of 630 GeV. This gave a rare opportunity to do QCD measurements at two widely separated center-of-mass energies using the same detector [4, 12]. As shown in Fig. 2.2(b), the leading uncertainties in the cross section measurement at 1800 GeV were jet energy scale and luminosity, both largely detector related systematics. By accounting carefully the correlations between these uncertainties at 1800 GeV and 630 GeV, the uncertainty on the ratio of cross sections at these center-of-mass energies was significantly reduced. The theory predictions showed excellent agreement with the measurement at 630 GeV and the agreement was also satisfactory for the ratio, as shown in Fig. 2.4(a). Despite a 10–15% difference in the absolute magnitude, the dependence of the ratio on the scaled jet transverse momentum $x_T = E_T/\sqrt{s}$ was very similar for data and theory.

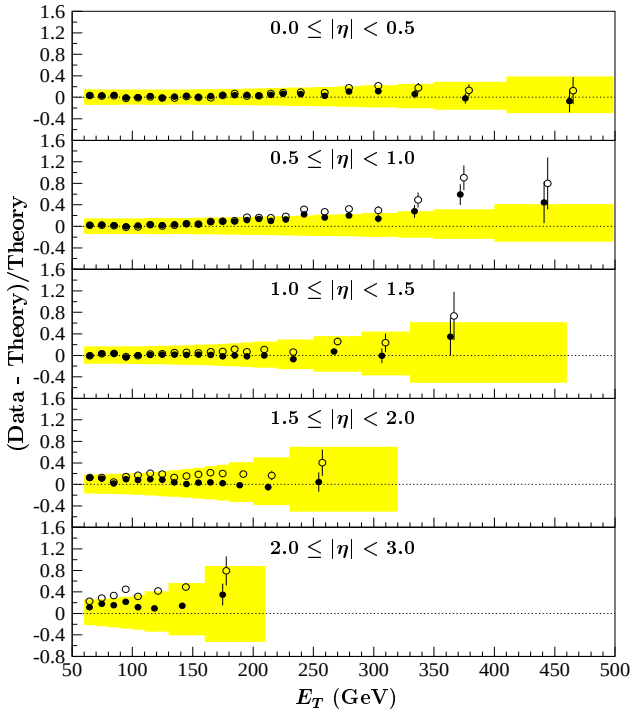

Figure 2.3: DØ Run I inclusive jet cross section compared to theory with CTEQ4M PDF in five pseudorapidity intervals [7]. The closed (open) circles show NLO QCD predictions calculated using JETRAD with CTEQ4M (CTEQ4HJ).

2.2.3 CDF Run I inclusive cone jet cross section

The CDF collaboration made measurements of the inclusive jet cross section comparable to DØ's measurements in Run Ia, but only covering the range $0.1 < |\eta| < 0.7$. The lower limit of $|\eta| = 0.1$ in the CDF measurement was dictated by the inconveniently placed gap in the CDF calorimeter at $|\eta| < 0.1$ [14]. The first measurement was published on a 19.5 pb^{-1} data set and an excess of events over theoretical predictions was seen at $E_T > 200$ GeV [13]. This prompted some speculation in the paper about the possibility of a quark substructure that could cause such an excess. This excess was not seen by DØ, however [6].

Later CDF Run Ib publication with 87 pb^{-1} of data was still in agreement with the earlier measurement, but by this time it was shown that an increased gluon density in the proton at high momentum fraction x could explain the relative increase in the observed cross section at high E_T [15]. This increase was implemented in the CTEQ4HJ PDF set [16] that gave special

emphasis to the CDF high-E_T data. The paper also showed that DØ and CDF measurements agreed at a 96% confidence level after accounting for all correlated and uncorrelated statistical and systematic uncertainties in the two measurements. The comparison after relative normalization is shown in Fig. 2.4. The remaining difference at high p_T, although within statistical uncertainties, is about 20–30%.

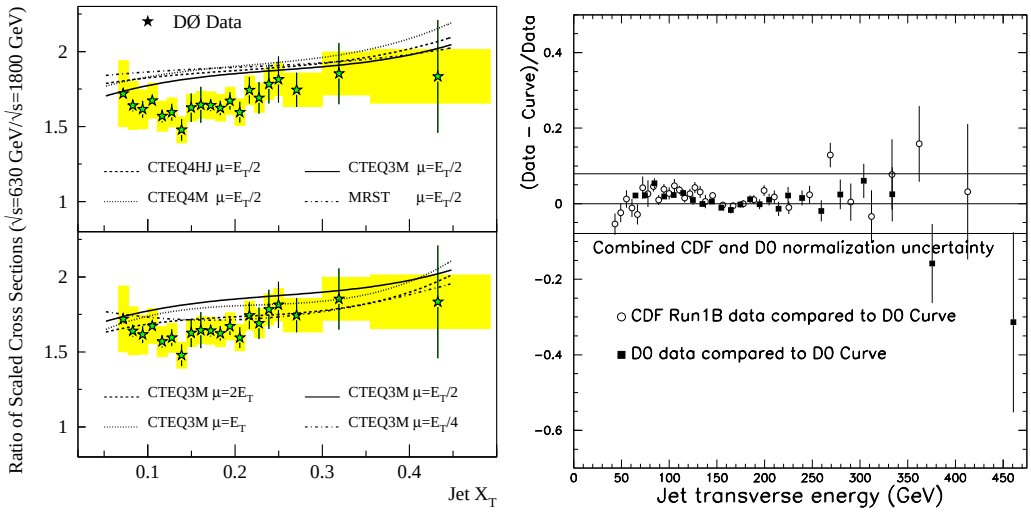

(a) (b)

Figure 2.4: (a) Ratio of scale invariant jet cross sections [12]. The stars are DØ data, the band is the systematic uncertainty, and the lines are the NLO predictions. (b) Comparison of DØ and CDF Run Ib data to DØ smooth curve in the region $0.1 < |\eta| < 0.7$ [12]. The data have been normalized to each other, with the error band showing uncertainty in the relative normalization.

2.2.4 CDF Run I two-jet differential cross section

Although the CDF collaboration did not publish the inclusive jet cross section at higher rapidities in Run I, they presented a two-jet differential cross section in Ref. [17]. In this study one of the jets was constrained to rapidity $0.1 < |\eta_1| < 0.7$ and the other in one of four rapidity bins in the range $0.1 < |\eta_2| < 3.0$. Comparison with all available NLO pQCD predictions showed relative excess in the cross section in the highest p_T bin, comparable to the excess observed in the inclusive jet cross section measurement in range $0.1 < |\eta| < 0.7$. This was interpreted as possible need for yet increased gluon density at high x. This is a plausible interpretation, as the earlier proposed

quark substructure would have shown relatively more excess events at low rapidities.

2.3 Tevatron Run II measurements

The Tevatron Run I measurements left a legacy of high interest in the possibility of seeing evidence for quark substructure in the high-E_T interactions. Although the updated PDF fits showed good agreement between data and theoretical predictions, a sizable discrepancy of 20–30% between DØ and CDF measurements remained at high E_T. This has in turn left a high degree of freedom for the gluon PDF fits at high momentum fraction x. With the factor of ten more luminosity and higher reach in p_T, the Run IIa measurements should be able to significantly constrain the high p_T gluon PDF and settle the issue of possible quark substructure in the observable energy range. It is also interesting to note that the uncertainty on the gluon PDFs is one of the leading uncertainties in new physics searches at the LHC [18].

Currently the only published inclusive jet measurements in Run IIa have come from CDF [19, 23, 25]. Preliminary results of the measurement covered in this thesis have been presented in [24].

2.3.1 CDF Run II inclusive jet cross section

The first Run II measurements of the inclusive jet cross section were published by CDF, based on a data set of 385 pb^{-1} and using the cone and k_T algorithms [23, 19]. The two algorithms are expected and observed to produce closely comparable results for high p_T jets, but can differ at low p_T depending on the k_T algorithm D parameter. The hadronization corrections grow rapidly as a function of D at low p_T and have an uncertainty of 10–20% at $p_T = 60$ GeV/c.

As shown in Fig. 2.5, the cone jet measurement shows 1–1.5σ excess over the latest theoretical predictions in the two highest p_T bins. It should be noted that the high p_T excess in Run I has already been included as increased gluon density at high x into the more recent PDF fits (CTEQ6M, CTEQ6.1M, MRST2004) [20, 21, 22], yielding good agreement between Run I data and theory, and Run II data and theory at $p_T < 450$ GeV/c. The data and theory at $p_T > 450$ GeV/c are in agreement, but the observed excess may be indicative of increased high-x gluon density. The rapid rise is hard to account with smooth gluon PDF fits and may be a statistical fluctuation and/or systematic bias. The Run I proposal of quark substructure is not

ruled out either, so it is important to confirm the CDF observations with an independent DØ measurement.

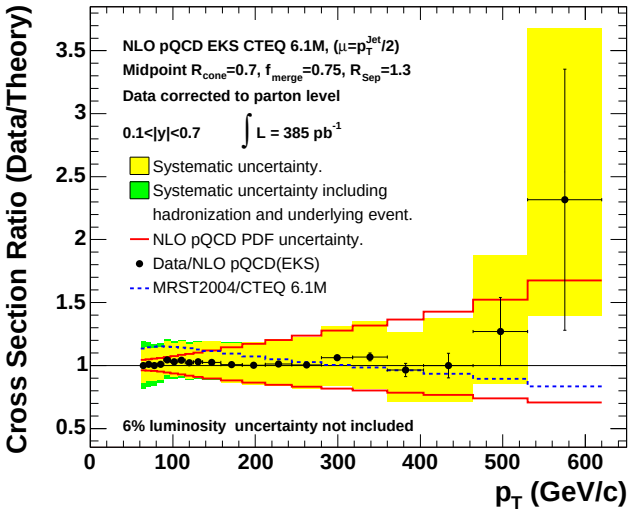

Figure 2.5: CDF Run II inclusive jet cross section measurement using the cone algorithm [19].

The latest CDF inclusive jet publication presents the inclusive jet cross section using the k_T algorithm in five bins at rapidities $|y^{\mathrm{JET}}| < 2.1$ [25] with 1.0 fb^{-1}. The agreement between theory and data is good. Again, it should be emphasized that the PDF fits have used Tevatron Run I data to constrain the gluon PDF at high x. The highest p_T bins have about 1 σ excess at all rapidities, as shown in Fig. 2.6(b).

2.4 Electroweak measurements

Not all constraints on the PDFs come from hadronic final states, *i.e.* studying jet production. The production of electroweak vector bosons also offers a way to constrain the PDFs. One example is the measurement of the asymmetry of W^+, W^- production at the Tevatron, others are measurements of the properties of W+jet and Z+jet production.

The CDF collaboration has published a measurement in Run I of W^+, W^- asymmetry by observing the charge asymmetry of the electrons and muons produced in W decays [33]. The W bosons are produced in the proton-antiproton collisions by the following leading order diagrams:

$$u + \bar{d} \rightarrow W^+, \quad d + \bar{u} \rightarrow W^-, \tag{2.1}$$

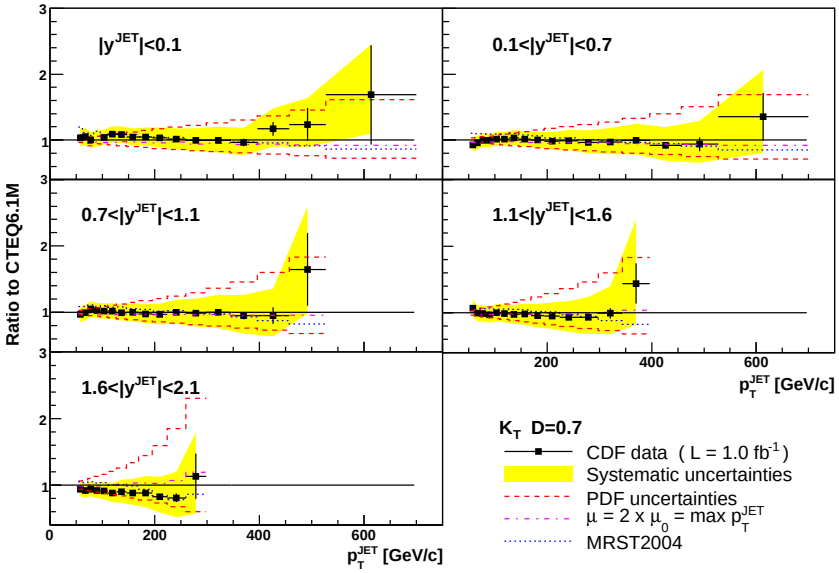

Figure 2.6: CDF Run II inclusive jet cross section measurement using the k_T algorithm [23].

so the W charge asymmetry is sensitive to the ratio of the d ($\bar{d}$) and u ($\bar{u}$) quark PDFs in the proton (antiproton). Since the two u valence quarks in a proton carry on average more momentum than the single d valence quark, the W^+ boson is boosted along the proton beam direction and the W^- along the antiproton beam direction, giving rise to charge asymmetry

$$A(y) = \frac{d\sigma(W^+)/dy - d\sigma(W^-)/dy}{d\sigma(W^+)/dy + d\sigma(W^-)/dy} \approx \frac{\rho(d)}{\rho(u)}, \tag{2.2}$$

where y is the W boson rapidity and the symbol ρ denotes the parton density. In practice only the muon and electron from $W \to e\nu$ and $W \to \mu\nu$ decays can be observed. The observed lepton asymmetry is then a convolution of the W production charge asymmetry and the asymmetry from the well-understood vector-axial ($V - A$) decay of the W. The CDF Run I measurement is an important constraint for the ratio of d and u PDFs [20].

The CDF collaboration has published the W asymmetry measurement in the $W \to e\nu$ channel with 170 pb^{-1} in Run II [34] and the DØ collaboration in the $W \to \mu\nu$ channel with 0.3 fb^{-1} [35]. The CDF collaboration has also a public preliminary result with 1 fb^{-1} in the $W \to e\nu$ channel [36].

2.5 Other QCD topologies

The measurement of the inclusive jet cross section involves a large variety of experimental uncertainties that affect the interpretation of the final results. It is therefore prudent to briefly review some recent measurements in the DØ QCD group that are subject to some of the same experimental uncertainties. These measurements share the data and many of the tools used in the inclusive jet cross section measurement. Each will be sensitive to the experimental uncertainties in a different way. Achieving consensus between the analyses grants an extra degree of confidence in the results of the inclusive jet cross section measurement.

The dijet production $p + \bar{p} \rightarrow \text{jet}_1 + \text{jet}_2 + \text{X}$ in the leading order of perturbation theory is fully described by three orthogonal kinematic variables, the invariant mass of the dijet systems M_{jj}, the angle between the jets in the center-of-mass frame θ^* and the boost of the dijet system $\eta_{\text{boost}} = (\eta_1 + \eta_2)/2$. This can be written as [37]

$$\frac{d^3\sigma}{d\eta_{\text{boost}} dM_{jj} d\cos\theta^*} = \frac{\pi\alpha_s^2(Q^2)}{2s^2}(2M_{jj}) \sum_{1,2} \frac{f(x_1, Q^2)}{x_1} \frac{f(x_2, Q^2)}{x_2} |m_{12}|^2, \quad (2.3)$$

where α_s is the strong coupling constant, Q is the hard scale that characterizes the parton scattering (which could be the jet p_T or the dijet mass M_{jj}) *etc.*), s is the center-of-mass energy squared of the proton-antiproton system, x_1 (x_2) is the fraction of proton (antiproton) momentum carried by the interacting parton, $f(x, Q^2)$ is the parton distribution function (PDF), and $|m_{12}|^2$ is the hard scattering matrix element.

Integrating Eq. 2.3 over boost and production angle results in the dijet mass spectrum. This measurement can constrain the PDFs like the inclusive jet cross section measurement, but it is more sensitive to high mass objects produced in the central rapidity regions. Integrating over mass and boost yields the dijet angular distribution. This is a good way to test the hard scattering matrix elements which is almost totally insensitive to the PDFs. Comparisons of suitable ratios of mass spectra and angular distributions to theoretical predictions can establish stringent limits on the presence of conjectured quark substructure (compositeness scale Λ).

In the leading order of perturbation theory, there are only two jets back-to-back with a scattering angle $\Delta\phi = \min(|\phi_2 - \phi_1|, 2\pi - |\phi_2 - \phi_1|) = \pi$. The higher order effects are apparent in the production of additional jets and in the decorrelation of the angle between the leading jets. The higher order behavior of QCD is probed by the three-jet mass spectrum and the dijet

azimuthal decorrelations, measured as the normalized cross section versus $\Delta\phi$.

The following sections will discuss the measurements on the dijet mass spectrum, dijet angular distributions (χ), dijet angular decorrelations ($\Delta\phi$) and three-jet mass spectrum in more detail.

2.5.1 Dijet mass

The dijet mass analysis measures the cross section for producing a given invariant mass of the two highest p_T jets. Dijets are produced in the leading order of perturbative QCD and form the main fraction of events in the inclusive jets analysis. By looking at the invariant mass M_{jj} of the leading jets the analysis increases the sensitivity to possible resonances at $Q^2 \sim M_{jj}^2$. New physics would most easily be seen as an increase of the dijet mass cross section at rapidities $|y| \sim 0$ relative to higher rapidities.

The dijet mass spectrum closely resembles the inclusive jet p_T spectrum as these two are related through

$$M_{jj} = \sqrt{(E_1 + E_2)^2 - (\vec{P}_1 + \vec{P}_2)^2} \approx p_T \sqrt{2\cosh(\Delta y)}, \qquad (2.4)$$

assuming massless, p_T balanced, back-to-back dijets. The main result of the dijet mass analysis is a lower limit on the scale of quark compositeness, $\Lambda > 2.4$ TeV, shown in Fig. 2.7(a) from DØ Run I measurement [38]. These data have also been used to set additional limits on quark compositeness [39]. The CDF Run I measurement of the dijet mass spectrum [40] is in good agreement with DØ results.

The dijet mass spectrum measurement has been updated once in Run II with 48 pb^{-1} and a preliminary version of jet energy scale [41]. The dijet mass spectrum for the full Run IIa data set has been studied in parallel with the inclusive jet cross section measurement, providing a complementary check of systematic uncertainties.

2.5.2 Dijet angular distribution

The dijet angular spectrum is usually derived versus the variable χ,

$$\begin{aligned} \chi &\equiv \exp(|y_1 - y_2|), \quad y = \frac{1}{2}\ln\left(\frac{1+\beta\cos\theta^*}{1-\beta\cos\theta^*}\right), \quad \beta = \frac{|\vec{p}|}{E}, \qquad (2.5) \\ \chi &\approx \frac{1+|\cos\theta^*|}{1-|\cos\theta^*|}. \end{aligned}$$

Using χ instead of θ^* flattens the angular spectrum and makes comparison to theory easier. The χ distribution is sensitive to the hard scattering matrix element, but almost completely insensitive to the PDFs. Figure 2.7 shows what the matrix element for Rutherford scattering, QCD and generic New Physics models looks like. Current measurements are in agreement with the QCD predictions [42], with recent Run IIa measurements at DØ extending to the $M_{jj} > 1$ TeV region [43].

The dijet χ measurement has been shown to be insensitive to the overall variations of the jet energy scale, but very sensitive to the relative energy scale at different rapidity ranges [43]. It therefore requires both small uncertainty in the rapidity dependence of the jet energy scale and precise understanding of the uncertainty correlations across rapidity to be sensitive to beyond Standard Model effects. These are also important ingredients when the inclusive jet cross section measurements are used for global PDF fits.

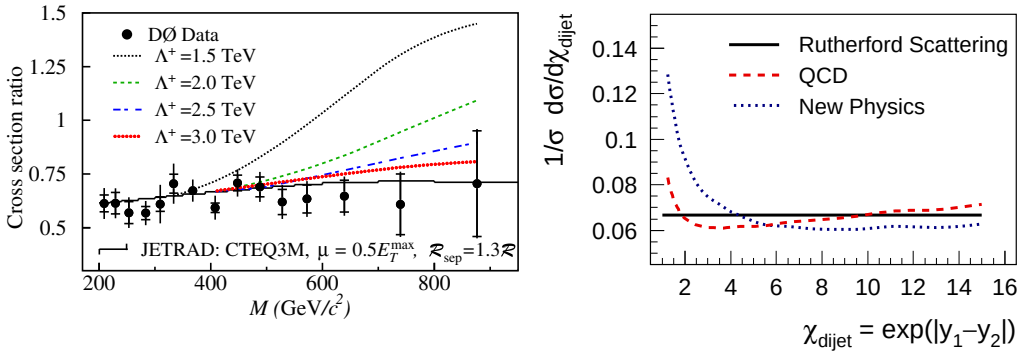

(a) (b)

Figure 2.7: Two probes for new physics: (a) Ratio of dijet mass spectra at $|\eta_{\text{jet}}| < 0.5$ and $0.5 < |\eta_{\text{jet}}| < 1.0$, with the theoretical curves for different quark compositeness scales Λ [42]. (b) Dijet angular spectrum versus dijet χ, showing the expected shapes for classical physics (Rutherford scattering), QCD and generic New Physics models [43].

2.5.3 Dijet azimuthal decorrelations

Multi-parton radiation is one of the more challenging aspects of QCD. A way to study radiative processes is to examine their impact on angular distributions, shown in Fig. 2.8 [44]. Dijet production in hadron-hadron collisions, in the absence of radiative effects, results in two jets with equal transverse momenta with respect to the beam axis and correlated azimuthal angles

$\Delta\phi_{\text{dijet}} = |\phi_{\text{jet},1} - \phi_{\text{jet},2}|$. Additional soft radiations causes small azimuthal decorrelations, whereas $\Delta\phi_{\text{dijet}}$ significantly lower than π is evidence of additional hard radiation with high p_T. Exclusive three-jet production populates $2\pi/3 < \Delta\phi_{\text{dijet}} < \pi$ while smaller values of $\Delta\phi_{\text{dijet}}$ require additional radiation such as a fourth jet in an event.

The results are well described in perturbative QCD at next-to-leading order in the α_s, except at large azimuthal differences where soft effects are significant. The Monte Carlo generators Herwig and Pythia are shown to describe data well, although Pythia needs increased initial state radiation (Pythia Tune A) for a good match to data.

The $\Delta\phi$ variable is fairly insensitive to the jet energy scale as additional jets are inferred from the azimuthal decorrelations and do not need to be reconstructed [45]. This provides a good independent test of the Monte Carlo generators that are used in the jet energy scale and jet p_T resolution derivation.

2.5.4 Three jet production

With the advent of NLO predictions for three-jet production [46] it has in principle become possible to use 2-jet and 3-jet production ratio and event shapes to extract α_s from a purely hadronic measurement. The three-jet mass spectrum would also probe the next-to-leading order properties of pQCD.

Dalitz distributions have been used as a practical way to analyze the three-jet production spectrum [47]. In this approach the three jet system is boosted into its center-of-mass frame and the three leading jets are numbered such that $E_3 > E_4 > E_5$. The Dalitz variables are defined as $X_i = E_i/m_{3-jet}$, where m_{3-jet} is the invariant mass of the 3-jet system. This naturally leads to $X_3 + X_4 + X_5 = 2$. The distribution of events in the X_3–X_4 plane, shown in Fig. 2.8, acts as a base for comparisons to NLO theory and Monte Carlo calculations. The first Run I results have been published by CDF [47], and DØ also has an ongoing analysis using similar techniques in Run II.

2.6 Summary and motivation for the measurement

In this review we have seen that earlier Tevatron measurements have already laid the groundwork for a precise measurement of the inclusive jet

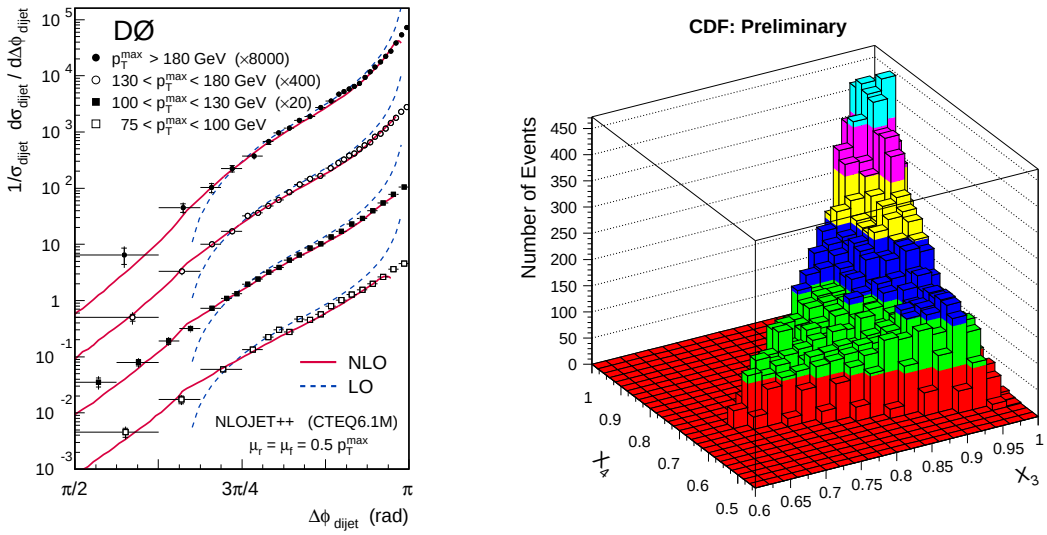

(a) (b)

Figure 2.8: (a) The $\Delta\phi_{\text{dijet}}$ distribution showing dijet azimuthal decorrelations [44]. Lines show leading order and next-to-leading order theoretical predictions. (b) Dalitz plot of three-jet production in the X_3–X_4 plane [47].

cross section. The Run I results have also been incorporated in the global PDF fits, resulting in increased gluon density at high p_T, a surprise at the time. The quark and low-x gluon PDFs have been stringently constrained by DIS measurements at HERA and at fixed target experiments, and by electroweak measurements at the Tevatron. This has left flexibility only to the high x gluon PDF, which is currently limited by the precision of HERA and Tevatron Run I measurements. Independent measurements of dijet angular distributions and azimuthal decorrelations have provided additional confirmation on the validity of the Standard Model and the implementation of its predictions in Monte Carlo models. Finally, new emerging analyses on three-jet production will test the validity of the higher orders of pQCD predictions. These measurements are important also for the LHC physics program and to look for beyond Standard Model effects.

From this review of past and current related measurements, two main goals stand out for the inclusive jet cross section measurement: precision measurement of the gluon PDF at high momentum fraction x and constraints on New Physics, particularly on the conjectured quark substructure (compositeness). The latter requires the former, as any claims of New Physics have as a prerequisite sufficient constraints on the parameters of existing models. There have been tempting hints of New Physics in Run I, but the standard

PDFs have shown enough flexibility to accommodate the observations within the Standard Model framework. The higher luminosity and energy reach of Run II should allow further constraints on the crucial parameters of the theory, finally substantiating or refuting the claims made in Run I.

On the experimental side there are three main requirements to reach the aforementioned physics goals: reduce systematic and statistical uncertainties at the very highest p_T bin of the measurement, extend the measurement to high rapidities, and carefully calculate the uncertainty correlations between measurement points. The high p_T measurement is the natural place to look for New Physics effects. The extension of the measurement to high rapidities, along with precise knowledge of the uncertainty correlations, will allow strong constraints on the PDFs and will facilitate the interpretation of the high p_T results in the Standard Model framework.

Chapter 3

Status of theoretical predictions

This chapter will review the current status of the theoretical predictions in quantum chromodynamics (QCD), the theory used for predicting the inclusive jet cross section. The theoretical framework naturally divides into sections on perturbative QCD (pQCD) predictions, associated experimentally determined parton distribution functions (PDFs), non-perturbative corrections, and finally on Monte Carlo generators. The Standard Model [48], the highly successful framework on which particle physics has been built for the past 40 years, is only briefly covered here as it is considered standard textbook material. The interested reader will find a useful introduction *e.g.* in Ref. [49].

3.1 Introduction to the Standard Model

The Standard Model of particle physics is in essence a description of the world at the very smallest distance scales. It is a relativistic quantum field theory that combines the familiar electromagnetic force with two other forces, the weak force and the strong force, only acting at sub-atomic distances. The dominant force in the macroscopic scales, gravity, is negligible at the distances normally considered in particle physics and is not part of the Standard Model.

According to the Standard Model, all the forces are mediated by force carrying particles, the spin-0 and spin-1 bosons, listed in Table 3.1. In addition, all the matter is made up of spin-1/2 particles, fermions, that come in two types, quarks and leptons. These are also listed in Table 3.1. The distinctive feature of the quarks is that they can interact through the strong force, in

Table 3.1: Elementary particles and some of their properties.

Fermions

	Generation 1		Generation 2		Generation 3		Charge
Quarks	Up Quark	u	Charm Quark	c	Top Quark	t	$+\frac{2}{3}$
	Down Quark	d	Strange Quark	s	Bottom Quark	b	$-\frac{1}{3}$
Leptons	Electron	e	Muon	μ	Tau	τ	$+1$
	Electron Neutrino	ν_e	Muon Neutrino	ν_μ	Tau Neutrino	ν_τ	0

Bosons

Electromagnetic force		Weak force		Strong force	
Photon	γ	Gauge bosons	Z^0, $W^\pm$	Gluons	g
Higgs field		Higgs boson	H		

addition to the weak and electromagnetic force felt by the other particles. Neutrinos carry no electric charge and interact only through the weak interaction. The quarks and leptons are divided into three generations, each with a different mass[1] and flavor, but otherwise identical properties. Only the neutrinos and the lightest particles of each generation are stable. All the ordinary matter in the universe is made of electrons, neutrinos, and up (u) and down quarks (d) inside protons (uud) and neutrons (udd).

The Standard Model comprises quantum electrodynamics (QED), electroweak theory, and quantum chromodynamics. The gauge symmetry group of the full Standard Model is the $SU(3) \times SU(2) \times U(1)$ group in which the sub-group $SU(3)$ represents QCD and $SU(2) \times U(1)$ the unified electroweak theory. It has been hypothesized that the symmetry group of the Standard Model is actually a subgroup of a single large symmetry group which unifies the forces at high energies (far beyond the current experimental reach). Such theories are known as Grand Unified Theories and they are usually linked to the currently popular supersymmetric models that predict the existence of heavier supersymmetric partners for all fermions and bosons, and a multitude of Higgs bosons.

[1]The neutrinos have been recently shown to have masses by atmospheric and solar neutrino measurements [65], *e.g.* by the Kamiokande [66] and Soudan mine [67] experiments.

3.1.1 Quantum electrodynamics and the weak force

The theory of electromagnetic interactions, QED, is the most precisely tested theory to date. It is a very powerful calculational tool when used with perturbation theory. In this approach the QED Lagrangian is developed into a Taylor series of the electromagnetic coupling constant α. Because the coupling constant has a small value, $\alpha \sim 1/137$ [114], the series converges very quickly.

The QED has been combined with weak interactions in the Weinberg-Salam-Glashow model, or the electroweak theory. According to this theory the weak interaction is identical with the electromagnetic force, except that its force carriers, the Z^0, W^+ and W^- vector bosons have a high mass that causes the force to have a very short range and be weak at low energies. At energies much higher than the Z mass of 91.1876 GeV [114] the electromagnetic and weak force unite into a single force. The validity of the electroweak theory has been established by the observation of the charged and neutral currents it predicts, and by the observation of the weak vector bosons.

The electroweak symmetry breaking has been explained by a hypothetical Higgs field that acquires a non-zero vacuum expectation value and creates the observed masses of the elementary particles, including the masses of the vector bosons Z and W [50]. A fundamental consequence of the Higgs field is the existence of its force mediator, the Higgs boson. This long-sought particle is the last missing piece of the Standard Model.

3.1.2 Quantum chromodynamics

The most interesting ingredient of the Standard Model for this thesis is QCD. It was developed following the same general symmetry principles that were so successful in formulating the $SU(2) \times U(1)$ electroweak theory. Quantum chromodynamics is based on the simplest symmetry group, $SU(3)$, that describes the observed multitude of baryons (three quarks) and mesons (quark and antiquark), jointly known as hadrons. In a sense the formulation of QCD could be compared to the impact the atomic model of protons, neutrons and electrons had for the periodic table of elements in chemistry. At the time QCD was formulated, physicists had already found hundreds of "elementary" particles. This multitude was then explained by the quark theory that forms the basis of QCD.

The charge-equivalent of the strong force is known as color. There are three colors, red, green and blue for quarks, and three corresponding anticolors for

antiquarks. According to this model a zero net color charge (white) can be obtained by adding equal amounts of red, green and blue, or by adding equal amounts of color and its corresponding anticolor. An interesting consequence of the $SU(3)$ symmetry is that there are eight different mediators of the strong force, known as gluons. In a simplistic picture each of the gluons carries a color and another anticolor[2].

The gluons can interact with themselves, unlike the photon or the vector bosons. This has important consequences for QCD that makes it very different from weak and electromagnetic force. Because of the gluon self-interactions the potential of the color field grows with distance between the color charges of quarks. At sufficiently large separations the field grows large enough to create quark-antiquark pairs from the vacuum. For this reason bare color charges, "naked quarks", cannot be observed at macroscopic distances larger than the size of the atomic nucleus. Only color-neutral combinations of three quarks or a quark and antiquark are allowed. This phenomenon is know as quark confinement. The second consequence of gluon self-interactions is that at very small separation the strong force becomes sufficiently weak that the quarks can be considered as essentially free particles. The so-called asymptotic freedom happens at distance scales smaller than the size of the proton, about 10^{-15} m.

In the simplistic model offered earlier, the protons that are collided at Fermilab are made of two up quarks and a down quark. The antiprotons would correspondingly consist of two anti-up quarks and an anti-down quark. The antiparticles are traditionally denoted by a bar, such that we can write proton as uud and antiproton as $\bar{u}\bar{u}\bar{d}$. The quarks in this static three-quark picture are called valence quarks. The actual structure of the proton is far more complex and dynamic as shown schematically in Fig. 3.1. In addition to the valence quarks the proton contains a number of so-called sea quarks, virtual quark and antiquark pairs briefly blinking into existence from vacuum before disappearing again. The lifetimes and momenta carried by the sea quarks are limited by the Heisenberg uncertainty principle, $\Delta E \Delta t \leq \hbar$. The strong color field inside the proton also means that a large number of gluons occupy the proton at any given time, most of these very soft.

The proton constituents — sea quarks, valence quarks and gluons — are jointly known as partons. The number and momenta of the partons are constantly evolving. The time-average momentum distributions of the partons,

[2]More precisely, each of the gluons carries equal amounts of color and anticolor, but not necessarily just one of each. There are eight orthogonal, non-white, combinations of colors plus anticolors and thus eight, not *e.g.* six or nine, different gluons.

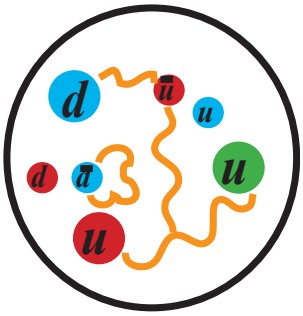

Figure 3.1: Schematic structure of the proton. Large disks represent the three valence quarks and small disks sea quarks, wiggly lines are gluons.

know as parton distribution functions (PDFs), are discussed in more detail in Section 3.3. The experimentally determined PDFs act as input for the pQCD and Monte Carlo calculations, described in the following section.

3.1.3 Numerical solutions of QCD

There have been three main approaches to solve the equations of QCD: lattice QCD and perturbative QCD, which are based on first principles, and the more phenomenological approach of using Monte Carlo models that borrows from pQCD.

In lattice QCD time and space are divided into small elements that are ordered into lattices. The discretized QCD equations are then solved for these elements, evolving the system in time. This approach is calculationally very heavy, even for relatively small lattices, because the equations operate in four dimensions and require multidimensional integration. Lattice QCD has been successful in calculating the masses of a few mesons, although these calculations have generally required years of computer time on large farms. It is also very useful for studying phenomena like quark confinement and quark-gluon plasma, but is rarely applied to interactions between particles.

Perturbative QCD imitates the successful application of perturbation theory to QED. The main problem in QCD is that the running coupling constant α_s is close to 1 at energies below about 1 GeV, which is the energy equivalent of the the mass of the proton, rendering the perturbative approach useless. At higher energies the magnitude of α_s decreases and at 15 GeV the coupling is roughly $\alpha_s \sim 0.1$, making perturbative calculations possible. The series still converge much more slowly than for QED. The best current predictions of perturbative QCD give barely 10% accuracy for the inclusive jet cross

section, while the precision of the QED predictions is measured in better than parts ber billion. The recent progress in pQCD is discussed in detail in Section 3.2 as it forms the main theoretical framework for this thesis.

The Monte Carlo models generate random events in a distinctly more phenomenological approach. Internally they often use a leading order matrix element calculation combined with a parton shower model to simulate the hard scatter. In addition, the Monte Carlo generators model some of the more complex non-perturbative aspects of QCD, such as the underlying event and hadronization. These processes are difficult to solve exactly so empirical models are used instead. The non-perturbative aspects of QCD are discussed in Section 3.4 and the leading Monte Carlo generators in Section 3.5. The Monte Carlo generators are used in this thesis for the modeling of the non-perturbative corrections to pQCD results. They are also used in combination with the detector simulation to test data-based analysis methods and derive small bias corrections for these methods.

3.2 Perturbative quantum chromodynamics

The perturbative QCD approach expands the QCD Lagrangian into a Taylor series of relatively simple interaction that can be visualized as Feynman diagrams. Figure 3.2(a) shows example diagrams in the leading order (LO) α_s^2 of perturbative QCD. The full set of leading order diagrams is presented in Fig. A.1 in Appendix A. These represent $2 \to 2$ scattering of the incoming partons from the proton and the antiproton. At high jet p_T the quark-antiquark annihilation/scattering process is dominant.

The scattering of partons inside the proton and the antiproton is shown schematically in Figure 3.3. The outgoing partons form jets by hadronizing. The hadronization process is complicated and must be described by non-perturbative QCD, covered later in Sec. 3.4. The cross section for the basic scattering process can be calculated in a fixed order α_s^m with the equation

$$\sigma = \sum_{ij} \int dx_1 dx_2 f_i(x_1, \mu_F^2) f_j(x_2, \mu_F^2) \hat{\sigma}_{ij} \left(\alpha_s^m(\mu_R^2), x_1 P_1, x_2 P_2, \frac{Q^2}{\mu_F^2}, \frac{Q^2}{\mu_R^2} \right), \tag{3.1}$$

where the summation goes over all the initial states of participating partons i and j. The parton distribution functions f_i, f_j multiply the matrix element, or point cross section, $\hat{\sigma}_{ij}$ for an interaction evaluated at a momentum transfer $Q^2 = E_T^2$. The parameters μ_F and μ_R indicate the factorization and renormalization scales, respectively. The x_1 and x_2 are the momentum

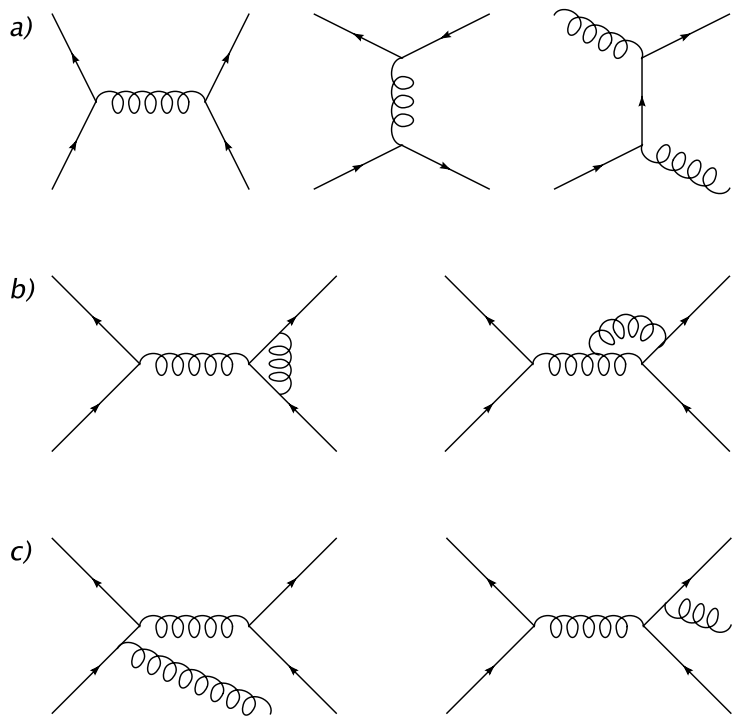

Figure 3.2: Leading pQCD Feynman diagrams at high p_T. (a) Leading order (LO) diagrams, (b) next-to-leading order (NLO) diagrams with virtual gluon loops, (c) NLO diagrams with initial state radiation (ISR) and final state radiation (FSR).

fractions of the total momenta P_1 and P_2 of the proton and the antiproton carried by the scattering partons.

The latest developments in pQCD use next-to-leading order (NLO) theory with the resummation of the leading logarithms of the next-to-next-leading order theory (NLL) in the so-called 2-loop approximation [51]. Figures 3.2(b) and 3.2(c) show examples of NLO contributions. These include the tree-level diagrams of three-jet production in Fig. 3.2(c), but also contributions from internal gluon loops in Fig. 3.2(b) although the nominal number of vertices is higher.

A proper treatment of pQCD requires the specification of a renormalization scale μ_R to remove non-physical infinities arising in a fixed order of the perturbation theory. These infinities are not present in the full theory. At lower orders of the theory the theoretical uncertainty on the jet cross section due to renormalization scale dependence is quite sizable. Typical choices set the μ_R and μ_F close to the hard scale Q, with half and twice of this scale used

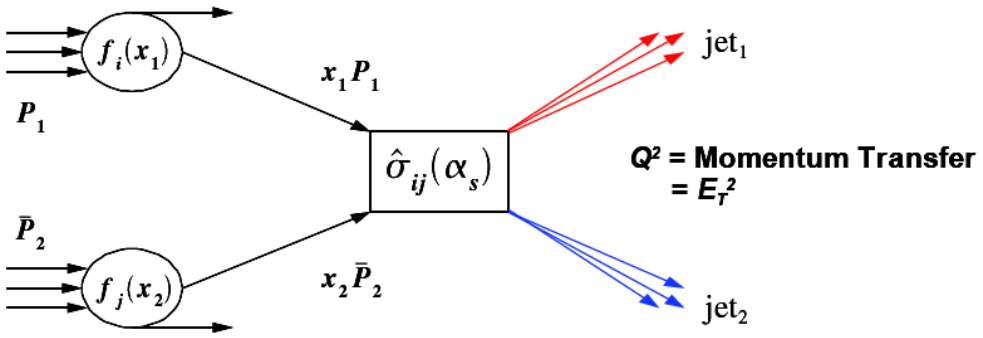

Figure 3.3: Schematic of a $2 \rightarrow 2$ scattering process of partons inside a colliding proton and antiproton. Only one parton of each hadron participates in the primary hard-scatter, denoted with the matrix element $\hat{\sigma}_{ij}$. The outgoing partons promptly hadronize into jets.

to estimate the theoretical scale uncertainty (DØ prefers $\mu_R = \mu_F = p_T$, whereas CDF does $\mu_R = \mu_F = p_T/2$). For NLO theory this uncertainty is in the order of 10% over the full p_T range of the inclusive jet cross section measurement as shown in Fig. 3.4. When the NLL corrections are added to NLO, the scale dependence is significantly reduced especially at the low end of the p_T spectrum.

3.2.1 pQCD generators

The pQCD jet cross sections are usually computed using Monte Carlo integration of Eq. 3.1 in LO or NLO. Although not explicitly written on the equation, the double-differential (versus transverse momentum and rapidity) inclusive jet cross section has cuts on the final state observables (p_T and y bins) that are easiest to implement using MC. The equations can also be solved analytically only up to NLO.

The current standard NLO Monte Carlo program is NLOJET++ [52] that is commonly used with the CTEQ6 family of PDFs [20, 21]. Evaluating the matrix elements using this program can be very time-consuming, taking days of CPU time, so estimating uncertainties using many different PDF sets is not very practical. Instead, NLOJET++ is only used to solve the matrix elements once for a grid in x and Q^2. The matrix elements are then used as cross section weights for *a posteriori* inclusion of arbitrary PDFs. A practical implementation of this approach is given in the fastNLO [53] program that can evaluate PDFs in seconds once the matrix elements have been calculated

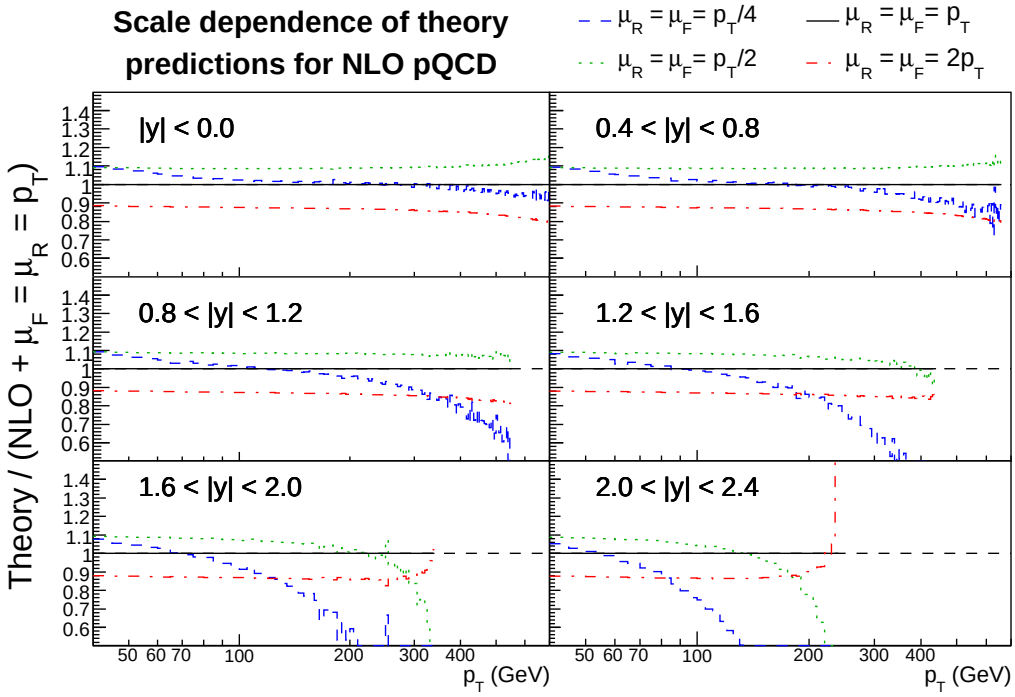

Figure 3.4: Uncertainty on the inclusive jet cross section due to the choice of the renormalization scale μ_R in NLO theory.

by NLOJET++. A unique feature in fastNLO is the inclusion of the $O(\alpha_s^4)$ threshold correction terms (in the 2-loop approximation mentioned earlier) to the inclusive jet cross section.

3.3 Parton distribution functions

In the simplest model of proton structure, the proton consist of three valence quarks, two up (u) quarks and a down quark (d). The strong color field between the quarks creates a large number of gluons (g) which interact among themselves, and may also give rise to virtual quark-antiquark pairs (quark loops) such as the strange quark-antiquark ($s\bar{s}$). At any given instant of time the proton contains a number of additional quarks and gluons, jointly known as partons, created by the dynamic interactions between the proton constituents. This dynamic contribution is known as the sea. Figure 3.5 shows the parton distribution functions for the leading proton constituents, u, d, g and s.

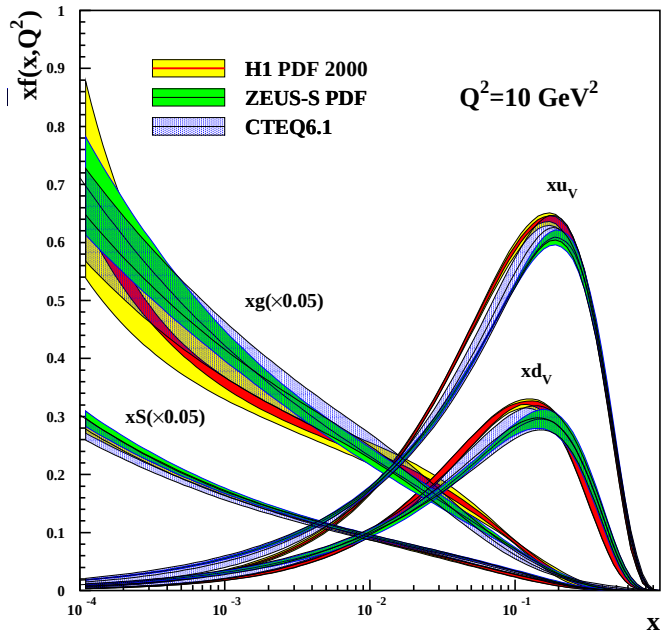

Figure 3.5: Proton parton distribution functions for gluons (g), sea quarks (S), the up valence quarks (u_v) and the down valence quark (d_v). The horizontal axis shows the momentum fraction x carried by each parton, and $f(x, Q^2)$ gives the probability density of finding a parton at given interval dx. The probability density is multiplied by the momentum fraction such that the area on the graph gives the total fraction of proton momentum carried by each parton type. Gluon and sea quark distributions are multiplied by 0.05 for presentation purposes.

It should be noted that the proton also contains small amounts of antiquarks, heavier quarks c, b, t and any other particles allowed by the Standard Model in the sea. The non-valence quarks have equal contributions of quarks and antiquarks such that the proton would contain *e.g.* similar amount of $\bar{s}$ as s shown in Fig. 3.5. The valence quark contribution is clearly visible on the PDF plot, with u_v carrying twice the fraction of proton momentum (area on the plot in linear scale) compared to d_v, and a significant amount of momentum is also carried by the low-x gluons. The non-valence u and d contributions are comparable to the strange quark sea, but the overall proton content is dominated by the gluon sea.

3.3.1 Experimental input for PDFs

The main source for the PDFs, especially for the quark part, have been the ep-scattering experiments H1 and ZEUS at HERA, discussed in Ch. 2, and fixed target experiments (BCDMS [26, 27], NMC [28]). The PDF uncertainties of CTEQ6.1 are mainly limited by the precision of H1 and ZEUS experimental uncertainties at low x, as can be appreciated by the size of the uncertainty bands in Fig. 3.5. The high x part of the PDFs is largely constrained by the fixed target experiments.

Due to the nature of the ep scattering (electrons do not directly interact with gluons), the HERA experiments are not sensitive to the gluon PDF in the leading order of pQCD. They do still provide the leading constraints to the gluon PDF at low x through higher order corrections, but especially the high-x gluon PDF remains relatively poorly constrained as it is only accessible via jets at HERA. Currently the leading constraints to the high-x gluons have come from the Tevatron Run I inclusive jet cross section measurements at high Q^2, and from the fixed target experiments at low Q^2.

3.3.2 Available PDF sets

CTEQ6.5M / CTEQ6.1M

The main PDF set used in this analysis is provided by the CTEQ collaboration, chosen over the MRST2004 fit because of its detailed PDF uncertainty analysis. The latest global fit from the CTEQ collaboration, dubbed CTEQ6.5M [150], utilizes DØ and CDF Run I measurements, as well as the most recent deep inelastic scattering (DIS) data from HERA and existing fixed target DIS and Drell-Yan (DY) data. A main feature of the CTEQ6.5M PDF set is the provision of 40 eigenvector basis PDF sets, representing 20 independent up and down variations of the PDFs within the 95% confidence level of the data sets used in the fit. Figure 3.6(a) shows the main parton distributions in the CTEQ6.5M fit and Fig. 3.6(b) shows the uncertainty in the gluon PDF[3] at a typical high p_T momentum transfer for the DØ experiment ($Q^2 = (500\ \text{GeV})^2$).

The earlier commonly used CTEQ6.1M [21] PDF set provides almost identical central prediction for the inclusive jet cross section measurement as CTEQ6.5M, but has almost twice as large PDF uncertainty. The CTEQ6.1M is almost equivalent to the CTEQ6M PDF set [20], but provides more reli-

[3]Such plots can be readily obtained from http://durpdg.dur.ac.uk/hepdata/pdf3.html.

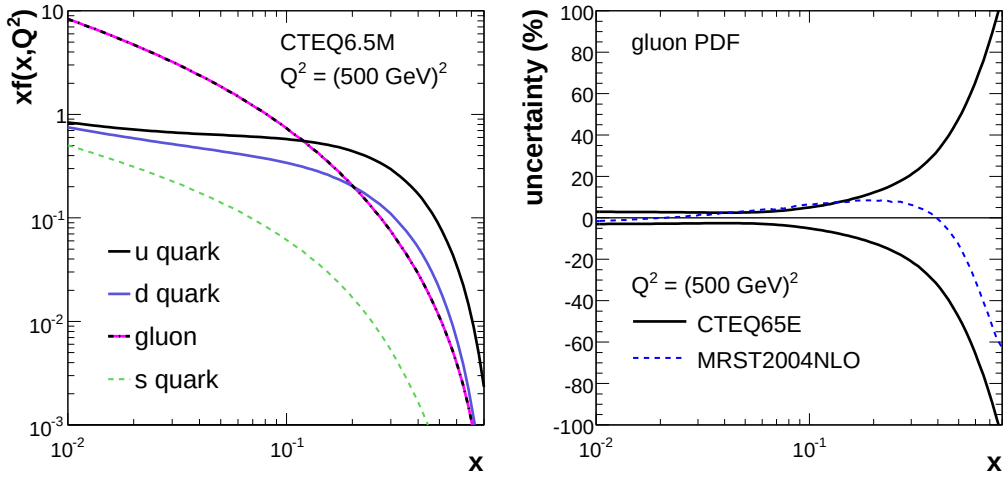

(a) (b)

Figure 3.6: (a) Main parton distributions for CTEQ6.5M PDF set. The up and down quark contributions include both valence and sea quarks.
(b) Uncertainty of the CTEQ6.5M gluon PDF (solid lines) compared to the ratio of MRST2004 and CTEQ6.5M central values (dashed line) in percentages at $Q^2 = (500\ \text{GeV})^2$ [54].

able and symmetrical uncertainties. Unlike in earlier CTEQ families of fits CTEQ4 and CTEQ5, the enhanced high-x gluon PDF is naturally part of the standard CTEQ6 description. Previously the Tevatron jet data was given special weight in the CTEQ4HJ, CTEQ5HJ fits, leading to increased high-x gluon PDF, whereas the more commonly used CTEQ4M and CTEQ5M had a more conventional fit with no special emphasis on Tevatron data.

MRST2004

Another widely used PDF parametrization is provided by Martin, Roberts, Stirling and Thorne (MRST). Their latest NLO global fit MRST2004 [22] has a new, more physical parametrization of the gluon distribution that provides an improved description of DØ Run I data at $|\eta| < 3.0$. The differences with respect to CTEQ6.5M central value are reasonably small, with the greatest difference being in the high-x gluon description. This difference is nevertheless within the CTEQ6.5M uncertainty band, as seen in Fig. 3.6.

Future QCD analyses from DØ may consider using the latest NNLO parametrization MRST2006 [64] when the NNLO fits from CTEQ become available.

The MRST2006 fit also provides a PDF eigenvector set comparable to the CTEQ6.5M.

Alekhin

The PDF fits by Alekhin [55] differ from CTEQ and MRST in that they only use DIS data, not the DY or Tevatron jet data. This gives Alekhin's fits a more predictive status than the "postdictions" of CTEQ and MRST. A central consequence is that the high-x gluon PDF is considerably lower than that for the recent CTEQ and MRST fits (-60– -80% at 600 GeV). It is, however, still almost within the CTEQ uncertainty band.

Alekhin's fits do not contain as much freedom for the high x gluon as the recent CTEQ and MRST fits. This extra freedom has been largely introduced to explain the Tevatron Run I data, and it is one of the motivations of this analysis to confirm or refute the Run I observations.

3.4 Non-perturbative QCD

3.4.1 Hadronization corrections

Perturbative QCD gives a simple picture of the parton-parton interactions as $2 \rightarrow 2$ or $2 \rightarrow 3$ processes. This is only part of the true picture. The outgoing partons carry color charge, and as such create strong color fields between themselves and the rest of the proton. With increasing separation, these color fields grow strong enough to create additional quark-antiquark pairs that will consume some of the energy and momentum of the original parton. This hadronization process continues until color charges are neutralized and there is not enough energy left to create additional quark-antiquark pairs. The process is non-perturbative and is currently only described by phenomenological models.

The end result of the hadronization is that the original parton is transformed into tens of mesons and baryons. These particles form what is here referred to as a particle jet, a collimated spray of particles and their decay products. The energy deposits of the particle jet are observed as a calorimeter jet, a collection of calorimeter energy clusters.

As some of the momentum of the original parton is lost to the proton or antiproton through the color fields present in the hadronization process, the observed energy of the calorimeter and particle jets is slightly lower than

that of the original parton giving rise to the jet. Figure 3.7 shows that the resulting corrections to the inclusive jet cross section are in the order of 5–20% for the momentum range of interest.

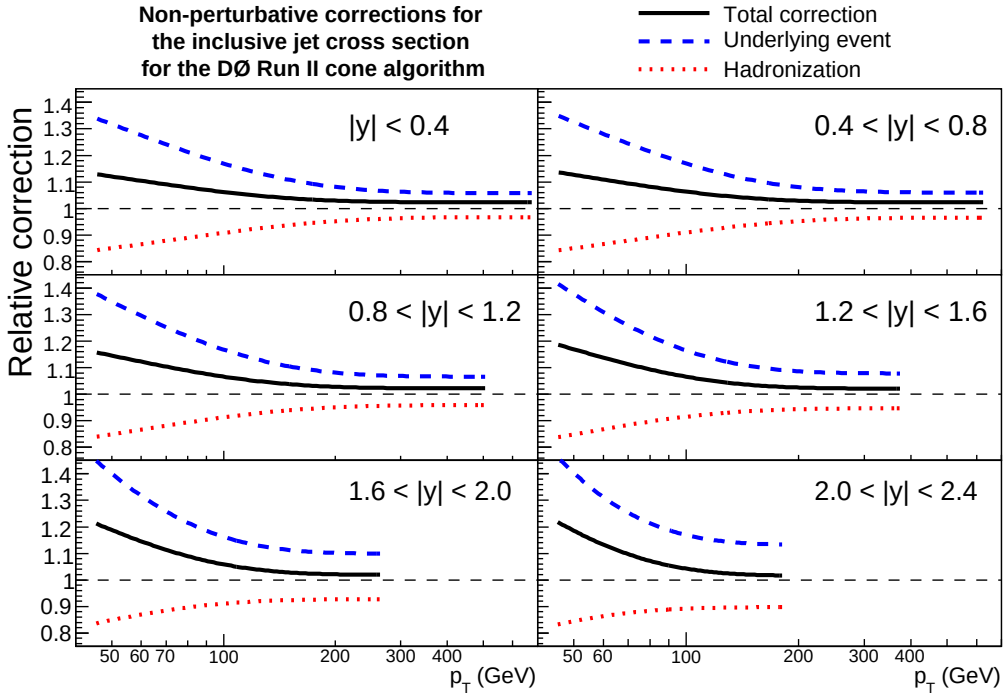

Figure 3.7: PYTHIA prediction for the size of hadronization and underlying event corrections to the inclusive jet cross section.

3.4.2 Underlying event

In addition to the hadronization process, the partons in the proton that did not take part in the hard scattering, generally referred to as spectators, carry a net color charge opposite in sign to that carried away by the scattered partons. This color charge interacts with the outgoing partons, soaking some of their energy, which then gets radiated as particles isotropically in all directions. The spectator partons may also have additional soft interactions independent of the hard scatter, producing more radiated energy. Some of this isotropic radiation overlaps with the jet cones, increasing the observed energy of the particle and calorimeter jets.

The non-perturbative corrections are best studied using phenomenological models of the hadronization process implemented in Monte Carlo event gen-

erators, discussed in the next section. Figure 3.7 shows the PYTHIA prediction for the hadronization and underlying event corrections to the inclusive jet cross section in the central region of the calorimeter. This result was obtained using PYTHIA v6.412 tune QW[56] with CTEQ6.1M PDFs. The prediction was tuned to to the Tevatron data, as discussed in the next section.

3.5 Monte Carlo event generators

Many particle physics processes are readily studied using Monte Carlo simulations that combine parton shower or matrix element hard scatter to non-perturbative hadronization and underlying event models, and finally to detector simulation. These Monte Carlo programs are referred to as event generators to distinguish them from the MC programs used for pure pQCD calculations. The Monte Carlo event generators can provide direct predictions of jet observables such as particle jet composition, particle multiplicities, energy spectra, distribution in $\eta - \phi$ space *etc.* The calorimeter jet properties often depend on these quantities in a complex way so many effects can be reliably studied only by feeding the full Monte Carlo simulation of an event through a detailed detector simulation. The detector simulation will create the tracker hits, muon detector hits and calorimeter energy deposits with realistic efficiencies, responses and resolutions, then digitize these and process through a simulation of the detector electronics before events are reconstructed in a process identical to data. The following sections discuss two favorite choices of Monte Carlo event generators, PYTHIA [96] and HERWIG [97], the detector simulation with GEANT and data-based pile-up.

3.5.1 Pythia

The DØ collaboration uses PYTHIA version 6.323 [57] with CTEQ6L1 [20] PDFs for primary Monte Carlo generation. PYTHIA hard scatter is based on a leading order QCD matrix element calculation and a parton shower model [58] whereby the participating partons radiate additional partons in a bremsstrahlung type process. This approach has been useful in describing the multijet topologies in data.

The resulting parton shower is hadronized (or "fragmented") using the Lund string model [59, 60], schematized in Fig. 3.8. In this model a color flux tube

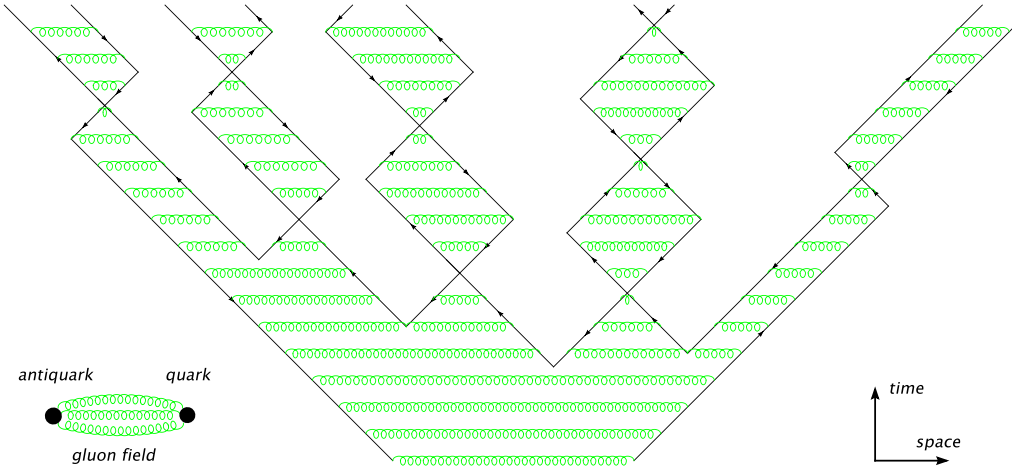

Figure 3.8: Schematic of the Lund string model. Breaks in the color flux tube (string) between quark and antiquark produce mesons ("yo-yo modes").

is formed between the outgoing quarks[4]. The flux tube acts as a massless relativistic string with a string constant $\kappa \sim 1$ GeV/fm. The lengths of the strings are of typical hadronic sizes, roughly 1 fm. As the quarks fly apart the potential energy stored in the string increases linearly. The string may break by producing a quark-antiquark pair. If either or both of the string remnants has sufficient energy, the fragmentation process continues iteratively on the string remnants. The fragmentation process ends when only on-mass-shell-hadrons remain, each hadron corresponding to a small piece of string with a quark in one end and an antiquark in the other. The hadronization model parameters have been tuned to LEP e^+e^- data.

The Lund model invokes the idea of quantum mechanical tunneling to create the string break-ups. This implies a suppression of heavy quark production, with $u : d : s : c \approx 1 : 1 : 0.3 : 10^{-11}$. Charm and heavier quarks are then expected to be only produced in the perturbative branchings $g \to q\bar{q}$.

Many of the resulting hadrons are unstable and quickly decay into observable stable (or almost stable) particles. The decays are based on experimental data on mass distributions and particle life-times. The decay products are normally distributed according to phase space, *i.e.* there is no dynamics involved in their relative distributions.

The remaining parts of the PYTHIA simulation involve the underlying event, including the beam remnants and multiple parton interactions. These are the least well understood aspect of the current generators, and only phe-

[4]Gluons will act as additional kinks in such flux tubes, or strings.

nomenological models exist. DØ uses the so-called "PYTHIA TUNE A" which was optimized to describe CDF Run I data.

Tunes of Pythia

Being largely based on phenomenological models, PYTHIA has a large number of changeable parameters. Several "tunes", or sets of these parameters, have been developed to get a good fit between PYTHIA and data. Of particular interest for this analysis are Rick Field's TUNE A and TUNE QW [56], both of which have been tuned to give a good description of previous Tevatron data, but with slightly different assumptions. The tuning has focused on giving a good description of the energy density in regions far from jets, affecting the underlying event description, and of the third jet distributions, affecting primarily the initial state radiation. The TUNE A has also been shown to give a good description of the jet shapes in dijet events [68].

3.5.2 Herwig

Although the physically well-motivated Lund string model used by PYTHIA has proved to be very successful in describing the hadronization process, and many other details of the high energy events are also reasonably successfully described, PYTHIA is not the final and only answer as the authors readily admit. Therefore it is often useful to compare to other event generators to get an idea of the uncertainties related to the physics models used.

HERWIG is another program successful in describing QCD events that takes many different approaches to the same basic physics. The latest version is HERWIG 6.5 [61]. The hard scatter and parton showers are modeled in a fashion similar to PYTHIA. The hadronization process is somewhat dissimilar and based on color clusters. In the cluster model color singlets are projected on a continuum of high-mass mesonic resonances (clusters). These decay to lighter well-known resonances and stable hadrons.

An important feature of HERWIG is the full inclusion of color coherence into the parton shower development. The quantum mechanical interference effects related to the color flow affect especially the spatial distribution of the third hardest jet in the event with respect to the positions of the two leading jets. Comparisons to data have shown that HERWIG provides a good description of the third hardest jet distributions, whereas the default PYTHIA description is not as good [63]. However, modification of some Pythia parameters like

PARP(67) that affect initial state radiation can produce comparably good fits to data [44].

3.5.3 Geant

The GEANT package [62] is not a Monte Carlo generator in the same sense as HERWIG and PYTHIA. Rather, it is a useful tool for propagating particles through matter on which the DØ Run II detector simulation is based. GEANT receives as input the stable hadrons produced by other Monte Carlo generators and models their passage through the dead and active material that makes up the detector. This description includes the productions of secondary particles by scattering off of the electrons and nuclei, and a model for the energy deposition and absorption by ionization and nuclear reactions.

As the incoming particles are tracked through the detector material they produce showers of secondary particles that may contain thousands of particles. The sheer number of particles combined with detailed calculations of energy loss and showering in material make the GEANT simulations computationally expensive. In some cases, such as in jet energy scale systematics studies, it is useful to replace the detailed detector simulation with a coarse parametrization of important effects in order to generate enough Monte Carlo statistics.

Pile up

Because the Monte Carlo underlying event simulations are known to be problematic and DØ detector simulation has suffered from some disagreement between data and Monte Carlo, the DØ collaboration has chosen an alternative route to describe the effects of high luminosities. In essence, the Monte Carlo event generation is based on a single interaction vertex. The effects of additional simultaneous proton-antiproton collisions are simulated by overlaying raw measured data on top of the Monte Carlo generated events. The raw data is collected with the Zero Bias trigger that has no other requirements than the timing of the bunch crossings. This procedure produces well the observed calorimeter energy density from the combination of the hard scatter, noise, pile-up and multiple interactions.

Chapter 4

Description of the DØ Detector

The DØ detector, shown in Fig. 4.1, is a large general purpose detector for the study of short distance phenomena at high energy proton-antiproton ($p\bar{p}$) collisions. The detector operates at the Fermi National Accelerator Laboratory's (Fermilab) Tevatron collider, studying proton-antiproton collisions at a center of mass energy of 1.96 TeV. The DØ detector was proposed in 1983 and operated successfully during Tevatron Run I in 1992–1996. The data collected at DØ led to the discovery of the top quark [69] and a measurement of its mass [70, 71, 72, 73, 74], a precision measurement of the mass of the W boson [75, 76, 77, 78, 79, 80, 81] and studies of jet production [6, 8, 4], among other accomplishments [82]. The Run I DØ detector is described in detail in Ref. [83].

For the Tevatron Run II, beginning in 2001, the DØ detector was upgraded to cope with Tevatron's increased luminosity and collision energy, and to improve the physics capabilities of the detector. The primary changes concerning this thesis were the installation of a solenoid magnet and a full upgrade of the readout electronics and trigger systems. Tevatron's collision energy was increased from 1.8 TeV in Run I to 1.96 TeV in Run II, and the peak luminosities have risen by over an order of magnitude. The upgraded Tevatron collider has 36 proton and antiproton superbunches colliding at intervals of 396 ns, compared to 6 bunches with 3500 ns between bunch-crossings in Run I. The high luminosity of the collider has meant that radiation hardness is a consideration for some detector components, and signal integration times have decreased, requiring faster electronics and upgraded trigger systems to be installed. The integrated luminosity of Tevatron Run II is expected to be between 4–8 fb^{-1} as opposed to the Run I integrated luminosity of 120 pb^{-1}, a factor of 40 improvement or more.

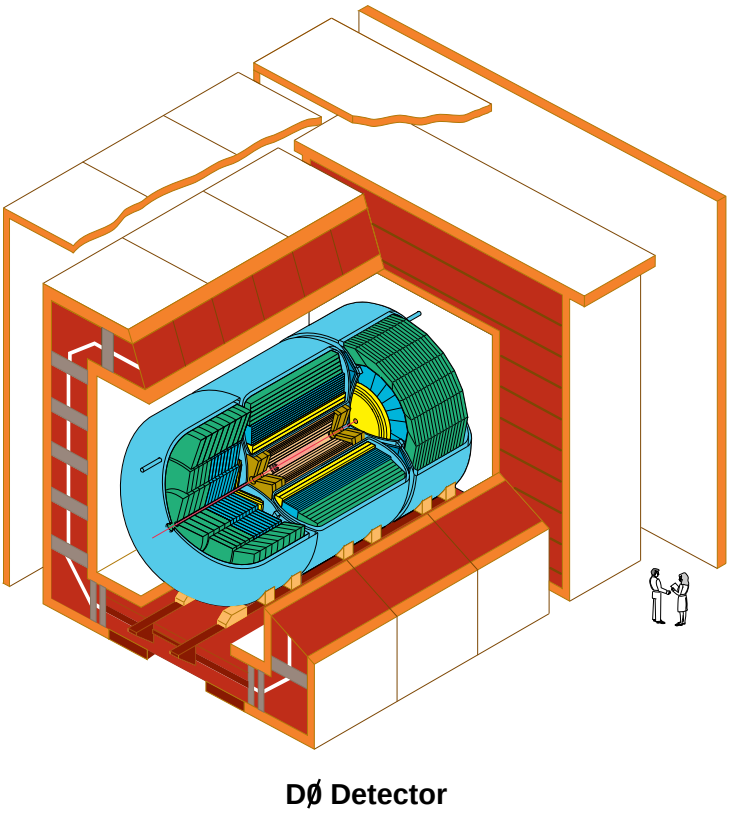

Figure 4.1: Isometric view of the DØ detector.

To improve the physics yield of the detector in Run I, the DØ detector was upgraded with new elements of the detector, including silicon microstrip tracker, central fiber tracker, solenoidal magnet, preshower detectors, forward muon detectors, and forward proton detectors. In this chapter we will focus on the detector components essential for the inclusive jet cross section measurement, whether old or new, and leave others to little or no mention. The upgraded DØ detector is described in detail in Ref. [84].

4.1 Tevatron collider

Although not strictly speaking part of the DØ detector, the Tevatron collider at Fermilab is an essential component of the experiment. The purpose of the collider is to provide the experiments with well controlled, tightly focused beams of protons and antiprotons that are collided at the center of the detector. The technical specifications require the interaction region (of

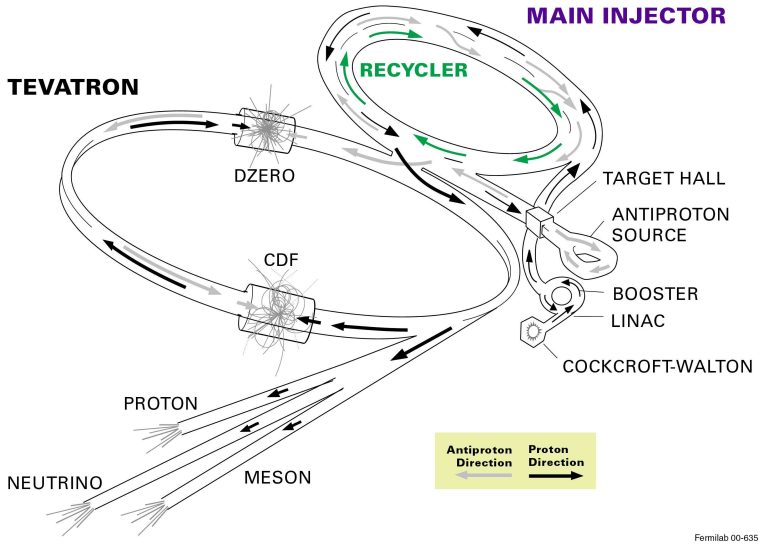

Figure 4.2: Fermilab Tevatron accelerator complex.

$\sigma_{x,y} \approx 40\mu$m, $\sigma_z \approx 30$ cm) to be within 1 mm of the geometric center of the detector in the transverse plane (xy) and centered to within a few centimeters of the middle point of the calorimeter in the longitudinal direction (z). The coordinate system is chosen to be right-handed, with z along proton direction and x pointing toward the center of the Tevatron ring. The following section will briefly outline the collider sybsystems, shown in Fig. 4.2.

The proton beam is created from a source of hydrogen gas (the antiprotons will be created at a later stage). The first stage of pre-acceleration is provided by the Cockroft-Walton. Inside this device the hydrogen gas is ionized to create negative ions that are accelerated to 750 keV. A linear accelerator will accelerate the ions to a further 400 MeV. At the end of the linear accelerator the ions pass through a carbon foil that strips the electrons and leaves just the positively charged protons. A small circular accelerator, the Booster, increases the proton beam energy up to 8 GeV.

The next step, Main Injector, serves multiple purposes. It's first task is to accelerate the protons to 150 GeV and insert them to the Tevatron ring. It also produces 120 GeV protons that are directed to a nickel target in the target hall to produce antiprotons that are then collected, focused and stored in the Accumulator ring (Antiproton Source). Once enough antiprotons have been collected, the Antiproton Source will send them to the Main Injector that accelerates them from 8 GeV to 150 GeV and injects them to the Tevatron ring, traveling in a direction opposite to the protons. In the final stage the

proton and antiproton beams are accelerated in the Tevatron ring to 980 GeV each. Before collisions are initiated the beams are "scraped" with collimators to remove unwanted halo particles and create tightly focused beams.

Accumulating sufficient numbers of antiprotons generally takes about 24 hours so the Main Ring will work in the antiproton production mode for quite some time before accelerating protons for injection in the Tevatron ring. Once a "store" is established in the Tevatron Ring, the Main Ring will keep accumulating antiprotons until the Main Control Room decides to dump the old beam and insert a new batch of protons and antiprotons. The stores usually last about 24 hours to allow enough time to collect antiprotons. The antiproton production rate is one of the main limiting factors for high sustained luminosities. To alleviate this problem the Main Ring tunnel has been installed with an Antiproton Recycler that stores the left-over antiprotons from the Tevatron ring, waiting to be re-injected.

4.2 Calorimeters

The calorimeters are the most important detector components for measuring high p_T jet properties, and an accurate and stable energy response is required for reliable jet cross section measurement. The DØ detector was constructed in Run I to provide a good measurement of electron, photon and jet energies in the absence of a magnetic field. In Run II the calorimeter remains the same. Despite a small added amount of dead material from the solenoid coil and reduced signal integration time the calorimeters, shown in Fig. 4.3, still retain most of their excellent energy measurement properties. However, several factors have decreased the high level of compensation between electromagnetic and hadronic showers that was the hallmark of the DØ detector in Run I, as will be discussed later in this section.

4.2.1 Central and end cap calorimeters

Both the electromagnetic and fine hadronic calorimeters are sampling calorimeters based on liquid argon and absorber plates of almost pure depleted uranium (U^{238}). The structure of the calorimeter cells is shown in Fig. 4.4. The incoming particles traversing the uranium absorber plates initiate showers of secondary particles that ionize argon in the gaps between the absorber plates. A high-voltage electric field collects the free electrons to the resis-

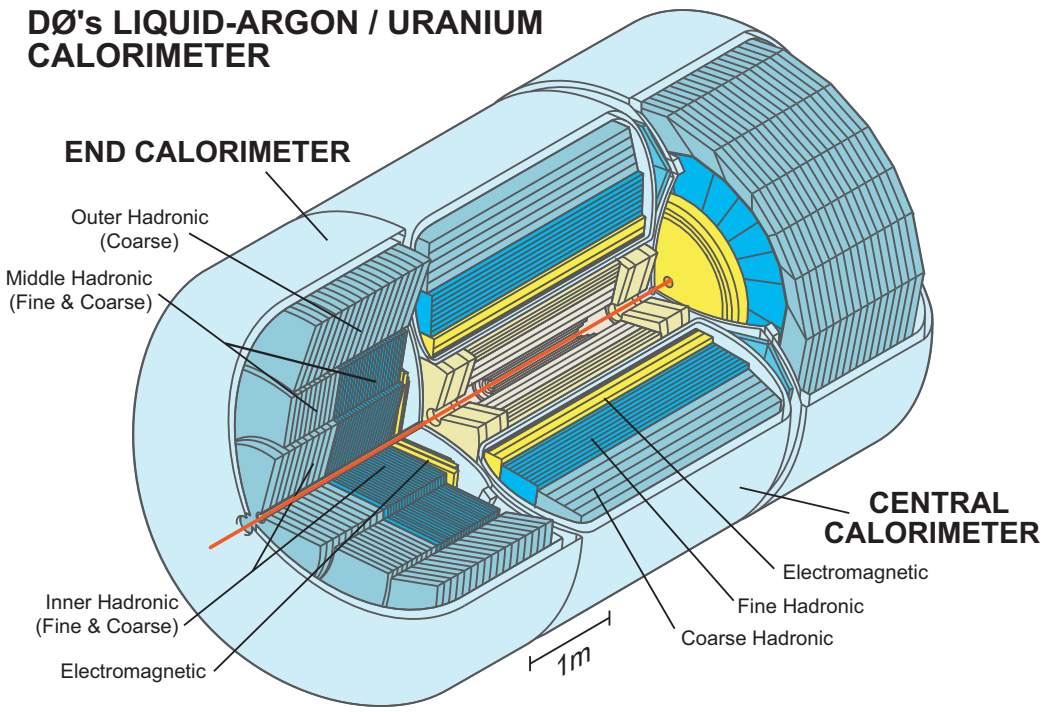

Figure 4.3: Isometric view of the central and two end calorimeters.

tively coated copper pads that act as signal boards. The copper coating on the inner surface is milled into the pattern needed for segmented readout.

The coarse hadronic calorimeter in addition deploys copper in central calorimeter (CC) and stainless steel in end cap calorimeter (EC) for the absorber plates. The choice of uranium absorber plates allows for a compact calorimeter system, leaving more room for the surrounding muon detector. Liquid argon provides a unit gain and stable, radiation hard calorimetry. On the downside, the use of liquid argon involves the complication of cryogenic systems. The fairly massive containment vessels (cryostats) add to the dead material in front of calorimeters and result in regions of uninstrumented material. For this reason the gap between CC and EC cryostats is instrumented with the intercryostat detector (ICD) and massless gap detectors (MG) without dedicated absorber plates.

The gap between absorber plates and read-out boards in the main calorimeters is 3.2 mm, leading to a 450 ns electron drift time across the gap. This provides a challenge with 396 ns between the bunch crossings in Run I (3500 ns in Run I). The calorimeter read-out electronics for Run II were designed for 132 ns between bunch crossings as was originally designed for

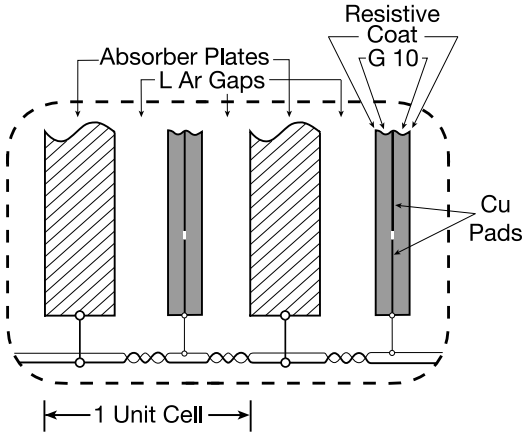

Figure 4.4: Schematic view of the structure of a calorimeter unit cell. Capacitor plates made of copper pads and G-10 fiberglass coated with resistive epoxy are sandwiched between depleted uranium absorbers and collect the charge liberated within the liquid argon gaps.

Run II. This shortened signal integration time has come with some cost to the performance of the calorimetry.

The DØ Run I calorimeter was nearly compensating (providing equal energy response to electrons and pions) with the e/π response ratio falling from about 1.11 at 10 GeV to about 1.04 at 150 GeV. This compares favorably [85] to the ratio 1.4 of most calorimeters. Part of this compensation was coming from the recovered energy of neutrons as they caused fissions of uranium nuclei, part from graduated absorber plate thicknesses. The time for the neutrons to thermalize before they can cause fissions is up to 1 μs [86], so much of this benefit is lost in Run II. Along with the recalibration of electromagnetic and hadronic calorimeter layer weights to accommodate shorter signal integration times this has reduced the level of compensation in the DØ Run II calorimeter, as will be discussed in Chapter 6. This has degraded the energy resolution and linearity of the calorimeters compared to Run I. Some of this degradation has been compensated in Run II with improved calorimeter cell response intercalibration, but the resolution still remains worse than it was in Run I.

The calorimeter is finely segmented to allow for a good position measurement of electrons, photons and jets. The pattern and transverse sizes of the readout cells are set by the transverse size of showers: $\sim$1–2 cm for EM showers and $\sim$10 cm for hadronic showers. In terms of variables more useful for physics, pseudorapidity η and azimuthal angle ϕ, the transverse size of particle jets

is $\Delta R = \sqrt{\Delta\eta^2 + \Delta\phi^2} \sim 0.5$. The calorimeter is segmented in 0.1 cells in η and $2\pi/64 \sim 0.1$ in ϕ at $|\eta| < 3.2$. This fine segmentation allows for probing the shape of the jets. At rapidities $|\eta| > 3.2$ the segmentation grows to 0.2 or more for both η and ϕ, but these high rapidities are not used for the jet cross section measurement because the jet triggers are limited to $|\eta| < 3.2$.

As shown in Fig. 4.5 the central calorimeter covers a range $|\eta| \lesssim 1$ and the two end cap calorimeters (north end cap, ECN, and south end cap, ECS) extend up to $|\eta| \approx 4$. The active medium in all these calorimeters is liquid argon. The calorimeters are kept within the cryostats at a constant temperature of approximately 80 K. The purity of the liquid argon is critical to the energy measurement as small amounts of contaminants, particularly oxygen, can have an impact on the measured signal. The contamination of the liquid argon was measured in the beginning of Run II [87] to be less than 0.30 ± 0.12 ppm for all three calorimeter cryostats. Contamination level of 1 ppm would result in approximately 5% signal loss. The purity has also been monitored with several radioactive sources *in situ*. The liquid argon purity has been extremely stable over time [84], resulting in a stable calorimeter response.

The electromagnetic calorimeter is composed of relatively thin 3 mm and 4 mm uranium absorber plates in CC and EC, respectively. The fine hadronic has slightly thicker 6 mm absorber plates, and the coarse hadronic is made of 46.5 mm of copper (CC) or stainless steel (EC). Useful measures for the depth of the calorimeter are *radiation lengths* (X_0) and *nuclear interaction lengths* (λ_A) for electromagnetic and hadronic particles, respectively. These are defined as the mean free path for bremsstrahlung in the material (gluon bremsstrahlung in the case of nuclear interaction lengths). The energy loss of the incoming particles behaves with distance according to

$$E_{\mathrm{em}}(d) = E_0 \exp^{-\frac{d}{X_0}}, \tag{4.1}$$

$$E_{\mathrm{had}}(d) = E_0 \exp^{-\frac{d}{\lambda_A}}. \tag{4.2}$$

The X_0 for uranium is 3.2 mm so each electromagnetic particle is expected to radiate once per plate, producing a quickly multiplying electromagnetic shower that is sampled at each step by the liquid argon. The shower maximum is expected to occur around $X_0 = 10$ where the EM calorimeter has finer segmentation for accurate position measurement of the incoming electrons and photons. The total depth of the EM calorimeter is about 20 X_0, containing electromagnetic showers well within the EM calorimeter. In contrast, hadronic particles interact more weakly, and the EM calorimeter only accounts for $\sim 0.8\lambda_A$. The fine hadronic layers compose additional 3 λ_A, and

the coarse hadronic another 3 λ_A. Overall the hadronic calorimeter at $\sim 7\lambda_A$ is deep enough to contain more than 98% of all the collision energy. However, a small uncertainty is accounted in jet calibration for possible punch-through of the very highest energy jets.

The hadronic showers develop quite differently compared to the electromagnetic showers that multiply copiously at each step. Most hadronic interactions produce one of the lightest mesons, pions π^+, π^- or π^0, each of these with probability 1/3. The charged pions continue to interact hadronically whereas the neutral pions quickly decay into two photons, producing a quickly multiplying electromagnetic shower. Except for the small amount of ionization produced by the charged hadrons, practically all the energy de-

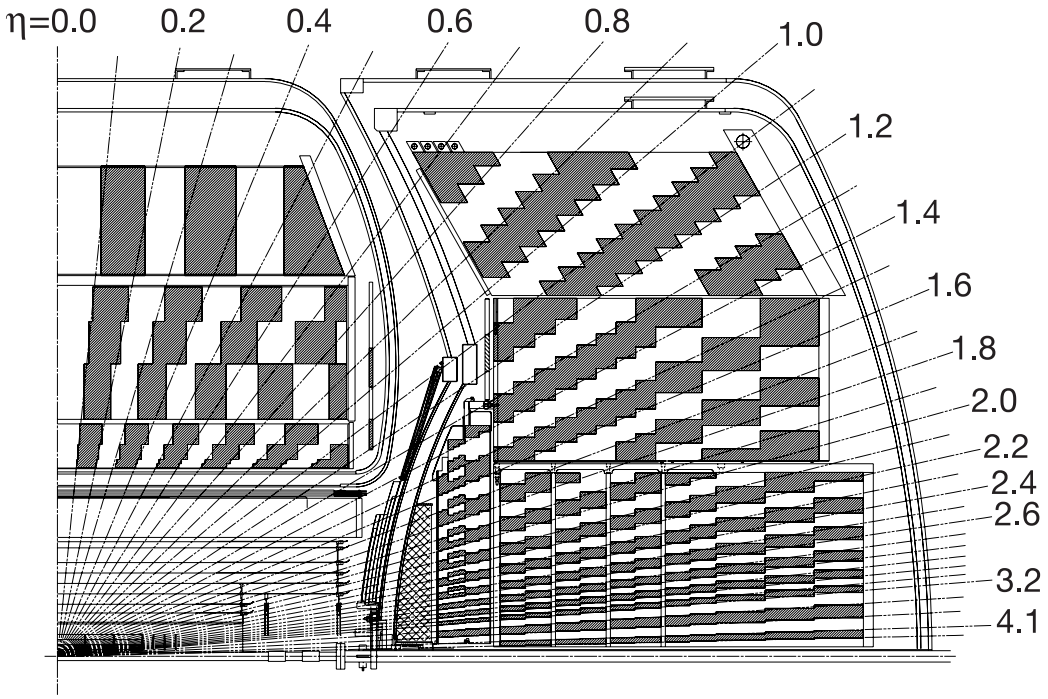

Figure 4.5: Side view of a quadrant of the DØ calorimeters showing the transverse and longitudinal segmentation pattern. The shading pattern indicates the cells for signal readout. The lines indicate the pseudorapidity intervals seen from the center of the detector. The intercryostat detector is visible as a thin tile in front of the EC cryostat at $1.1 < |\eta| < 1.4$ and the massless gaps as thin tiles inside the CC cryostat at $0.8 < |\eta| < 1.2$ and the EC cryostat at $1.0 < |\eta| < 1.4$.

posited by hadronic jets comes from the electromagnetic showers produced by the π^0s. Fluctuations in the fraction of π^0s produced at each step cause large stochastic fluctuations in the amount of measured energy, accounting for the much poorer energy resolution of jets than electrons.

4.2.2 Intercryostat detector and massless gaps

The region between the central and end cap cryostats is instrumented with the intercryostat detector (ICD) and massless gaps (MG). The ICD and MG detectors provide energy measurement for the otherwise poorly instrumented region between the cryostats at roughly $0.8 < |\eta| < 1.4$, where the depth of the dead material coming from cryostat walls, stiffening rings and cables varies rapidly with rapidity.

The ICD relies on photomultipliers (PMTs) recording the signal from plates of scintillating plastic and covers the region $1.1 < |\eta| < 1.4$ in rapidity. The signal from the ICD is stretched to match that of the EM calorimeter and provides a good approximation to the EM calorimetry that is absent at $1.2 < |\eta| < 1.35$. Many of the photomultipliers were recycled from Run I and have shown aging problems in Run II. To increase their response some PMTs have been operated at a high voltage above their designed limit, resulting in unstable response as a function of time and luminosity. Several aging PMTs were later replaced for Run IIb.

The ICD is supplemented by the massless gap detectors that are placed inside the cryostat walls in CC and EC at $0.8 < |\eta| < 1.2$ and $1.0 < |\eta| < 1.3$, respectively. The massless gaps collect electrons liberated by the liquid argon and have signal boards identical to the standard calorimeter modules. Unlike other calorimeter cells, they do not have dedicated absorber plates (hence are *massless*), but measure instead showers that develop in the cryostat walls, calorimeter support structures and other cells.

4.2.3 Preshower detectors

The preshower detectors, shown in Fig. 4.6, act as both calorimeters and tracking system. The central preshower (CPS) is placed between the solenoidal magnet and central cryostat, and the forward preshower (FPS) is placed in front of the end cap cryostat just around the luminosity monitor. Their purpose is to aid in electron identification and background rejection for both triggering and offline reconstruction. The preshower detectors are based on triangle shaped scintillator strips that are placed in two stereo layers. Elec-

trons will readily shower in the material in front of the preshower and the shower can be measured with several preshower scintillator strips. Other particles will generally only leave a minimum ionizing trail in one strip. The preshower detectors will also aid in matching between tracks and calorimeter showers, and in recovering electromagnetic energy losses in the solenoid magnet, cables and supports.

The preshower detectors are not directly used in this thesis, but the CPS shower shape measurements form an important part of the photon identification cuts that are used in the jet energy scale measurement, described in Chapter 6.

4.3 Tracking

Tracking is a second important sub-system for jet physics. Although not directly used in jet reconstruction, tracking is needed to reconstruct the interaction vertices in each bunch crossing and to separate the hard interaction vertex from the additional minimum bias interactions. The vertex resolution directly affects the resolution of the measured jet transverse momentum p_T. The interaction region at DØ is relatively long, $\sigma = 23$–30 cm, compared to the transverse size of the interaction region of $\sigma \approx 40$ μm and the maximum allowed transverse offset from the detector center of 1 mm. Misidentification of the hard interaction vertex could have a potentially large effect on the jet cross section measurement.

The tracking system has been completely upgraded since Run I to take advantage of the latest solid state technologies. The inner tracking system, silicon microstrip tracker (SMT), uses microelectronics semiconductor technology for precise tracking with 35 μm vertex resolution along the beamline and 15 μm vertex resolution in the $r - \phi$ plane for tracks of over 10 GeV/c at $\eta = 0$. The outer tracking system, central fiber tracker (CFT), uses scintillating fiber technology to complement the SMT and also acts in hardware track triggering. The track triggering capabilities of the CFT are not used for jet physics, however, as this relies entirely on calorimetry. Both detectors are placed in a 2 T magnetic field of the superconducting solenoid magnet to allow momentum measurement of the tracks. The overall central tracking system is shown in Fig. 4.6. The following sections will discuss the solenoid magnet, SMT and CFT in more detail. The track reconstruction will be discussed in Chapter 5.

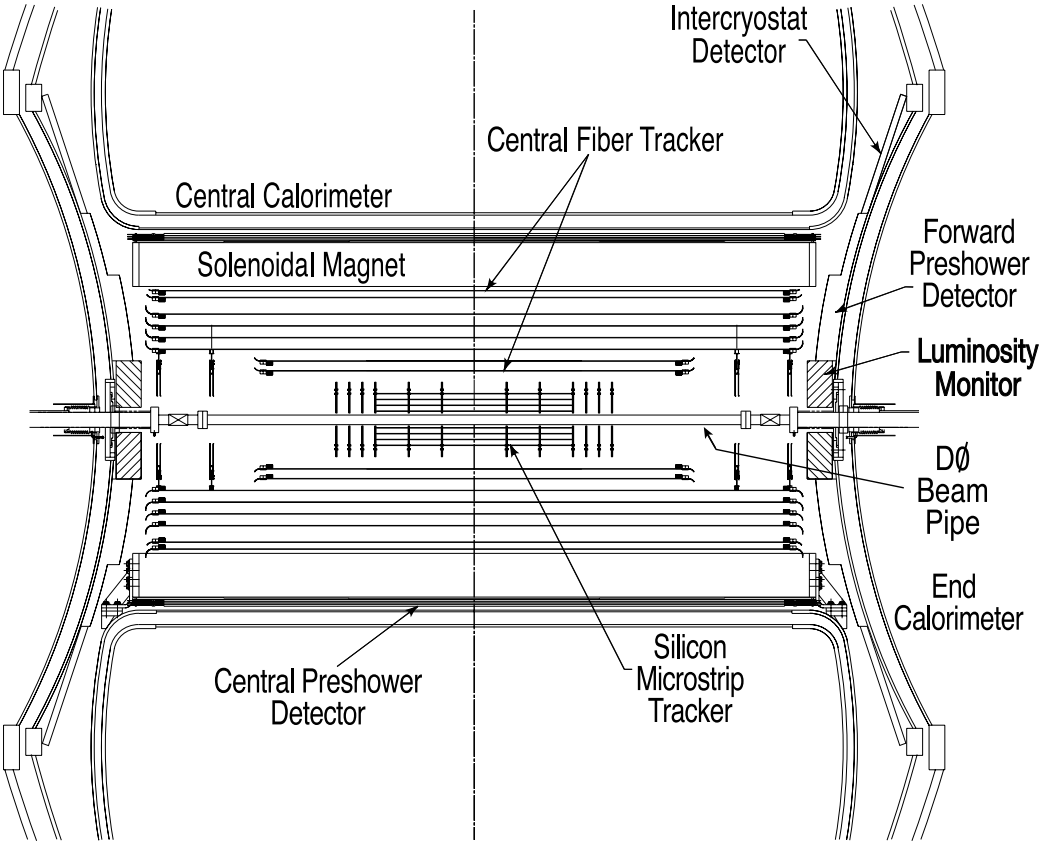

Figure 4.6: The central tracking system is composed of the inner silicon microstrip tracker and outer central fiber tracker. Not to scale.

4.3.1 Solenoid magnet

The central tracking system is fully inside the 2 T magnetic field provided by the superconducting solenoid magnet, also shown in Fig. 4.6. The solenoid magnet is placed in front of the central calorimeter cryostats and accounts for 0.87 X_0 of material that is sampled by the central preshower detectors placed between the solenoid and the cryostats. The magnet was designed to optimize momentum resolution and track pattern recognition. It also allows E/p measurement of electrons that can be used in calibration of the EM calorimeter at low p_T.

4.3.2 Silicon vertex tracker

The vertex position is most accurately measured by the inner silicon microstrip vertex tracker, shown in Fig. 4.7. The detector is composed of six barrel sections with four readout layers each and twelve intersecting disks of double-sided wedge detectors called "F-disks". At higher η the F-disks are complemented by four large diameter disks, "H-disks". Each of the H-disks is built from 24 full wedges, consisting of two single sided "half" wedges mounted back-to-back to avoid gaps between the wedges. Overall the SMT contains 912 readout modules and 792,576 channels. The SMT strips have a pitch 50–62.5 μm in the barrel and F-disk. The stereo layers are angled at 30° in the F-disks and at 90° in the layers 1 and 3 of each barrel to aid in accurate track reconstruction.

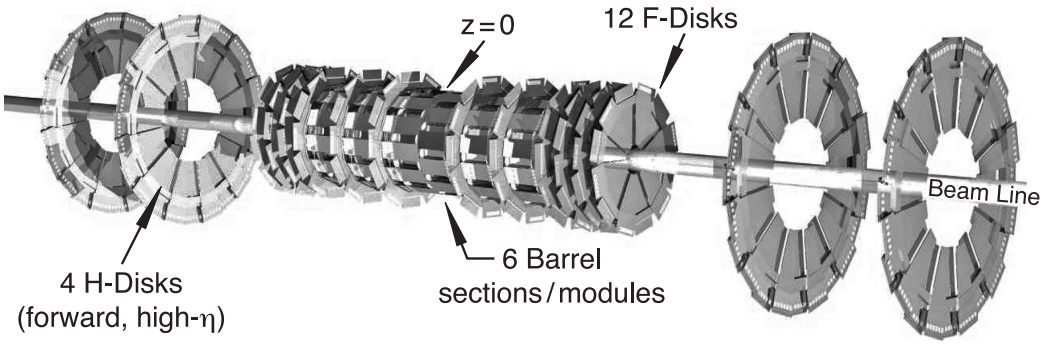

Figure 4.7: The disk and barrel design of the silicon microstrip tracker.

The length scale of the central tracker is set by the length of the longitudinal vertex distribution with $\sigma \sim 25$ cm. The centers of the H-disks are located at $|z| = 100.4$ cm and 121.0 cm and the centers of the F-disks are at $|z| =$ 12.5, 25.3, 38.2, 43.1, 48.1, and 53.1 cm. This geometrical information has relevance for the physics analysis as the vertex distribution has significant tails outside the ~ 50 cm acceptance of the F-disks. The track reconstruction efficiency drops rapidly for $|\eta| > 1$ and $|z_0|$ >40–50 cm with $\eta \times z_0 > 0$ as this region is only covered by the two H-disks, complicating track reconstruction. Consequently the cross section analysis limits $|z| < 50$ cm to reduce the impact of vertex misidentification.

Figure 4.8 shows the approximate region in $z_0 - \eta$ plane where tracks can be reconstructed using the SMT alone. The z-position resolution for vertices reconstructed from tracks in this SMT fiducial region is good, better than[1]

[1]The quoted values are for the largest σ in a double gaussian fit. Single gaussian fits give σ less than half of these values.

55 μm (180 μm) for vertices at $|z_0| < 36$ cm ($|z_0| > 36$ cm) [88]. Outside the SMT fiducial region the requirement to have at least two SMT hits per track is removed, increasing track and vertex reconstruction efficiency.

The SMT has also been a stable detector with a low number of dead channels. When leaving final testing before installation 99.5% of the detectors were functional. The fraction of functional high density interfaces (HDIs) was 94% in October and 89% in February 2005 [84]. Most of the operational problems have been caused by problems other than the silicon detector itself, such as low voltage power supply failures.

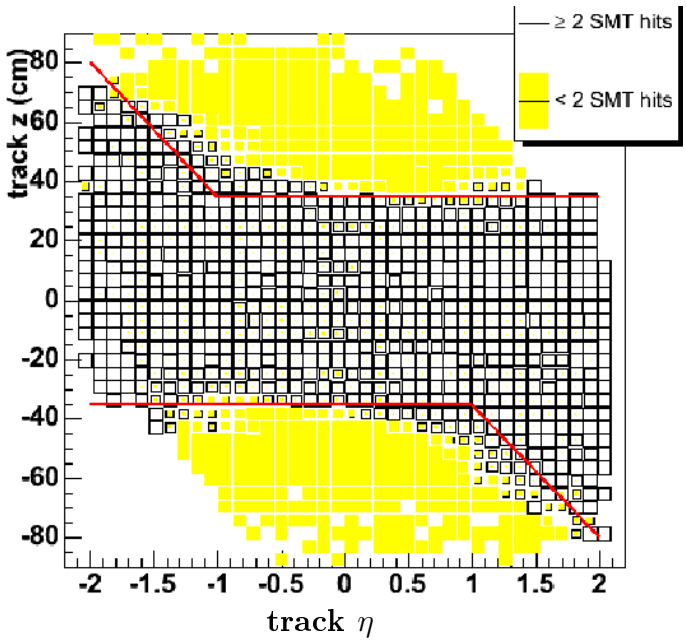

Figure 4.8: Silicon microstrip tracker (SMT) fiducial region.

4.3.3 Central fiber tracker

The central fiber tracker complements the SMT by providing additional coverage for high-z_0, high-η tracks. Each CFT layer is based on a double layered ribbon of scintillating fiber, with the two layers offset by half a fiber width to provide full coverage and assist in angle measurements. The scintillating fibers are 835 μm in diameter so the hit position resolution is more limited than for the SMT. Each barrel has one axial doublet ribbon along the beam direction (Z) and a second stereo doublet at a $\pm 3^\circ$ angle, with the sign alternating between different barrel layers. Each doublet layer has an inherent

resolution of about 100 μm. The CFT has also been stable over time, with 2-3% of the CFT fibers dead [89]. The dead fibers have a very little impact on the global tracking efficiency, and they can be "turned on" in the L1 trigger to prevent dead areas.

4.4 Muon system

The muon detector system forms the outermost part of the DØ detector, shown as a box like structure surrounding the calorimeter in Fig. 4.1. With the exception of neutrinos, muons are the most penetrating particles produced in the particle collisions. They penetrate the calorimeters and surrounding shielding with ease when practically all the other debris from the collision gets absorbed.

The bulk of the muon detectors is built from a combination of proportional drift tubes (PDTs) in the central region, and smaller and faster mini drift tubes (MDTs) in the forward ($1.0 \leq |\eta| \leq 2.0$) region. Both are separated in to three layers (A, B, C). To allow for stand-alone momentum reconstruction of the muons the muon system is supplemented with toroidal magnets in the central and end-cap regions. The toroids are placed between B and C layers of the muon detector. The stand-alone muon momentum resolution for the forward muons is about 20% of the muon momentum at $p_T < 40$ GeV/c. The overall muon momentum resolution up to $p_T \approx 100$ GeV/c is defined by the central tracking (SMT and CFT).

The PDTs are surrounded by Aϕ scintillation detectors on the inside and cosmic cap and bottom scintillation counters on the outside. As the name suggests, the cosmic cap and bottom counters provide a fast timing signal to associate muons with the proper bunch crossing and discriminate against cosmic muon background. They are also used in muon triggering. In the forward region the MDTs are supplemented with muon trigger scintillation counters that cover rapidities up to $|\eta| \approx 2.0$.

The muon triggers are useful for providing an uncorrelated trigger for high p_T jets that can be used to derive the trigger efficiency for the calorimeter based single jet triggers, as we will discuss in Sec. 8.4. In this context it is useful to note that the muon system below the calorimeter is limited by the calorimeter support structures, shown in Fig. 4.1, and electronics housing. This creates a deficit in muon triggers in $5\pi/4 \leq \phi \leq 7\pi/4$. The muon system is also useful in identifying cosmic ray showers using event displays, as discussed in Ch. 8.

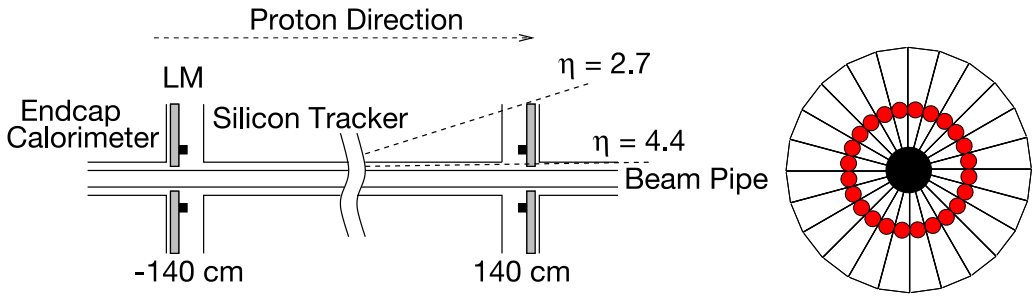

Figure 4.9: The Luminosity Monitor, shown from the side (left) and along the beamline (right). Each side has 24 scintillator tiles radiating from the center. The red dots in the front view, black boxes in the side view, are photomultiplier tubes.

4.5 Luminosity monitor

The primary purpose of the luminosity monitor (LM) is to provide an accurate measure of the luminosity at the interaction region. This is needed to normalize any cross section measurement made at DØ. In addition, it provides a measurement of the halo rates (stray protons or antiprotons escaping the beam), makes a fast measurement of the vertex z coordinate and identifies crossings with multiple $p\bar{p}$ collisions. Figure 4.9 shows a schematic of the luminosity monitor. The LM is placed between the central tracking system and the end cap calorimeter cryostat at $2.7 < |\eta| < 4.4$, close to the beam line.

The luminosity monitor is based on scintillating tiles that detect the particles coming from inelastic collisions on both sides of the interaction point. The inelastic collisions form the major part of $p\bar{p}$ interactions, rest comes from diffractive interactions that are often only detected on one side. The luminosity $\mathcal{L}$ is determined from the average number of observed interactions $\bar{N}_{LM}$ at the luminosity monitor using the formula

$$\mathcal{L} = \frac{f\bar{N}_{LM}}{\sigma_{LM}}, \tag{4.3}$$

where f is the collision frequency and the σ_{LM} is the cross section for inelastic collisions measured at the LM, including acceptance and efficiency of the LM. Because of the difficulty of determining the actual number of multiple interactions using LM only, the average number of observed interactions is inferred by Poisson statistics from the frequency of no observed collisions during beam crossings, a method called "counting zeroes".

The LM comes equipped with a time-of-flight detector that has a resolution of 200 ps (6 cm/c), limited by the varying path lengths taken by the light inside the scintillator tile. The timing information is used to reconstruct the vertex z position using the time difference between the opposite luminosity monitors. Practically all inelastic collisions occur at $|z| < 100$ cm, whereas halo typically produces $|z| \approx 140$ cm, the distance of the LM from detector center. The requirement $|z| < 100$ cm is then used to identify beam-beam collisions.

The LM has a few properties that will affect the luminosity measurement, discussed in Chapter 8. i) The PMTs that detect the light signals from the scintillators are unshielded from magnetic fields. When the solenoid magnet is turned on, the approximately 1 T fringe field from the solenoid at the luminosity monitors' position reduces the gain of the PMTs by a factor of 30 [90]. Changes in the solenoid field are then expected to affect the luminosity measurement. The magnetic field is stable during normal running and does not significantly affect the luminosity measurement, but the solenoid current was changed once during Run II. ii) The LM is subject to hard radiation produced mainly by the $p\bar{p}$ interactions that is therefore irreducible. Radiation damage causes some darkening of the scintillating material that can lead to modest ($\approx$10%) light loss at the edge closest to the beam pipe after 3 fb^{-1} [91]. This will lead to a small reduction in the measured luminosity with integrated dose. The PMTs themselves have special fused silica (quartz) windows that are largely immune to radiation damage [92].

4.6 Trigger systems

The DØ Run II detector sees particle collisions at a rate of 1.7 MHz. This is equivalent to the 396 ns between bunch crossings, with 2/3 of the available "ticks" or radio-frequency buckets filled with particles and others empty. A combination of dedicated hardware and software triggers is used to preselect interesting events and reduce the event rates before they are written to tape at a rate of about 50 Hz. To achieve a reduction in the event rate by a factor of about 30,000, the trigger is divided into three levels, L1, L2 and L3, each having more time and information available for the trigger decision than the previous one. The first two levels, shown in Fig. 4.10 are hardware based, whereas the third trigger level is software based and runs on commodity processors. Figure 4.11 shows on overview of the data flow between the different trigger levels and the event rates they are required to handle: the 1.7 MHz incoming at Level 1 is reduced to 1.6 kHz input at Level 2, 1 kHz

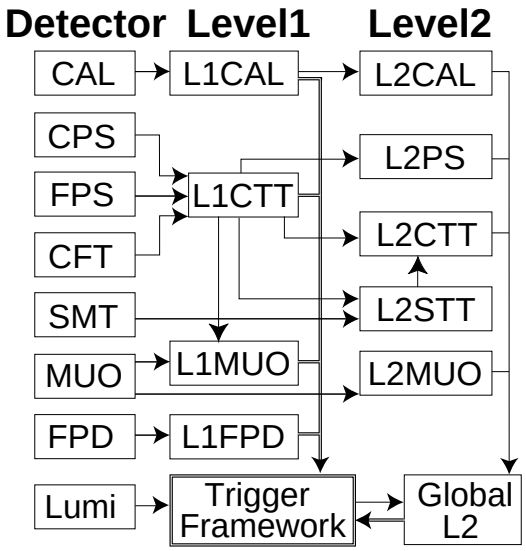

Figure 4.10: Overview of the Level 1 and Level 2 trigger subsystems. Arrows indicate the information flow from subsystem to another.

input at L3 and finally 50 Hz output from L3 to tape. The Trigger Framework communicates with the different trigger levels. In the following an overview of these triggers will be given, with emphasis on the components relevant for triggering jets.

4.6.1 Level 1 trigger

The first level of the trigger system is required to output a trigger decision in 3.5 μs, corresponding to the time between bunch-crossings in Run I. This equals ten bunch crossings in Run II. To avoid dead-time, data from the detector is queued in L1 buffers, as shown in Fig. 4.11, while the trigger decision is pending. The L1 trigger communicates with the Trigger Framework that passes accepted events in the L1 buffer to L2.

Due to the small amount of time available at L1, the trigger decision is based on very rough detector information from subsystems shown in Fig. 4.10. Objects available for the trigger decision are electromagnetic (EM), hadronic (H) and (EM+H) trigger towers that are summed in both depth and transverse coordinates ($\Delta\eta \times \Delta\phi = 0.2 \times 0.2$) in the L1 calorimeter trigger (L1Cal); central tracker trigger (L1CTT) and muon system trigger (L1Muon) tracks, both separately and combined; and L1 forward proton detector trigger (L1FPD)

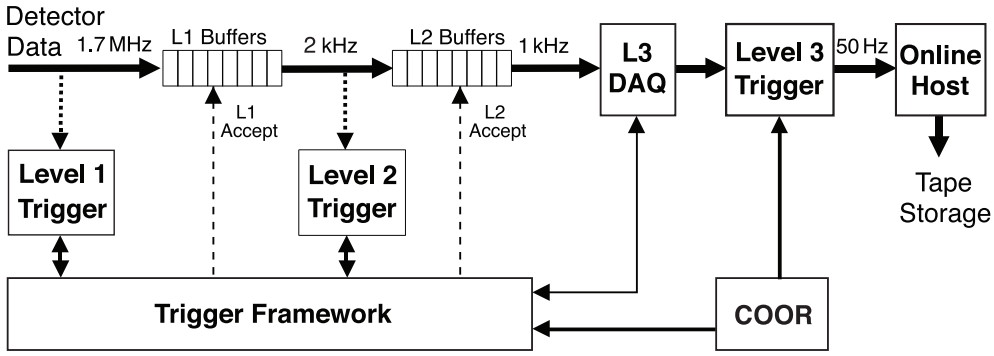

Figure 4.11: Schematic of the data flow in the trigger and data acquisition system.

for diffractive events by protons or antiprotons scattered at very small angles. For jet physics we are mainly interested in the L1Cal.

4.6.2 Level 2 trigger

The Level 2 trigger has a number of subsystem specific preprocessors that form physics objects from data coming from L1, as shown in Fig. 4.10. These subsystem preprocessors include calorimeter, tracks, muons and preshower. The L2 can also combine data over the detector to form more complex objects. The preprocessed physics objects are transmitted to L2 Global trigger for trigger decision. Each L1 trigger bit is mapped to a specific L2 script. The L2 jet algorithm will be described in Sec. 4.7.2.

4.6.3 Trigger framework

The L1 and L2 trigger decisions are coordinated through the Trigger Framework. An important additional function that the Trigger Framework performs is the application of prescales at L1. Events that otherwise fulfill the trigger conditions are randomly passed only a fraction 1/prescale of the time to keep the rate of more common triggers balanced with those that occur rarely. Low p_T jets are especially copious at the Tevatron. To balance the rate of the lowest p_T jet trigger ($p_T > 8$ GeV/c) with that of the higher p_T jet triggers, prescales of up to a million are used at higher luminosities. Only the highest p_T jet trigger ($p_T > 125$ GeV/c) is always kept unprescaled. The trigger framework includes the prescale information into the luminosity cal-

culation and also provides a large number of scalars that allow the counting of trigger rates and dead times.

4.6.4 Level 3 trigger

The Level 3 trigger runs on a farm of commodity processors. It is software based, highly configurable and can perform a limited reconstruction of the whole event. Each L2 trigger bit is mapped to one or more L3 filters. As a specific example, the L3 jet filter reconstructs jets using high-precision calorimeter readout ($\Delta\eta\times\Delta\phi = 0.1\times0.1$). The reconstructed primary vertex position[2] and removal of hot calorimeter cells allows accurate reconstruction of jet energy and p_T. The jet reconstruction is not quite as precise as for the full offline reconstruction, but the trigger turn-ons are dramatically sharper than at L1 and L2, quickly plateauing at 100% efficiency.

4.6.5 Data acquisition

The DØ data acquisition system (DAQ) consists of the Level 3 DAQ and the online host. The L3DAQ is designed to handle a continuous data rate of 250 MB/sec, corresponding to 1 kHz input rate from L2, with each event about 250 kB in size. After being partially reconstructed at L3, the accepted events are passed to the online host at a rate of about 50 Hz (12.5 MB/sec of 250 kB events). The events sent are tagged with an identification that corresponds to the hardware and software trigger elements they passed. At the online system the events are assigned to a data stream and then sent to their final repository, a robotic tape system three kilometers from the detector.

4.7 Trigger scripts

The DØ experiment continually updates the trigger lists to optimize data taking with increasing luminosity, improve the trigger turn-ons and trigger efficiency and to include new requests by physics groups. Each trigger is composed of a combination of L1, L2 and L3 trigger terms. The single jet triggers available for the inclusive jet analysis in Run IIa are listed in Table 4.1. These have significantly varying turn-ons, and only a subset is

[2]The reconstructed vertex position was available, but not used for Run IIa single jet triggers. Instead, nominal vertex position (0,0,0) was used.

used for the final analysis, as discussed in Chapter 8. The different trigger terms are briefly discussed in the following sections.

4.7.1 L1 trigger scripts

The L1Cal allows the experiment to trigger globally on $\sum E_T$ and $\not\!\!E_T$ with four different thresholds and on local variables based on the EM transverse energy and the total EM plus hadronic (H) transverse energy. The local variables can use individual trigger towers with size 0.2×0.2 in $\eta \times \phi$ and large EM+H tiles covering 4×8 trigger towers in $\eta \times \phi$. Typical L1 triggers for jets are cuts on 1–4 trigger towers with E_T more than 3–7 GeV per tower. The L1 trigger terms used in Run IIa for single jet triggers are listed in Table 4.1. For the triggers listed here, the E_T at L1 is calculated with respect to the nominal vertex at (0,0,0).

The L1 trigger terms are of the generic type CJT(n, x), indicating that n L1 trigger towers with at least $E_T > x$ GeV of transverse energy are required. The towers can be, and very often are, widely separated and corresponding to different jets. The L1 trigger covers detector pseudorapidity up to $|\eta| = 3.2$ unless otherwise indicated.

4.7.2 L2 trigger scripts

The Run IIa L2 jet algorithm clusters 5×5 groups of calorimeter trigger towers that are centered on seed towers. The seed towers are E_T ordered trigger towers with $E_T > 2$ GeV. Overlapping L2 jets may be considered as separate jets, or shared towers can be assigned to the highest E_T jet, depending on L2 scripts criteria.

It is not uncommon that single jet triggers will pass events directly from L1 to L3 without running a L2 script, as shown in Table 4.1. When used, the L2 trigger runs one of the L2 tools JET(0,7) and JET(0,5). The difference is the minimum required jet E_T, 7 GeV or 5 GeV, respectively. If L2 jets are reconstructed, the highest E_T jet is required to have E_T above a given threshold.

The infrequent application of L2 scripts in single jet triggers in Run IIa is explained by the slow turn-on of the L1Cal trigger. For low p_T triggers the L1 is still significantly inefficient for thresholds that are useful at L2. Even when applied, the L2 trigger is not a very strong requirement. The situation has

much improved in Run IIb with the new L1Cal trigger that can reconstruct L1 jets from multiple towers.

4.7.3 L3 trigger scripts

The L3 jets come in two varieties used in single jet triggers[3], SCJET_8 and SCJET_15. Both run a simple cone algorithm. They calculate E_T using the nominal vertex position at (0,0,0) and return jets with $E_T > 8$ GeV and $E_T > 15$ GeV, respectively. At least one jet in the event is required to be above the given E_T threshold. Despite the similarities of the two algorithms, the eventual observed trigger turn-ons are significantly lower for SCJET_8.

[3]Level 3 jet SCJET5_PV3 is also available and uses the reconstructed primary vertex position for p_T calculation.

Table 4.1: Single jet triggers used in Run IIa. Trigger list versions with similar terms are reported together. Only trigger versions used in data taking are listed. The L1 term is abbreviated from CJT(n,x) for n L1 towers with $E_T > x$ GeV. The L3 tools JT8 and JT15 are abbreviated from the L3 tool names SCJET_8 and SCJET_15.

Trigger	Trigger lists	L1 term	L2 E_T	L3 tool	L3 E_T
JT_8TT	v11–v14	(1,5)	-	JT8	8
JT_15TT	v12–v14	(2,3)	-	JT8	15
JT_15TT	8.00, 8.10	(2,3)×(1,5)	-	JT8	15
JT_25TT_NG	v14	(3,5)	-	JT8	25
JT_25TT_NG	v12–v13	(2,5)	-	JT8	25
JT_25TT_NG	8.20–v11	(2,5)	-	JT15	25
JT_45TT	14.00,14.10	(4,5)	-	JT8	45
JT_45TT	v12–v14	(2,5)	-	JT8	45
JT_45TT	v8–v11	(2,5)	-	JT15	45
JT_65TT	v12–v14	(3,5)	20	JT8	65
JT_65TT	v9–v11	(3,5)	20	JT15	65
JT_65TT	v8, 9.20	(3,5)	-	JT15	65
JT_95TT	v13–v14	(3,5)	50	JT8	95
JT_95TT	13.00	(4,5)	50	JT8	95
JT_95TT	v12	(4,5)	30	JT8	95
JT_95TT	v9–v11	(4,5)	30	JT15	95
JT_95TT	v8, 9.20	(4,5)	-	JT15	95
JT_125TT	v14, 13.00	(4,5)	60	JT8	125
JT_125TT	v13	(3,5)	60	JT8	125
JT_125TT	v12	(4,7)	-	JT8	125
JT_125TT	v8, v10–v11 9.41, 9.42	(4,7)	-	JT15	125
JT_125TT	v9	(4,5)	-	JT15	125

Chapter 5

Data used in the analysis

Chapter 4 focused on the detectors and physical systems required to collect data from the particle interactions. In this chapter we continue with the series of processing and reprocessing steps, skimming and data quality control that the data undergoes before it ends up in analyzers' plots, and eventually, to physics papers. We also summarize major data-taking epochs, luminosity calculation and trigger lists that naturally divide the data into subsets for control of the stability of the result.

5.1 From detector to tape

As discussed at the end of Chapter 4, the raw data coming from the DØ detector reaches its final repository in the robotic tape system maintained at the Feynman computing center a few kilometers from the detector. The quality of the data is continually monitored as it is being sent to the tapes.

The DØ control room is manned 24/7 by a five-person[1] shift crew during data taking. The CFT, SMT and CAL+muon subsystems are monitored by dedicated subsystem shifters that can flag runs as bad for their subsystem in case of hardware problems. The run quality is later rechecked offline. The DAQ shifter oversees that all subsystems are working nominally and that data keeps flowing through the trigger system and to the tape at an acceptable rate. The DAQ shifter is also responsible for starting and stopping data-taking runs, selecting trigger lists and updating prescale sets to keep the data taking optimized for the continually falling luminosity during a store. The shift captain oversees the shift crew. The captain also monitors the

[1] In Run IIb there have been only four shifters after combining SMT and CFT shifts.

continually updated physics plots[2] of the ongoing run and acts as a liaison between the Tevatron Main Control Room and the shift crew.

Information on the run conditions and prescales are stored in the Oracle-based Runs Database and on the trigger lists in the Trigger Database. The raw data, as well as reconstructed data sets, are accessible to the DØ collaborators through the sequential access via meta-data [93] (SAM) data-handling system.

5.1.1 Raw data

The raw data is stored using DØ event data model (EDM). This is a library of C++ classes and templates that support the implementation of reconstruction and analysis software. A main feature of the EDM is the event, a class that represents a single beam crossing. The raw output of the detector, results of trigger filter processing and of many different reconstruction tasks are stored in the event.

The full raw dataset collected by DØ during Run IIa is roughly 1000 TB in size, equivalent to about 150 m stack of dual-side DVDs[3], half the height of the Eiffel Tower. The full Run IIa dataset contains about 1.4 billion events, of which about 98 million belong to the QCD skim used in this analysis. The data is stored in several formats of increasingly enriched physics content

- Data summary tier (DST) contains all information required to perform any physics analysis, including limited re-reconstruction of high-level physics objects. This format is now seldomly used and is not written out by default for new reconstruction passes.
- Thumbnail (TMB) is a physics summary format originally less than one tenth the size of the DST format. The latest version TMB++ has grown to contain enough information for most analyses to replace the original DST and TMB formats.
- Common analysis framework (CAF) format is a physics summary format based on ROOT [94]. The ROOT trees are processed starting from TMBs, with similar information content, slightly smaller size and significantly faster read access.

[2]The monitoring of physics plots was handled by a dedicated Global Monitoring shifter in the beginning of Run IIa.

[3]Estimated using 8.5 GB capacity and 1.2 mm thickness.

The format of choice for this analysis is CAF. Although being similar in size to TMB, CAF allows for quick reading of only the selected branches of the data. It is also integrated into the CAF environment, a collaboration-wide framework for setting up analyses and sharing high-level code. The CAF format was introduced by the Data Format Working group [95] at the end of Run IIa in order to homogenize the data formats used by the collaboration. It replaces earlier list-of-variables type ROOT n-tuples produced by qcd_analyze in the QCD group.

5.1.2 Monte Carlo

The DØ collaboration has a simulated model of the DØ detector to study how the physical events are turned into measured quantities. The basic technique utilized in all particle physics experiments is Monte Carlo (MC), whereby large number of events are randomly generated from weighted distributions of a particular final state and then processed through detailed detector simulations.

The simulated Monte Carlo data is used to verify the data-based analysis methods for internal consistency and to assign bias corrections, whenever it is reasonable to assume that the relative biases are similar in data and MC. Many analytical expressions are used to minimize the differences between data and MC from known sources; the residual differences in data and MC comparison are then taken as a systematic uncertainty or corrected for.

The Monte Carlo is also used to extrapolate the corrections to regions of phase space where data has limited statistics. To obtain a reliable extrapolation using MC, the simulation needs to describe the calorimeter response to the percent level. This has required much work, because the DØ detector elements were not calibrated in a test beam like was done *e.g.* at CDF. The MC simulation has been gradually improved by doing targeted tuning to data, *e.g.* by comparing electron responses in the $Z \to e^+e^-$ and by comparing the jet responses in the γ+jet channel. This has lead to significant improvements that include an improved simulation of the electromagnetic showers and scaled single pion response.

Several Monte Carlo generators are available for the production of physics processes, but the one most commonly used in this analysis is Pythia [96] tune A. Several of Pythia default parameters have been modified to better fit CDF Run I data. These include e.g. increased initial state radiation. Another commonly used event generator is Herwig [97]. Both generators rely

on leading order (LO) predictions of inclusive jet cross section, but differ in the hadronization model.

The particles produced in the Monte Carlo event generators are propagated through the detector elements using the CERN program GEANT v3.21. The GEANT program traces the particles through the detector, determines where they intersect active areas and simulates their energy depositions and secondary interactions.

The DØ detector simulation (DØSIM) takes the GEANT energy deposits as an input and accounts for various detector-related effects such as detector inefficiencies, noise from detector and electronics, analog signal shaping and digitization of the data. A recent innovation at DØ has been to overlay Zero Bias data to Monte Carlo to simulate the effect of multiple interactions and pile-up (the effect the previous interactions have on the current bunch crossing). This has been shown to significantly improve the agreement between data and Monte Carlo, as compared to a pure Monte Carlo simulation of multiple interactions.

The Monte Carlo output from DØ SIM is fully equivalent to the raw data produced by the detector, and can be run through the same reconstruction software. The events include additional MC information that can be used to correlate the detector data and reconstructed objects with the original generator output.

5.2 Reconstruction

The high-level physical objects (hits, tracks, jets etc.) in the events used for physics analyses are reconstructed by the DØ offline reconstruction software (RECO). It is a CPU intensive program that processes recorded collider events and simulated MC events. The RECO is run on offline production farms and the results are stored in the central data storage system, SAM.

The first step of reconstruction associates electronics channels with detector elements and applies detector-specific calibration constants. Geometry constants are used to associate detector elements (energies and positions) to physical positions in space. For many of the detectors the output from this step is in the form of clusters (for calorimeter) or hits (for tracking detectors).

The second step focuses on the tracking detectors and reconstructs global tracks from the hits in the SMT and the CFT. This is the most CPU intensive part of the reconstruction.

The third step, vertexing, uses the global tracks to find primary vertex candidates. These are the locations of the $p\bar{p}$ interactions. Secondary vertex candidates are identified next. These are associated to the decays of long-lived particles such as B or D mesons, containing a heavy-flavor b or c quark, respectively. Such secondary vertices are generally displaced by a few tens of micrometers to a few millimeters from the primary vertex, a small distance by comparison to the interaction region length of about 30 cm, but sizable compared to the few tens of microns of the transverse size of the interaction region.

In the final step the information from the preceding steps are combined using a wide variety of algorithms to reconstruct more specific physics objects and final states. The electron, photon, muon, neutrino ($\not\!\!E_T$) and jet candidates are found first, after which RECO identifies candidates for heavy-quark and tau decays.

5.2.1 Vertex reconstruction

The reconstruction of the primary interaction vertex is an important step in RECO. The position obtained for the hard-scatter vertex affects the calculation of $\not\!\!E_T$ and p_T for high-level physics objects. The main quantity of interest for this analysis is the primary vertex z position, and whether the primary vertex candidate is really associated to the jets we observe, i.e. to the hard-scatter vertex.

The vertex reconstruction has two main steps: vertex finding and vertex fitting. DØ currently uses an Adaptive vertex fitting algorithm [98], first proposed and implemented by the CMS collaboration and successfully used by the H1 collaboration [99]. This replaces the earlier approach that used the Kalman Filter algorithm [100] for vertex finding and a 2-pass tear-down approach [101] for vertex fitting. The Adaptive algorithm is designed to deal with mis-associated and mis-reconstructed tracks. The main improvement is reduced sensitivity to multiple interactions, leading to more reliable selection of the vertex associated to the hard interaction. For high p_T jets the improvement is not so significant.

The selection of the hard-scatter vertex uses a probabilistic method that assigns a probability for each vertex that it comes from a minimum bias interaction [102]. The probability is obtained by looking at the $\log_{10} p_T$ distribution of the tracks with $p_T > 0.5$ GeV/c from minimum bias processes. The product of the probabilities is calculated for each vertex, and the product is then weighted to make it independent of the total number of tracks. The

vertex with the lowest minimum bias probability is chosen as the primary vertex.

5.2.2 Jet reconstruction

Figure 5.1 shows an example of jets in the calorimeter. Although the jets are rather obvious by eye, precise definitions are elusive and detailed, and have taken years of development. The current jet reconstruction algorithm used at DØ is called the "Run II cone algorithm" [103]. This is an iterative cone algorithm that considers calorimeter energy deposits as massless four-vectors to construct the jet four-vector. The four-vector direction is calculated using the primary vertex position. The resulting jets are massive by construction if the jet cone contains more than one calorimeter cluster. This is in contrast with the Run I cone algorithm [104, 105] that summed calorimeter scalar E_T to construct massless jets. These algorithms are sometimes referred to as the "E-scheme" (adding four-vectors) and "E_T-scheme" or "Snowmass convention", respectively.

An alternative jet reconstruction scheme, the k_T algorithm [106], is based on particle (calorimeter cluster) distance in momentum space instead of real space. The k_T algorithm has been used by the LEP experiments and CDF, but is currently not in active use in analyses at DØ. It is theoretically favored as it is not subject to complications arising from the so-called split-merge procedures, but it is in practice challenging at the hadron colliders that have large amounts of background energy from underlying event and multiple interactions at high luminosity.

To compare with the older QCD papers it is important to note a few key differences:

- tranverse momentum p_T is used instead of transverse energy $E_T = E \cdot \sin\theta$
- rapidity y is used instead of pseudorapidity η
- reconstructed jets are massive, $m_{\text{jet}} \neq 0$

The Run I algorithm would have resulted in $E_T = p_T$ and $\eta = y$, but these variables are now different due to jet mass $m \neq 0$.

The jet reconstruction has three basic parameters: cone size $R_{\text{cone}} = 0.7$, $p_{T,\text{min}} = 6$ GeV/c, overlap fraction $f = 50\%$. The first two parameters are used in jet reconstruction, the third in split-merge procedure. The following

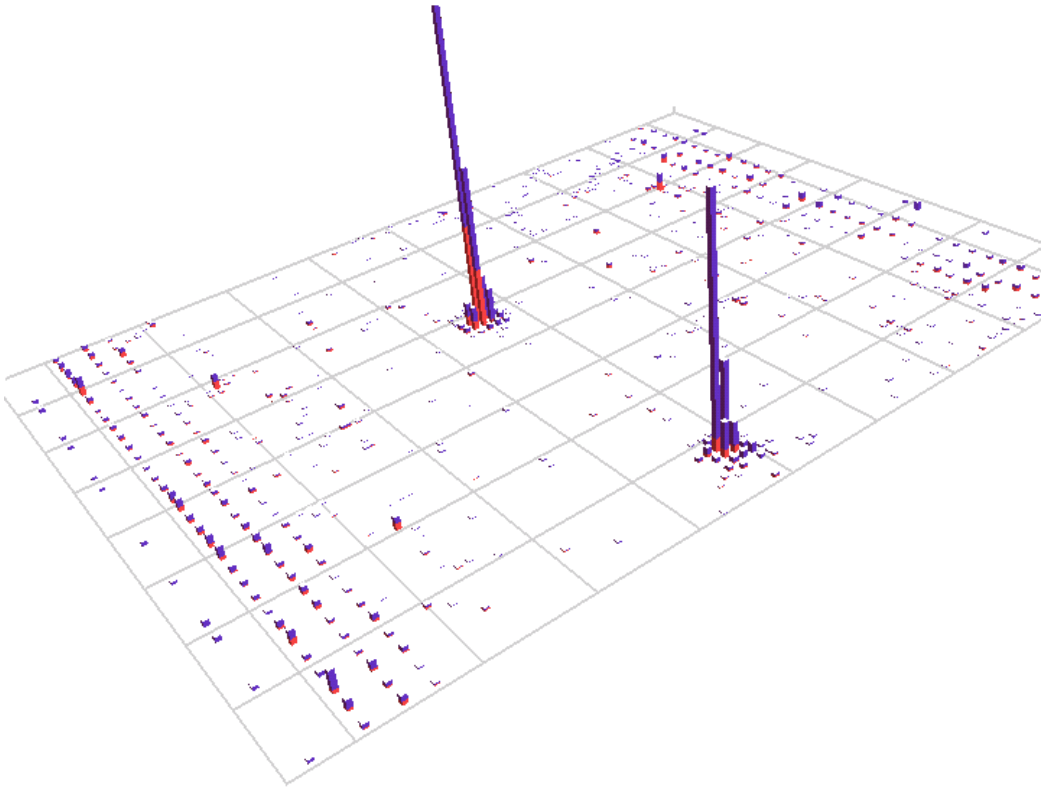

Figure 5.1: Example of a high-p_T dijet event in the DØ calorimeter. The cylindrical calorimeter surface is rolled open into an $\eta \times \phi$-plane. The two jets are produced back-to-back in ϕ at $\eta \approx 0$ and the high-$|\eta|$ region is filled with particles from the proton and antiproton remnants.

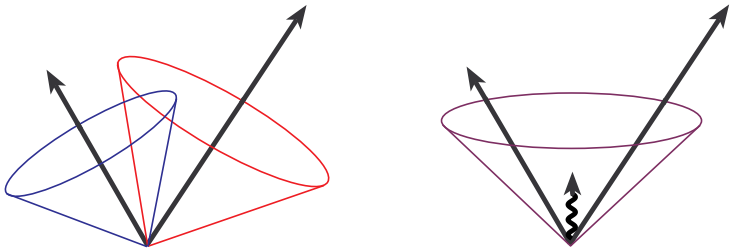

Figure 5.2: Illustration of infrared sensitivity in the cone algorithm. A small amount of soft radiation added between jets can create an additional seed and cause two previously separate jets to be merged.

section will cover these in more detail. DØ also reconstructs jets with $R_{\text{cone}} = 0.5$, but these are not used in QCD analyses because the smaller cone size results in more showered energy outside the cone, making the p_T calibration more sensitive to detector effects. Smaller cone sizes benefit from lower noise and better angular resolution, but the energy range in the inclusive jet cross section measurement is sufficiently high that neither of these considerations is important.

Run II cone algorithm

The Run II cone algorithm starts by using all "particles" (calorimeter energy deposits in experiment, stable particles in particle level MC, and partons in perturbative QCD) as seeds for jet reconstruction. These seeds are used as center points for proto-jets. All particles within $\Delta R = \sqrt{(\Delta\eta)^2 + (\Delta\phi)^2} \leq R_{cone}$ are added to the proto-jet, and the direction of the resulting four-vector is used as the center point for a new cone. This procedure is iterated until a stable solution is found with the cone axis parallel to the proto-jet axis.

The use of seeds can potentially cause the algorithm to be infrared sensitive, i.e. additional particles with $p_T \to 0$ can introduce additional starting points and change the behavior of the algorithm. This behavior is illustrated by the Fig. 5.2. Ideally a seedless algorithm could be used, where four-momentum combinations of all particle partitions would be used as starting points. This leads to $2^n - 1$ possible starting points, where n is the number of particles. While this may be practical for pQCD with limited number of partons, it is computationally expensive for experimental data with thousands of calorimeter towers. The current algorithms use both seeds and proto-jets to limit the needed computational resources, and the addition of mid-points to regain infrared safety, as discussed below.

After the first round of iterations mid-points between pairs of proto-jets are used as additional seeds and the iterative procedure is repeated as above. This additional step makes the algorithm infrared safe: vanishingly small energy deposits between two nearby jets won't cause the algorithm to merge two jets if they would not have been merged otherwise. Infrared safety is important from a theoretical viewpoint as otherwise the algorithm is not applicable in perturbative QCD to produce predictions[4].

The obtained list of stable proto-jets may contain many overlapping and identical jet candidates. Identical solutions and proto-jets with $p_{T,\mathrm{jet}} < p_{T,\mathrm{min}}/2$ are removed from the list of jets. The latter step is not required by the algorithm, but speeds up recontruction and can avoid the excessive merging of many noise or minimum bias jets. The remaining proto-jets are handled by the split and merge procedure to remove overlaps. It is important to note that the splitting and merging does not begin before all the stable proto-jets have been found. The behavior of the algorithm would be otherwise difficult to predict. Figure 5.3(a) shows a schematic of the Run II cone algorithm.

In case two proto-jets have overlapping cones, the proto-jets are merged if they contain more than a fraction f (typically 50% as used at DØ) of $p_{T,jet}$ in the overlap region. Otherwise the jets are split with the particles in the overlap region being assigned to the nearest jet. In both cases the jet axes are recomputed. The algorithm works on the highest p_T proto-jet to maintain a well-defined behavior. After each step the ordering is updated as it may change when jets are being split and merged. Always operating on the highest p_T proto-jet preferentially reconstructs jets of maximal p_T. The proto-jets surviving the split-and-merge are then promoted to jets. The fully specified split-and-merge procedure is presented in Fig. 5.3(b) from [103]. This method will perform predictably even with multiple splits and merges, but note that there is no requirement that the centroid of a split or merged proto-jet will still precisely match with its geometric center.

Kinematic variables

The Run II cone algorithm specifies the jet kinematics directly as a four-vector (E, p_x, p_y, pz), or alternatively using the variables (E, p_T, y, ϕ). These are calculated from all the particles inside the cone radius, or calorimeter

[4]Additional clustering parameter R_{sep} was introduced in Run I to make the perturbative QCD calculations infrared safe [5], but this approach was not very satisfactory theoretically.

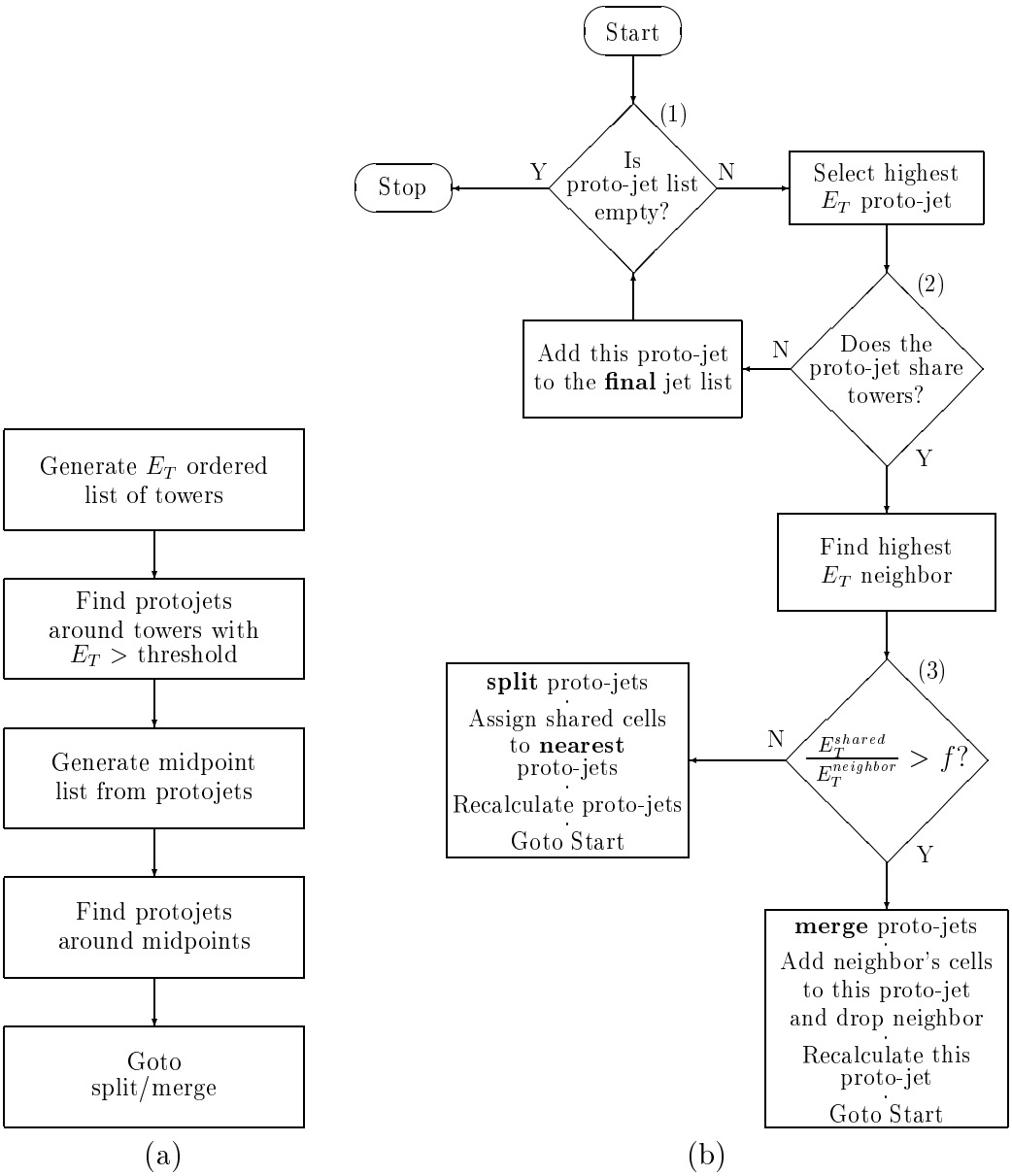

Figure 5.3: (a) Schematic of the Run II cone algorithm. (b) Flow diagram of fully specified split-and-merge procedure for Run II cone algorithm.

towers in the case of experimental data

$$i \in C \quad : \quad \sqrt{(y^i - y^C)^2 + (\phi^i - \phi^C)^2} \leq R, \tag{5.1}$$

where $y^i = \eta^i$ and ϕ^i are the coordinates of massless particles or towers and y^C, ϕ^C are the coordinates of the cone center. The centroids of these jets are defined using four-vector addition in the E-scheme

$$p^C = (E^C, p^C) = \sum_{i \in C} (E^i, p_x^i, p_y^i, p_z^i), \tag{5.2}$$

$$\bar{y}^C = \frac{1}{2} \ln \frac{E^C + p_z^C}{E^C - p_z^C}, \quad \bar{\phi}^C = \tan^{-1} \frac{p_y^C}{p_x^C} \tag{5.3}$$

Jets are "stable" cones with $\bar{y}^C = y^C = y^J$ and $\bar{\phi}^C = \phi^C = \phi^J$. The split-and-merge procedure may cause the jet centroid and cone center to be slightly offset for the final jets, and the jet to include towers outside the cone defined in Eq. 5.1. In either case the final jet variables are calculated from all the particles or towers assigned to the jet using

$$p^J = (E^J, p^J) = \sum_{i \in J=C} (E^i, p_x^i, p_y^i, p_z^i), \tag{5.4}$$

$$p_T^J = \sqrt{(p_x^i)^2 + (p_y^i)^2}, \tag{5.5}$$

$$y^J = \frac{1}{2} \ln \frac{E^J + p_z^J}{E^J - p_z^J}, \quad \phi^J = \tan^{-1} \frac{p_y^J}{p_x^J}. \tag{5.6}$$

5.3 Fixing, refixing and calibration

As the understanding of the complex DØ detector has grown and reconstruction algorithms have improved, the full DØ data set has been reprocessed twice to incorporate the latest advancements. The farms at Fermilab reconstruct events at approximately the same rate as they are recorded; three years worth of data takes three years to process locally. To reprocess a full data set on a time scale of six months, the data is distributed internationally using SAMGrid [107] to participating computing centers. For the PASS3 (p17) reprocessing these sites included Canada's WestGrid, the University of Texas at Arlington, CCIN2P3 in Lyon, France and FZU in the Czech Republic. A small portion of the data was also reprocessed in farms at Fermilab.

The improvements implemented in reprocessing have included better calorimeter calibration constants, updated hot cell lists and algorithm improvements such as the Adaptive Vertexing. A very important ingredient for jet

physics has been the inclusion of calorimeter cell-level η and ϕ intercalibration [108, 109, 110, 111]. This has been shown to improve jet p_T resolutions by up to 20% compared to the beginning of Run IIa [112, 113]. Such a low-level calibration can only be done efficiently before jet reconstruction, requiring in practice full reprocessing.

5.3.1 Calorimeter cell-level calibration

The calorimeter cell electronics are calibrated by sending a pulse of known charge into the readout and comparing this to the measured charge. In this way the response can, at least in principle, be linearized in each individual channel and the gains of the different channels equalized. This method cannot, however, equalize any differences between cells rising e.g. from mechanical differences. To this end, data-based methods have been developed to intercalibrate cells in η and ϕ [108].

In the first step the EM calorimeter is calibrated in ϕ in constant η rings using the ϕ-symmetry and the exponentially falling p_T spectrum of the collision products [109]. In short, the energy of a given cell is assumed to take the form

$$E_i = \alpha_i E_s, \tag{5.7}$$

where α_i is the calibration constant. Different cells in the same η ring are required to have the same number of events $N(E_s)$ above the energy threshold E_s

$$N_i(E_i) = \int_{E_i}^{\infty} g(E')dE' = \int_{E_s}^{\infty} f(E)dE = N(E_s) \Rightarrow E_i = \alpha_i E_s, \tag{5.8}$$

where $N_i(E_i)$ is the number of events above the energy threshold E_i in the cell we want to intercalibrate. The cell-wise and average p_T spectra, $g(E')$ and $f(E)$, respectively, are exponentially falling so a small change in α_i translates into a large change in $N_i(E_i)$.

The η-intercalibration of the EM calorimeter is derived by looking at the mass of the Z boson reconstructed from $Z \rightarrow e^+e^-$ decays in different η rings. The mass of the Z boson, 91.1876 ± 0.0021 GeV [114], is known to high accuracy from LEP experiments so the absolute energy scale of the EM calorimeter can also be normalized with respect to this constant. The performance of the η-ϕ intercalibration has been checked by comparing the observed Z mass peak width to the true width, 2.4952 ± 0.0023 GeV [114].

The fine hadronic calorimeter is calibrated using the same approach for ϕ-intercalibration [110]. The data was collected using a dedicated trigger for

calibration to reduce trigger biases. Due to the large number of events, roughly 10 million, required to calibrate 6000 calorimeter cells at about 1% accuracy for the central calorimeter, the calibration data was taken parasitically using the monitor stream. This way the trigger rate for the calibration did not reduce the band-width available for physics data-taking. It was also not required to reconstruct the calibration events, reducing the impact on the collaboration's CPU resources.

The internal calibration of each ϕ tower was improved by fitting the relative weights of the four fine hadronic layers. Due to statistical limitations, the ICR and the region $|\eta_{\text{det}}| > 2.4$ were calibrated on tower level only.

In the final step the fine hadronic calorimeter η rings were equalized using a sample of QCD dijet events [111].

5.4 Data quality

As the old saying goes, your results are only as good as your data. The DØ detector is a large and challenging collection of hardware, and like any other sensitive instrument, may malfunction from time to time. Among common problems are high-voltage systems sparking and producing jet look-alikes, coherent noise producing erroneous firing of the triggers, or cosmic rays hitting the detector and depositing large amounts of energy. Sometimes full detector sub-systems are removed from data-taking due to problems. The DØ data quality group is charged with identifying and removing data of bad or poor quality.

As a first line of defense, all runs having problems in one or more detector sub-systems during data taking are marked as bad in Run Database. The runs usually last for 2-4 hours, but may be shorter, especially if problems are encountered during data-taking. DØ maintains lists of bad runs separately for calorimeter, CFT, SMT and Muon subsystems. The bad run lists can be later extended in case latent problems are discovered.

A typical signature for problems in the calorimeter is that the missing-E_T in the event is not balanced. Most bunch crossings produce closely balanced missing-E_T, with the balance only occasionally broken by statistical fluctuations in the energy measurement or a high-energy neutrino. Another tell-tale signature is a large number of "jets" found in a restricted region of the calorimeter. The Jet/MET group scans data in luminosity blocks to find ones that would have abnormally high average missing-E_T or other obvious problems. The luminosity block (LBN) is the basic unit of luminosity mea-

surement, normally about 60 seconds in length. The bad LBNs lists are used to remove short periods of bad data. If the bad LBNs are very recurrent within a run, the whole run may be marked as bad. Conversely, problems sometimes appear only at the end of a long run, and the run that was originally marked as bad may be recovered and only the ending marked in the list of bad LBNs.

The recorded events are later scanned for known problems by the data quality group. As new problems are discovered, the algorithms are updated to look out for the signatures for these problems. For problems frequent within a limited time the runs or LBNs are marked as bad. For more isolated occurrences the event may get a calorimeter fail flag. These flags mark events where something unusual happened, but only a few events per LBN were affected. The current calorimeter quality flags include "coherent noise", "noon noise", "empty crate" and "ring of fire". The coherent noise is by far the dominant flag, removing a few percent of the events overall. Others are generally removing much less than 1% of the events.

In addition to actual data-quality problems, some LBNs are also removed because they cannot be normalized. Such LBNs are often too short to have enough events for a reliable luminosity estimate, or the trigger or luminosity system have had problems that prevented the book-keeping necessary for later luminosity calculation.

5.5 Luminosity

No cross section measurement would be complete without integrated luminosity to normalize it. The final Run IIa luminosity is presented in Ref. [115]. As already briefly mentioned in Sec. 4.5, the luminosity $\mathcal{L}$ is determined by measuring the counting rate of inelastic proton-antiproton collisions with the luminosity monitor (LM) system [116, 84]

$$L = \frac{1}{\sigma_{\text{eff}}} \frac{dN}{dt}, \tag{5.9}$$

where σ_{eff} is the effective inelastic luminosity seen by the LM. Both DØ and CDF have agreed to use a common total inelastic cross section for luminosity determination, $\sigma_{\text{inelastic}}(1.96\text{ TeV}) = 60.7 \pm 2.4$ mb, measured by the CDF and E811 collaborations [117]. The effective cross section σ_{eff} differs from the total inelastic cross sections $\sigma_{\text{inelastic}}$ by the efficiency and geometric acceptance of the luminosity system. Both efficiency and acceptance are determined from a

detailed Monte Carlo simulation of the luminosity system. The LM hardware is shown in Fig. 4.9 and detailed in Sec. 4.5.

In practice, the luminosity is determined from the rate of zero counts by inverting equation

$$P(0) = e^{-\mu} \times \left(2e^{-\mu_{SS}/2} - e^{-\mu_{SS}}\right), \tag{5.10}$$

where $P(0)$ is the fraction of bunch-crossings not having in-time hits in both north and south LM counters and $\mu \propto \mathcal{L}$ is the average number of collisions per bunch-crossing registered in both LM counters. The μ_{SS} is the average number of collisions only firing one of the arrays. The second term in parenthesis on the right accounts for the possibility of multiple interactions each firing only one side of the LM. The $P(0)$ is measured separately for each of the 36 bunches over an interval of about 60 s (one LBN), long enough to collect enough events to reduce the statistical uncertainty in $P(0)$ well below 1%, but short enough that the instantaneous luminosity only changes negligibly[5].

The effective cross sections determined at the end of Run IIa are $\sigma_{\text{eff}} = 48.0 \pm 2.6$ mb and $\sigma_{SS} = 9.4$ mb [118]. Changes in the detector and the luminosity system that affect the luminosity measurement divide the Run IIa into five periods listed in Table 5.1. The total Run IIa luminosity is determined starting from σ_{eff} at the end of Run IIa and back-propagating corrections. Overall the recorded luminosity for Run IIa is 1315.1 pb^{-1}, with an uncertainty of 6.1%.

Table 5.1: Major data taking periods in Run IIa that have similar luminosity normalization adjustments.

Period	Run range	Luminosity	Corrections applied
A	151814–196584	525.3 pb^{-1}	Magnet correction
B	201537–202151	7.8 pb^{-1}	Baseline correction
C	202152–204805	142.3 pb^{-1}	Dead time correction
D	204806–211214	435.9 pb^{-1}	NIM to VME, radiation damage
E	211223–215670	203.8 pb^{-1}	Final σ_{eff} and σ_{SS}

[5]This is true up to luminosities of about $250{\cdot}10^{30}$ cm^{-2}s^{-1}. This luminosity was first exceeded in Run IIb on Jan 8, 2007.

5.6 Subsets of data

The DØ Run IIa data taking spanned a time period of almost four years from April 19 2002 to February 22 2006, with the first commissioning runs starting on November 29 2001. This is a relatively long time, and improvements have been going on in detector systems, luminosity monitoring, triggering and accelerator operations throughout Run IIa. The DØ detector is shut down and taken out of the collision hall for repairs and upgrades roughly once a year. Trigger lists are updated periodically every few months to optimize data taking. In addition, changes to other sub-systems are tested and implemented during data taking periods.

The different upgrades set the timescale over which the inclusive jet measurement would be expected to be stable. Changes affecting the luminosity system are listed in Table 5.1. The major trigger list versions are listed in Table 5.2. Changes in single jet triggers, as listed in Table 4.1, have mostly taken place between major versions of trigger lists. The major shutdowns are listed in Table 5.3 along with minor divisions in data-taking.

Table 5.2: Major trigger list versions and their approximate run ranges. The run ranges for consecutive trigger lists may overlap as the trigger lists are being commissioned. Changes affecting the trigger system are also listed.

Run range	Trigger list	Comment
157476 – 160554	v07	First trigger list
157713		L1 trigger $\lvert\eta\rvert \to 2.4$
160582 – 167015	v08	
167019 – 170246	v09	
168948		L2 jet $3 \times 3 \to 5 \times 5$
169521		1/4 of $\lvert\eta\rvert > 2.4$ and ICR added to readout
170247 – 174802	v10	
172174		L1 trigger $\lvert\eta\rvert \to 3.2$
– 174802		L1 read-out varied between 2.4–3.2
174845 – 178721	v11	Full $\lvert\eta\rvert < 3.2$ coverage at L1
178069 – 194597	v12	
180915		New calibration for L1 calorimeter
194567 – 208144	v13	
207217 – 215670	v14	

Table 5.3: Summary of major shut-downs and data-taking periods in Run IIa.

Major period	Run range	Comment
1	139500 – 149613	Commissioning
2	151814 – 157120	Tracker Comes Alive
3	157476 – 160554	Building the Trigger List 1
3	160584 – 167015	Building the Trigger List 1
4	167019 – 170374	Building the Trigger List 2
		January 2003 shutdown
5	172174 – 178559	2003 Winter Data
6	178722 – 180956	2003 Summer Data
		October 2003 shutdown
7	184951 – 190370	Winter 2003–2004
		March 2004 shutdown
8	191266 – 194552	Spring 2004
9	194567 – 196584	Summer 2004
		August 2004 shutdown
10	201537 – 204801	Winter 2004: Solenoid Field Lower
11	204803 – 207351	Spring 2005
12	207728 – 212107	Summer 2005
13	211292 – 212107	Fall 2005
		November 2005 shutdown
14	212900 – 215670	Winter 2005–2006
		February 2006 shutdown
		Run IIa ends

Chapter 6

Jet energy scale

6.1 Overview

The purpose of the jet energy scale (JES) is to provide a link between the initial particles produced in the hard scatter process, as described by theory, and the calorimeter energy deposits clustered into calorimeter jets, as measured by experiment. This process involves the hadronization of the outgoing partons into showers of stable or long-lived particles, the particle jets, as shown in Fig. 1. To compare data and theory, they need to be corrected to a common level. At DØ this common level is chosen to be particle jets, which requires us to correct the calorimeter jet energies back to the particle level, and apply non-perturbative corrections (hadronization and underlying event) to theory to move from parton to particle level. The common level is chosen to be the particle level to avoid introducing theoretical uncertainties from the non-perturbative corrections to experimental data. Other choices are also possible; the CDF experiment *e.g.* has chosen to correct calorimeter jet energies to parton level.

The main effects that need to be accounted for when correcting jet energies to the particle level are offset energy (E_{offset}), calorimeter response (R) and detector showering (S). These corrections can be expressed in a simple formula

$$E_{\text{ptcl}} = \frac{E_{\text{cal}} - E_{\text{offset}}}{R \cdot S}. \tag{6.1}$$

The offset energy includes electronics noise, calorimeter noise from uranium decays, pile-up from previous interactions and energy from multiple interactions during a bunch crossing. The underlying event energy is not considered as part of energy offset at DØ, because the underlying event energy is in-

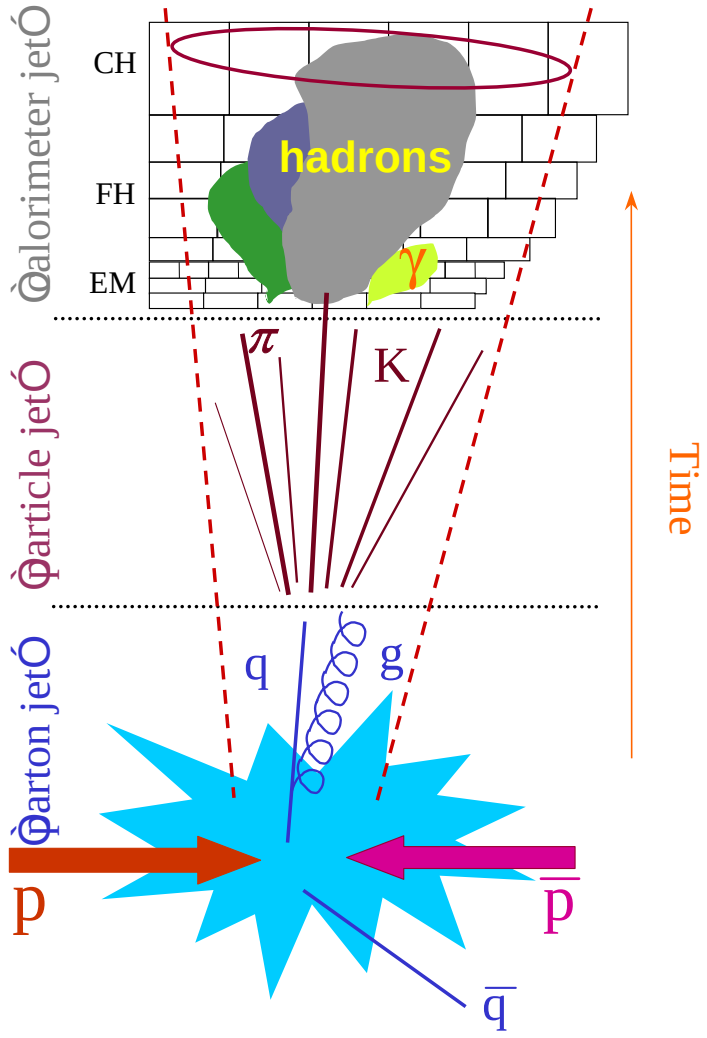

Figure 6.1: Parton, particle and calorimeter jets.

cluded in the jet also at particle level. The calorimeter response R gives the average fraction of measured calorimeter energy for the particles inside the particle jet cone. The detector showering is the fractional net flow of energy in and out of the jet cone due to detector effects, such as the magnetic field, scattering from dead material, shower development in the calorimeter and finite cell size. It is defined as the ratio of the response-corrected calorimeter jet energy and the particle jet energy in the absence of offset. The detector showering specifically does not include physics showering, where some of the initial parton energy is showered outside the jet cone. These corrections will be discussed in more detail in the following chapters.

The Monte Carlo prediction of the jet response, offset and showering at DØ has traditionally been rather poor due to lack of test beam data. For this reason the jet energy scale derivation relies heavily on data-based methods. This is in contrast to the methods used at CDF, where test beam data and careful tuning of the Monte Carlo have allowed JES to be determined mainly relying on the detector simulation. It should be noted, however, that also the Monte Carlo side at DØ has seen significant improvements during the development of Run IIa JES, as we will discuss later. These improvements include overlaying zero bias (ZB) data events on MC events to simulate noise and multiple interactions for offset, more refined true showering definition, and the tuning of single pion response to bring data and MC into agreement.

The simple corrections in Eq. 6.1 are not sufficient when the goal is to bring JES to a percent-level precision. For this reason we will also discuss biases in offset and response due to suppression of calorimeter energies (zero suppression bias), in the missing-E_T projection fraction (MPF) method used to measure response (topology bias), in jet angle measurement (rapidity bias) and the complications caused by the mass of the jets produced by the Run II cone jet algorithm (four-vector corrections).

Much of the work on JES described here has been published in more detail in Refs. [119, 120]. This chapter focuses particularly on the corrections for p_T and y of $R_{\text{cone}} = 0.7$ jets in the inclusive jet and dijet samples that are relevant for this thesis. Primary original work by the author in Sections 6.4, 6.8 and 6.10 and relating to dijet calibration is also given more emphasis.

6.1.1 Exact definitions

Many of the observables in data are sensitive to varying combinations of offset, response and showering. This is further complicated by the need for additional bias corrections for each sub-correction. In order to consistently combine all corrections it is necessary to provide "true" definitions for Monte Carlo at particle and calorimeter cell level so that observables can be appropriately corrected. This is especially true for showering, for which an appropriate definition remained elusive in Run I, adding large uncertainties to the showering corrections.

The energy of a particle jet is defined as the sum of the energies of all particles belonging to the particle jet

$$E_{\text{jet}}^{\text{ptcl}} = \sum_{i \in \text{ptcljet}} E_i. \tag{6.2}$$

The measured energy of a calorimeter jet $E_{\text{jet}}^{\text{meas}}$ is a combination of visible energy E^{meas} from particles in the particle jet, outside particles that come in and offset energy E_{offset}

$$E_{\text{jet}}^{\text{meas}} = \sum_{i \in \text{ptcljet}} E_i^{\text{meas}} S_i + \sum_{i \notin \text{ptcljet}} E_i^{\text{meas}} S_i + E_{\text{offset}}, \tag{6.3}$$

where S_i is the fraction of energy each particle contributes inside the calorimeter jet cone. The offset corrected energy is then defined by reordering this relation

$$E_{\text{jet}}^{\text{meas}} - E_{\text{offset}} = \sum_{i \in \text{ptcljet}} E_i^{\text{meas}} S_i + \sum_{i \notin \text{ptcljet}} E_i^{\text{meas}} S_i. \tag{6.4}$$

The right hand-side is defined in a sample with no offset energy, *i.e.* no zero bias (ZB) overlay. This means that E_{offset} also contains any particle jet energy that becomes visible because offset energy increases the total above the cell-energy thresholds. These zero suppression effects to offset and response are discussed in Section 6.7.

The response is defined as a ratio of the visible particle energies to the original particle jet energy

$$R = \frac{\sum_{i \in \text{ptcljet}} E_i^{\text{meas}}}{E_{\text{jet}}^{\text{ptcl}}}. \tag{6.5}$$

This quantity is independent of which particles actually fall within the calorimeter jet boundaries. It is also a natural definition when the MPF method, described in Section 6.3.1, is used to measure the calorimeter jet response because this method is equally insensitive to the actual jet cone. However, the cone size does change which subset of the particles in the hadronic recoil belongs to the particle jet. The resulting topology bias is discussed in Section 6.6.

In order to satisfy Eq. 6.1 the true showering is necessarily defined as

$$S_{\text{jet}} = \frac{\sum_{i \in \text{ptcljet}} E_i^{\text{meas}} S_i + \sum_{i \notin \text{ptcljet}} E_i^{\text{meas}} S_i}{\sum_{i \in \text{ptcljet}} E_i^{\text{meas}}}. \tag{6.6}$$

This is the ratio of the measured energy inside the calorimeter jet cone to the total visible energy from the particle jet regardless of the jet cone. This exact definition is used to correct any bias in the data-based measurement of the showering, as discussed in Section 6.5.

6.2 Offset

The offset energy consists of all the energy in the jet not related to the hard scatter. The offset energy is divided into three distinct categories, noise and pile-up (NP), multiple interactions (MI) and underlying event (UE). These components are detailed below.

The NP part consists of detector and electronics related contributions. The leading sources are noise in the calorimeter and electronics, and decays of the uranium nuclei in the calorimeter depositing some energy in the cells. The pile-up is the energy left in the calorimeter during previous collisions. Because of the short time between collisions (396 ns), the electronics signal may not have fully decayed before the next crossing. The baseline is subtracted from the signal just before the bunch-crossing so pile-up may also have a negative sign. A typical NP offset for $R_{\text{cone}} = 0.7$ cone jets in the central calorimeter (CC) and in the end caps (EC) is about 0.2 GeV for an average jet. The intercryostat region (ICR) has higher gain detectors, and consequently the typical NP offset is about four times higher, 0.8 GeV.

The MI part of the offset is the energy deposited by additional MB collisions during the bunch crossing. Part of this energy is underlying event for MB collisions, part MB jets that are of low energy and often not reconstructed. Because all MB collisions should be on equal footing, the MI offset is expected to increase linearly with the number of additional interactions. This linearity has been observed to hold up to at least ten additional interactions, as shown in Fig. 6.2, after which statistics run out. The multiple interactions typically deposit about 0.2 GeV in CC per additional interaction. The energy density increases strongly at higher rapidities, but the typical contribution to transverse momentum is fairly constant $p_T^{\text{MBoffset}} \approx 0.2$ GeV$/c$ per interaction in CC and EC, slightly more in ICR.

The UE offset comes from the primary interaction, but is not directly related to the hard-scattered partons. It is the energy deposited by additional interactions in the same hard event (initial and final state radiation) and is generally isotropically distributed in the transverse plane, ϕ. It is possible to estimate the UE offset from data for MB interactions. However, this same UE offset is not necessarily applicable for hard scatter interactions or different physics processes due to *e.g.* color flow effects. The UE offset is therefore not part of the common JES corrections, but is separately calculated for the inclusive jet production in Chapter 8. The UE offset for MB events is typically about 0.2 GeV in CC.

The offset energies are measured from data using minimum bias and zero

bias (ZB) events. Both events are collected at a constant rate of about 0.5 Hz. The only requirement for ZB events is coincident timing with the beam crossing, and MB events require in addition hits in the luminosity monitors (LM), indicating that an inelastic collision took place. The offset is estimated as the average energy density in all calorimeter towers (including ones with no energy after zero suppression) within a detector η-ring. The offset energy for given jet cone is then calculated by summing the average offset in towers within the cone radius of the jet center at (η, ϕ).

The NP offset is determined from ZB events without inelastic collisions, requiring a veto for LM hits. The luminosity monitor is not 100% efficient so events with reconstructed primary vertices are vetoed in addition. The UE offset contribution is estimated as the difference between ZB with LM veto and MB events with a single vertex. The UE offset is not used in the final JES corrections. The MI offset for $N-1$ additional interactions is finally the difference in MB offset between events with N and 1 primary vertices. The formulae can be summarized as

$$E_{\mathrm{NP}} = E^{\mathrm{offset}}_{\text{ZB with LM veto}}, \tag{6.7}$$

$$E_{\mathrm{UE}} = E^{\mathrm{offset}}_{\text{1 MB}} - E^{\mathrm{offset}}_{\text{ZB with LM veto}}, \tag{6.8}$$

$$E_{\mathrm{MI}}(N) = E^{\mathrm{offset}}_{N\text{ MB}} - E^{\mathrm{offset}}_{\text{1 MB}}, \tag{6.9}$$

$$E_{\mathrm{offset}}(N) = E_{\mathrm{MI}}(N) + E_{\mathrm{NP}}. \tag{6.10}$$

Figure 6.2 shows the average MB energy versus primary vertex multiplicity for a few η rings, clearly showing the linear dependence of the offset on the number of vertices. The linear fits are used in implementing the corrections. Some luminosity dependence for offset with constant vertex multiplicity has been measured and is applied in JES, but this effect is quite small ($\sim 10\%\cdot(MI(n+1) - MI(n))$.

The average vertex multiplicity for Run IIa inclusive jet data is between 1.5–2.0, meaning that the average offset in CC is about 0.5 GeV, of which 0.3 GeV is from MI offset and 0.2 GeV from NP offset. The contribution to p_T is about 0.5 GeV/c in CC and EC, and 0.8 GeV/c in ICR. At $p_T = 50$ GeV/c (uncorrected $p_T \sim 30$ GeV/c) this leads to about 1.5–2.5% correction on the final jet energy, with the importance of the offset quickly diminishing at higher energy.

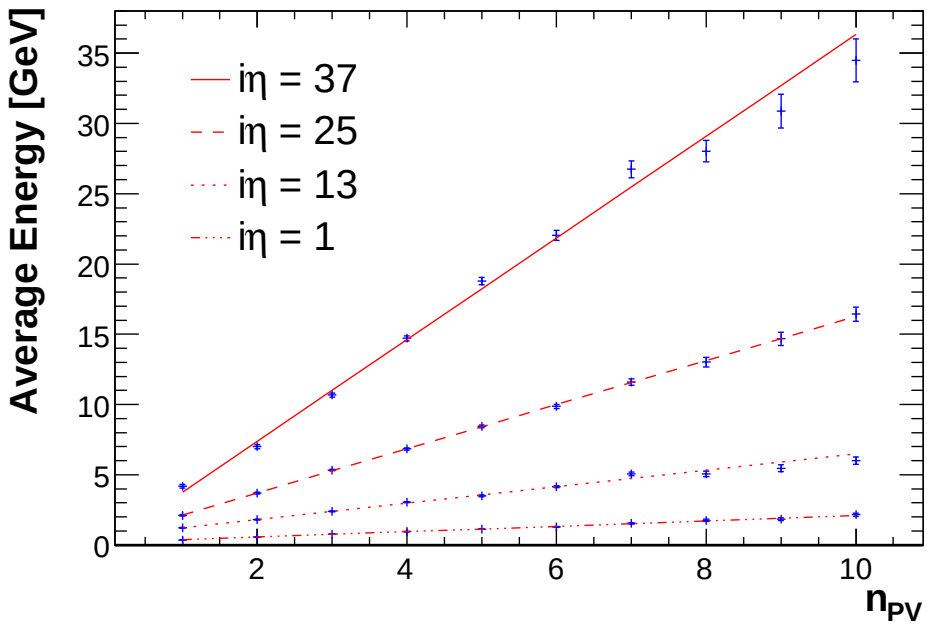

Figure 6.2: Average MB Offset energy as a function of number of primary vertices for different $i\eta$ rings.

6.3 Central calorimeter response

The response is broken here into two parts $R = R_{\rm cc}(E) \cdot F_\eta(\eta_{\rm det}, E)$. This is both to factorize the response correction to simplify its derivation and to facilitate the derivation of a sample specific JES. Measurements have shown that the standard calibration sample γ+jet and the dijet jet sample used in this thesis have significantly different responses. The F_η part, the η-dependent correction, is derived from data for both samples, but $R_{\rm cc}(E)$, the central calorimeter response, can only be derived from the γ+jet sample. Tuned Monte Carlo studies are used to derive a dijet-specific $R_{\rm cc}(E)$.

The calorimeter response is by far the largest correction for the calorimeter jet energies. The calibration is done in several steps starting from the "standard candle" Z boson mass, using several different physics samples to translate this into the final jet energy calibration. In the first step the electrons are calibrated using the Z mass reconstructed from $Z \rightarrow e^+e^-$ decays. The electron calibration is then transferred to photons using MC to simulate the small response differences due to interaction with dead material. The scaled photon energy is used to set the jet energy scale for central jets us-

ing momentum conservation in γ+jet events. Finally, the forward jets are calibrated against central jets (and photons) using dijet (and γ+jet) events. This process is briefly detailed in the following, before going into more detail in the following sections.

The electron energy scale is calibrated first using $Z \to e^+e^-$ events. The peak of the invariant mass distribution of di-electron pairs is matched with the mass of the Z boson that was measured with high precision by the LEP experiments [121]. The good resolution of the electron energy measurement combined with reasonably high statistics of $Z \to e^+e^-$ events leads to 0.5% uncertainty in the calibration of the electron energy scale. This gives the first reference point in the form of electron energy scale.

There are no processes available at the Tevatron that would produce electrons and jets simultaneously in sufficiently high quantities[1] for calibration purposes. The γ+jet events on the other hand are quite copious, allowing them to be used for calibration up to about $p_T = 250$ GeV/c with 1 fb^{-1} of data. The reach will further increase with higher luminosity. The electron energy scale is transferred to photons, with additional corrections due to dead material, and jets are calibrated with back-to-back photons using transverse momentum conservation.

Although fairly copious, the γ+jet events alone are not sufficient for calorimeter equalization with high granularity. The γ+jet sample is supplemented with dijets, where the central jet is calibrated with γ+jet events, and the forward jet is calibrated against the central jet again using momentum conservation. This method is discussed in detail in the next section.

The electron energy scale sets the rough energy scale of the EM component $f_{\rm em}$ of the jets, which would then be set to $R_{\rm em} = 1$. Indeed, highly electromagnetic jets have been observed to have a response very close to 1. The hadronic component $f_{\rm had}$ of the jets interacts more weakly and leads to lower response $R_{\rm had} < 1$. The jet shower produces about 1/3 π^0's that interact electromagnetically (through instant $\pi^0 \to \gamma + \gamma$) at each step of the secondary showering, *i.e.* when the hadrons in the shower interact with the nuclei to produce more hadrons [122]. As the initial jet energy increases the number of the secondary showering steps increases, leading to asymptotic $f_{\rm em} \to 1$, $f_{\rm had} \to 0$. Combined with $R_{\rm had} < R_{\rm em} = 1$, this means that jet response is

[1] Z+jet, where $Z \to e^+e^-$ is a useful process at low jet p_T, but is produced in relatively small quantities at the Tevatron. This channel may be available at the end of Run II, and at the LHC.

less than one, asymptotically approaching one at infinite energy[2].

6.3.1 Transverse momentum balancing methods

There are currently three methods based on transverse momentum conservation that can be used for jet energy scale measurement in γ+jet events. The basic assumption is that the incoming protons have no transverse momentum p_T, and the sum of the initial transverse momenta of the hard-scatter partons is essentially zero, $\sum_i \vec{p}_{T,i} = 0$. Because the longitudinal momenta p_Z of the proton remnants going into the beam pipe is not measured, no constraints (except kinematic limit $E < 980$ GeV/c) can be set for the sum of the longitudinal momenta $\sum_i p_{z,i}$. It is further assumed that the photon and particle jets retain $\sum_i \vec{p}_{T,i} = 0$. Showering effects and non-reconstructed jets may slightly change this, but these effects are accounted for in appropriate bias corrections. The photon is assumed to be calibrated, $R_\gamma = 1$, so that the measured quantities can be related to the jet response and showering.

The most basic method is called ΔS, where

$$\Delta S = \frac{p_{T,\text{jet}} - p_{T,\gamma}}{p_{T,\gamma}}. \tag{6.11}$$

The photon and jet are required to be back-to-back with no additional jets (from leading primary vertex). The ΔS method is very sensitive to soft radiation (additional non-reconstructed jets) and particle level imbalance, but directly probes the p_T of the reconstructed objects. If the biases are assumed negligible or corrected for, and $p_{T,\text{ptcljet}} = p_{T,\gamma} = p_{T,\text{ptcl}}$

$$\Delta S = R \cdot S - 1. \tag{6.12}$$

A more general method based on ΔS is the hemisphere method, which is later used for JES closure tests. In this method the transverse momenta of all the reconstructed objects are projected to the photon axis

$$H = \frac{\sum_i \vec{p}_{T,i} \cdot \vec{p}_{T,\gamma}}{|\vec{p}_{T,\gamma}|}. \tag{6.13}$$

This definition is especially useful for final states with multiple jets, and reduces to ΔS when $N_{\text{jet}} = 1$ and $\Delta\phi(\gamma, \text{jet}) = \pi$. Again, when the biases

[2]The power law formula $R = 1 - aE^{m-1}$, with $a \approx 1$, $m \approx 0.7$ and E in GeV, takes advantage of this simple view and has been shown to fit measured response well. For historical reasons more than anything else the response is still parametrized with a quadratic logarithm formula that gives an equally good fit.

are assumed negligible and jets and photon balanced at particle level, the closure test will give $|H| = 1$ when all jets are correctly calibrated.

Both ΔS and hemisphere method measure a combination of response and showering. The sensitivity to showering is reduced when the p_T balance is measured using the missing-E_T projection fraction (MPF) method. This method could be thought of as a generalization of the hemisphere method where reconstructed objects are replaced with calorimeter towers. The vector sum of all the calorimeter towers (including those of the photon) equals the missing E_T in the event, which is projected to the normalized photon vector, hence the name of the method. The MPF method is usually directly defined through the missing-E_T

$$R_{\mathrm{MPF}} = 1 + \frac{\vec{\not{E}}_T \cdot \vec{p}_{T,\gamma}}{|\vec{p}_{T,\gamma}|^2}. \tag{6.14}$$

In the MPF method the photon is balanced against the hadronic recoil, $\vec{p}_{T,\gamma} + \vec{p}_{T,\mathrm{had}} = 0$. When the jet is required to be back-to-back with the photon, and no additional jets are allowed in the event, the hadronic recoil response can be identified with the jet response. This is the default method used in jet energy scale determination.

Because the hadronic recoil corresponds to the parton level energy rather than particle level energy, subtle biases can be present if the particle jet core and physics showered component respond differently. The hadronic recoil may also contain soft jets that are not reconstructed. These topological biases and other biases in the MPF method are discussed later in Section 6.6.

The jet response depends on the particle jet energy so the results are usually binned in energy. However, the measured jet energy has poor resolution and can lead to a large bias in the response measurement. To avoid the resolution bias, the estimator

$$E' = p_T^{\gamma} \cosh \eta_{\mathrm{jet}} \tag{6.15}$$

is used instead. The E' is strongly correlated to the particle level jet energy and has much better resolution than the measured jet energy.

6.3.2 Photon energy scale

All the methods based on momentum balance discussed in the previous section assume that the photon is properly calibrated with $R = 1$. Any error in this calibration will directly translate into an error on jet energy scale, making the photon energy scale a crucial component of the JES determination.

The photons are only selected in the best measured part of the calorimeter, $|\eta^{\gamma}| < 1.1$, to limit the uncertainty in photon calibration.

In the first approximation the photon response is identical to the electron response, as both objects interact electromagnetically producing similar showers in the calorimeter. However, there are subtle differences in how these two particles interact with the material in front of and inside the calorimeter. This is already evident from the fact that the charged electrons deposit enough energy in the tracker to have their tracks reconstructed, whereas the neutral photons do not. There is a significant amount of dead material in front of the calorimeter and the solenoid magnet so that these small differences in energy losses are amplified. Overall, the photons loose slightly less energy in the dead material and have higher response than electrons.

The electron energy scale is determined from data to about 0.5% accuracy using $Z \rightarrow e^{+}e^{-}$ decays. There is currently no data-based method to derive the response difference between electrons and photons so MC simulations tuned to reproduce the electron response in data are used instead [123, 124, 125, 62]. The leading uncertainty in the description is the amount of dead material in front of the calorimeter, which is estimated to be $0.17X_0$–$0.36X_0$. Figure 6.3 shows the central correction and the resulting variation in the ratio of electron and photon energy scales in tuned MC compared to the default MC.

6.3.3 Background contamination

A small fraction of jets have most of their energy in a leading π^0 that immediately decays to a pair of photons. If the photons in the pair are sufficiently close as they often are, and there is little activity around the photons, the jet can mimic an isolated single photon typical of γ+jet events. Because the cross section of γ+jet events is 3–4 orders of magnitude lower than that of dijet events [126], the EM-jets contribute a significant background for true γ+jet events.

The γ+jet sample purity can be improved by tightening photonID cuts, although the efficiency for real photons is also reduced. The photonID group has provided three sets of photonID cuts, loose, medium and tight [127, 128], that are used to study the background contamination effects in JES. It is also important to note that tighter photonID cuts significantly change the EM-jet response, as discussed in next section. Tight cuts lead to a response quite similar to that of photons as a high fraction of the energy is deposited into a leading π^0 that decays into two photons. The true photon response can also

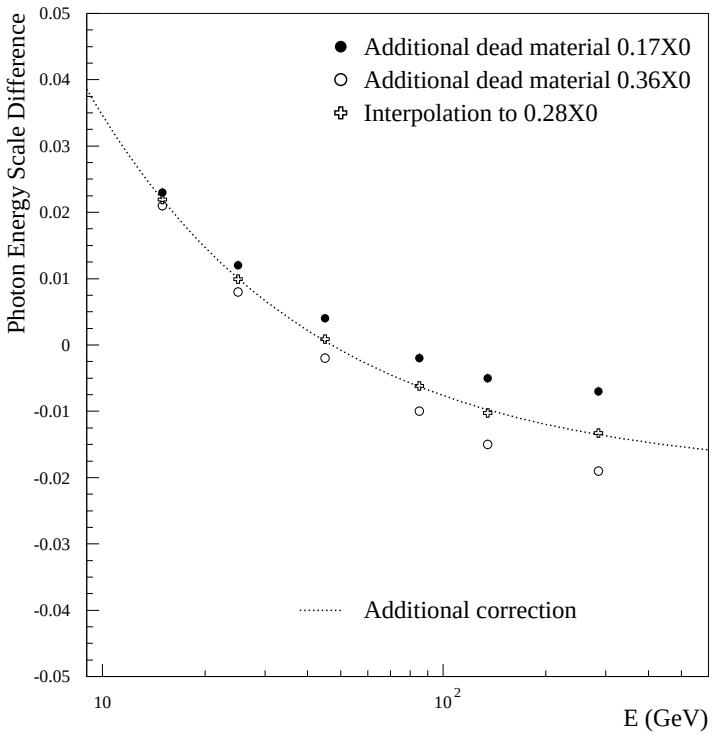

Figure 6.3: Difference of photon energy scale relative to electron energy scale in tuned MC and default MC. The variation is due to the uncertainty in the amount of additional dead material in units of radiation length X_0.

slightly change with tighter cuts, but this effect is considered small enough to be accounted in the systematics.

The purities for different photonID cuts in CC are shown in Fig. 6.4(a). The current default γ+jet sample is based on tight photonID. Quarks and gluons are more likely to radiate additional jets than photons so topological cuts such as cutting on the number or p_T of additional jets, or $\Delta\phi$ between the photon and the jet, can affect the relative cross sections of dijets and γ+jets. In fact, introducing the constraint to have exactly one jet in the γ+jet events significantly purifies the mixed sample. The current purities are based on $N_{\rm jet} = 1$ and $\Delta\phi > 3.0$. The dijet events are more likely to have jets at high rapidities than γ+jet events so that a jet rapidity dependence of the sample purity is observed. Figure 6.4(b) shows the lower purity in EC for tight photonID. The purity is calculated and fitted using MC cross

sections, but the results are also confirmed by comparing several calorimeter variable distributions for the photon candidates between data and mixed MC (template fits).

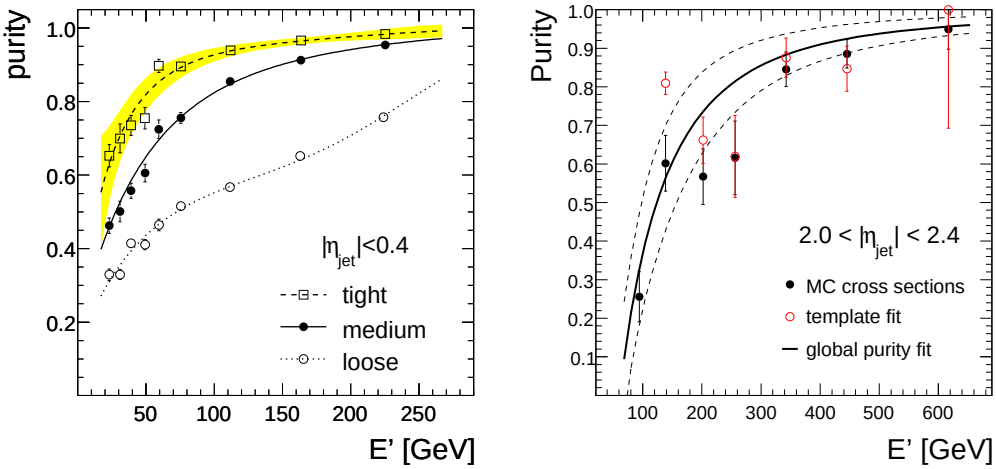

(a) (b)

Figure 6.4: (a) γ+jet sample purity in CC for different photon ID cuts calculated using MC cross sections. (b) γ+jet sample purity in EC for tight photonID using both MC cross sections and template fits to data.

6.3.4 Combined correction

To reduce the uncertainty in JES due to background contamination in γ+jet events to the lowest attainable level, the EM-jets are considered as part of the calibration sample and their response is derived in detail. The EM-jets have more hadronic activity than true photons and hence lower response, but with the difference to true photons decreasing with tighter cuts. The γ+jet and EM+jet samples are mixed according to the Monte Carlo cross sections after photonID cuts. The purities have also been cross-checked using neural network outputs in data, but these results have lower statistical precision.

The jet response measured in the γ+jet sample is corrected for both photon and EM-jet energy scales relative to the electron energy scale, weighted by the MC cross sections of signal and background. The combined correction to the measured response in CC in the γ+jet sample is shown in Figs. 6.5(a)–(b) for the medium and tight photonID cuts. The combined corrections for different photonID cuts are quite different at low p_T, with the medium sample

providing the best cancellation between the photon energy scale and background contamination corrections in CC. The combined correction provides quite consistent results for different samples after corrections, as shown in Figs. 6.6(a)–(b) for CC before and after corrections. The small residual differences may be partly due to changing photon response, as such differences are also observed in pure γ+jet MC. These small residuals are included in the photon ID systematics.

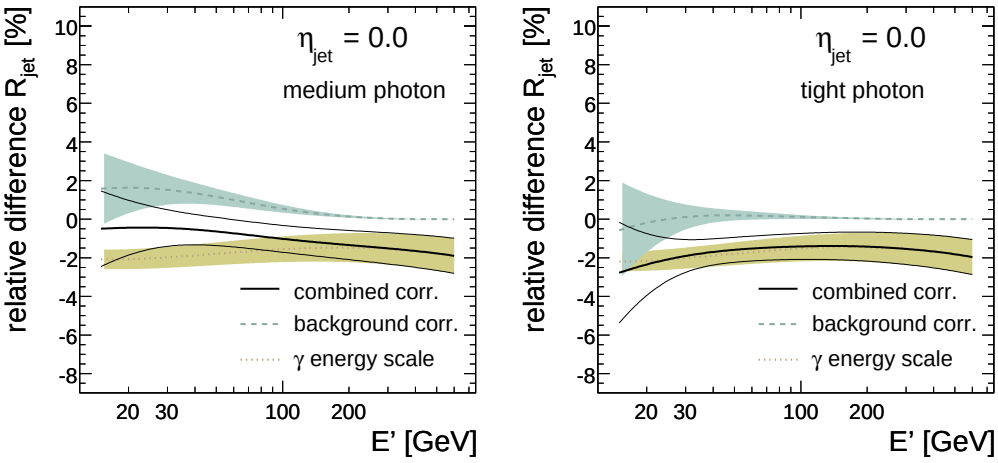

(a) (b)

Figure 6.5: Combined correction to measured jet response and its uncertainty in CC for (a) medium photon ID, and (b) tight photonID.

6.3.5 High energy extrapolation

The statistics of the γ+jets sample limit the direct response measurements in CC to $E' < 350$ GeV. The measured low energy response has to be extrapolated to the highest jet energies at ~ 600 GeV, introducing significant statistical uncertainty from the fit in CC. For higher rapidities this limitation is avoided because the high energies are directly calibrated using the dijet sample with central-forward topology, as discussed in Section 6.4. To avoid statistical uncertainty of more than two percent at high-p_T in CC, Monte Carlo models are used to constrain the high-p_T response, as was done in Run I [129].

The most significant limitation for the MC approach is that the default MC does not reproduce the measured response in data. This is mainly because of

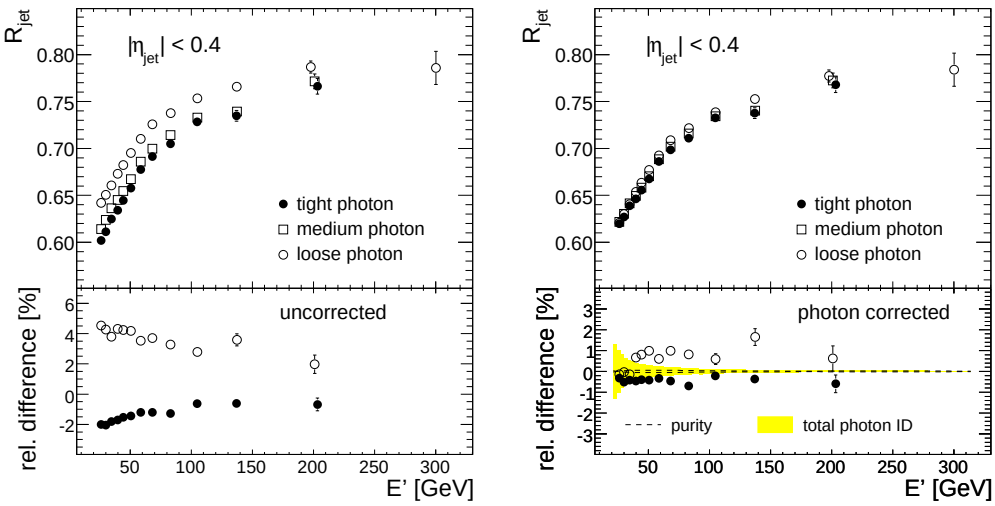

(a) (b)

Figure 6.6: The γ+jet CC response in data for different photon ID cuts (a) before combined correction, (b) after combined correction.

the poor description of the single pion response in default MC. The description of the measured response is improved by scaling the energies deposited by hadrons in MC by factor

$$k(E_h; A, B, C) = R(E_h; A, B, C)/R_\pi^{\mathrm{MC}}(E_h), \tag{6.16}$$

where the parametrization is done as a function of the true hadron energy E_h. The R_π^{MC} is the single pion response in MC, parametrized using the power law formula as

$$R_\pi^{\mathrm{MC}}(E) = c_2[1 - a_2(E/E_0)^{m_2-1}], \tag{6.17}$$

with $E_0 = 0.75$ GeV, $a_2 = 0.588$, $m_2 = 0.456$ and $c_2 = 0.870$. The scaled pion response is parametrized as

$$R(E) = c_1[1 - a_1(E/E_0)^{m_2-1}], \tag{6.18}$$

where $a_1 = A \cdot a_2$, $m_1 = B \cdot m_2$ and $c_1 = C \cdot c_2$. The scaling parameters (A, B, C) are fitted by varying them until the γ+jet MC reproduces the jet response measured in the γ+jet data in CC. Figure 6.7 shows the measured jet response in data with the high energy extrapolation using MC. The direct fit to data using a quadratic logarithmic formula is in good agreement with the MC-based extrapolation, but the high energy extrapolation uncertainties are significantly reduced using MC.

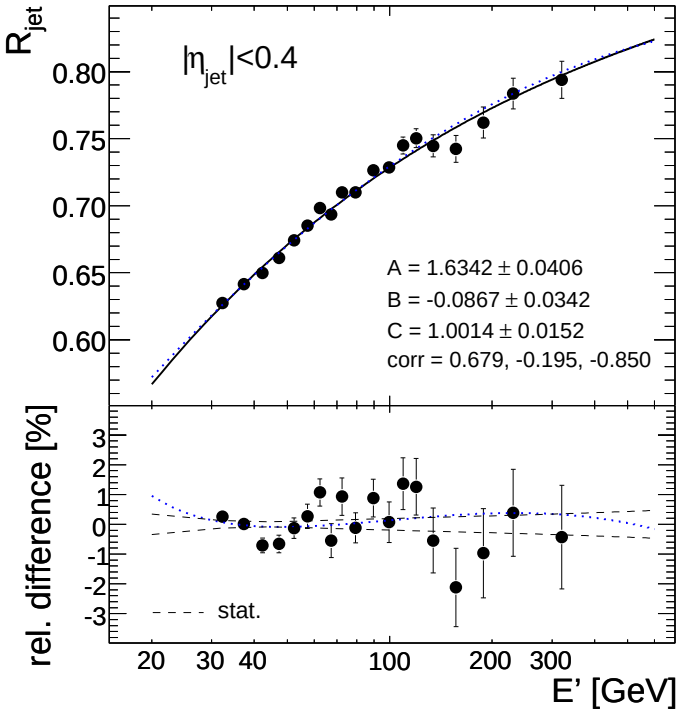

Figure 6.7: MPF CC response in data with fit from MC using parametrized single pion response. The dotted line shows the direct quadratic logarithmic fit to data.

The trade-off of using MC for high energy extrapolation is the dependence on the MC simulation of fragmentation and gluon fraction. The fragmentation model uncertainty is estimated by comparing the results from two different physics generators, Pythia and Herwig. As discussed in Chapter 3, these two generators presents the two extremes of the current main stream physics generators. To simplify the comparison, the underlying event modeling has been turned off. The results obtained using the scaled single pion response are presented in Fig. 6.8(a). Both models agree on the highest energy response, but there are significant differences at low energies. Because the single pion response has been specifically tuned to reproduce data response roughly in the range 40–100 GeV/c, the fitted curve at $E > 100$ GeV will represent high energy uncertainty when the range 40–100 GeV is fixed to 0. This leads to about 0.8 % uncertainty at $E' = 600$ GeV, which is however significantly less than the statistical uncertainty of a pure data fit.

The uncertainty due to gluon fraction is estimated using the CTEQ6.1M

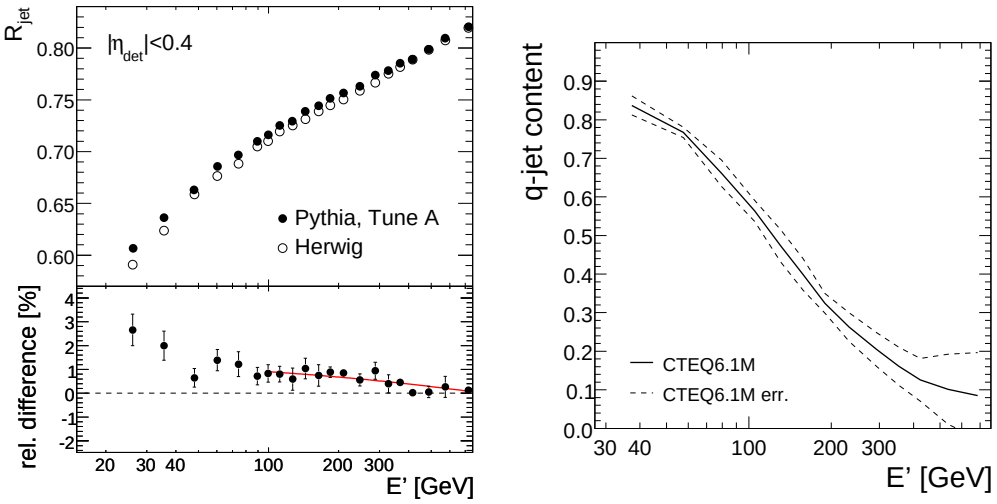

(a) (b)

Figure 6.8: (a) Response in MC using scaled single pion response with Pythia and Herwig. The underlying event simulation is turned off to highlight differences arising from the jet fragmentation model. (b) Quark-initiated jet fraction for central rapidity ($|\eta| < 0.4$) jets and its uncertainty estimated using Pythia and CTEQ6.1M PDFs.

PDFs[3] that provide an orthogonal set of 20 up and down variations of the PDFs. The resulting gluon fractions are calculated using Pythia, and the variations from the central value are added in quadrature. Figure 6.8(b) shows the central value for the fraction of quark-initiated jets and the unsmoothed error band. When combined with the differences in quark and gluon-initiated jet responses, as discussed in more detail in the next subsection and shown in Fig. 6.10, this produces an uncertainty estimate on the high energy extrapolation due to gluon fraction, or PDFs. The resulting variations in the response are about 0.2% overall, and do not significantly impact the overall uncertainties.

6.3.6 Dijet specific central calorimeter response

The methods presented so far allow for a precise measurement of the MPF response in CC for the γ+jet sample. As we will see in Section 6.4, the central-forward topologies allow the forward MPF response to be measured

[3]The more recently published CTEQ6.5M PDF set has almost the same central values, but uncertainties smaller by about a factor two so the uncertainty is slightly overestimated.

with a similar high precision relative to CC in both γ+jet and dijet samples. However, it is not obvious if the central jet response measured in the γ+jet sample is applicable to dijets with the same low uncertainties. Monte Carlo studies have shown that this assumption does not hold at the percent level precision.

The response differences between γ+jet and dijet samples stem from the different physics processes that produce the jets. As shown in Fig. 6.9, the MC γ+jets sample mostly consists of parton level quarks at low jet energy and gluons at high jet energy. For dijet MC this behavior is reversed, with mostly gluons at low energy and quarks at high energy. Similar behavior is expected for data, but not necessarily guaranteed, as the gluon fraction may depend on both the order of the perturbation theory and the PDFs used. The default MC is produced using Pythia with LO pQCD model and CTEQ 6.1M PDFs as input. Especially the poorly constrained high-p_T gluon PDF may produce a potential feed-back loop, as it affects the gluon fraction, which in turn affects JES and hence the measured inclusive jet cross sections that are the most important input for PDF fits that constrain the gluon PDF.

The gluon-initiated jets have lower response than quark-initiated jets because they have on average higher particle multiplicity with softer particles. The underlying reason for this is the higher color charge carried by the gluons than the quarks. This behavior has been established in data by measurements at LEP [130] that estimate the charged particle multiplicity in gluon-initiated jets to be about 50% higher than in quark-initiated jets. The CDF measurements utilizing γ+jet and dijet events confirm this behavior at the Tevatron [131]. The soft particles lead to low jet response due to steeply falling single pion response at low energy. The single pion response measured in Run II is steeper than in Run I, due to *e.g.* more dead material and shorter signal integration times, which may explain why no significant response differences between different samples were reported in Run I. Figure 6.10 shows the quark and gluon-initiated jet response differences measured in MC simulation with scaled pion response.

The expected inclusive jet response in data is estimated using the same MC with scaled pion response that was successfully used to fit the response in the γ+jet sample in the previous section. An important cross-check for this parametrization is a comparison to the single pion response directly measured from data [132] in Fig. 6.11. This method determined the calorimeter pion response using the energy measured by the tracker for isolated single pions in Zero Bias and track-triggered events. The differences in the important energy range $E_\pi > 1.5$ GeV are small and within statistical uncertainties, although

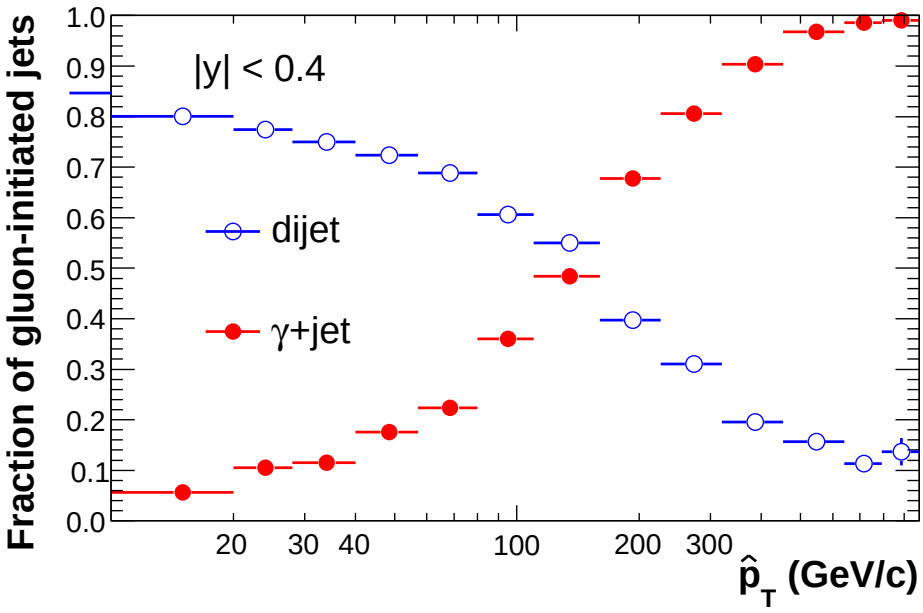

Figure 6.9: Fraction of quark and gluon-initiated jets in γ+jet and dijet samples in CC.

the two methods are very different. The ratio of CC jet responses for γ+jet and dijet samples in scaled MC is shown in Fig. 6.12, with a corresponding error band estimated from the uncertainties in gluon fraction and single pion response.

6.3.7 Uncertainties

The uncertainty related to central calorimeter response for γ+jets mainly comes from the uncertainty in photon energy scale, as shown in Fig. 6.13. The photonID uncertainty comes from the EM-jet background (purity and EM-jet energy scale uncertainty), as shown in Fig. 6.5, and contributes mainly at energies below $E' = 50$ GeV/c. To avoid double counting, the residuals after the combined correction in Fig. 6.6(b) are not included in the JES systematics. The observed difference between tight and medium photonID at low p_T is considered to be consistent with the uncertainties in photonID and the difference above 50 GeV/c is accounted for by the later application of topology bias corrections.

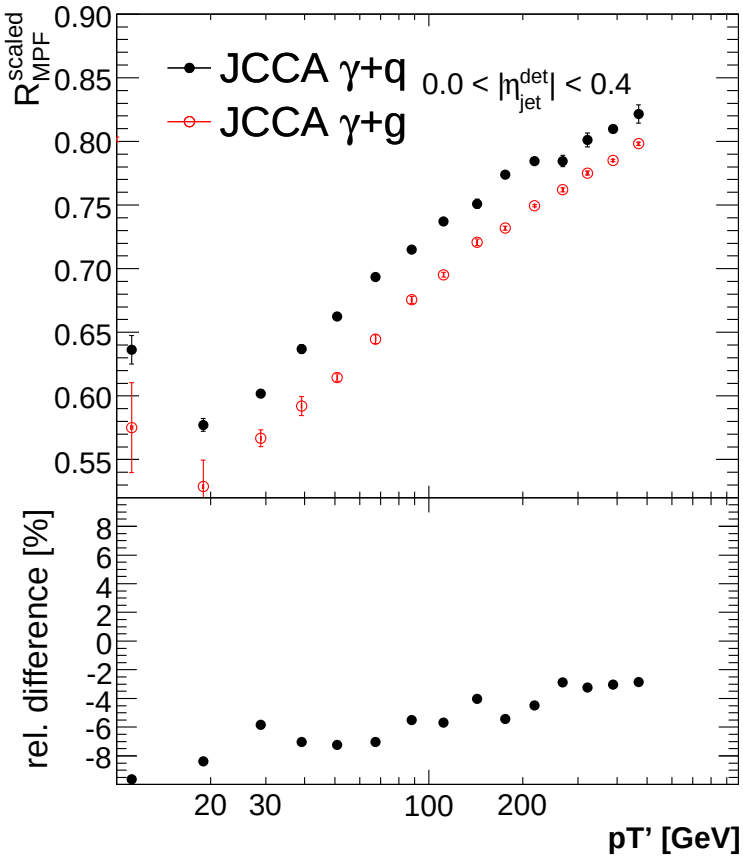

Figure 6.10: Quark and gluon-initiated jet responses and their relative difference measured in scaled γ+jet MC without ZB overlay.

The statistical uncertainty in the central calorimeter response has been greatly reduced by the application of MC high energy extrapolation, as shown in Fig. 6.7. The trade-off is the dependence on the MC description of jet fragmentation and gluon fraction. Of these two, the fragmentation model, taken as the difference between Pythia and Herwig, has the most significant uncertainty.

6.4 Eta dependent corrections

The purpose of the η-dependent corrections is to equalize the jet response everywhere in the calorimeter. The response versus ϕ is measured to be practically constant and is not separately corrected. The η dependence of

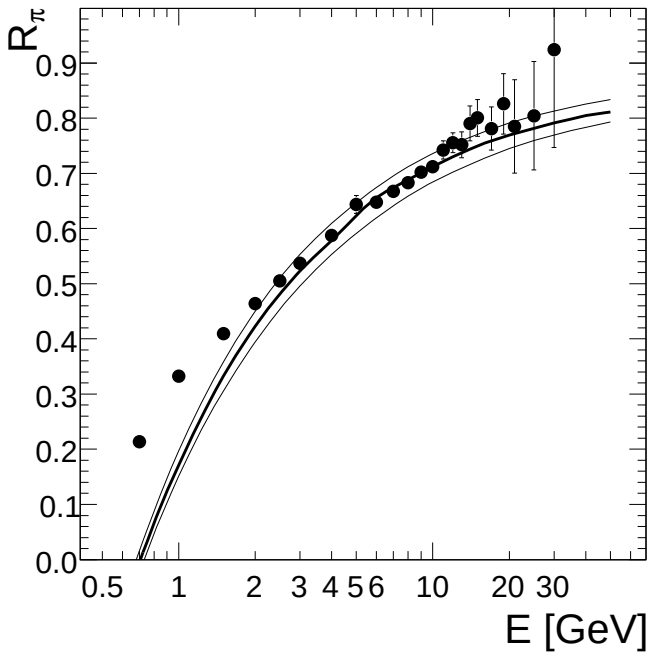

Figure 6.11: Single pion response measured in data (full circles) compared to the scaled single pion response from MC (solid line with uncertainty band). The data measurement at $E < 2$ GeV is not reliable due to trigger bias.

the response is mostly due to the changing calorimeter detector elements, especially in ICR, differing amounts of dead material and the angle of incidence varying with η. The η-dependent corrections aim to bring the response to the same level as in CC so that the same $R_{\rm cc}(E)$ can be applied to the η-dependence corrected energies everywhere in the calorimeter. This leads to the definition

$$F_\eta(E, \eta_{\rm det}) \equiv R(E, \eta_{\rm det})/R_{\rm cc}(E), \tag{6.19}$$

where R is the detector response at $\eta_{\rm det}$ for jet energy E, $R_{\rm cc}$ is the central calorimeter response and F_η is the η-dependent correction, which may also have residual energy dependence.

When using transverse momentum balance for two objects at different rapidities, these objects will have different energies, and because of response energy dependence, also different response even in a homogeneous calorimeter. This can be expressed as a function of $\eta_{\rm det}$ when E' is replaced with $E' = p'_T \cosh \eta_{\rm det}$

$$R_{\rm cc} \;=\; p_0 + p_1 \log(E'/E_0) + p_2 \log^2(E'/E_0) \tag{6.20}$$

$$\Rightarrow R_{\rm cc} = \hat{p}_0 + \hat{p}_1 \log(\cosh \eta_{\rm det}) + \hat{p}_2 \log^2(\cosh \eta_{\rm det}), \quad (6.21)$$

where the parameters $\hat{p}_i$ are related to the original parameters p_i by

$$\hat{p}_0(p'_T) = p_0 + p_1 \log(p'_T/E_0) + p_2 \log^2(p'_T/E_0), \quad (6.22)$$
$$\hat{p}_1(p'_T) = p_1 + 2p_2 \log(p'_T/E_0), \quad (6.23)$$
$$\hat{p}_2(p'_T) = p_2. \quad (6.24)$$

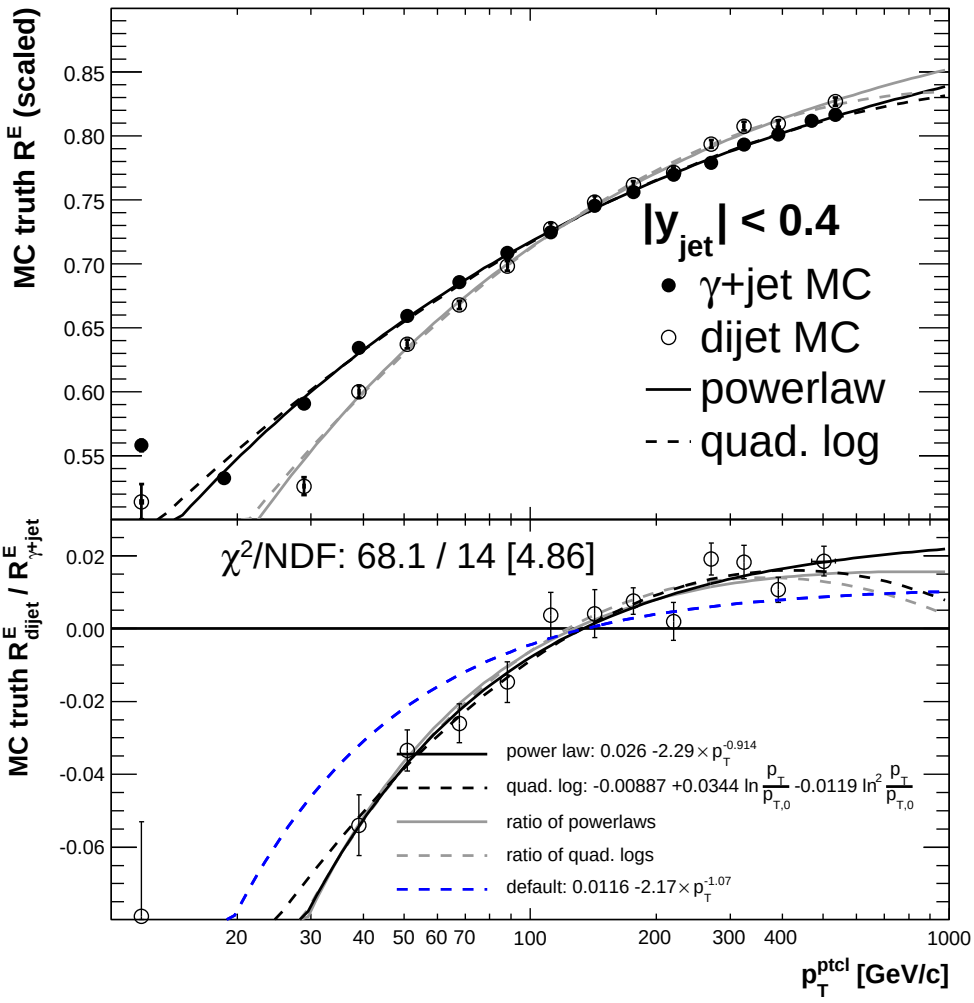

Figure 6.12: Ratio of CC jet responses in γ+jet and dijet samples estimated from MC with scaled single pion response. Fits using both power law and quadratic log functions to ratio and original points are shown for comparison. The power law fit to the ratio is chosen as the most physical description at high p_T. The dashed blue line shows the corresponding fit from default MC.

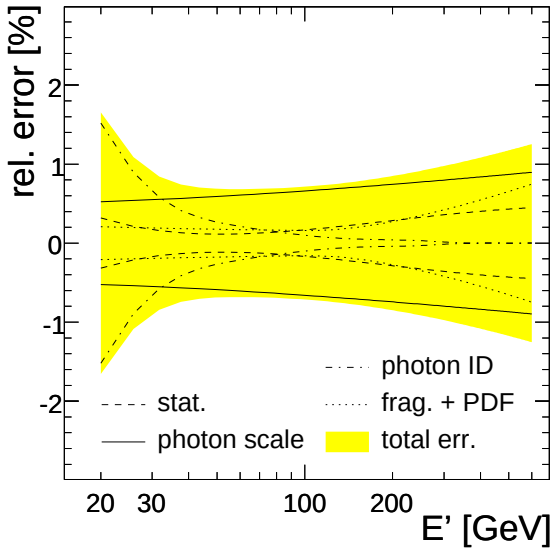

Figure 6.13: Total uncertainty of the CC response determination.

This inherent response η-dependence must be taken into account in the measurement of F_η using p_T balance. The equalized calorimeter response is returned to follow this ideal curve in $\eta_{\rm det}$. It should be noted that to fulfill the above equation, the new variable p'_T must be defined as

$$p'_T \equiv \frac{E'}{\cosh \eta_{\rm det}^{\rm probe}} = \frac{p_{T,\gamma} \cosh \eta_{\rm phys}^{\rm probe}}{\cosh \eta_{\rm det}^{\rm probe}}. \tag{6.25}$$

The calorimeter is equalized using both dijet and γ+jet samples. The dijet sample is the most important one, bringing high statistics and high reach in energy for the forward region. The specific procedure applied to dijets will be discussed in the following Sections. The γ+jet sample allows consistent derivation of the absolute response in EC, but suffers from lower statistics and low purity in EC. It is possible to use the γ+jet sample at lower p_T than the dijet sample[4] so that the combined sample has greater span in energy than either alone.

By combining and contrasting the two samples it is possible to reach reduced statistical and systematic uncertainties. Contrasting the two samples has uncovered important response differences arising from the initial parton

[4]This is due to inefficient triggering for dijets, and the situation may be improved in Run IIb.

composition of the jets, which was already briefly discussed in Section 6.3.6. For this reason the JES used in this thesis is specifically designed for dijet (inclusive jet) events, whereas the recommended JES for the rest of the DØ collaboration is designed for γ+jet events.

6.4.1 MPF method for dijets

The MPF method for dijets works in principle identically to that in γ+jet events, when one of the jets is fully calibrated

$$R_{\mathrm{MPF}} = 1 + \frac{\vec{\not{E}}_T \cdot \vec{p}^{\,\mathrm{tag}}_{T,\mathrm{corr}}}{|\vec{p}^{\,\mathrm{tag}}_{T,\mathrm{corr}}|}. \tag{6.26}$$

This calibration can be done for jets in CC using the response derived from γ+jet events in the previous Section 6.3.4. In practice the calibration of the central jets is omitted except for p_T binning purposes, because the dijet sample is only used to calibrate forward jets relative to central jets so that

$$\frac{R(p_T \cosh\eta, \eta_{\mathrm{det}})}{R_{\mathrm{cc}}(p_T)} = \hat{p}_3 \left(1 + \frac{\vec{\not{E}}_T \cdot \vec{p}^{\,\mathrm{tag}}_{T,\mathrm{meas}}}{|\vec{p}^{\,\mathrm{tag}}_{T,\mathrm{meas}}|}\right). \tag{6.27}$$

The factor $\hat{p}_3$ contains additional corrections for resolution bias and a method calibration factor p_3, which are discussed later. The calibration sample is selected to consist of back-to-back jets with $\Delta\phi > 3.0$, of which at least one is in CC. No additional jets are allowed in the event. The jet in CC is later referred to as "tag", the other jet "probe". If both jets are in CC, both assignments of tag and probe are considered. It is also possible to assign tag and probe randomly, but in this case the results would not necessarily be reproducible exactly.

The binning variable E' for the dijet sample is defined as

$$E' = C_{\mathrm{bias}} p^{\mathrm{tag}}_{T,\mathrm{corr}} \cosh\eta_{\mathrm{probe}}, \tag{6.28}$$

where $p^{\mathrm{tag}}_{T,\mathrm{corr}}$ replaces the p^{γ}_T used with the γ+jet sample and C_{bias} corrects for the bias due to the poor energy resolution of central jets compared to photons.

6.4.2 Resolution bias for dijets

The MPF method for dijets is complicated by the poor p_T resolution of the jets. The steeply falling p_T spectrum creates a situation where more jets

migrate into a given p_T bin from low p_T than from high p_T, as shown in Fig. 6.14. This causes the average particle level p_T in each bin to be biased with respect to average corrected tag jet p_T. No selection is performed on the probe jet so that its average corrected p_T equals the particle level p_T. This creates an artificial p_T imbalance that biases the MPF response.

The resolution bias can be expressed as an integral over all particle p_T contributing to a given bin of measured p_T, by folding the p_T spectrum $f(p_T)$ with resolution $g(p_T - p_T^{\text{ptcl}}, \sigma)$

$$\left\langle p_T^{\text{ptcl}} \right\rangle = \frac{\int_0^\infty f(p_T^{\text{ptcl}}) g(p_T - p_T^{\text{ptcl}}, \sigma) p_T^{\text{ptcl}} dp_T^{\text{ptcl}}}{\int_0^\infty f(p_T^{\text{ptcl}}) g(p_T - p_T^{\text{ptcl}}, \sigma) dp_T^{\text{ptcl}}}. \tag{6.29}$$

For MPF response the correction can be expressed as

$$\delta p_T^{\text{meas}} = \langle p_T^{\text{meas}} \rangle - \left\langle p_T^{\text{ptcl}} \right\rangle, \tag{6.30}$$

$$R_{\text{MPF}}^{\text{corr}} = \langle R_{\text{MPF}} \rangle (p_T^{\text{meas}}) \left(1 + \frac{\delta p_T^{\text{meas}}}{p_T^{\text{meas}}} \right)^{-1}. \tag{6.31}$$

In a simplified situation with exponentially falling p_T spectrum, $f(p_T) = \exp(-\alpha p_T)$, and Gaussian smearing with constant resolution, $g(p_T - p_T^{\text{ptcl}}, \sigma) = \text{Gauss}(p_T - p_T^{\text{ptcl}}, \sigma = \text{const})$, Eq. 6.29 can be integrated analytically to yield

$$\begin{aligned} \left\langle p_T^{\text{ptcl}} \right\rangle &= \frac{\int_{-\infty}^\infty \exp(-\alpha p_T^{\text{ptcl}}) \exp(-\frac{(p_T - p_T^{\text{ptcl}})^2}{2\sigma^2}) p_T^{\text{ptcl}} dp_T^{\text{ptcl}}}{\int_{-\infty}^\infty \exp(-\alpha p_T^{\text{ptcl}}) \exp(-\frac{(p_T - p_T^{\text{ptcl}})^2}{2\sigma^2}) dp_T^{\text{ptcl}}} \\ &= p_T - \alpha\sigma^2. \end{aligned} \tag{6.32}$$

Typical values in CC are $\alpha = 0.05$ GeV^{-1}, $\sigma/p_T = 0.2$–0.05, leading to a bias of 5–10%. This large bias is clearly observed when looking at the p_T imbalance between two jets in CC, both corrected or uncorrected, which by construction (tag jet chosen randomly) is 0 in the absence of bias.

The resolution bias can be accurately corrected using Eq. 6.30, when both the p_T spectrum and the p_T resolution are known sufficiently precisely. The fact that the CC jets are balanced in the absence of the resolution bias is used to calibrate the resolution bias correction, reaching less than one percent uncertainty for the resolution bias correction at all rapidities. The accurate resolution bias correction needs three main inputs

1. Jet p_T resolution for jets at $|\eta_{\text{det}}| < 0.4$, $g(p_T - p_T^{\text{ptcl}}, \sigma)$
2. Tag jet particle level p_T spectrum as a function of $\eta_{\text{det}}^{\text{probe}}$ for the specific topology $|\eta_{\text{det}}^{\text{tag}}| < 0.4$ and $N_{\text{jet}} = 2$, $f(p_T^{\text{ptcl}}, \eta_{\text{det}})$

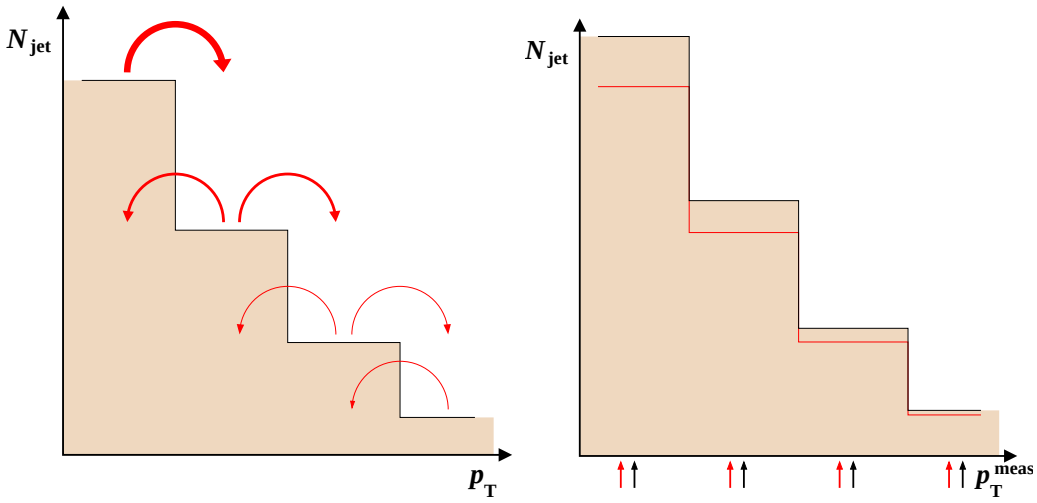

(a) (b)

Figure 6.14: Source of resolution bias in dijet MPF method. (a) The poor jet p_T resolution causes jets to migrate in and out of p_T bins. (b) Combined with a steeply falling p_T spectrum the net effect is increase in the observed number of jets, with $\langle p_T^{\text{meas}} \rangle$ (black arrow) being larger than $\left\langle p_T^{\text{ptcl}} \right\rangle$ (light arrow) in each bin of p_T^{meas}.

3. Residual bias calibration to ensure $F_\eta = 1$ in $|\eta_{\text{det}}^{\text{tag,probe}}| < 0.4$, p_3

These three components are discussed separately in the following sections. The total correction is shown in Fig. 6.15.

Jet p_T resolution

The jet p_T resolution is derived in detail after full JES corrections in Ch 7. For the purpose of resolution bias correction of F_η it is sufficient to correct the jets only for the offset and central response discussed in the previous sections. The p_T resolution is derived as

$$\sigma_{\text{raw}} = \sqrt{2} \cdot \text{RMS}\left(\frac{p_{T,2} - p_{T,1}}{p_{T,2} + p_{T,1}}\right), \quad |\eta_{1,2}| < 0.4, \tag{6.33}$$

$$\sigma_{\text{part}} = k_{\text{soft}}\sigma_{\text{raw}}, \tag{6.34}$$

$$\sigma_{\text{corr}} = \sqrt{(k_{\text{soft}}\sigma_{\text{raw}})^2 - \sigma_{\text{MC}}^2}, \tag{6.35}$$

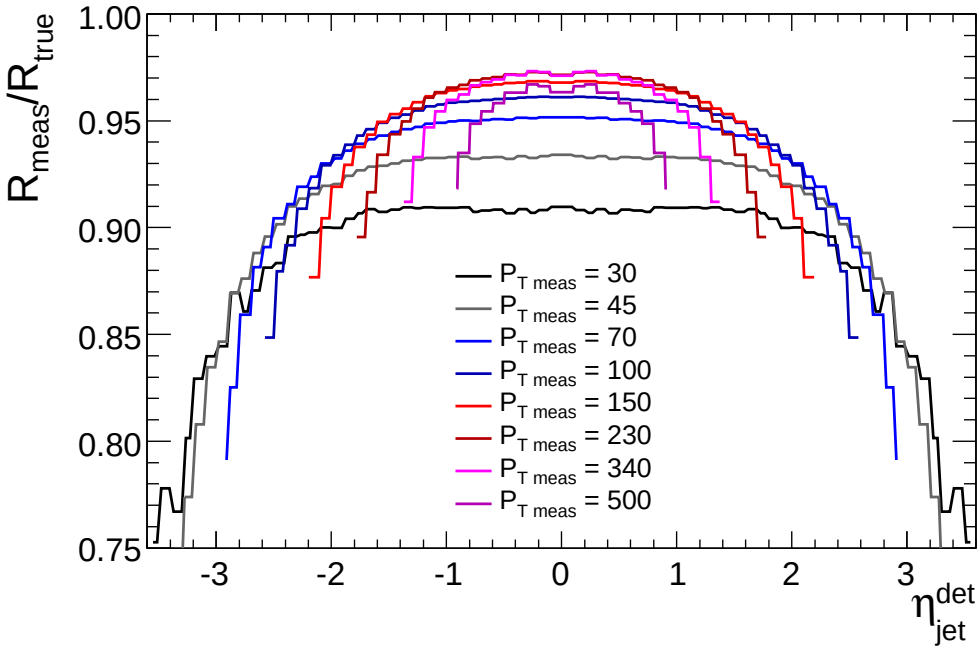

Figure 6.15: Resolution bias in measured F_η^{dijet}.

where k_{soft} is a correction for soft radiation (additional non-reconstructed jets) and σ_{MC} is a correction for particle level imbalance (fragmentation, showering). These corrections are discussed in detail in Ch. 7.

The effective resolution needed for the bias correction is the partially corrected resolution σ_{corr}, which is verified using MC. This includes contributions from both detector resolution and the particle level imbalance. The MPF method balances the full hadronic recoil including non-reconstructed jets against the central jet so the soft radiation effects are absorbed in the missing-E_T and do not increase the bias. The resolution uncertainty is in the leading order absorbed to the calibration factor p_3 and does not affect the determination of F_η. The residual uncertainty is estimated by varying the resolution between the extremes of σ_{raw} and σ_{corr}, as shown in Fig. 6.16.

For practical purposes the MPF method is applied to pairs of uncorrected jets. The energy dependent central response correction improves the resolution by about 10% so the resolution for uncorrected jets is calculated using

$$\frac{\sigma}{p_T} \to \frac{\sigma}{p_T}\left(1 + \frac{R'_{\text{cc}}(p_T)p_T}{R_{\text{cc}}(p_T)}\right). \tag{6.36}$$

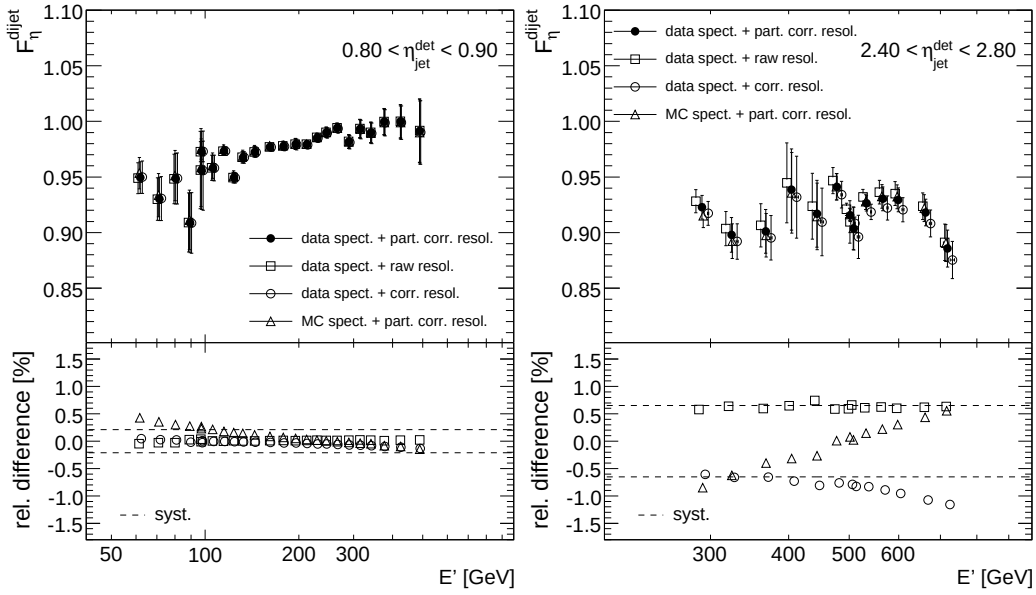

Figure 6.16: Comparison of the relative response in dijet data for different alternatives of the resolution bias correction. The lower plot shows the difference to the nominal choice of data spectrum with partially corrected resolution.

Dijet p_T spectrum

The tag jet p_T spectrum is determined directly from data in 0.1 bins of $\eta_{\rm det}^{\rm probe}$ with the cuts $|\eta_{\rm det}^{\rm tag}| < 0.4$ and $N_{\rm jet} = 2$. The raw measured p_T spectra are unfolded to the particle level using the fully corrected p_T resolution $\sigma_{\rm corr}$ and the ansatz method discussed in Ch. 8. The ansatz function is modified from Eq. 8.20 to include both jets in the kinematic limit term of power β

$$f(p_T,\eta) = N_0(\eta)\left(\frac{p_T}{p_{T,0}}\right)^{-\alpha(\eta)}\left[\left(1-\frac{2p_T}{\sqrt{s}}\right)\left(1-\frac{2p_T\cosh\eta}{\sqrt{s}}\right)\right]^{\beta(\eta)/2} \cdot \exp(-\gamma(\eta)p_T), \quad (6.37)$$

where N_0, α, β and γ are the ansatz parameters and $p_{T,0} = 100$ GeV/c. These ansatz functions are then used in Eq. 6.29 to calculate the resolution bias correction. The unfolded p_T spectra are also determined from MC for comparison, with the difference between data and MC spectra included in the systematics as shown in Fig. 6.16.

Residual bias calibration

Small imperfections in the resolution bias correction due to resolution uncertainty can be calibrated out by using the fact that in an unbiased sample the measured relative MPF response is exactly 1 in CC ($|\eta_{\rm det}| < 0.4$). This is also necessary to ensure that the η-dependent corrections will not change the measured CC jet response. The calibration factor p_3 is determined from Eq. 6.27 by requiring the right hand side to be exactly 1.

Because uncertainty in CC resolution changes the bias correction by roughly the same amount at all rapidities for the same p_T, the overall uncertainty is significantly reduced. As shown in Fig. 6.16, the uncertainty due to resolution is only about 0.6% at $2.4 < \eta_{\rm det} < 2.8$. The corresponding variation in the calibration factor p_3 is 0.5–2%. At lower rapidities the uncertainty is reduced, approaching 0 at $\eta_{\rm det}$=0 as shown in Fig. 6.20.

6.4.3 Relative response sample dependence

The F_η measured from the dijet and γ+jet samples in data have overall quite different scales as shown by Fig. 6.19 and the scale factor in Fig. 6.18(d), particularly in the forward region. These differences are qualitatively well explained by the response differences for quark and gluon initiated jets and the very different fraction of quark and gluon initiated jets in the γ+jet and dijet samples, shown in Fig. 6.10 and Fig. 6.9, respectively. The quantitative agreement is also significantly improved when the single pion response in MC is tuned to that in data, which increases the differences between quark and gluon initiated jets.

The qualitative behavior of this difference has been studied by measuring the γ+quark and γ+gluon responses (R_q and R_g in CC, respectively) and the fraction of gluon jets in MC. For γ+jet sample a single parametrization of gluon jet fraction ($f_g(E,\eta)$) is enough, for dijets the gluon jet fraction is parametrized separately for tag jets in CC ($f_g^{\rm tag}(E)$) and probe jets when the tag is a gluon jet ($f_g^g(E,\eta)$) or a quark jet ($f_g^g(E,\eta)$). The parametrizations are shown in Appendix B. Using these parametrizations the F_η for the two samples can be calculated as

$$F_\eta^{\gamma+{\rm jet}} = \frac{f_g(E,\eta)R_g(E) + (1-f_g(E,\eta))R_q(E)}{f_g(E,0)R_g(E) + (1-f_g(E,0))R_q(E)}, \quad (6.38)$$

$$F_\eta^{\rm dijet} = f_g^{\rm tag}\left(\frac{E}{\cosh\eta}\right)\frac{f_g^g(E,\eta)R_g(E) + (1-f_g^g(E,\eta))R_q(E)}{R_g(E/\cosh\eta)} \quad (6.39)$$

$$+ \quad \left(1 - f_g^{\text{tag}}\left(\frac{E}{\cosh\eta}\right)\right) \frac{f_g^q(E,\eta)R_g(E) + (1 - f_g^q(E,\eta))R_q(E)}{R_q(E/\cosh\eta)}.$$

The result versus rapidity is shown in Fig. 6.17. The ratio of F_η for the two samples follows closely the same quadratic $\cosh\eta$ form as the ideal response rapidity dependence in Eq. 6.21. The energy dependence of the ratio is very weak for the range $50 < p_T < 200$ GeV/c where the γ+jet and dijet samples overlap so the sample dependence for F_η (scale factor SF_η) is parametrized simply as

$$SF_\eta(\eta_{\text{det}}) \equiv F_\eta^{\text{dijet}}(E,\eta_{\text{det}})/F_\eta^{\gamma+\text{jet}}(E,\eta_{\text{det}}) = 1 + p_1\cosh\eta + p_2\cosh^2\eta. \quad (6.40)$$

This form is used for the global fit in data and the result is shown in Fig. 6.18. The scale factor is 1 at $\eta_{\text{det}} = 0$ because $F_\eta^{\text{dijet}} = F_\eta^{\gamma+\text{jet}} = 1$ by definition in CC.

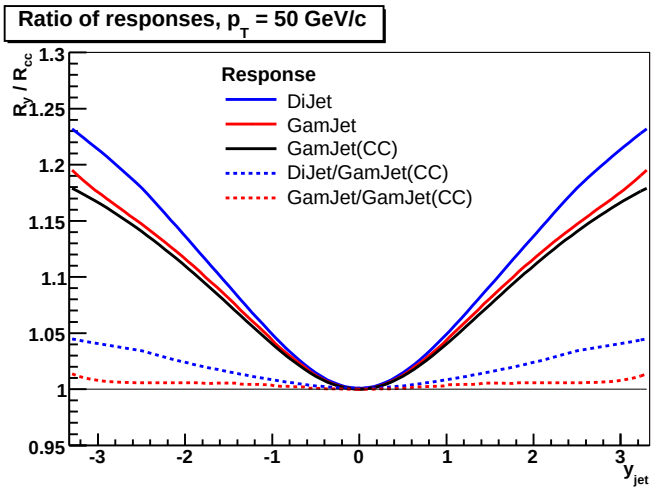

Figure 6.17: Qualitative relative response versus y_{jet} at p_T=50 GeV/c. The solid black line shows the relative response due to response energy dependence alone, using the γ+jet CC response. The solid blue and red lines also account for the energy and rapidity dependence of the gluon fraction. The dashed lines give the ratio to the nominal CC response. The ratio of the dashed lines is almost constant at $50 < p_T < 200$ GeV/c and is used as a "scale factor" between the η-dependent corrections measured in the γ+jet and dijet samples.

6.4.4 Global fit of η-dependent corrections

The leading principle for the fit of η-dependent corrections has been to minimize the freedom for energy and rapidity dependence in order to fit the F_η with small statistical uncertainties and fine granularity in η_{det}. This also makes the extrapolation in energy more stable and reliable. The measurement is made in 0.1 bins of η_{det} (wider in EC), but the parametrizations are smoothed over much wider rapidity regions.

The response energy dependence is fitted using the same quadratic logarithmic formula as in CC so that F_η is a ratio of two quadratic logarithmic responses

$$F_\eta(E', \eta_{\mathrm{det}}) = \frac{p_0(\eta_{\mathrm{det}}) + p_1(\eta_{\mathrm{det}})E' + p_2(\eta_{\mathrm{det}})E'^2}{R_{\mathrm{cc}}(E/\cosh\eta)}. \tag{6.41}$$

The parameters p_i are fitted as a function of η_{det}, with most freedom allowed for the overall scale p_0.

The calorimeter structure naturally divides the response parametrizations into central calorimeter (CC), intercryostat region (ICR) and end caps (EC). The transition region between CC and EC behavior is roughly $1.1 < |\eta_{\mathrm{det}}| < 1.4$. Within EC and CC regions the response is expected to depend on the angle of incidence. The length of material X traversed by the jet shower relative to normal incidence X_0 is $X/X_0 = \cosh\eta$ in CC and $X/X_0 = 1/|\tanh\eta|$ in EC. Powers of these functions are used in fitting the rapidity dependence for the parameters p_i. The resulting fits are shown in Figs. 6.18(a)–(c).

Both p_2 and p_1 have only four parameters each, two for CC and two for EC. Two of the parameters give the asymptote at $\eta_{\mathrm{det}} = 0$ and $|\eta_{\mathrm{det}}| \to \infty$, two describe the slope of $((X/X_0)^m - 1)$. The functional shapes (powers m of X/X_0) are chosen to provide a good fit to data. The ICR region interpolation range is fixed to reproduce the observed behavior in data. The p_0 also has the same four parameters as p_2 and p_3, but in addition narrow rapidity regions are allowed to have additional scale factors to provide a good fit to data. The precision of the calorimeter cell level η-intercalibration that is performed before JES is 1–2% [111] in CC and EC so the additional scale factors, whose size is generally 1% or less, are presumed to account for these residuals. In ICR and $|\eta_{\mathrm{det}}| > 2.4$ the scale factors can be larger because no η-ϕ-intercalibration was performed there.

The differences between γ+jet and dijet scale factors are accounted for by the scale factor SF_η that is constant versus energy. Its parametrization is given in Eq. 6.40 and the result of the fit to data is shown in Fig. 6.18(d). The global

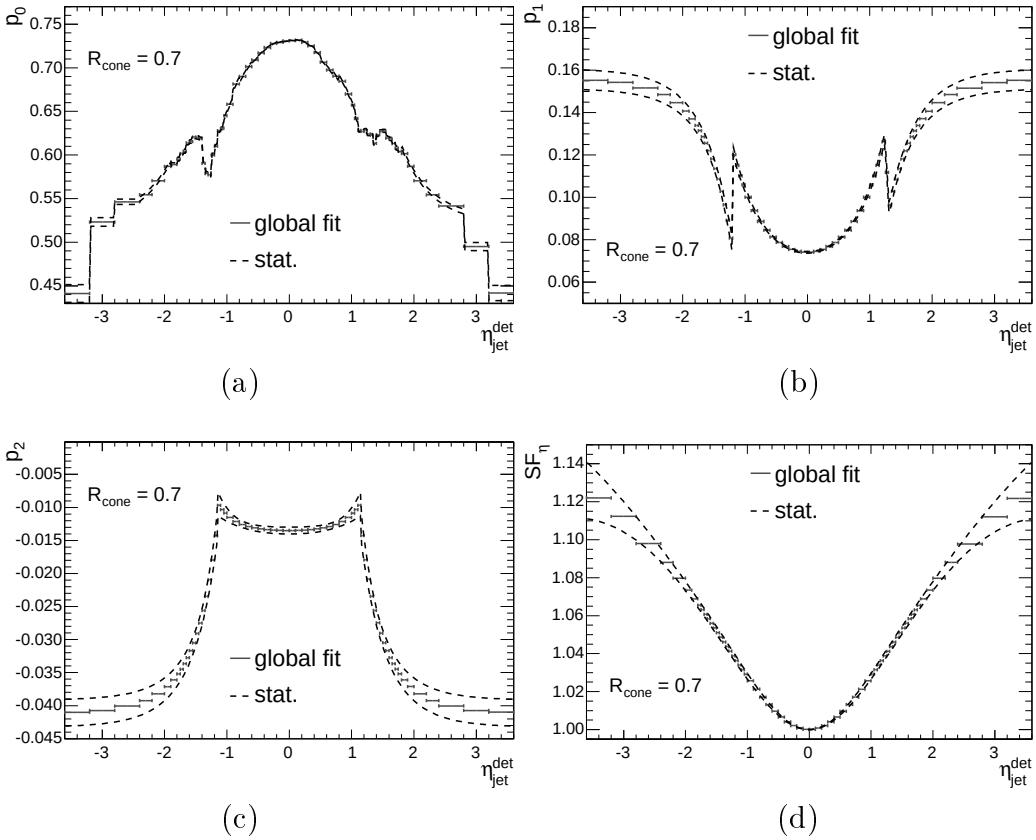

Figure 6.18: Parameters of η-dependent corrections versus $\eta_{\rm det}$.

fit procedure accounts for the fact that the jets in the EM-jet background of γ+jet sample have the same response as in dijet sample. The photon and EM-jet scales and γ+jet sample purities are taken from MC and the jet responses for pure dijet and γ+jet samples are fitted from data simultaneously in the global fit procedure. As shown in Figs. 6.19, the simultaneous fit to both samples in data is good with the total χ^2/NDF between 1–2 in each rapidity bin. The resulting statistical uncertainty of the fit is less than 1% over the full kinematic range even in the most forward regions. The reliability of the extrapolations in energy have been verified with MC.

6.4.5 Uncertainties

The application of resolution bias corrections and the global fit procedure combined with the high statistics of the dijet sample have been enough to push the uncertainties in η-dependent corrections to less than 1% at $|\eta_{\rm det}| <$

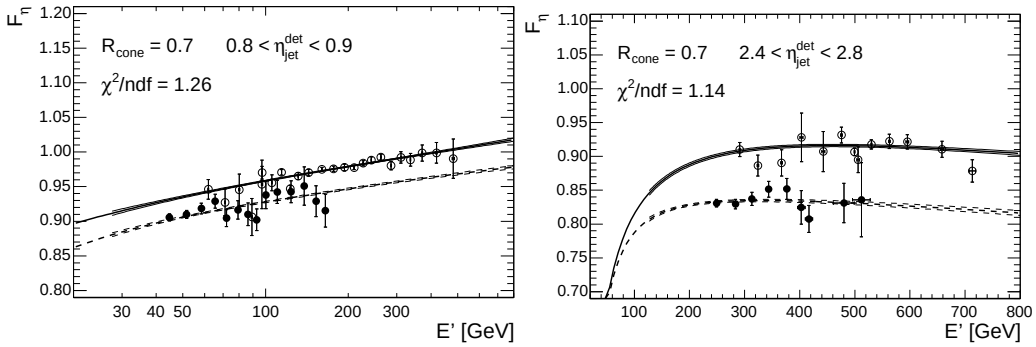

Figure 6.19: Simultaneous fit of the η-dependent correction F_η in γ+jet (full circles, dashed line) and dijet (open circles, solid line) data.

2.8 for the dijet sample, as shown in Fig. 6.20. The statistical uncertainty of the global fit (shown at $p_T = 50$ GeV/c in Fig. 6.20) is practically negligible in the phase space relevant for the inclusive jet cross section measurement, $p_T > 50$ GeV/c and $E < 800$ GeV/c at $|y| < 2.4$. The leading systematic is the average fit residual in 0.4 wide bins of $|\eta_{\rm det}|$, which is estimated to be 0.5% at $0.4 < |y| < 2.4$ and constant versus energy. This residual accounts for the scatter of the data points around the central fit and covers possible variation in the shape of the fit function. The resolution bias correction contributes $\geq 0.5\%$ at $|\eta_{\rm det}| > 2.0$, but is smaller toward $\eta_{\rm det} = 0$. This uncertainty covers the jet p_T resolution and dijet cross section uncertainties in the bias correction, as shown in Fig. 6.16.

6.4.6 Response stability in time

The response stability in time has been tested by breaking the full data set into the trigger lists listed in Table 5.2. The response in CC is observed to be stable to within 1% as shown in Fig. 6.21(a). This is expected as the liquid Argon-Uranium calorimeter is generally very stable. The behavior is similar in EC. In contrast, the response in the intercryostat region is observed to vary by up to 10% as shown in Fig. 6.21(b). This behavior is attributed to the unstable gains of the aging photomultiplier tubes (PMTs) used to measure the signal from the scintillator tiles of the intercryostat detector. The time and luminosity dependence of the relative gains is particularly strong for some PMTs in the region $1.2 < |\eta_{\rm det}| < 1.4$ that have been replaced for Run IIb.

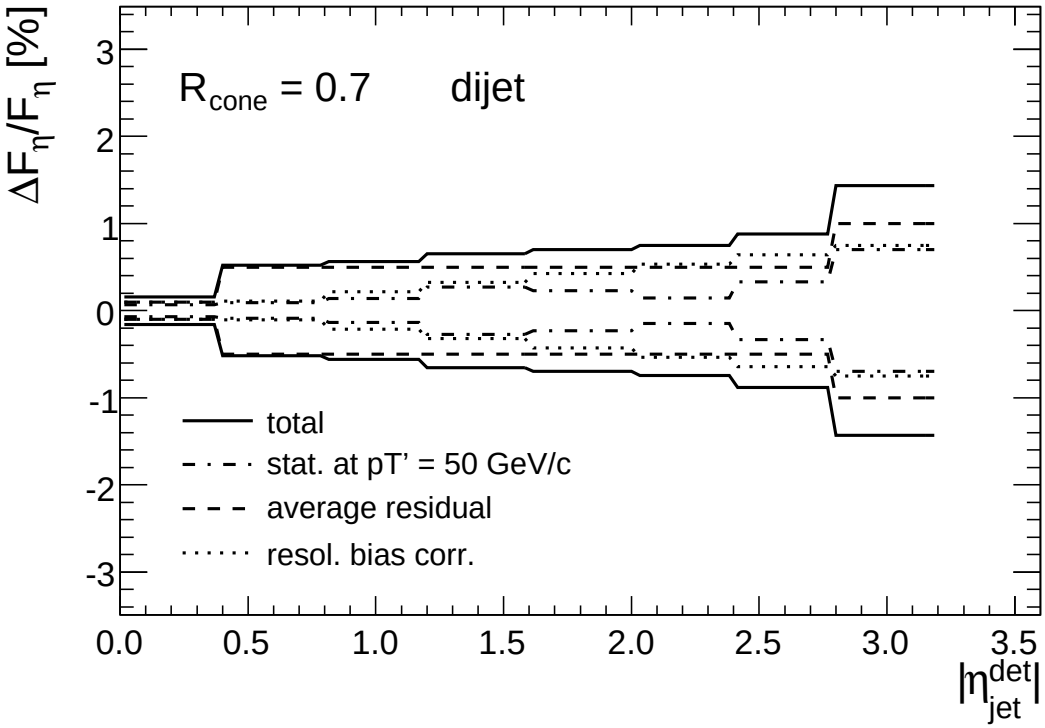

Figure 6.20: Summary of the η-dependent correction uncertainties.

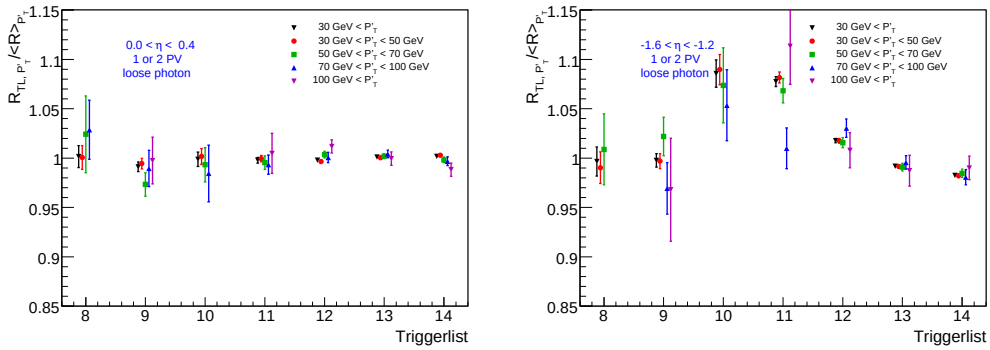

(a) (b)

Figure 6.21: (a) Response time dependence in CC for different p_Ts. (b) Response time dependence in ICR for different p_Ts.

The response time dependence does not directly become an uncertainty for JES when the JES is derived using exactly the same sample as used in the analysis. However, triggers weight time periods and luminosities differently, which leads to potentially large residuals when the time dependence is strong. To avoid problems with JES trigger dependence, only the run range 191000–213084 (see Table 5.3) has been used in this analysis. This covers trigger lists v12.18—v14 (see Table 5.2) where the ICR response is relatively stable as shown in Fig. 6.21. This run range also avoids later problems with degraded resolution (Ch. 7) and inefficient triggers (Ch. 8). The ICR response is roughly 0.5–1.0% lower for the shorter run range than for the full sample. This analysis uses η-dependent corrections that have been rederived specifically for the run range 191000–213084 to avoid residual uncertainty from the JES time dependence.

6.5 Showering corrections

Jets are extended objects and deposit their energy over a wide area in the calorimeter. When the cone algorithm is used, some of this energy is often deposited outside the jet cone, leading to loss of energy compared to the original parton[5]. This process is called physics showering and accounts for part of the difference between parton and particle level jet energies (the rest is explained by underlying event). In addition, there is energy flow in and out of the calorimeter jet cone due to interactions with the magnetic field, dead material and finite calorimeter cell size. This is called detector showering and it is corrected in JES to bring jets back to particle level.

In most cases the detector showering decreases the measured jet energy because the energy density around the jet cone axis falls steeply toward the edges of the cone. Additional smearing in the energy deposition causes net energy flow along the slope, out of the cone. At low energy it is possible that the calorimeter jet cone is pulled toward energy deposits just outside the edge of the cone that fluctuated high, leading effectively to a positive net energy flow. Such a cone migration effect is visible as a slight dip or step in the energy density profile just at the edge of the cone radius.

The energy profiles are created by summing the energy in the cells at a given radius from the cone axis. The profiles are calculated for back-to-back γ+jet events, and show the jet core at $\Delta R = 0$ and the photon contribution

[5]In contrast, the k_T algorithm associates particles by distance in momentum space and does not exhibit physics showering.

at $\Delta R \geq \pi$. The energy density in the range $R_{\text{cone}} < \Delta R < \pi$ is primarily offset energy. Figure 6.22 shows an example of the showering profiles in MC without ZB overlay (*i.e.* with only the underlying event offset). These profiles are used to determine the true detector showering. An additional fixed energy profile for NP+MI offset is added for data and MC with ZB overlay, as shown in Figs. 6.23.

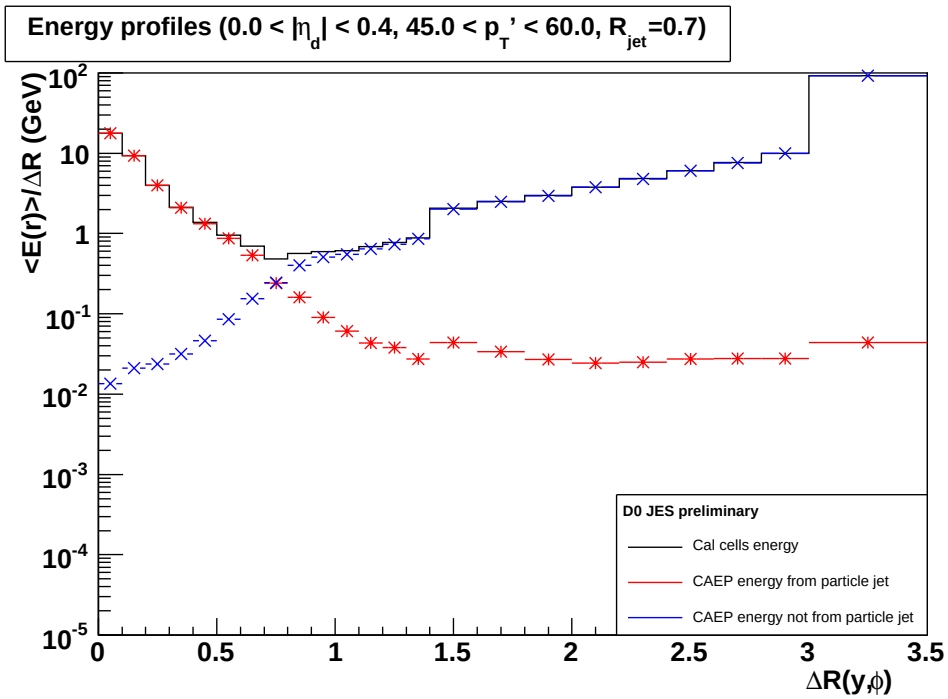

Figure 6.22: Jet energy profile for γ+jet MC without ZB overlay at $|y| < 0.4$ and $45 < p_T < 60$ GeV/c.

6.5.1 Data-based measurement

The cell-level information from Monte Carlo is used to generate energy density profiles for particles originating from inside the particle jet, outside particles and offset. The sum of these profiles (templates) is fitted to the measured energy profile in data, yielding weights for the inside and outside profiles that are needed to account for possible response differences between data and MC. The well-known offset profile is kept fixed. Figure 6.23 shows an example of the template fits in data.

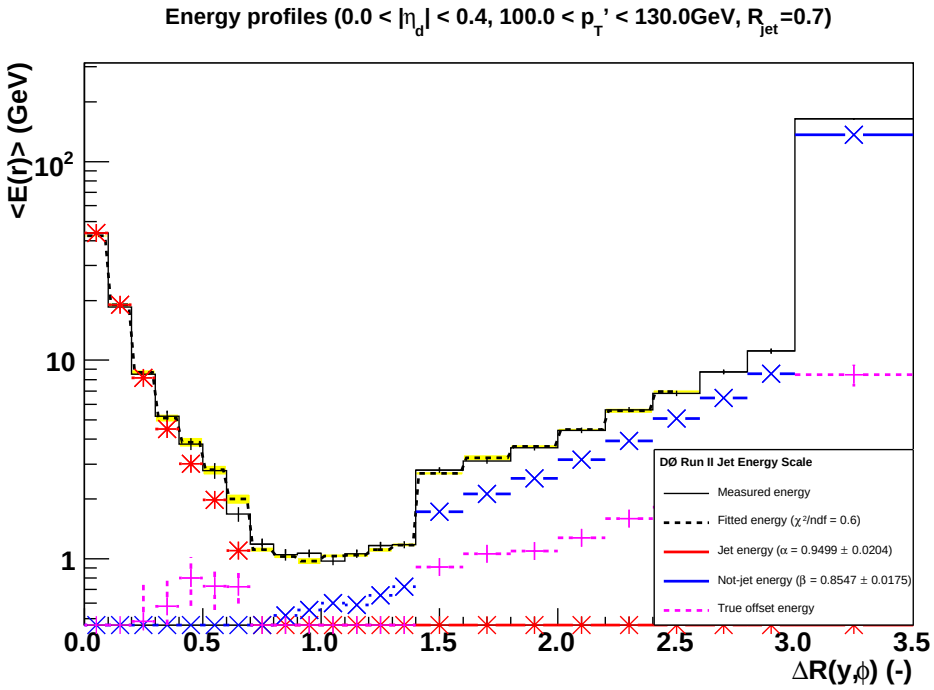

Figure 6.23: Jet energy profile fit to γ+jet data at $|\eta_{\rm det}| < 0.4$ and $100 < p_T < 130$ GeV/c.

The showering correction estimate $\hat{S}$ is obtained by comparing the total particle energy within calorimeter jet cone to that from the original particle jet using the fit-weighted templates

$$\hat{S} = \frac{\sum_{\Delta R=0}^{R_{\rm cone}} E_{\rm in} + \sum_{\Delta R=0}^{R_{\rm cone}} E_{\rm out}}{\sum_{\Delta R=0}^{\infty} E_{\rm in}}. \tag{6.42}$$

The bias in the method is derived by performing the same template fitting and calculation in Monte Carlo where the true showering answer $S_{\rm MC}^{\rm true}$ is available and can be compared to the measured estimator $\hat{S}_{\rm MC}$. This allows the showering estimator for data $\hat{S}_{\rm data}$ to be calibrated to give the true data showering

$$S_{\rm data} = \hat{S}_{\rm data} \cdot \frac{S_{\rm MC}^{\rm true}}{\hat{S}_{\rm MC}}. \tag{6.43}$$

The showering correction determined from γ+jet data using the data-based method is in very good agreement (difference $< 0.3\%$) with the MC truth showering correction from the γ+jet MC with tuned single pion response. The dijet showering correction is determined directly from MC truth with

the tuned dijet MC, which allows stable showering fits up to the highest energies. The dijet showering correction is determined separately for energy and p_T, with the p_T showering correction for dijet data shown in Fig. 6.24.

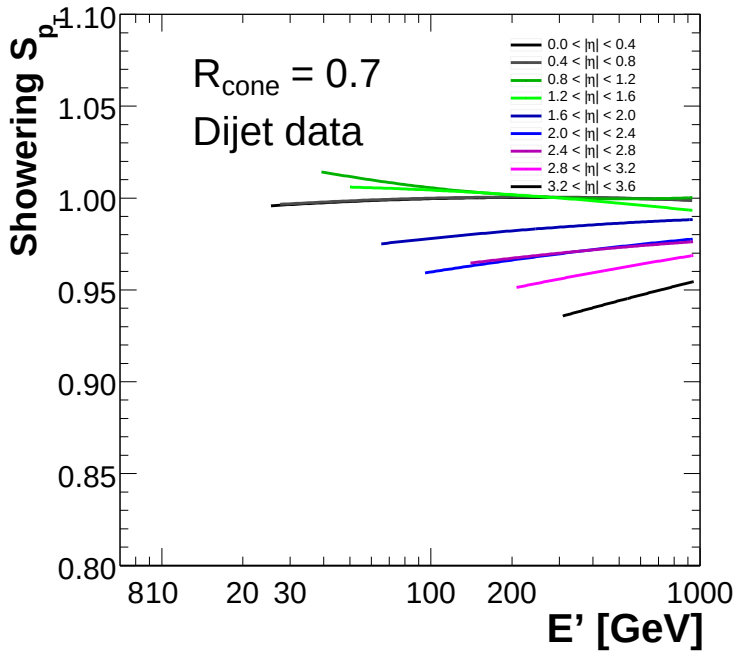

Figure 6.24: Dijet p_T showering in scaled MC.

6.5.2 Physics motivation for showering

The showering corrections in Fig. 6.24 are smallest at high p_T in CC and largest at low p_T in EC. The jets get more boosted at high energy, which reduces their transverse size and hence also detector showering at high p_T. The jets are also more boosted in the forward direction, but the definition of the jet cone in η-ϕ-space keeps them round and roughly constant in size for given p_T. In real space θ-ϕ (or x-y) coordinates the jet cone shrinks significantly in the θ-direction at higher rapidities. Because detector showering takes place in the θ-ϕ coordinates, it is strongly increased at higher rapidities.

The p_T showering correction is overall smaller than the energy showering correction by about 1–3%. This is because the p_T profiles are weighted by a factor $\cos(\Delta R)$ in the ϕ direction compared to the energy profiles, which reduces energy flow by a factor $\cos(0.7) = 0.76$ at the cone edge $R_{\text{cone}} = 0.7$.

The profiles are also weighted in the η direction by $1/\cosh(\eta)$, which increases S when the rapidity bias (discussed in Section 6.8) tilts jets toward CC. The difference is largest in ICR, leading to positive net p_T flow and $S > 1$ at low p_T.

The p_T dependence of the showering corrections is steeper for dijets than for γ+jets because of quark and gluon jet differences, as in the case of response. The gluon jets are overall wider than quark jets and undergo more detector showering. The differences can be up to 1–2% at the edges of the phase space ($p_T > 50$ GeV/c, $E < 600$ GeV).

6.6 Topology bias (MPF response bias)

The MPF method balances a photon or a central jet against a full hadronic recoil, but the measured MPF response is interpreted as a response of the probe jet. This interpretation is biased at a percent level precision because the hadronic recoil includes particles from outside the probe jet. These additional particles are generally softer than those in the core of the jet and are expected to lower the response of the recoil with respect to that of the core of the jet.

The bias of the MPF response is determined in tuned MC by comparing the MPF response to the true response defined at particle level. The result for p_T response is shown in Fig. 6.25. The bias is overall about 1%, with little p_T or rapidity dependence at $p_T > 50$ GeV/c.

The MPF response bias for p_T is fairly small, $\sim 1\%$, because the method based on p_T balance and the cone size $R_{\text{cone}} = 0.7$ is large enough to contain most of the hadronic recoil in the absence of additional soft non-reconstructed jets. It is interesting to note that the bias is significantly larger, 2–4%, for $R_{\text{cone}} = 0.5$ jets. This is expected from the response difference between the hard particles in the core of the jet and soft particles closer to the edges. The MPF response itself is very insensitive to the cone size.

The MPF response bias for energy has more rapidity dependence than for p_T. The rapidity bias (discussed in Section 6.8) tilts jets toward the center of the calorimeter and causes the jet p_T to be overestimated with respect to the jet energy. This effect is particularly strong in the ICR, where the rapidity bias of 0.04 at $\eta = 1.4$ causes an effective p_T change of 3–4% relative to energy[6]. Because the MPF method is based on p_T balance, the p_T response is well

[6]In the absence of mass, $p_T = E/\cosh(\eta)$ so the Δp_T bias can be estimated from $\Delta\eta$ bias by $\Delta p_T/p_T = \cosh(\eta)/\cosh(\eta + \Delta\eta) - 1$.

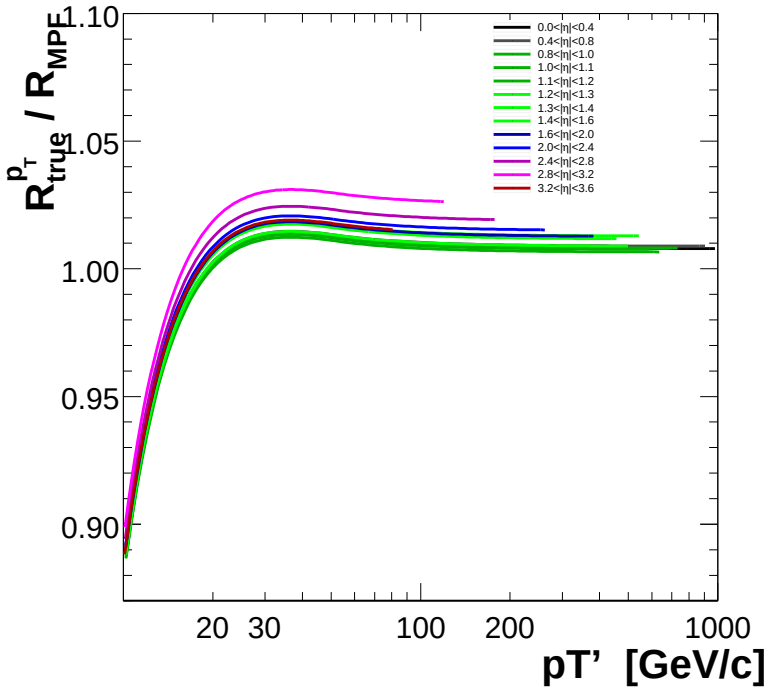

Figure 6.25: Topology bias in MPF method for p_T response determination.

estimated and the E/p_T difference is folded to the MPF response bias for energy.

The MPF response bias was separately determined for γ+jet and dijet samples using tuned MC, but the two were found to be in good agreement at permille level and within the MC statistics. Because the equivalence was not obvious *a priori*, the differences are assigned as additional systematics.

In conclusion, it is found that the MPF method is well-suited for calibrating the p_T of $R_{\text{cone}} = 0.7$ cone jets, with a small bias of about 1%. For energy calibration and for other jet algorithms the bias is potentially large.

6.7 Zero suppression bias

The cell energies measured in the DØ calorimeter are zero-suppressed in order to reduce the number of non-zero cell energy values that need to be stored on disk or tape. With data compression this leads to significant saves in needed storage capacity. The noise in each cell is typically Gaussian distributed around zero (after baseline calibration), with σ giving one standard deviation

fluctuation over the baseline noise. The algorithm used for zero-suppression keeps isolated calorimeter cells only if their energy is higher than 4σ. Cells adjacent to jets are kept if their energy exceeds a lowered threshold of 2.5σ.

The zero-suppression algorithm produces a small positive noise offset contribution because of the asymmetric zero suppression (negative energies are never kept) for cells with no real energy. For cells close to jets the positive offset is increased because of the lowered zero-suppression thresholds. For cells with high enough real energy deposits, as within the jet core, the zero-suppression produces no effect and positive and negative noise offset contributions are expected to cancel.

Offset energy due to multiple interactions increases in the jet core as this energy is less likely to get zero-suppressed. This offset energy is likely to depend on the shape and width of the jet, but such effects are averaged over in the full sample.

The overall effect is that the true offset is significantly increased inside the jet environment, by up to a factor of four compared to the average energy density measured from outside jets in ZB and MB events. The correction factor for true offset, k_O, is defined as

$$k_O = \frac{\langle E_{\text{meas}}(\text{no ZB overlay})\rangle}{\langle E_{\text{meas}}(\text{ZB overlay}) - E_{\text{offset,meas}}\rangle}, \tag{6.44}$$

where the same MC events are reconstructed with and without ZB bias overlay (offset). The ratio of averages is used instead of the average of ratio so that the correction properly factorizes when used with other bias correction, also defined as ratios of averages.

Figure 6.26 shows the offset zero-suppression bias in CC for MC with unsuppressed ZB overlay. This situation closely corresponds to data. The bias increases at low p_T where the offset contribution is largest. The bias also increases with the number of primary vertices (PVs) as this linearly increases the offset from multiple interactions. The overall offset bias correction is determined for the average number of primary vertices, which is close to 1.5 for the Run IIa data.

The bias in offset is almost perfectly canceled by an opposite bias in the MPF response, defined as

$$k_R = \frac{\langle R_{\text{MPF}}(\text{no ZB overlay})\rangle}{\langle R_{\text{MPF}}(\text{ZB overlay})\rangle}, \tag{6.45}$$

because the increased offset inside the jet decreases the missing-E_T in the direction of the jet. This artificially increases the estimated MPF response.

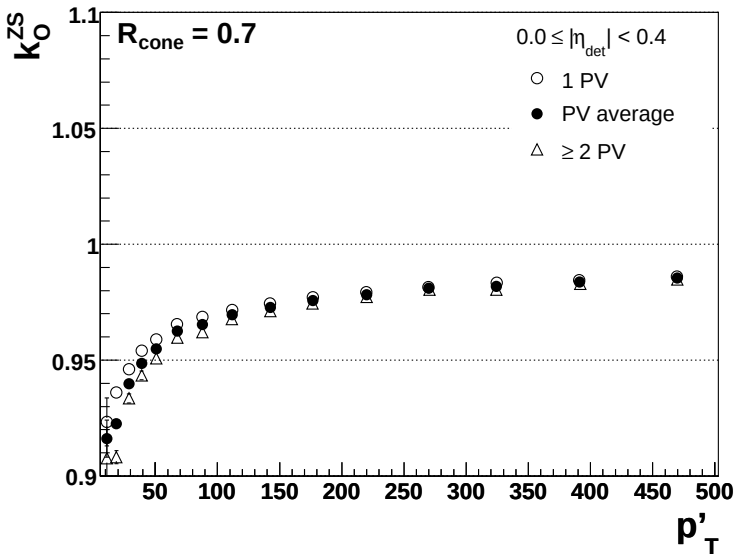

Figure 6.26: Offset zero-suppression bias (k_O) at $|\eta_{\rm det}| < 0.4$ in the unsuppressed ZB overlay case that corresponds to data.

The offset bias on the opposite narrow photon cluster is small and does not counteract the bias on the jet side.

Because the zero suppression biases in offset and response cancel so closely, only the ratio k_O/k_R is used for final corrections to simplify the fitting procedure and to reduce the uncertainties related to the separate corrections. Figure 6.27 shows the zero-suppression bias k_O/k_R in CC. The bias is $\leq 0.5\%$ at $p_T > 50$ GeV/c in all rapidity regions and vanishes at high p_T.

The small residual bias k_O/k_R is possibly attributed to the imperfect cancellation between the samples used to measure offset and response. The samples used in this analysis and in the offset measurement have no restrictions on the number of primary vertices, whereas the sample used for the response measurement requires $n_{\rm vtx} = 1$ or 2 in addition to vetoing all additional jets. This decreases the average number of multiple interactions and the amount of offset, and hence the zero-suppression bias. The residual bias is equivalent to a change in k_O by about 0.5 additional interactions.

6.8 Rapidity bias

The inclusive jet cross section is measured in bins of rapidity so a reliable measurement requires the rapidity to be also properly calibrated. The small

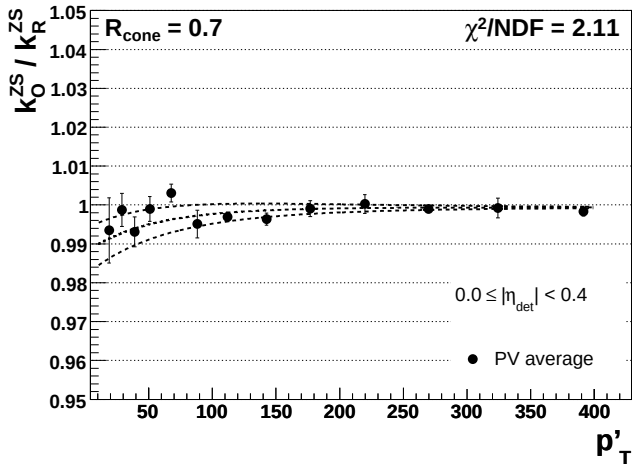

Figure 6.27: The zero suppression bias k_O/k_R in CC. The dashed lines show the uncertainty attributed to the bias correction.

rapidity bias is best estimated from MC truth. Figure 6.28 shows the rapidity bias in several bins of energy. The rapidity is generally biased toward the central calorimeter, with the largest deviations observed in ICR. Such biases were already observed in Run I [4].

The bias in Run II is about twice as large at highest as in Run I, and comes from two sources: (i) detector effects in ICR give rise to bumps similar in size and shape to those observed in Run I. The bias is observed to be slightly different for north and south sides, but only in ICR. (ii) The cone algorithm itself gives rise to a bias that increases steadily toward EC. This effect is similar to the difference observed between the DØ Run I cone algorithm that uses scalar E_T and the Snowmass algorithm that computes four-vector variables like the Run II cone algorithm. The underlying cause for either effect is not fully understood.

The rapidity bias is fitted with a smooth 2D-function versus $p_T^{\rm ptcl}$ and $y_{\rm reco}$ using the global fit method. The measurement is done in bins of $p_T^{\rm ptcl}$ and $y_{\rm ptcl}$ to avoid resolution bias effects. The rapidity then is mapped back to

$$\langle y_{\rm reco}\rangle = \langle y_{\rm ptcl}\rangle + \Delta y \tag{6.46}$$

before fitting to avoid an iterative procedure when applying the correction. The fit function

$$\begin{aligned} f(y) &= p_0 y + {\rm sign}(y) c_a \exp\left(-\frac{(|y|-\mu_a)^2}{2\sigma_a^2}\right) + c_s \exp\left(-\frac{(|y|-\mu_s)^2}{2\sigma_s^2}\right) \\ &\quad + {\rm sign}(y) p_1 (|y|-2)^2 \theta(|y|-2) \end{aligned} \tag{6.47}$$

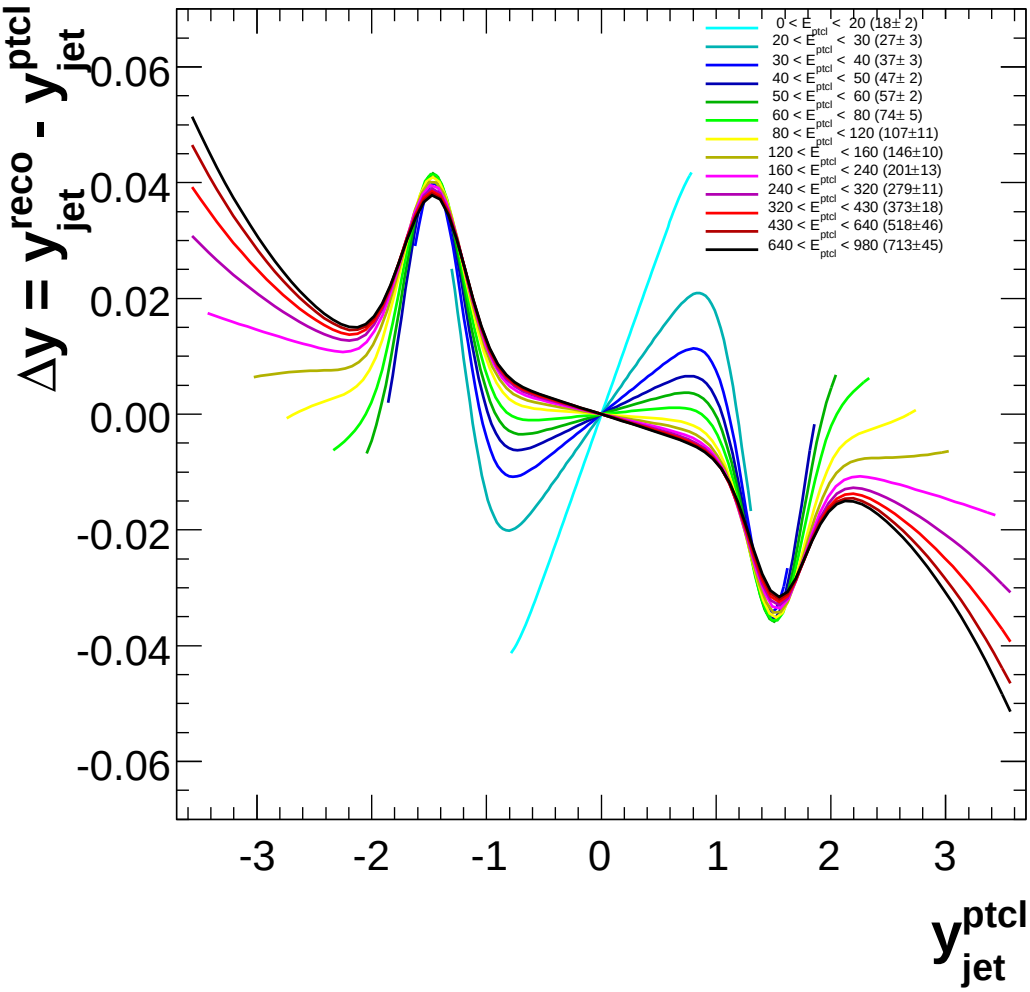

Figure 6.28: Rapidity bias estimated from MC truth.

is symmetric on north and south sides except for the Gaussian peaks in ICR that are about 0.01 higher on the north side. The θ is the Heaviside step function.

The terms linear (p_0) and quadratic (p_1) in y account for the tendency of the jets to be biased towards the center of the calorimeter, with the bias increasing with $|y|$ especially rapidly at $|y| > 2.0$. The dominant Gaussian (c_a) accounts for the increased tilt toward center of the calorimeter in the ICR and the second Gaussian (c_s) for the small north/south asymmetry in the magnitude of the bias.

6.9 E' mapping

All the corrections presented so far have been measured in terms of E' for simplicity. To properly apply the corrections in data, the results need to be mapped to uncorrected energies, or uncorrected energies need to be mapped to E'. To avoid deriving mapping for each sub-correction separately, the latter approach has been used. Before applying any other corrections except offset, the E' is solved from the equation

$$E_{\text{meas}} - E_{\text{offset}} = (R \cdot S \cdot k_{\text{bias}} S_P)(E') \cdot E', \tag{6.48}$$

where response R, detector showering S, zero-suppression and topological bias corrections k_{bias} and physics showering S_p are evaluated at E' and the offset E_{offset} is subtracted from the measured energy E_{meas}.

Equation 6.48 is solved using Newton's method to find x with $f(x) = 0$,

$$x_{n+1} = x_n - \frac{f(x_n)}{f'(x_n)}, \tag{6.49}$$

with the derivative $f'(x)$ evaluated numerically. This is a reasonably fast approach, and is used on an event-by-event basis. If CPU consumption were an issue, the equation could be solved and parametrized for an average set of parameters with little loss of precision.

Compared to standard JES corrections, one additional correction $S_P = E_{\text{ptcl}}/E'$, the physics showering, is needed to account for the fact that E' corresponds to the parton level energy, whereas JES corrections only correct energy up to particle level E_{ptcl}. This correction is negligibly small in the central calorimeter, but grows to about 5% in the forward region. Fortunately, the overall JES correction is only logarithmically dependent on E'. The uncertainty in the input E' translates to an uncertainty on the JES correction C as

$$\Delta C \approx \frac{dC}{dE'} \cdot \Delta E' \approx 0.1 \cdot \frac{\Delta E'}{E'}, \tag{6.50}$$

so that a relative error of 1% in E' only produces an error of 0.1% in C. The mapping using Eq. 6.48 is tested in γ+jet MC to be precise to $< 3\%$ at $p_T > 50$ GeV/c.

6.10 Four-vector corrections

The traditional jet energy scale is applied by scaling jet energy and p_T by a single correction factor for energy and keeping the direction of the jet

constant. Because jet rapidity and mass are both biased, this will leave also p_T miscalibrated. A proper four-vector correction requires a rotation of the jet and relative scaling of energy and p_T.

As shown in earlier sections, the independent calibration factors for energy, p_T and rapidity are already available. There is no need to assume any bias for ϕ so all four components of the four-vector are covered. The jet four-vector in the CAF[7] framework is defined by an uncorrected four-vector using E, P, η and ϕ and a correction factor C for JES. The following equations are used to calculate the "uncorrected" quantities corresponding to a single correction factor C using the corrections for energy (C), p_T (C_{pt}) and rapidity bias (Δy)

$$E_{\mathrm{corr}} = C \cdot E_{\mathrm{meas}}, \qquad p_T^{\mathrm{corr}} = C_{pt} \cdot p_T^{\mathrm{meas}}, \tag{6.51}$$

$$y_{\mathrm{corr}} = y_{\mathrm{meas}} - \Delta y, \qquad \phi_{\mathrm{corr}} = \phi_{\mathrm{meas}}, \tag{6.52}$$

$$\Rightarrow \tag{6.53}$$

$$p_Z^{\mathrm{corr}} = \frac{e^{2y_{\mathrm{corr}}} - 1}{e^{2y_{\mathrm{corr}}} + 1} E_{\mathrm{corr}}, \qquad \theta_{\mathrm{corr}} = \arctan(p_T^{\mathrm{corr}}, p_Z^{\mathrm{corr}}) \tag{6.54}$$

$$\eta_{\mathrm{corr}} = -\ln(\tan\left(\frac{\theta_{\mathrm{corr}}}{2}\right)), \qquad P_{\mathrm{corr}} = \sqrt{(p_T^{\mathrm{corr}})^2 + (p_Z^{\mathrm{corr}})^2} \tag{6.55}$$

$$\Rightarrow \tag{6.56}$$

$$E_{\mathrm{uncorr}} = E_{\mathrm{corr}}/C, \qquad P_{\mathrm{uncorr}} = P_{\mathrm{corr}}/C, \tag{6.57}$$

$$\eta_{\mathrm{uncorr}} = \eta_{\mathrm{corr}}, \qquad \phi_{\mathrm{uncorr}} = \phi_{\mathrm{corr}}. \tag{6.58}$$

The kinematic variables used in this analysis are p_T and y. As discussed in previous sections, both are individually calibrated. The uncertainties are also assessed separately for energy and p_T. Because the response calibration methods are better suited for p_T, this slightly reduces the calibration uncertainty for p_T compared to energy in some cases.

6.11 Jet energy scale and uncertainty summary

Figure 6.29 summarizes the JES corrections at central and forward rapidity, and Fig. 6.30 summarizes the corrections at low p_T and at high energy. The corrections range between 1.2–1.6 for the kinematic range of the cross section measurement ($|y| < 2.4$, $p_T > 50$ GeV/c, $E < 600$ GeV). The response corrections are by far the largest corrections for energy and p_T. The response corrections increase at low p_T and high rapidities, where showering correc-

[7] Common Analysis Format

tions also start to be significant. The offset corrections are important only at the lowest p_T range.

The JES uncertainties are summarized in Fig. 6.31 for central and forward rapidity, and in Fig. 6.32 for low p_T and high energy. The uncertainties vary between 1.2–2.5% for the kinematic range in the cross section measurement. Like the total JES correction, the JES uncertainty is also dominated by the response corrections. The main components from the central response calibration and η-dependent corrections were described in Sections 6.3 and 6.4, and summarized in Figs. 6.13 and 6.20, respectively.

6.12 Conclusions

The JES uncertainties have been reduced by about a factor two in CC and a factor ten in EC since the first preliminary JES calibration and cross section measurement was made in 2006 [24]. A major portion of the work for this thesis has been dedicated to reducing these uncertainties to their current level. The current JES uncertainties of 1.2–2.5% are currently the best available at hadron colliders. For comparison, the CDF experiment reports a JES uncertainty of 2–3% [133, 25].

6.13 Closure tests for jet energy scale

An integral part of the jet energy scale determination is an independent test of the corrections, called a closure test. In an implementation of a complex set of corrections bugs are possible, and the interplay between sub-corrections can cause subtle effects that are easily neglected. The closure test itself is also subject to a number of uncertainties (otherwise it would be used for JES determination!) so that closure will only be required to within the quoted uncertainties of the closure test and JES combined.

The closure tests are performed on a larger set of event topologies than the derivation when possible, and bins in rapidity and p_T are made reasonably wide to limit statistical uncertainties. This section presents the closure test results of most interest to the inclusive jets cross section analysis, *i.e.* the closure test of central calorimeter energy corrections in the γ+jet sample (absolute JES), the transfer of γ+jet energy scale to dijet p_T scale and the closure test of η-dependent corrections in the dijet sample. In some cases the

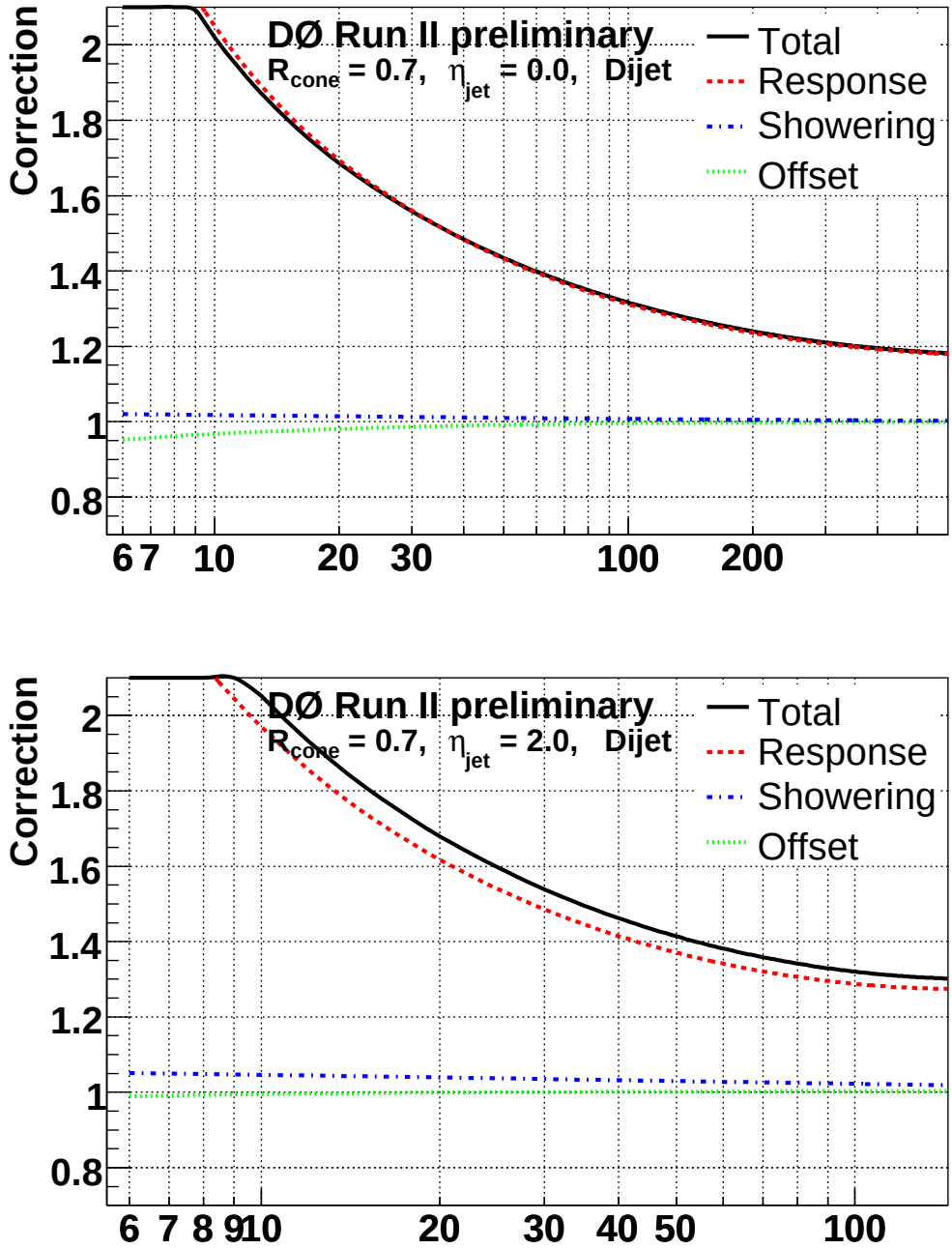

Figure 6.29: Jet energy scale corrections by component versus uncorrected p_T at $\eta_{\rm det} = 0$ and $\eta_{\rm det} = 2.0$.

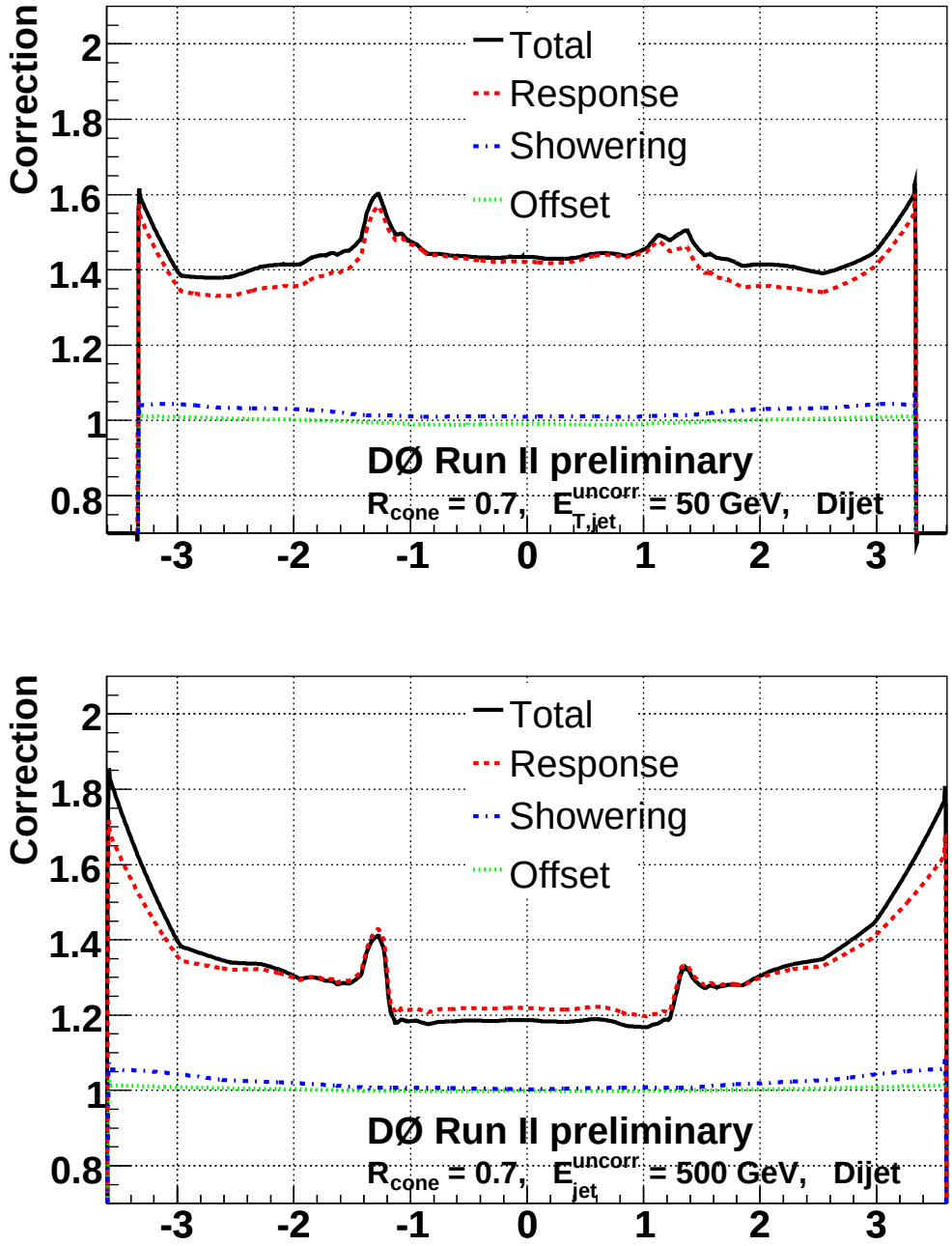

Figure 6.30: Jet energy scale corrections by component versus η_{det} at uncorrected $p_T = 50$ GeV$/c$ and uncorrected $E = 500$ GeV.

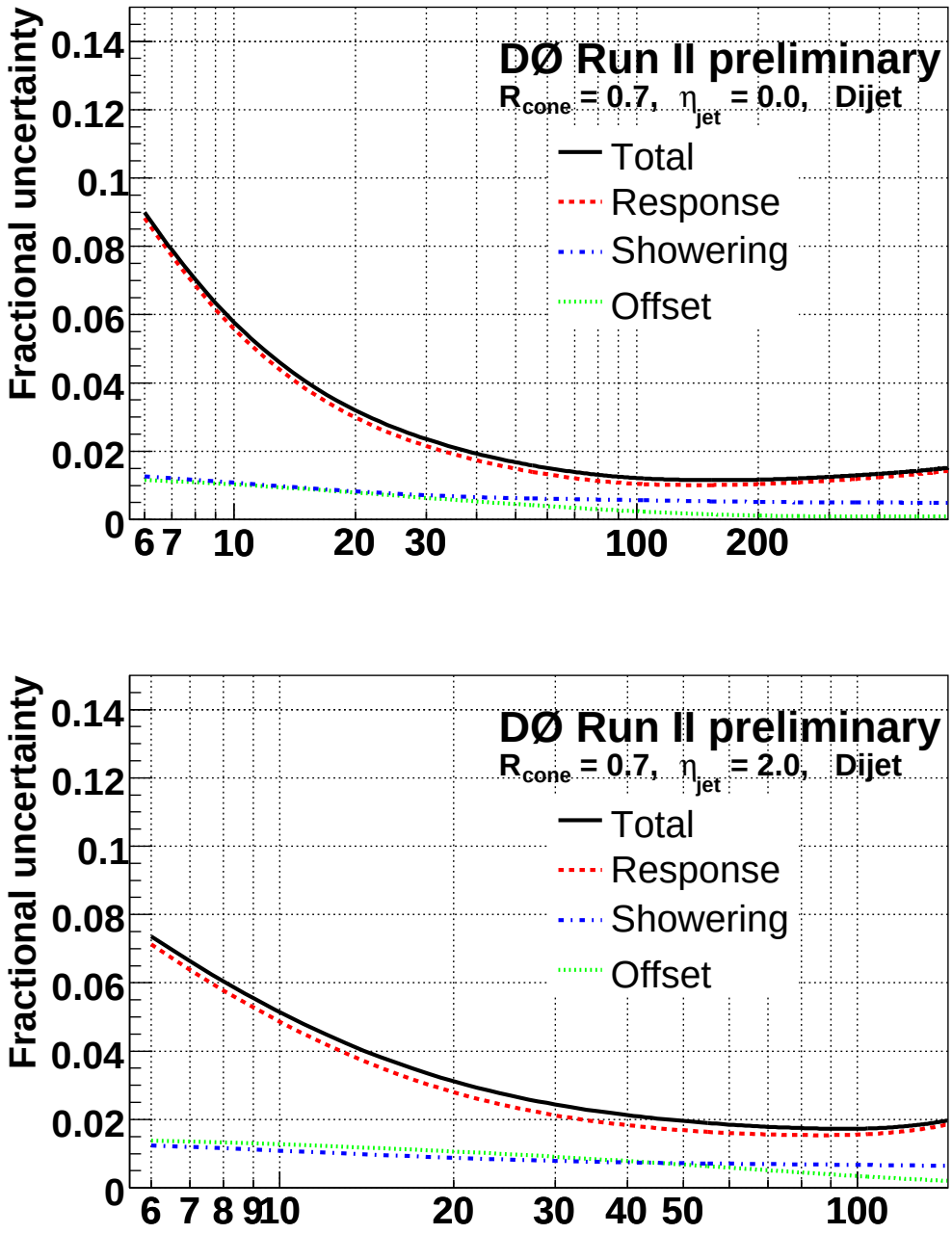

Figure 6.31: Jet energy scale uncertainties by component versus uncorrected p_T at $\eta_{\text{det}} = 0.0$ and $\eta_{\text{det}} = 2.0$.

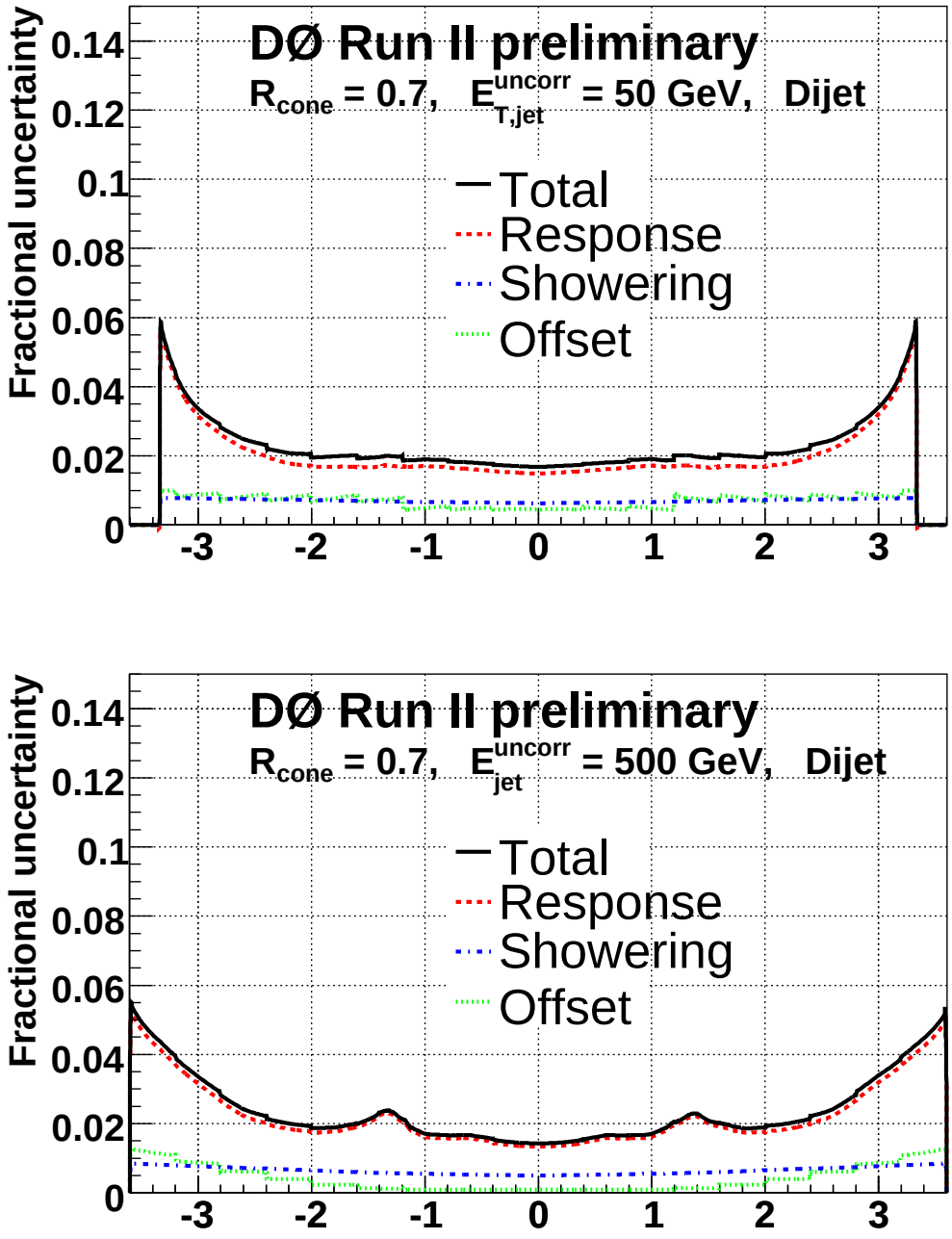

Figure 6.32: Jet energy scale uncertainties by component versus η_{det} at uncorrected $p_T = 50$ GeV/c and uncorrected $E = 500$ GeV.

closure test has been separately performed for both energy and p_T, but only the p_T results are quoted here.

6.13.1 Closure test of absolute JES

The closure test of the absolute JES, *i.e.* the central calorimeter corrections, is done by first establishing direct closure in the γ+jet MC and then comparing the mean jet energy in data and MC in bins of (p'_T,$\eta_{\rm det}$).

Direct closure test in MC

The direct closure test sample is γ+jet MC with $n_{\rm jet} \geq 1$, $n_{\rm vtx} \geq 1$. No upper limits are placed on the number of jets or primary vertices to ensure consistency with the average zero-suppression bias correction. The direct closure test variable is defined as

$$D = \frac{\left\langle E_{\rm jet}^{\rm corr} \right\rangle}{\left\langle E_{\rm jet}^{\rm ptcl} \right\rangle}, \tag{6.59}$$

where $E_{\rm jet}^{\rm corr}$ is the corrected jet energy and $E_{\rm jet}^{\rm ptcl}$ is the energy of the closest particle jet matching the reconstructed jet within $\Delta R < R_{\rm cone}/2$. The closure is tested in bins of (p'_T,$|\eta_{\rm det}|$) and is shown in Fig. 6.33 for $|\eta_{\rm det}| < 0.4$.

Closure test for data

The closure test sample in data is selected consistently with the MC sample. The γ+jet sample in data has significant dijet background so the EM+jet MC sample is mixed with the γ+jet MC with the purity determined from the MC cross section. The closure variable in data is the ratio of average corrected energies in data and MC,

$$D = \frac{\left\langle E_{\rm jet}^{\rm corr,data} \right\rangle}{\left\langle E_{\rm jet}^{\rm corr,MC} \right\rangle}. \tag{6.60}$$

Because the goal is to verify the closure in data, it is important to account for any remaining differences between data and MC that could bias the closure observable. The differences in the single pion response in data and in MC result in a larger response difference between the γ+jet and dijet samples in

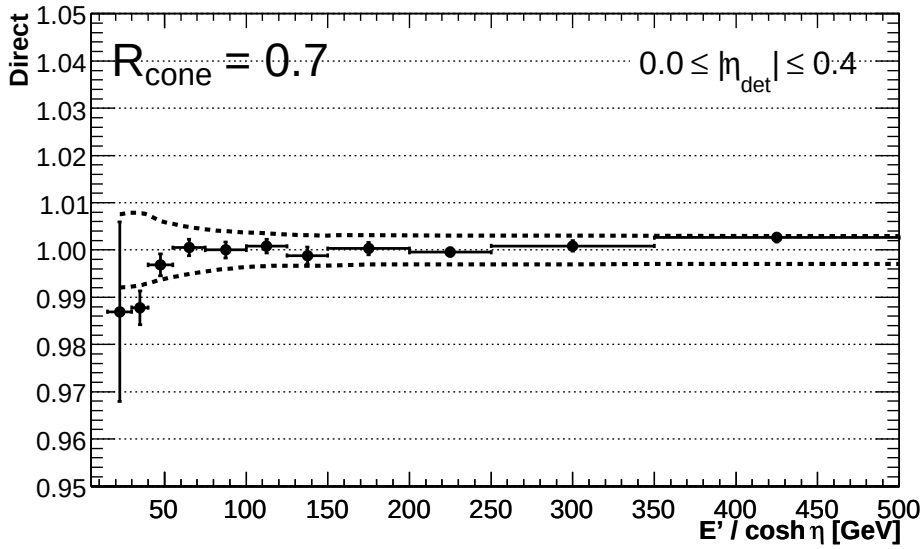

Figure 6.33: Direct JES closure test in γ+jet MC as a function of p'_T at $|\eta_{\rm det}| < 0.4$. The points correspond to the value of the direct closure test variable (see Eq. 6.59) and the dashed line represents the total jet energy scale uncertainty.

data than in MC. This difference is estimated using MC with the single pion response tuned to data. The relative difference in the dijet response is about 4% at $p_T \sim 30$ GeV/c. Because the γ+jet sample purity at $p_T \sim 30$ GeV/c is about 70%, this results in a $4\% \cdot (1 - 0.7) = 1.2\%$ bias on the closure observable that is corrected for.

Additional corrections are also applied on the photon energy scale to account for data and MC differences. These corrections are estimated using the special MC with increased dead material and improved GEANT simulation to match the electron response in data. The photon energy scale corrections affect the closure test variable indirectly through the p'_T binning.

The closure in data relative to MC is shown in Fig. 6.34 for $|\eta_{\text{det}}| < 0.8$. Because the data and MC JES uncertainties are largely uncorrelated, they are added in quadrature to create the error band for the closure test. The uncertainties inherent in the closure test have not been included, however.

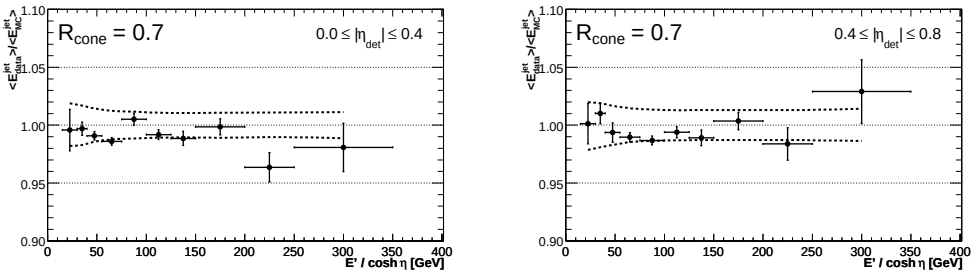

Figure 6.34: Relative data-to-MC closure test as a function of p'_T at $|\eta_{\text{det}}| < 0.4$ and $0.4 < |\eta_{\text{det}}| < 0.8$. The points correspond to the value of the closure variable (see Eq. 6.60) whereas the dashed line represents the total jet energy scale uncertainty from data and MC.

6.13.2 Closure test of dijet p_T scale

The previous section established the validity of the absolute jet energy scale correction in the γ+jet sample. Practically every sub-correction has been rederived to obtain the corresponding p_T scale for the dijet sample, which needs to be tested separately. There is no direct handle on the absolute p_T scale in dijet data so only the consistency of the methods is tested in MC. The closure test variable is

$$\Delta p_T = \frac{\langle p_T^{\text{reco}} \rangle}{\left\langle p_T^{\text{ptcl}} \right\rangle} - 1, \tag{6.61}$$

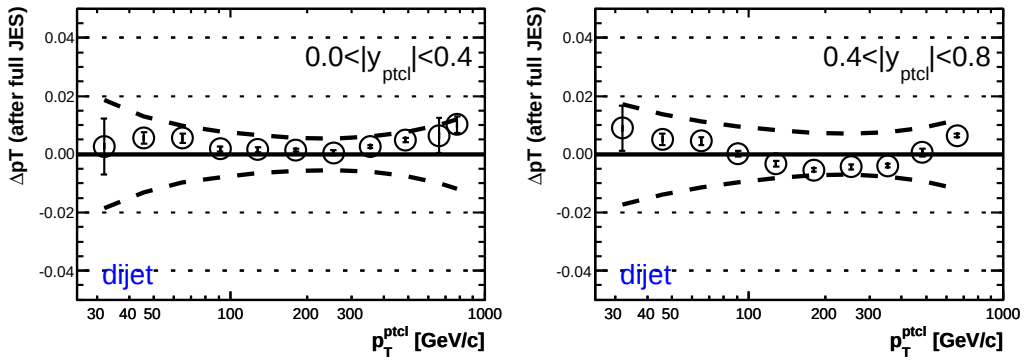

Figure 6.35: Direct jet p_T closure plots for p_T^{ptcl}, y_{ptcl} binning in the dijet sample. The error band shows MC JES uncertainty.

where reconstructed jets are matched to the highest p_T particle jet within $\Delta R < R_{\mathrm{cone}}$ and the result is binned in p_T^{ptcl} and y_{ptcl} for consistency with the cross section measurement. The sample is selected to have exactly two back-to-back jets with $\Delta\phi > 3.0$. The result for the closure test in CC is shown in Fig. 6.35.

The closure test result has been corrected for the low p_T bias at $p_T < 50$ GeV/c by using the fitted Gaussian mean of $(p_T^{\mathrm{reco}}/p_T^{\mathrm{ptcl}} - 1)$ instead of the closure test variable in Eq. 6.61. The Gaussian mean is fitted to the part of the distribution where $p_T^{\mathrm{reco}} > 15$ GeV/c to avoid the 6 GeV/c reconstruction threshold for uncorrected p_T.

Closure test of inclusive jet p_T scale

The dijet sample is only a fraction of the inclusive jet sample so the question of closure for the inclusive jets still remains. The non-leading jets are often radiated gluons so the inclusive jet sample has higher gluon-jet content and potentially lower response than the dijet sample. To test this difference, closure test with Eq. 6.61 is repeated on the inclusive jet sample without any cuts on n_{jet} or $\Delta\phi$. The jet p_T closure for the inclusive jet sample is shown in Fig. 6.36 for CC.

There is indeed a difference of about 1–2% on average between inclusive jet and dijet residual Δp_T at $p_T \sim 30$ GeV/c in CC, but the difference rapidly gets smaller at higher p_T and in the more forward regions. The closure tests indicate that the residual in CC is in fact slightly smaller for the inclusive jets than for dijets. For this reason no additional correction is applied, but

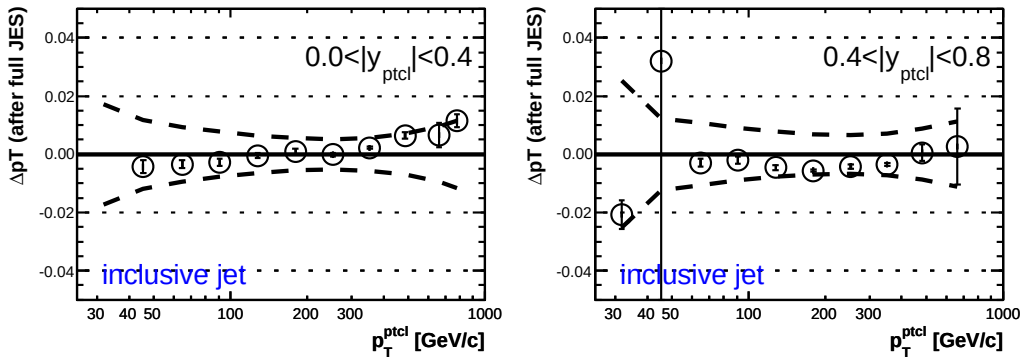

Figure 6.36: Direct jet p_T closure plots for p_T^{ptcl}, y_{ptcl} binning in the inclusive jet sample. The error band shows MC JES uncertainty. The high fluctuations at $p_T < 50$ GeV/c are caused by large relative MC weights for low $\hat{p}_T$ bins.

half of the inclusive jet to dijet response difference is taken as a systematic for JES. The resulting uncertainty is less than 0.5% at $p_T > 50$ GeV/c.

6.13.3 Closure test of η-dependence

The JES η-dependence closure is based on the p_T asymmetry between a central calorimeter jet and a forward jet

$$A = \frac{p_{T,2} - p_{T,1}}{p_{T,2} + p_{T,1}}, \quad |y_1| < 0.8. \tag{6.62}$$

This is related to the ratio of residual JES ($\Delta p_T + 1$) for the central jet r and the forward jet R by

$$\frac{R}{r} = \frac{1 + \langle A \rangle}{1 - \langle A \rangle} \approx 1 - 2A, \tag{6.63}$$

when $\left\langle p_{T,1}^{\mathrm{ptcl}} \right\rangle = \left\langle p_{T,2}^{\mathrm{ptcl}} \right\rangle$. The closure variable is sensitive to additional jets and showering and requires in practice events with only two jets back-to-back. The same $\Delta\phi > 3.0$ and $N_{\mathrm{jet}} = 2$ cuts as for direct dijet closure are used. The events are binned in the average p_T of the two jets, $0.5 \cdot (p_{T,1} + p_{T,2})$, which has the benefit that effects due to resolution bias largely cancel.

The dijet asymmetry is practical for a closure test because most effects other than JES for the two leading jets cancel to a large extent. The physics showering and soft radiation effects are symmetric for the central-forward dijet system and the leading jets are balanced to better than about 0.2% at particle level. The soft radiation bias for reconstructed jets is corrected for by

raising the reconstruction threshold and extrapolating to 0 GeV/c threshold, but the bias is at a permille level.

The largest systematic bias turns out to be resolution bias, although this effect largely cancels in the average p_T binning. The resolution bias is of the order of 1–2% in ICR and is explicitly corrected for, as discussed in the following section. The remaining method biases are corrected by the factor $C_{\mathrm{bias}} = ((\Delta p_T^{\mathrm{forward}} + 1)/(\Delta p_T^{\mathrm{central}}) + 1)/(R/r)$ determined from MC, where the Δp_T is the dijet p_T direct closure test variable of Eq. 6.61 and the R/r of Eq. 6.63 is determined after all the other bias corrections. This correction is negligible ($\leq 0.2\%$) in most bins at $p_T > 50$ GeV/c, except in $0.8 < |y| < 1.2$, where the bias is a constant 0.6%.

Resolution bias in closure

Despite binning in average jet p_T there is significant resolution bias left for central-ICR jet pairs because the jet resolutions for these regions differ substantially. The bias is roughly proportional to $\partial f(p_T)/(f(p_T)\partial p_T)(\sigma_2^2 - \sigma_1^2)$, where $f(p_T)$ is the dijet p_T spectrum and σ_2 and σ_1 are the p_T resolutions of the two jets. The bias on the asymmetry is calculated through integration as

$$\delta A = \frac{\int_{x=0}^{\infty}\int_{z=-p_T}^{p_T} f(x,y_1,y_2)g(p_T-z,x,y_1)g(p_T+z,x,y_2)\cdot z/p_T dxdz}{\int_{x=0}^{\infty}\int_{z=-p_T}^{p_T} f(x,y_1,y_2)g(p_T-z,x,y_1)g(p_T+z,x,y_2)dxdz},$$

$$\text{where} \qquad x = p_T^{\mathrm{ptcl}}, \quad z = (p_{T,2} - p_{T,1})/2, \quad p_T = (p_{T,2} + p_{T,1})/2. \qquad (6.64)$$

Here y_1 is the rapidity of the central jet, y_2 is the rapidity of the forward jet, $f(p_T^{\mathrm{ptcl}}, y_1, y_2)$ is the dijet p_T spectrum already used in Section 6.4.2 and $g(p_T^{\mathrm{reco}}, p_T^{\mathrm{ptcl}} y)$ is the jet Δp_T distribution (jet p_T resolution), which is derived in Chapter 7 after the JES corrections. The resulting bias in ICR is shown in Fig. 6.37.

6.13.4 Final η-dependence closure test

The η-dependence closure results shown in Fig. 6.38 have been corrected for particle level imbalance, soft radiation, resolution bias and method bias, although most of these corrections are very small ($\leq 0.2\%$). The statistical uncertainty is the uncertainty of the fit to the residual of the quadratic logarithmic function of p_T. The method uncertainty includes primarily the uncertainty in the ratio of CC and EC resolutions (resolution bias correction)

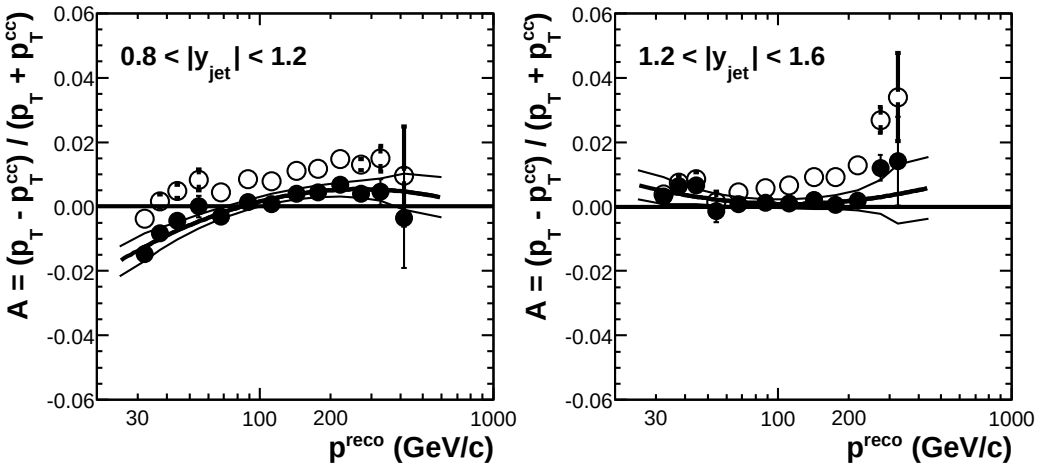

Figure 6.37: Asymmetry measurement in ICR. Open circles are before, full circles after the resolution bias correction. The error band covers $\pm 1\sigma$ variation in the ratio of the ICR and CC resolutions.

and the residual of the method bias determination. The JES uncertainty is the uncertainty of the ratio of the central and forward JES. The different uncertainty sources are added incrementally in quadrature ($\oplus$) for the error bands.

The full uncertainty correlation information is propagated to both the JES and the resolution uncertainties. The correlated shifts of the p_T of the central and the forward jets are evaluated in the ratio R/r for each uncertainty source. For example, the JES uncertainty is calculated by

$$\Delta\frac{R}{r} = \sqrt{\sum_s \left(\frac{1+\Delta_s C(p'_T, y_{\text{forward}})}{1+\Delta_s C(p'_T, y_{\text{central}})} - 1\right)^2}, \tag{6.65}$$

where the JES uncertainty $\Delta_s C(p'_T, y)$ is evaluated at $y = y_{\text{forward}}$ and $y = y_{\text{central}} = 0$ for each uncertainty source s.

It is important to note that the JES and closure in Fig. 6.38 are only applicable to the run range 191000—213064 due to the JES time dependence discussed in Section 6.4.6. The same JES applied to the full Run IIa data sample results in about 1% closure test residual (R/r-1) at $1.2 < |y| < 1.6$ and a smaller residual in the surrounding bins. The JES has also been derived for the full sample, but using the more restricted run range allows to remove the uncertainty due to time dependence and makes the jet p_T spectra from different triggers match better.

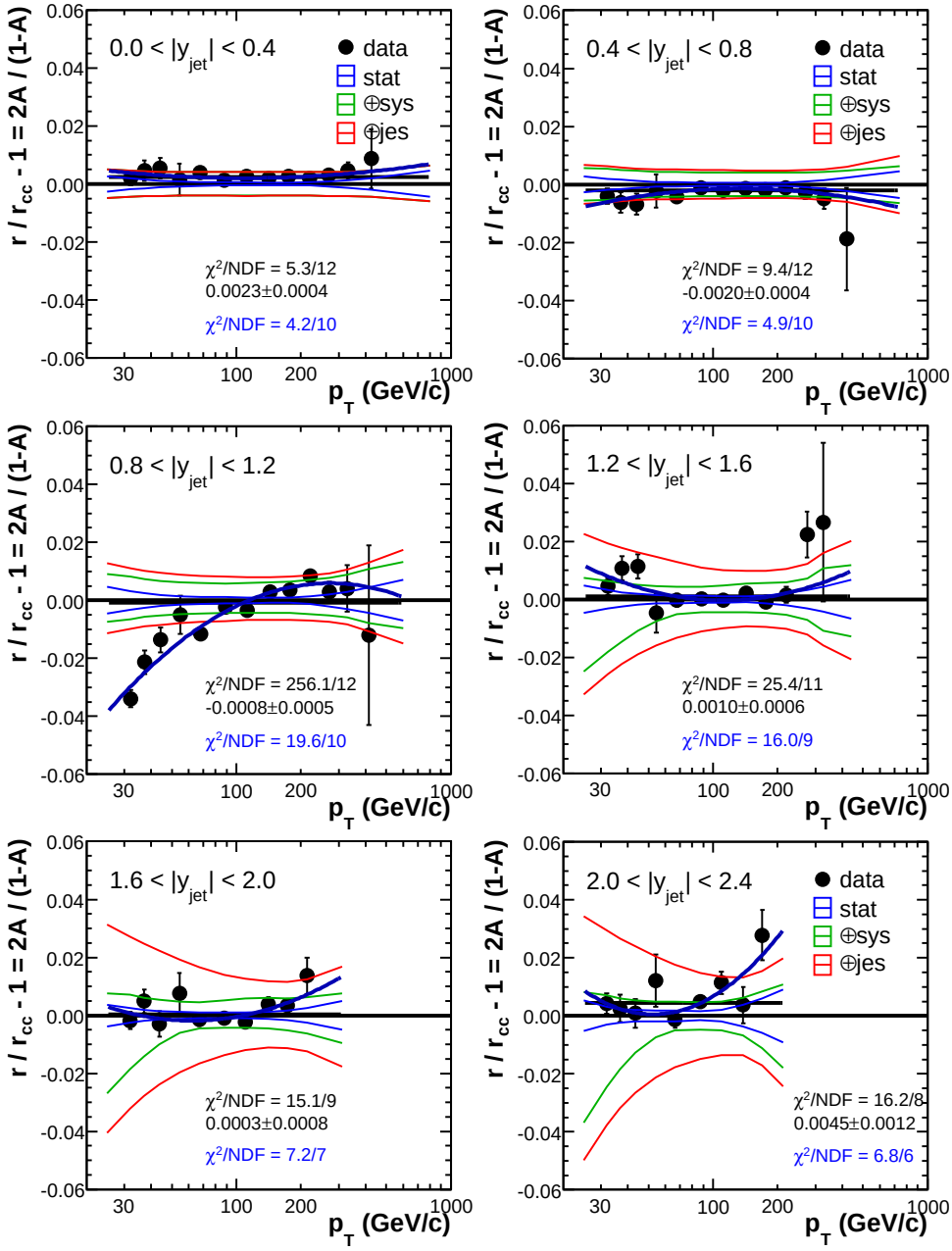

Figure 6.38: JES η-dependence closure for dijets in run range 191000–213064, with the JES specifically derived for this restricted run range. The uncertainty bands cover incrementally the statistical uncertainty of the quadratic logarithmic fit (stat), the closure method uncertainty (sys) and the correlated JES uncertainty. The inset text shows the χ^2/NDF and the value for a constant fit to the residual (top and middle lines, straight fit) and the χ^2/NDF for the quadratic logarithmic fit (bottom line, curved fit).

The largest observed deviation is in the bin $0.8 < |y| < 1.2$ at $p_T < 80$ GeV/c. This is in ICR, which is the most difficult region of the calorimeter to calibrate due to rapid changes in the response as a function of η. The closure test is also complicated by the large resolution bias in ICR and the rapid changes in the jet p_T resolution as a function of η. While the observed deviation could be real and not just a systematic bias in the closure test, the closure is still good to within 1.5–2σ at $p_T > 50$ GeV/c. This is acceptable for the measurement in a restricted region of the phase space. The shapes and magnitude of the assigned JES systematics cover for the observed deviation and the global PDF fits in Ch. 8 show no strong pull in this region.

Chapter 7

Jet p_T and y resolutions

7.1 Overview

The jet p_T resolutions are the second most important component in the inclusive jet cross section measurement. They are needed in the unfolding of the jet cross section, as will be discussed in Chapter 8. The rapidity resolution is also used in unfolding, although its relative impact is much smaller. The p_T resolutions also have uses in many other applications. In the context of this thesis the p_T resolutions have been applied to resolution bias corrections (Sec. 6.4.2) and to test the relative JES closure in detail (Sec. 6.13). The application to other analyses is discussed in the original study [112] that also provides an extended set of plots. Earlier studies of the jet p_T resolutions are discussed in Refs. [113, 41, 12].

The jet p_T resolution is derived from the width of the dijet asymmetry distribution, which is based on transverse momentum balancing. This method requires corrections for the presence of additional unreconstructed jets (soft radiation), momentum imbalance at the particle level and asymmetry bias due to non-Gaussian tails. The jet p_T resolutions are determined primarily from dijet data using the same sample as is used for the cross section analysis. The parts modeled by MC are the p_T imbalance at the particle level, which is generally a correction of less than 10%, and the shape of the Δp_T distribution, which is nearly Gaussian and creates an asymmetry bias of less than 10%.

The closure of the method is tested in MC, and the residuals are added as an uncertainty. Uncertainties are also estimated for all the sub-corrections. The overall uncertainty is 5–8% for $p_T > 50$ GeV/c and $|y| < 2.4$. The fitted Δp_T

distribution shapes from MC are used in all applications of jet p_T resolutions.

The rapidity resolution has much smaller impact on the cross section measurement than p_T resolution and is determined from MC alone. The full rapidity unfolding correction is later conservatively taken as a small uncertainty.

7.2 Dijet asymmetry

The jet p_T resolutions are determined starting from the dijet asymmetry A

$$A = \frac{p_{T,1} - p_{T,2}}{p_{T,1} + p_{T,2}}. \tag{7.1}$$

The transverse momenta of the two jets can be assumed balanced if they are back-to-back and no additional jets are present. The $\Delta\phi > 3.0$ and $N_{\text{jet}} = 2$ cuts are applied in selecting the dijet sample. The number of primary vertices is not constrained. The jets are ordered in absolute rapidity, $|y_1| < |y_2|$, so that the asymmetry distribution is expected to be symmetric around 0 after JES corrections. The variance of the asymmetry distribution can be written as

$$\sigma_A^2 = \left|\frac{\partial A}{\partial p_{T,1}}\right| \sigma_{p_T,1}^2 + \left|\frac{\partial A}{\partial p_{T,2}}\right| \sigma_{p_T,2}^2, \tag{7.2}$$

which allows the jet p_T resolution to be calculated from the asymmetry.

For two jets in the same rapidity region (and, of course, at the same p_T) the jet p_T resolutions σ are the same on average. The asymmetry can then be simply related to p_T resolution by

$$\text{RMS}(A) = \frac{\sqrt{(\text{RMS}(p_{T,1}))^2 + (\text{RMS}(p_{T,2}))^2}}{\langle p_{T,1} + p_{T,2} \rangle} = \frac{\sigma_{p_T}}{\sqrt{2} p_T}, \tag{7.3}$$

where RMS is the root-mean-squared of the asymmetry distribution. This directly gives the relative p_T resolution σ/p_T as $\sqrt{2} \cdot \text{RMS}(A)$. The equation assumes $\langle p_{T,1} \rangle = \langle p_{T,2} \rangle = p_T$ and $\text{RMS}(p_{T,1}) = \text{RMS}(p_{T,2}) = \sigma$.

For two jets in different rapidity regions the resolutions cannot be assumed equal, but it is possible to solve the resolution σ_2 if the σ_1 is already known

$$\text{RMS}(A_{1,2}) = \frac{\sqrt{\sigma_1^2 + \sigma_2^2}}{2 p_T} \tag{7.4}$$

$$\Rightarrow \frac{\sigma_2}{p_T} = \sqrt{4 \cdot \text{RMS}(A_{1,2})^2 - \frac{\sigma_1^2}{p_T^2}} \tag{7.5}$$

$$= \sqrt{4 \cdot \mathrm{RMS}(A_{1,2})^2 - 2 \cdot \mathrm{RMS}(A_{1,1})^2}. \quad (7.6)$$

The indexes for $A_{1,2}$ and $A_{1,1}$ indicate that the former is measured in a topology with the two jets in different rapidity regions, and the latter with both jets in the same rapidity region. The topologies with one jet central ($|y| < 0.8$) and one more forward are very important for measuring p_T resolutions in EC. The statistics for the sample with two jets forward are much lower than having one jet central and the other forward.

7.3 Soft radiation correction

The resolutions determined from the asymmetry are biased due to the presence of additional non-reconstructed jets in the sample. Even though the jet reconstruction threshold of $p_T^{\mathrm{uncorr}} = 6$ GeV/c $\Rightarrow$ $p_T^{\mathrm{corr}} \approx$ 12–15 GeV/c is fairly low compared to typical jet $p_T > 50$ GeV/c and the $\Delta\phi > 3.0$ also limits soft radiation, the soft radiation still has significant impact at low p_T. This is partly due to high QCD cross section for soft radiation ($\sigma(N_{\mathrm{jet}} > 2) \approx \sigma(N_{\mathrm{jet}} = 2)$) and the fact that the events that pass the $\Delta\phi > 3.0$ cut and have soft jets tend to have the soft jet parallel to one of the leading jets in ϕ, maximally impacting the relative p_T balance.

The soft radiation correction is determined directly from data, minimizing the dependence on the MC description of response and p_T resolutions. The impact of soft radiation increases when the jet reconstruction threshold $p_{T,\mathrm{cut}}^{\mathrm{uncorr}}$ is moved to higher p_T^{uncorr}. The asymmetry is measured using consecutive thresholds $p_{T,\mathrm{cut}}^{\mathrm{uncorr}}$=6, 7, 8, 10, 12, 15, 20 and 40 GeV/c and extrapolated back to ideal $p_{T,\mathrm{cut}}^{\mathrm{uncorr}}$=0 GeV/$c$ using a linear fit, shown for CC in Fig. 7.1(a)–(b).

The linear fit describes the behavior well below the saturation threshold $p_{T,\mathrm{cut}}^{\mathrm{uncorr}} \approx p_T/3$. At higher $p_{T,\mathrm{cut}}^{\mathrm{uncorr}}$ the asymmetry does not change much simply because the soft jets, which are generally parallel to one of the leading jets in ϕ after the $\Delta\phi > 3.0$ cut, would change ordering with second leading jets. This is evident from p_T balancing assuming all jets are parallel or anti-parallel in ϕ

$$\begin{aligned} p_{T,1} - p_{T,2} - p_{T,\mathrm{soft}} &= 0, \quad p_{T,1} \geq p_{T,2} \geq p_{T,\mathrm{soft}} && (7.7)\\ \Rightarrow p_{T,\mathrm{soft}} &\leq (p_{T,2}/2 + (p_{T,1} - p_{T,\mathrm{soft}})/2) && (7.8)\\ \Rightarrow p_{T,\mathrm{soft}}^{\mathrm{uncorr}} &\leq R_{\mathrm{soft}} \cdot \frac{2}{3} \cdot p_{T,av}, && (7.9) \end{aligned}$$

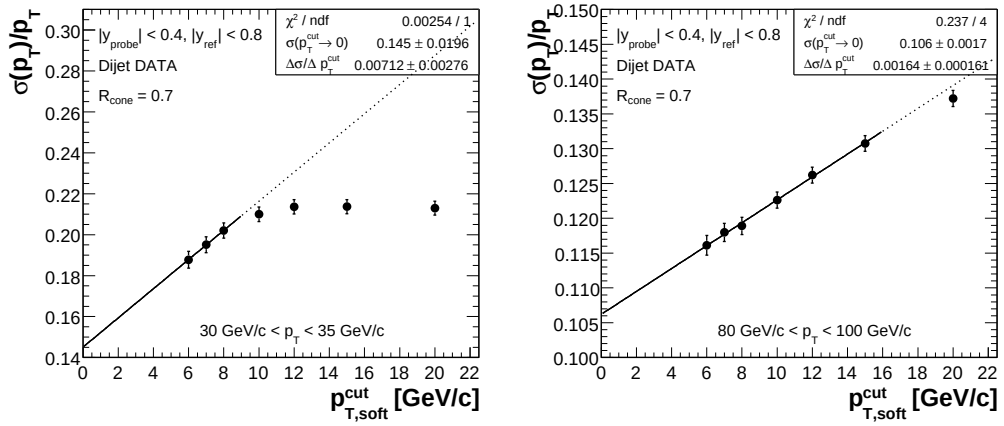

Figure 7.1: Examples of fits of soft radiation dependence in CC measured in data. The distributions are well described by a linear fit below $p_{T,\text{saturation}} \approx p_T/3$ (solid line). The dashed line shows the extrapolation of the fit to higher thresholds.

where the response $R_{\text{soft}} \approx 0.4$–$0.6$ at low p_T for data. Because of the saturation the linear fits are only done up to $p_{T,\text{cut}}^{\max} \leq p_{T,\text{av}}/3$ where the increase in asymmetry is still linear. The linear behavior is checked for each $p_{T,\text{av}}$ bin separately, but the saturation only affects bins with $p_{T,\text{av}} < 100$ GeV/c. At $p_T < 30$ GeV/c there are only two usable points, which limits the reliability of the extrapolation.

The soft radiation correction is calculated as

$$k_{\text{soft}} = \frac{\sigma_{\text{raw}}(p_{T,\text{cut}} \to 0)}{\sigma_{\text{raw}}(p_{T,\text{cut}} = 6 \text{ GeV}/c)}. \tag{7.10}$$

To better describe the low p_T region and limit the statistical fluctuations, the k_{soft} versus p_T is fitted with

$$k_{\text{soft}}(p_T) = 1 - \exp(-p_0 - p_1 p_T). \tag{7.11}$$

This describes the distribution well and enforces the physical behavior $k_{\text{soft}} \to 1$ at $p_T \to \infty$. The fits for CC are shown in Fig. 7.2(a)–(b) for data and pure MC particle jets.

The soft radiation correction in reconstructed MC is very similar to that in data, shown in Fig. 7.2(a), despite the response and resolution differences. The results are roughly statistically consistent so the better measured and more stable soft radiation correction fits from data are used for both data and MC. The soft radiation correction increases only weakly with p_T up to

$|y| = 2.0$ and then increases little faster for higher rapidities. The relative impact of the soft radiation correction is larger for the pure particle jets, shown in Fig. 7.2(b), because the particle level imbalance is much smaller than the detector resolution.

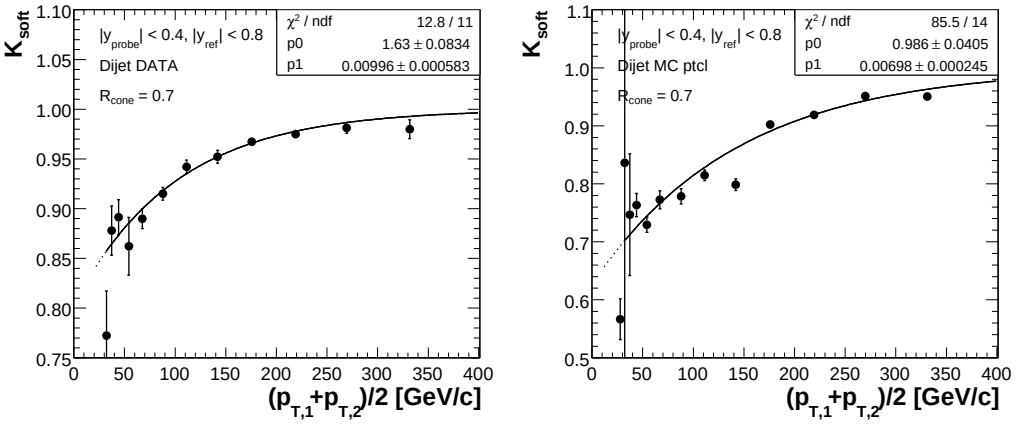

Figure 7.2: Soft radiation correction in CC for (a) dijet data and (b) particle level dijet MC.

7.4 Particle level imbalance correction

Even in the ideal situation of only two particle jets and no soft radiation the two jets are not necessarily perfectly balanced. In the leading order of perturbation theory the two partons are produced perfectly balanced in p_T, assuming the colliding partons had no primordial p_T inside the proton. Interaction with the other partons in the proton after the hard scatter can distribute some of the p_T to proton remnants and underlying event, and the fragmentation effects cause some energy and p_T to be showered outside the jet cone. The latter effect, called physics showering, is expected to be the dominant cause of p_T imbalance at particle level.

The transition from physics showering due to fragmentation to soft radiation due to initial and final state radiation may not be sharp and falls in the regime of non-perturbative QCD that is less well understood than the perturbative regime. For this reason the soft radiation correction and particle level imbalance correction may be entangled at some level. Particle jets also have an inherent reconstruction threshold, although much lower than the reconstruction threshold for calorimeter jets. To remove the overlap between soft radiation correction and particle level imbalance correction, the particle

level imbalance is determined from MC using the method introduced for soft radiation corrections in data

$$k_{\rm soft}^{\rm MC} = \frac{\sigma_{\rm raw}^{\rm ptcl}(p_{T,\rm cut}^{\rm ptcl} \to 0)}{\sigma_{\rm raw}^{\rm ptcl}(p_{T,\rm cut}^{\rm ptcl} = 6\ {\rm GeV}/c)}, \quad (7.12)$$

$$\sigma_{\rm MC} = k_{\rm soft}^{\rm MC}\sigma_{\rm raw}^{\rm ptcl}. \quad (7.13)$$

The soft radiation correction at particle level is about 0.75 at $p_T = 50$ GeV/c in CC, as shown in Fig. 7.2(b). The corrected $\sigma_{\rm MC}$ is shown in Fig. 7.3 compared to corrected p_T resolution.

The particle level imbalance $\sigma_{\rm MC}$ is subtracted in quadrature from the soft radiation corrected resolution ($k_{\rm soft}\sigma_{\rm raw}$) to get the corrected resolution,

$$\sigma_{\rm corr} = \sqrt{(k_{\rm soft}\sigma_{\rm raw})^2 - \sigma_{\rm MC}^2}. \quad (7.14)$$

The relative correction due to particle level imbalance is about 7–9% in CC, 2–6% in ICR and EC for $p_T > 50$ GeV/c, with larger correction at low p_T.

The particle level imbalance correction uses the RMS value of the particle level imbalance, which is supported by the Monte Carlo closure tests. The difference between the Gaussian σ and RMS can be up to a factor of two. The large tails shown in Fig. 7.4 are caused by muons (μs) and neutrinos (νs) produced in the parton shower that are invisible energy for the particle jet algorithm used in standard DØ MC. The μs and νs are produced especially in the decay chains of b-jets, which account for 1–2% of the total inclusive jet cross section [134]. This is consistent with the tails being about two orders of magnitude lower than the main peak. The shift to JES due to unaccounted for μs and νs is explicitly corrected for in Ch. 8. This increases the cross section by about 2%.

7.5 Shape of the Δp_T distribution

The jet p_T resolution describes the distribution of $\Delta p_T = p_{T,\rm reco}/p_{T,\rm ptcl} - 1$ by RMS(Δp_T). In the simplest approximation this distribution is Gaussian, with $\sigma_{\rm Gauss} = RMS(\Delta p_T)$. This assumption holds well particularly at low p_T in CC and EC. At high p_T the Δp_T distribution produces non-Gaussian tails in all rapidity regions, as shown in Fig. 7.5(a) for $|y| < 0.4$, because the calorimeter is not thick enough to contain the full energy of all hadronic showers. In ICR the Δp_T distribution shown in Fig. 7.5(b) is augmented by another non-Gaussian tail, which is modeled by a second Gaussian that

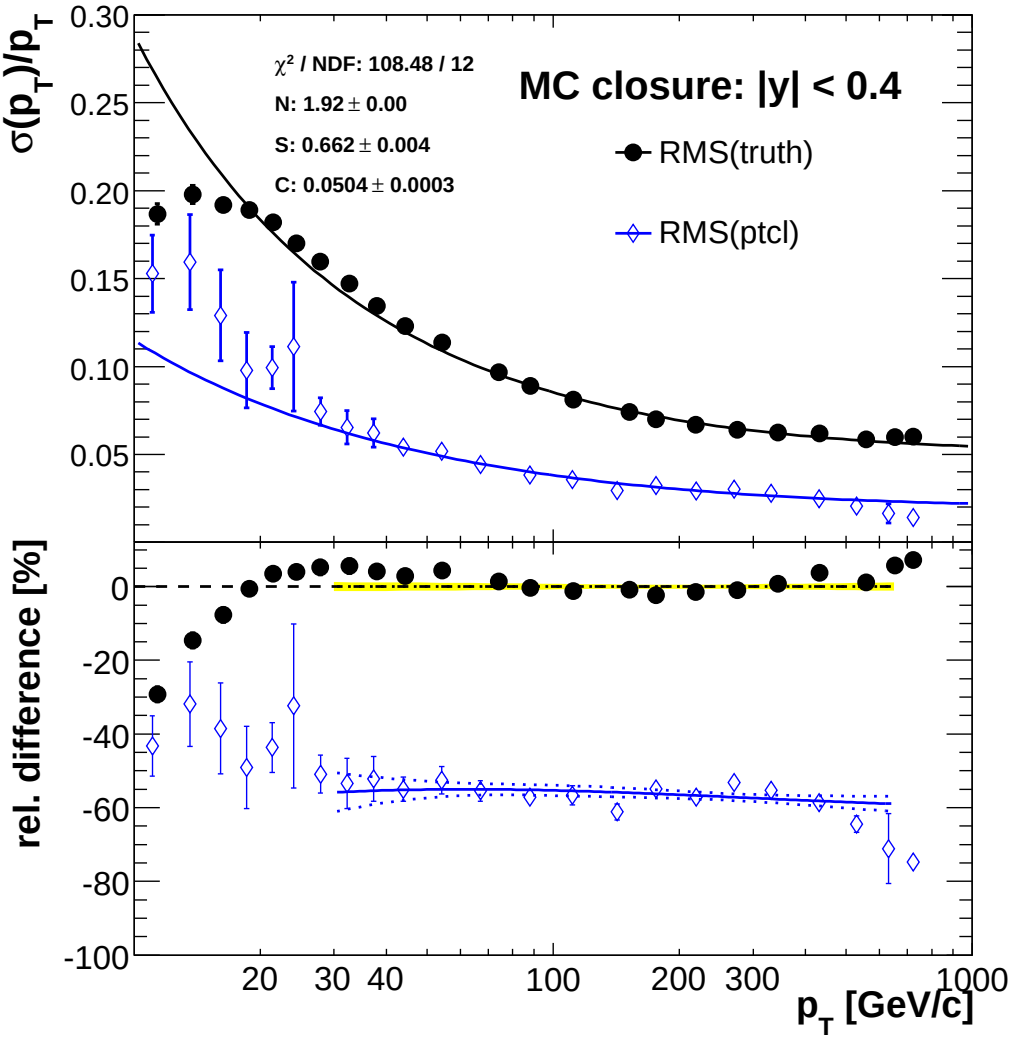

Figure 7.3: Monte Carlo particle level imbalance σ_{MC} = RMS(ptcl) (open diamonds) compared to the true jet p_T resolution RMS(truth) (full circles) in CC. Lower plot shows the ratio of the upper graphs to the MC resolution fit. The fit parameters N (noise), S (stochastic) and C (constant) are discussed in Sec. 7.8.

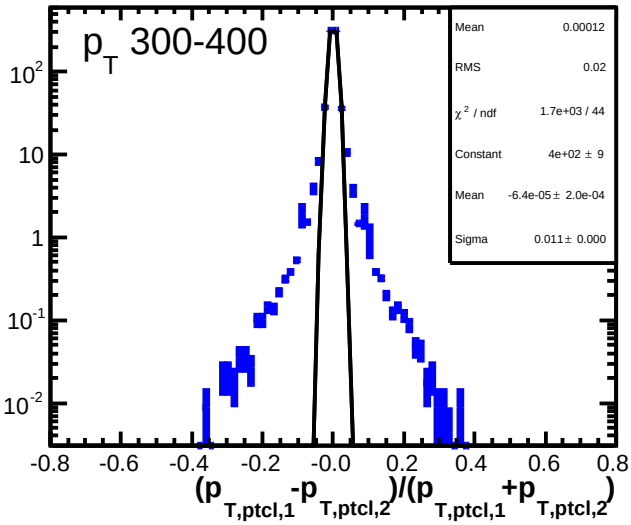

Figure 7.4: Example of non-Gaussian tails in particle level imbalance caused by invisible energy from μs and νs in the bin $300 < p_T < 400$ GeV/c. The solid line shows a Gaussian fit to the distribution.

is wider and slightly displaced. The ICR tails are best explained by the changing structure of the calorimeter in this region.

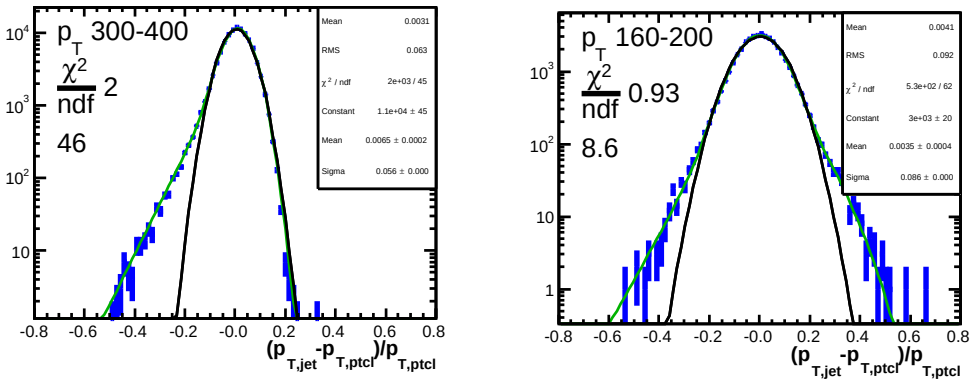

Figure 7.5: Examples of (a) punch-through at $|y| < 0.4$ in the bin $300 < p_T < 400$ GeV/c and (b) ICR tails at $0.8 < |y| < 1.2$ in the bin $160 < p_T < 200$ GeV/c. The black line shows a Gaussian fit ($\chi^2/NDF = 46$ and 8.6), the gray (green) line the fit with tails ($\chi^2/NDF = 2$ and 0.93).

The non-Gaussian tails are parametrized using MC truth[1], and the width of the Δp_T distribution is then scaled to match the resolution in data. The jet p_T resolutions are described by their RMS, which is well-defined for both the MC truth Δp_T distributions and the asymmetry distributions in data. A requirement for all the MC parametrizations is that the arithmetic mean of the Δp_T distribution is fixed at 0. This ensures consistency with JES that calibrates the arithmetic mean of the Δp_T distribution and not the Gaussian mean, which is not well-defined for non-Gaussian distributions.

Punch-through

The depth of the DØ calorimeter is around seven nuclear interactions lengths λ as shown in Fig. 7.7. Although this is thick enough to contain low p_T jets, some high p_T hadronic showers can punch through and lose a fraction of their energy outside the calorimeter. This is often evidenced by the muon detector receiving spurious energy deposits behind the punch-through jets. As a result, the difference between the RMS and Gaussian σ in MC truth is up to 20% in CC at $p_T = 600$ GeV/c.

The punch-through is modeled with an exponentially distributed energy loss with parameter λ for a fraction P of the jets

$$\delta(x) \rightarrow (1-P)\delta(x-\mu) + P\lambda \exp\left(\lambda(x-\mu)\right)\theta(\mu - x), \tag{7.15}$$

$$x = \frac{p_T}{p_T^{ptcl}} - 1, \quad 0 \leq P \leq 1, \quad \lambda > 0, \quad \langle x \rangle = \mu - \frac{P}{\lambda}. \tag{7.16}$$

Here $\delta(x)$ is the Dirac's delta function and $\theta(x)$ is the Heaviside step function. The parameter μ is introduced so that the mean of the distribution can be shifted to $\langle x \rangle = 0$ as JES requires.

The observed Δp_T distribution folds the δ-function and exponentially decaying punch-through $g_{\text{punch}-\text{through}}(x, \mu, P, \lambda)$ of Eq. 7.15 with Gaussian detector resolution $g_{\text{det}}(x, 0, \sigma)$. The folding is computed analytically[2] after replacing the integration range by $(-\infty, \infty)$

$$\begin{aligned} g(x, \mu, \sigma, P, \lambda) &= g_{punch-through}(\mu, P, \lambda) \otimes g_{det}(0, \sigma)(x) \\ &= \int_0^{980} \left((1-P)\delta(y-\mu) + P\lambda \exp\left(\lambda(y-\mu)\right)\theta(\mu - y)\right) \end{aligned}$$

[1]MC truth refers to the accessing of particle level information that is not available in data.

[2]The symbolic evaluation was performed using Mathematica.

$$\cdot\frac{\exp\left(-\frac{(x-y)^2}{2\sigma^2}\right)}{\sqrt{2\pi}\sigma}dy \tag{7.17}$$

$$\Rightarrow g(x,\mu,\sigma,P,\lambda) = (1-P)g_{det}(x,\mu,\sigma) + \frac{P\lambda}{2}\cdot\exp\left(\lambda(x-\mu+\frac{\lambda\sigma^2}{2})\right)$$
$$\cdot\text{erfc}\left(\frac{x-\mu+\lambda\sigma^2}{\sqrt{2}\sigma}\right). \tag{7.18}$$

The mean and RMS of this new distribution are analytically calculated as[3]

$$\langle x\rangle = \mu - P/\lambda, \tag{7.19}$$
$$\text{RMS}(x) = \sqrt{\langle x^2\rangle - \langle x\rangle^2} = \sqrt{\sigma^2 + P(2-P)/\lambda^2}. \tag{7.20}$$

The functional form in Eq. 7.18 is fitted to the MC truth resolutions in each p_T and y bin. The parameters P and λ are fixed in an iterative procedure to the simplest polynomials that give overall good fits. Physical behavior for the punch-through tails is ensured by requiring that $P(p_T \to 0) \to 0$, $P \in [0,1]$ and $\lambda > 0$. In addition, the analytically calculated RMS of Eq. 7.20 is required to match that of the MC truth Δp_T distributions.

Non-uniform calorimeter thickness causes parameter P to vary with η_{det}, with the thinnest region and highest P around $\eta_{\text{det}} = 0.65$. The fraction of high energy pions in a jet increases with energy and so does the punch-through fraction P. Parameter λ also increases with energy, but has no rapidity dependence. The final parameterizations are shown in Fig. 7.6.

Intercryostat region

Some non-Gaussian structure is expected in ICR [135] because the stable uranium-liquid Argon calorimeter is partly replaced by less precise scintillator material and aging photomultiplier tubes of the intercryostat detector (ICD). In addition, ICR is the middle region between central and forward cryostats and has a gap in the EM calorimeter coverage. These effects cause a fraction of the jets to have worse resolution and shifted average response compared to the rest.

The ICR tails are reasonably well described by replacing the main Gaussian in Eq. 7.18 by a double-Gaussian and keeping the punch-through tail

[3]Folding with $g_{det}(x,0,\sigma)$ does not change the mean of $g_{punch-through}$, and only adds σ in quadrature to the total RMS. The RMS for the sum of the two components is $\text{RMS} = \sqrt{f\cdot\text{RMS}(1)^2 + (1-f)\cdot\text{RMS}(2)^2 + f(2-f)(\text{MEAN}(1)-\text{MEAN}(2))^2}$, where $f = \frac{N_1}{N_1+N_2}$.

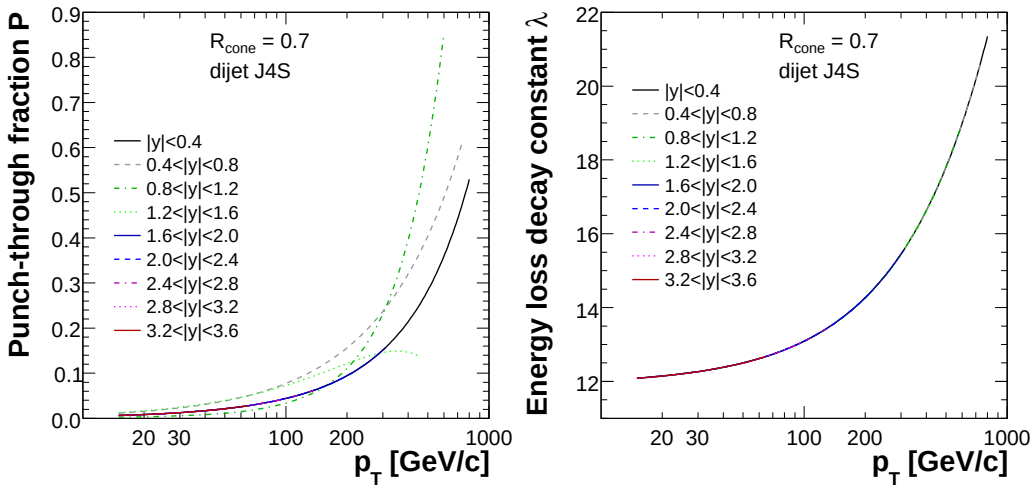

Figure 7.6: Parameters of the punch-through fits as a function of p_T for different rapidity regions. The parameter P models the punch-through fraction (left), the parameter λ is the exponential decay constant of the fractional energy loss (right). The thinnest region of the calorimeter is around $\eta_{det} = 0.65$, where the P is expected to be highest. The CC and EC are fitted with a single curve for P, as are all regions for λ.

unmodified. This leads to the following parametrization

$$\begin{aligned} g(x,\mu,\sigma) &= (1-P)\left((1-H)g_{det}(x,\mu,\sigma) + Hg_{det}(x,\mu+\mu_H,\kappa\sigma)\right) \\ &\quad + \frac{P\lambda}{2}\cdot\exp\left(\lambda(x-\mu+\frac{\lambda\sigma^2}{2})\right)\cdot\mathrm{erfc}\left(\frac{x-\mu+\lambda\sigma^2}{\sqrt{2}\sigma}\right). \quad (7.21) \end{aligned}$$

Here a fraction H of non-punch-through jets are shifted by μ_H relative to the central Gaussian and have their resolution degraded by a factor κ. The mean and RMS can be analytically calculated

$$\langle x\rangle = \mu - P/\lambda + \Delta\mu, \quad \Delta\mu = H(1-P)\mu_H \quad (7.22)$$

$$RMS(x) = \sqrt{(1+H(\kappa^2-1))\sigma^2 + H(1-P)(\mu_H-\Delta\mu)^2 + \Delta\mu^2 + P(2-P)/\lambda^2}. \quad (7.23)$$

As in the case of punch-through, the functional form in Eq. 7.21 is fitted to the MC truth resolutions in each p_T and y bin. The parameters H, μ_H and κ are then fixed to the parametrizations that give overall good fits. Parameter H has constant values $\sim$0.11 and $\sim$0.02 in ICR at $0.8 < |y| < 1.2$ and $1.2 < |y| < 1.6$, respectively, and is zero elsewhere. Parameter μ_H

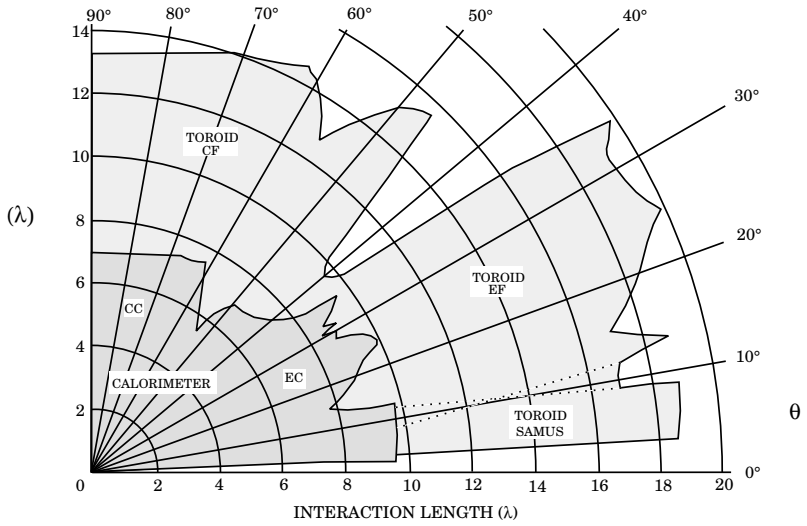

Figure 7.7: Thickness of the DØ calorimeter expressed in units of nuclear interaction lengths λ for different jet angles. The thinnest parts of the calorimeter at 55° and 15° correspond roughly to $\eta_{det} = 0.65$ and $\eta_{det} = 2.0$, respectively. The thick region at 20°–40° corresponds to η =1.0–1.7.

is parametrized as a quadratic log function like response. Parameter κ is parametrized as a ratio of two resolution fits

$$\kappa = \sqrt{N^2 + (\kappa_0 S)^2 p_T + (\kappa_1 C)^2 p_T^2} / \sqrt{N^2 + S^2 p_T + C^2 p_T^2}, \qquad (7.24)$$

where $N \approx 1$, $S \approx 0.8$ and $C \approx 0.06$. This functional form assumes that a fraction of the events has higher stochastic (S) and constant (C) terms than the rest, but leaves the small low p_T noise contribution (N) unaffected. The fits for μ_H and κ are shown in Fig. 7.8 and the parameters are given in Table 7.2.

The fitted parameters for the tails in all rapidity regions as well as the fit functions are provided in Tables 7.1 and 7.2.

7.6 Asymmetry bias

The tails at $\Delta p_T > 0$ in the Δp_T distribution are enhanced in the measured dijet asymmetry because the p_T^{avg} migrates up to a region of phase space with lower cross section, whereas the tails at $\Delta p_T < 0$ are reduced for the same reason. As long as the Δp_T distribution is symmetric the two effects

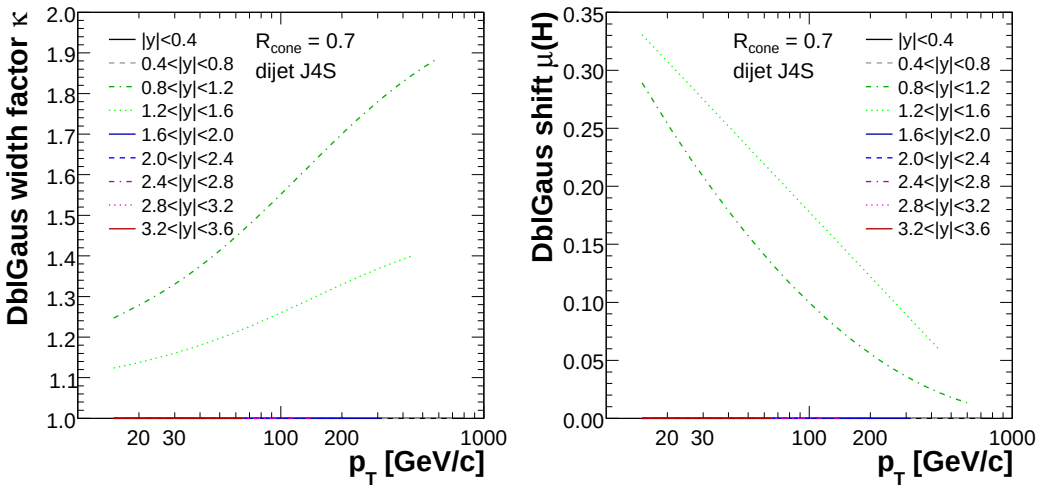

(a)

Figure 7.8: Parameters of the double-Gaussian fit in ICR: (a) relative widening κ and (b) relative shift μ_H compared to the main Gaussian. The relative fraction H of jets in the second Gaussian is ∼0.11 at $0.8 < |y| < 1.2$ and ∼0.02 at $1.2 < |y| < 1.6$.

Table 7.1: Parameters of the punch-through tails. The $|y| < 0.4$ and $|y| > 1.6$ are fitted to a single curve for P, as are all regions for λ.

	P_0	P_1	λ_0	λ_1
$\lvert y\rvert < 0.4$	0.000409	3.16e-07	11.9	0.0118
$0.4 < \lvert y\rvert < 0.8$	0.000764	8.76e-08	11.9	0.0118
$0.8 < \lvert y\rvert < 1.2$	0.000118	2.18e-06	11.9	0.0118
$1.2 < \lvert y\rvert < 1.6$	0.00085	-1.21e-06	11.9	0.0118
$1.6 < \lvert y\rvert < 2.0$	0.000409	3.16e-07	11.9	0.0118
$2.0 < \lvert y\rvert < 2.4$	0.000409	3.16e-07	11.9	0.0118

$$P = P_0 + P_1 \cdot p_T, P \in [0,1],$$
$$\lambda = \lambda_0 + \lambda_1 \cdot p_T.$$

compensate and the resulting bias is small. However, the Δp_T distribution is considerably asymmetric particularly at high p_T due to the punch-through.

The bias on the measured asymmetry is estimated by folding the parametrized Δp_T distribution from MC truth with the parametrized dijet cross section from data that was used in JES in Section 6.4.2. The bias is determined as a ratio of the ideal asymmetry $A^2_{\text{ideal}} = (\sigma_1^2 + \sigma_2^2)/(2p_T^2)$ and the

Table 7.2: Parameters of the ICR tails.

	H	κ_0	κ_1	$\mu_{H,0}$	$\mu_{H,1}$	$\mu_{H,2}$
$\lvert y\rvert < 0.4$	0	1	1	0	0	0
$0.4 < \lvert y\rvert < 0.8$	0	1	1	0	0	0
$0.8 < \lvert y\rvert < 1.2$	0.106	1.18	2.04	0.0997	-0.0732	0.014
$1.2 < \lvert y\rvert < 1.6$	0.0239	1.1	1.5	0.178	-0.0805	0
$1.6 < \lvert y\rvert < 2.0$	0	1	1	0	0	0
$2.0 < \lvert y\rvert < 2.4$	0	1	1	0	0	0

$$\kappa = \frac{\sqrt{1.1^2+0.794^2\cdot\kappa_0^2\cdot p_T+0.0608^2\cdot\kappa_1^2 p_T^2}}{\sqrt{1.1^2+0.794^2\cdot p_T+0.0608^2\cdot p_T^2}},$$
$$\mu_H = \mu_{H,0} + \log(0.01p_T)\cdot(\mu_{H,1} + \log(0.01p_T)\cdot\mu_{H,2}).$$

numerically integrated asymmetry $A_{\rm exp}$

$$\begin{aligned}
x &= p_T^{ptcl}, \quad z = \delta p_T = (p_{T,2} - p_{T,1})/2, \quad p_T = (p_{T,2} + p_{T,1})/2,\\
w &= \int_0^{980}\int_{-p_T}^{p_T} f(x,y_1,y_2)g(p_T - z,x,y_1)g(p_T + z,x,y_2)dxdz,\\
\langle z\rangle &= \int_0^{980}\int_{-p_T}^{p_T} f(x,y_1,y_2)g(p_T - z,x,y_1)g(p_T + z,x,y_2)zdxdz,\\
\langle z^2\rangle &= \int_0^{980}\int_{-p_T}^{p_T} f(x,y_1,y_2)g(p_T - z,x,y_1))g(p_T + z,x,y_2)z^2dxdz,\\
\sigma^2_{A_{ideal}} &= (\sigma_1^2+\sigma_2^2)/(4p_T^2), \quad \sigma^2_{A_{exp}} = \langle z^2\rangle/(wp_T^2) - \langle z\rangle^2/(w^2p_T^2),\\
\sigma_A &= \sigma_{A_{\rm meas}}\cdot\frac{\sigma_{A_{ideal}}}{\sigma_{A_{exp}}} = \sigma_{A_{\rm meas}}k_{\rm bias},
\end{aligned} \tag{7.25}$$

where $f(p_T^{\rm ptcl}, y_1, y_2)$ is the dijet p_T spectrum, $g(p_T^{\rm reco}, p_T^{\rm ptcl}, y)$ is the Δp_T distribution from MC truth and $A_{\rm meas}$ is the dijet asymmetry measured from data. The resolutions σ_1 and σ_2 are the RMS of $g(p_T^{\rm reco}, p_T^{\rm ptcl}, y)$ at $y = y_1$ and $y = y_2$, respectively. The p_T resolution in data is worse than in MC truth, but both $\sigma_{A_{\rm ideal}}$ and $\sigma_{A_{\rm exp}}$ are scaled by the same factor and the difference cancels out to leading order in the ratio. The impact of the bias correction is negligible in CC, ICR and at low p_T, but grows up to 10% at the highest p_T in EC, where the cross section falls steepest and causes the punch-through tails to largely disappear in the measured asymmetry.

7.7 Final result

In summary, the corrected jet p_T resolution is given by

$$A_{\rm ref} = \frac{p_{T,2}-p_{T,1}}{p_{T,2}+p_{T,1}}, \quad |y_{1,2}|<0.8 \tag{7.26}$$

$$A = \frac{p_{T,2}-p_{T,1}}{p_{T,2}+p_{T,1}}, \quad |y_2|>|y_1|, |y_1|<0.8 \tag{7.27}$$

$$\frac{\sigma_{p_T}}{p_T} = \sqrt{k^2_{\rm soft}(4(k_{\rm bias}A)^2 - 2(k_{\rm bias,ref}A_{\rm ref})^2) - \sigma^2_{\rm MC}}, \tag{7.28}$$

where the measured asymmetry A is corrected for soft radiation $k_{\rm soft}$, particle level imbalance $\sigma_{\rm MC}$ and asymmetry bias $k_{\rm bias}$. The results are statistically consistent with the slightly simpler approach

$$\tilde{A} = \frac{p_{T,2}-p_{T,1}}{p_{T,2}+p_{T,1}}, \quad |y|_{\rm bin,min}<|y_{1,2}|<|y|_{\rm bin,max} \tag{7.29}$$

$$\frac{\sigma_{p_T}}{p_T} = \sqrt{2(\tilde{k}_{\rm soft}\tilde{k}_{\rm bias}\tilde{A})^2 - \tilde{\sigma}^2_{\rm MC}}, \tag{7.30}$$

where the corrections $\tilde{k}_{\rm soft}$, $\tilde{k}_{\rm bias}$ and $\tilde{\sigma}_{\rm MC}$ have been derived for the corresponding topology. However, the former method benefits from much higher statistics which allow the data-based measurement to be made up to $|y|<2.4$ with relatively small statistical uncertainty.

The resolution results are also consistent with the resolution measurements from the γ+jet sample

$$\frac{\sigma^{\gamma+\rm jet}_{p_T}}{p_T} = \frac{\sqrt{\left(k^{\gamma+\rm jet}_{\rm soft}A_{\gamma+\rm jet}\right)^2 - P\sigma^2_\gamma - P\sigma^2_{\rm MC,\gamma+jet}\cdots}}{\sqrt{-(1-P)\sigma^2_{\rm EM} - 2(1-P)\sigma^2_{\rm MC,EM+jet}\cdots}} \\ \sqrt{-P(1-P)(\mu_{\gamma+\rm jet}-\mu_{\rm EM+jet})^2}, \tag{7.31}$$

where the measured asymmetry in the γ+jet sample with purity P is corrected for the EM+jet background peak being shifted with respect to the γ+jet component ($\mu_{\gamma+\rm jet}-\mu_{\rm EM+jet}$), for the photon and EM-jet resolutions (σ_γ, $\sigma_{\rm EM}$) and the particle level imbalance in the two different samples ($\sigma_{\rm MC,\gamma+jet}$, $\sigma_{\rm MC,EM+jet}$). These corrections amount up 40% of the p_T resolution. Due to the higher systematic uncertainties there is little benefit from combining the γ+jet sample with the dijet sample for the resolution determination to improve the fit at low p_T.

7.8 Fit of the resolution

The measured resolutions are fitted with the parametrization

$$\frac{\sigma_{p_T}}{p_T} = \sqrt{\frac{N^2}{p_T^2} + \frac{S^2}{p_T} + C^2}, \tag{7.32}$$

where N is called the noise term, S the stochastic term and C the constant term. As the names suggest, N parametrizes fluctuations due to noise and offset energy from multiple interactions, S parametrizes the stochastic fluctuations in the amount of energy sampled from the jet hadron shower and C parametrizes fluctuations that are a constant fraction of energy such as detector disuniformities or instabilities and the error on the calibration. Figure 7.9 shows an example of the resolution fit in CC.

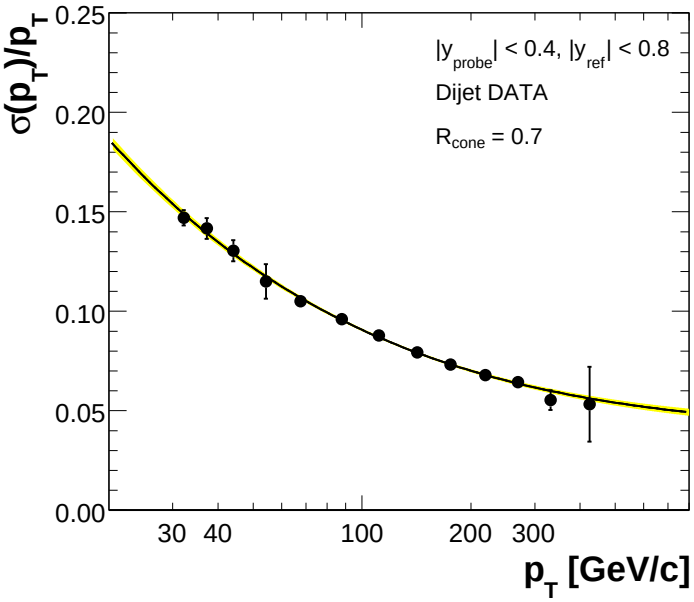

Figure 7.9: Jet p_T resolution in CC. The central fit is shown as a solid line and the fit uncertainty as a shaded band.

Noise term

The noise term is significant only at very low p_T, < 30 GeV/c. It is poorly constrained by data fits alone, with an uncertainty in the order of a couple of GeV/c. To better constrain the noise term, its value is fixed to the average

fit from MC truth, 2.07 GeV/c, with ± 1 GeV/c taken as uncertainty. This agrees with the offset estimated from data that can be used as an estimate for N.

The size of the noise term estimated from offset in data is in the order of a couple of GeV/c. This estimate uses an average of about 0.5 additional interactions with 0.6 GeV/c of offset p_T per interaction, 0.3 GeV/c from noise and multiplying the total by response ($\sim \times 2$ at $p_T \approx 20$ GeV/c) and zero-suppression bias ($\sim \times 1.5$) to give 1.8 GeV/c. In addition, the RMS of offset is assumed to be equal to the mean, which is generally true for an exponentially falling distribution. The almost linear dependence of N on the number of multiple interactions, *i.e.* the amount of offset, is qualitatively confirmed with MC truth, which supports estimating the noise term by the average offset.

Stochastic term

The stochastic term is the limiting factor at low to medium p_T. It represents the statistical (=stochastic) fluctuations in the amount of measured energy and is higher for sampling calorimeters than for homogeneous ones. Each particle in the jet shower can be thought to ionize on average a given amount of atoms per unit energy while passing through the calorimeter. The stochastic fluctuations are related to the number of these ionized particles. With a simple formulation

$$\sigma_S \propto \frac{1}{\sqrt{E_{meas}}} = \frac{1}{\sqrt{RE}} = \frac{1}{\sqrt{Rp_T \cosh(\eta)}} \tag{7.33}$$

$$\Rightarrow S \propto \frac{1}{\sqrt{R\cosh(\eta)}}, \tag{7.34}$$

we get that the stochastic term S has weak p_T dependence through the response energy dependence, and we fit an effective value. The stochastic term generally decreases versus rapidity, but increases in ICR where the fraction of sampled energy is particularly low.

Constant term

The constant term C is the limiting factor at high p_T. It encompasses all the effects that are directly proportional to the jet energy. These may include some fraction of the integrated signal being lost, *e.g.* along with late-reacting neutrons, relative cell calibrations or instability. It has been proposed that

the higher constant term in Run II (RMS $\approx 6\%$, $\sigma_{\text{gauss}} \approx 5\%$ in CC) compared to Run I ($\sigma_{\text{gauss}} \approx 3\%$ in CC [4]) is primarily due to a fraction of the signal from slow neutrons being lost due to the short signal integration time.

7.9 Results

The final fit results are shown in Fig. 7.10 and summarized in Fig. 7.11. The fit parameters are provided in Table 7.3. The resolutions in CC and EC are comparable due to the similar composition of the calorimeter, with the resolutions slightly better at low p_T in EC due to the factor $1/\cosh\eta$ for S in Eq. 7.34. The ICR resolutions are up to 50% worse than CC resolutions due to lower and less stable response and non-uniform detector structure in ICR.

Table 7.3: Parameters of the RMS fits versus p_T for data.

	N(oise)	S(tochastic)	C(onstant)
$\lvert y\rvert < 0.4$	2.07	0.703	0.0577
$0.4 < \lvert y\rvert < 0.8$	2.07	0.783	0.0615
$0.8 < \lvert y\rvert < 1.2$	2.07	0.888	0.0915
$1.2 < \lvert y\rvert < 1.6$	2.07	0.626	0.1053
$1.6 < \lvert y\rvert < 2.0$	2.07	0.585	0.0706
$2.0 < \lvert y\rvert < 2.4$	2.07	0.469	0.0713

7.10 Test of method in Monte Carlo

The true jet p_T resolution is defined as

$$\frac{\sigma}{p_T} = \text{RMS}\left(\frac{p_T^{\text{reco}} - p_T^{\text{ptcl}}}{p_T^{\text{ptcl}}}\right) \quad \text{versus} \quad p_T^{\text{ptcl}}, \tag{7.35}$$

where the reconstructed jet and particle jet are uniquely[4] matched within $\Delta R < R_{\text{cone}}/2$. The goal of the data-based resolution measurement is to estimate the equivalent resolution in data. The method itself can be tested in MC by comparing the jet p_T resolution derived from reconstructed jets

[4]Unique matching is here taken to mean that there is no other reconstructed jet within $\Delta R < R_{\text{cone}}$ from the particle jet, and no other particle jet within $\Delta R < R_{\text{cone}}$ from the reconstructed jet. This is to avoid ambiguity due to the split-and-merge procedure.

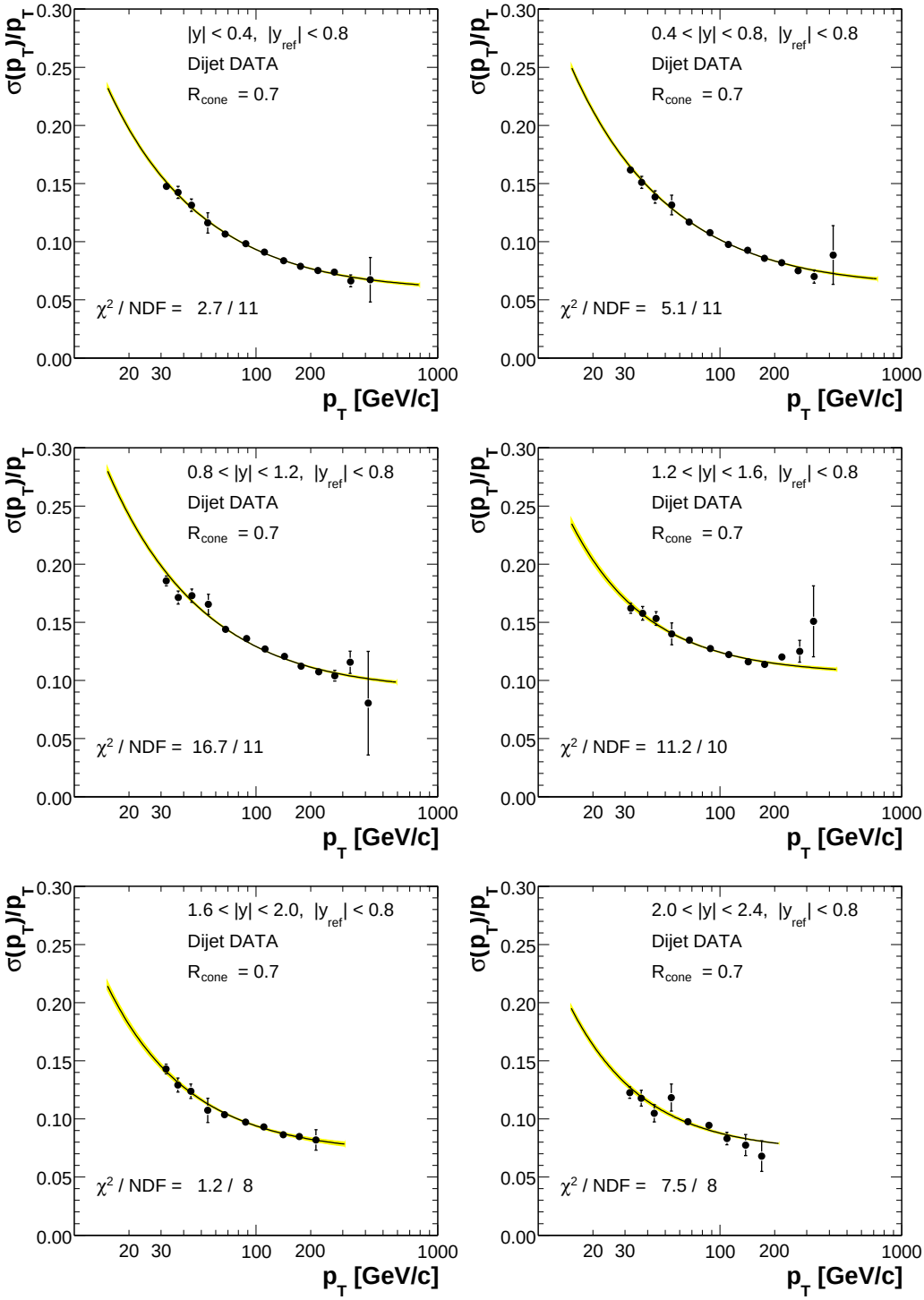

Figure 7.10: Jet p_T RMS resolution fits in data. The fit uncertainty is shown as a shaded band around the fit.

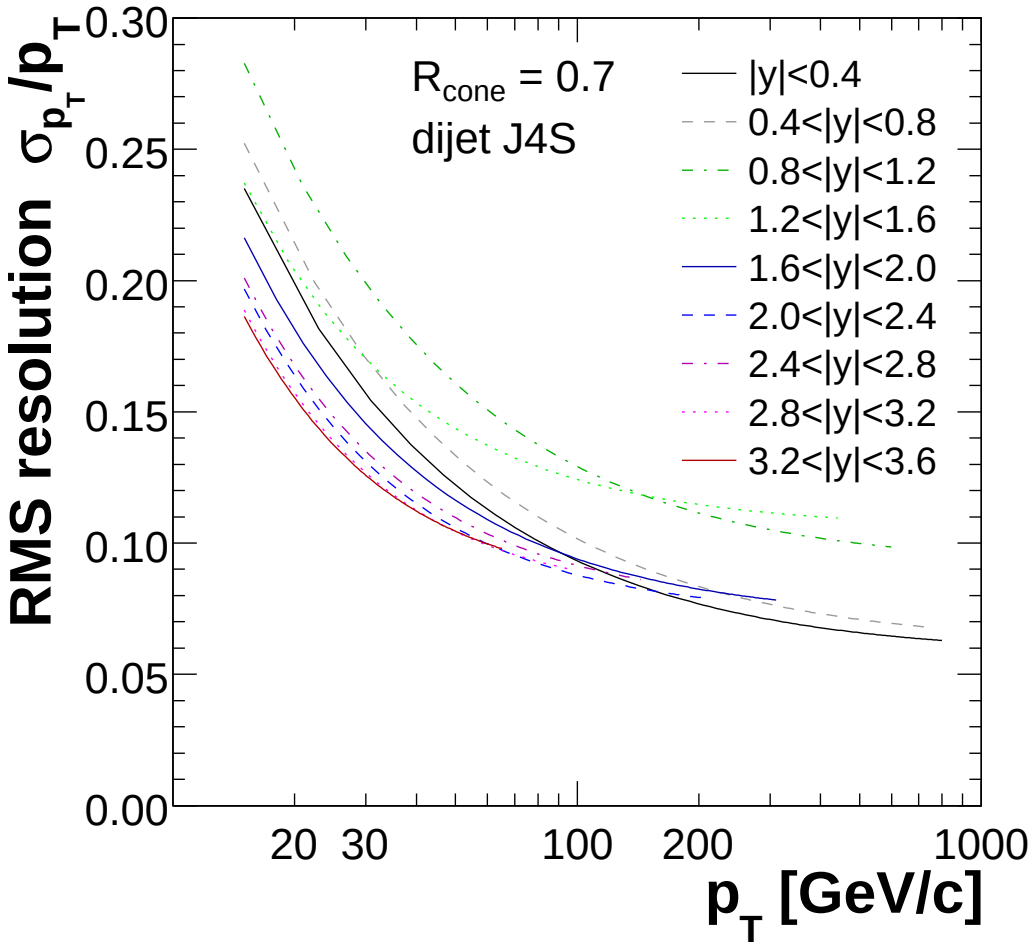

Figure 7.11: Summary of jet p_T RMS resolution fits in data.

alone to the MC truth in the same sample. The method biases are small when all the resolutions are measured using their RMS values, as shown in Fig. 7.12.

The largest residuals are observed in the $0.8 < |y| < 1.2$ bin and at low p_T in the $|y| > 1.6$ region. The problems in the former bin are most likely explained by complications caused by the relatively large non-Gaussian ICR tails that are shown in Fig. 7.5(b). Their shape and magnitude are not as well known as the shape of the punch-through tails, which leads to a larger systematic uncertainty. The ICR tails are included in the analysis systematics by scaling them by a factor of two, which also accounts for possible data-to-MC differences. The latter region in EC suffers at low p_T in the reconstructed MC data from large fluctuations due to high MC weights, which complicates the closure test. The residual is not well explained and is therefore fully accounted for in the systematic uncertainties. The residual also decreases rapidly at $p_T > 50$ GeV/c and so has a relatively small impact on the analysis. The observed residuals as well as the statistical uncertainty of the reconstructed MC fit in Fig. 7.12 are added in quadrature to the total resolution uncertainty.

7.11 Resolution uncertainty

The resolution uncertainties, shown in Fig. 7.14 for CC and EC, come primarily from the statistical uncertainties in the fits and from reasonable envelope curves to cover any residuals in the fits. The systematic uncertainty is broken into components in Fig. 7.13. The total uncertainty is generally 5–8% over the full kinematic range covered by the inclusive jet cross section measurement ($p_T > 50$ GeV/c).

The noise term is varied within ± 1 GeV/c to cover luminosity dependence at low p_T, and also the fact that it is constrained to the MC truth value in the final fits. The difference between RMS and Gaussian σ is a sizeable contribution in CC, but small in ICR and EC.

Another important source of uncertainty is the MC closure test with its limited statistics in EC. The closure test has some residual at $0.8 < |y| < 1.2$ in ICR and at $p_T < 100$ GeV/c in EC so both the statistical uncertainty and the residuals are conservatively added to the total uncertainties.

In addition to the uncertainty on the RMS, ICR region is also assigned shape uncertainty whereby the ICR tails are significantly reduced ($H \to H/2$, $\kappa \to (1+\kappa)/2$, $\mu_H \to \mu_H/2$). This accounts for the possibility that JES z_{vtx}-

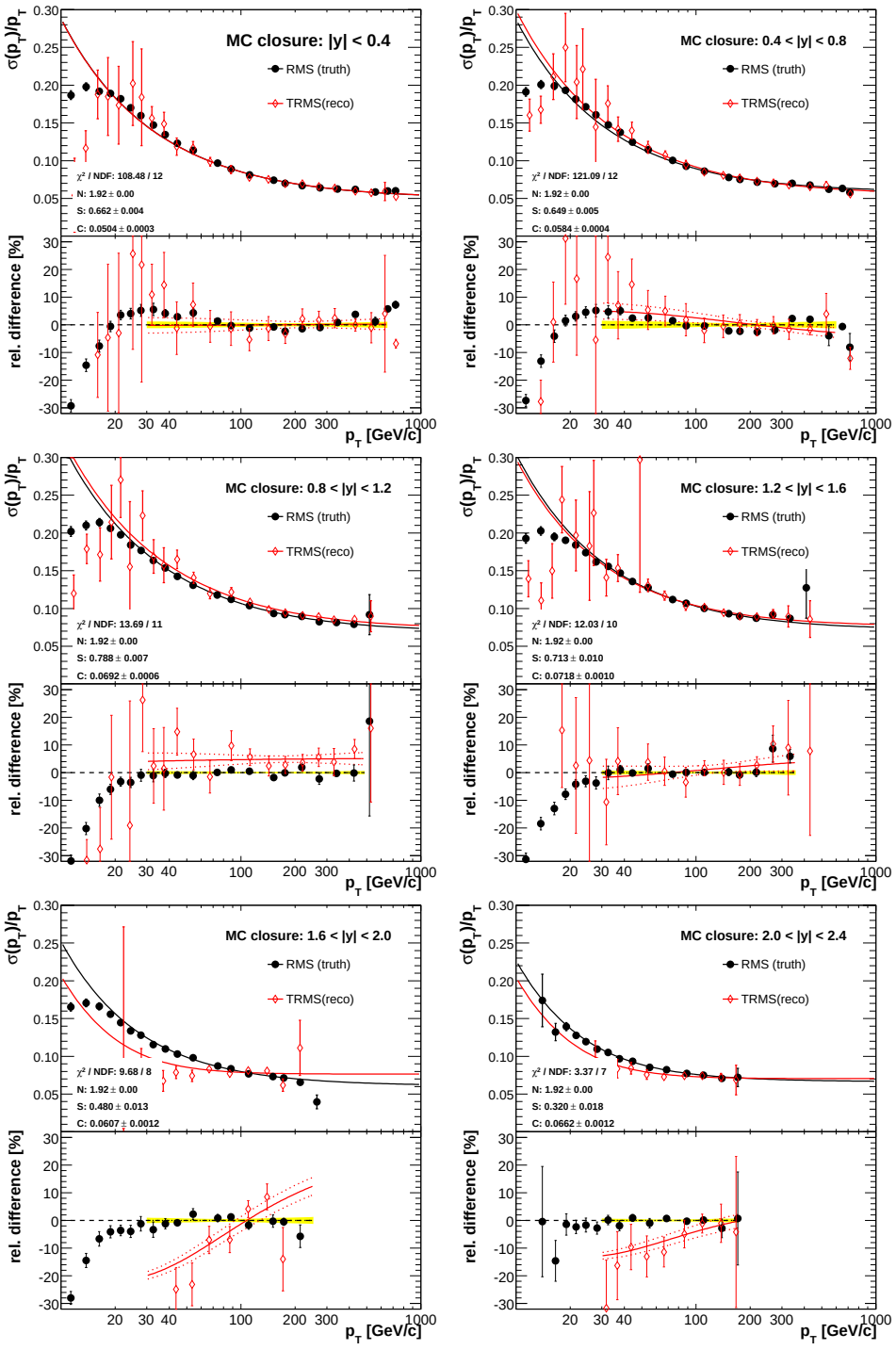

Figure 7.12: Jet p_T resolution closure in MC. The shaded band shows the fit uncertainty for MC truth, the dashed lines show the fit uncertainty for reconstructed MC. Lower plots show the ratio to the MC truth fit.

dependent calibration has reduced the tails in data. The $z_{\rm vtx}$-dependent calibration is not performed in MC due to lack of statistics and *a priori* smaller dependence.

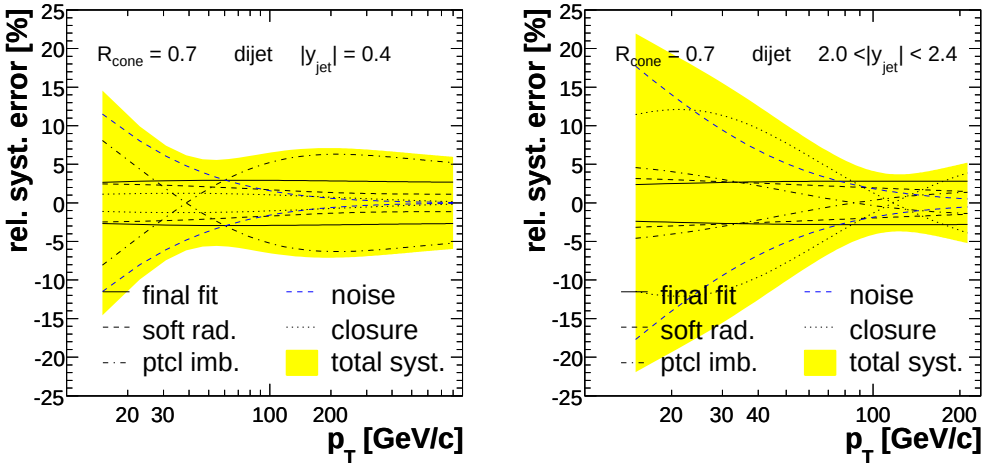

Figure 7.13: Jet p_T resolution systematic uncertainty in data at $|y| < 0.4$ and $2.0 < |y| < 2.4$.

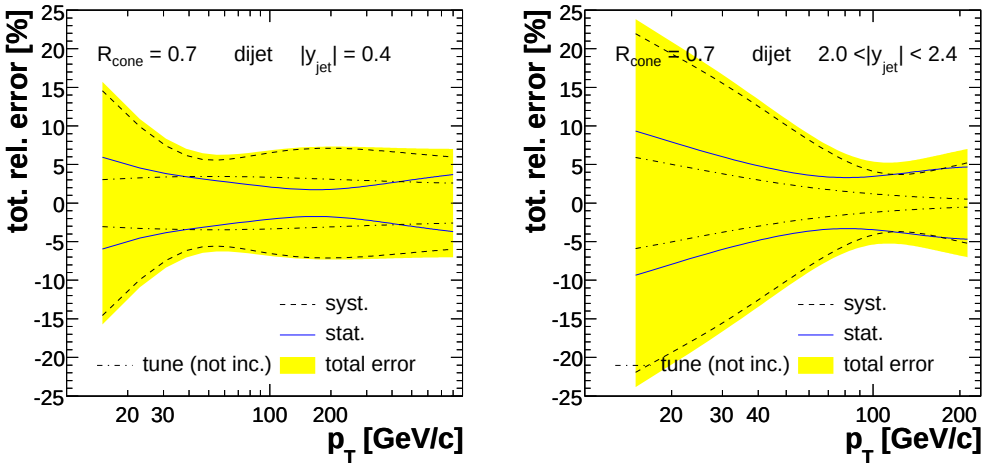

Figure 7.14: Jet p_T resolution total uncertainty in data at $|y| < 0.4$ and $2.0 < |y| < 2.4$.

7.12 Jet rapidity resolution

The rapidity resolution is a small effect which is best determined from MC. The reconstructed jets are uniquely matched to particles jets within $\Delta R < R_{\rm cone}/2$ and jets are binned in ($y_{\rm ptcl}$,$p_T^{\rm ptcl}$) to avoid resolution bias. Binning in $p_T^{\rm ptcl}$ instead of $E_{\rm ptcl}$ makes the resolution relatively flat versus $y_{\rm ptcl}$.

The $\Delta y = (y_{\rm reco} - y_{\rm ptcl})$ distributions have non-Gaussian tails, with the RMS(Δy) up to twice that of the Gaussian σ_y. The rapidity resolutions are determined as the RMS values, with the total rapidity unfolding later conservatively taken as a small systematic.

The rapidity resolution determined in the bin $60 < p_T^{\rm ptcl} < 80$ GeV/c is shown in Figure 7.15. The resolution varies smoothly versus rapidity in CC and EC, but has a sharp transition in ICR. The shape is similar in other $p_T^{\rm ptcl}$ bins, but the transition region moves toward CC at high p_T. The energy dependence is well described by a powerlaw $\sigma_y = \sigma_0 + \sigma_1 p_T^m$, with the dependence separately parametrized for CC, ICR and EC.

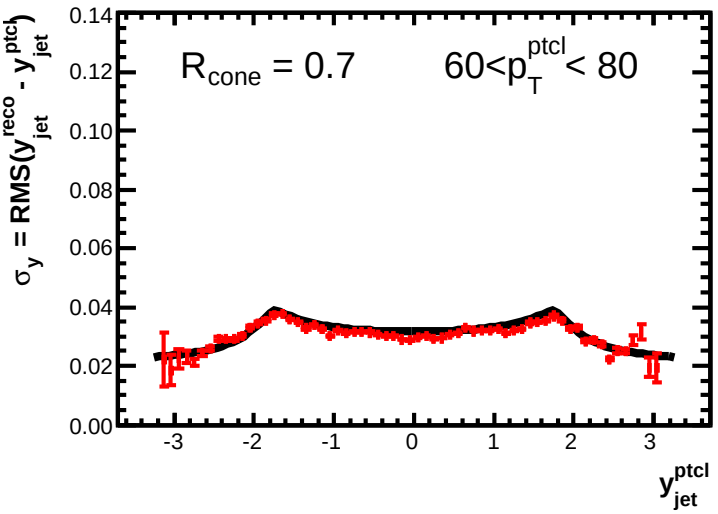

Figure 7.15: Rapidity RMS resolution fit at 60 GeV/$c < p_T^{\rm ptcl} < 80$ GeV/c.

The rapidity bins are wide compared to the rapidity resolution so that bin-to-bin migration only takes place at the bin edges. It is important that the resolution is smoothly parametrized versus rapidity so that the correct resolutions are used at the bin edges. The rapidity resolution is parametrized with a 2D function

$$\sigma_y \;=\; \sigma_{\rm CC} + (\sigma_{\rm ICR} - \sigma_{\rm CC})\frac{\cosh^2 y - 1}{\cosh^2 \mu - 1}, \quad \text{if} \quad |y| < \mu, \tag{7.36}$$

$$\sigma_y = \sigma_{\rm EC} + (\sigma_{\rm ICR} - \sigma_{\rm EC})\frac{\tanh^{-2} y - 1}{\tanh^{-2} \mu - 1}, \quad \text{if} \quad |y| \geq \mu, \tag{7.37}$$

$$\tag{7.38}$$

whose parameters are given in Table 7.4. The rapidity resolution fit is shown in Fig. 7.16.

Table 7.4: Rapidity resolution fit parameters.

Parameter	p_0	p_1	p_2	function
$\sigma_{\rm cc}$	0.007976	1.217	-0.9394	$p_0 + p_1 \cdot p_T^{p_2}$
$\sigma_{\rm icr}$	0.004265	0.9231	-0.7806	$p_0 + p_1 \cdot p_T^{p_2}$
$\sigma_{\rm ec}$	0.01197	1.324	-1.101	$p_0 + p_1 \cdot p_T^{p_2}$
μ	1.685	-0.2	—	$p_0 + p_1 \log(0.01 \cdot p_T)$

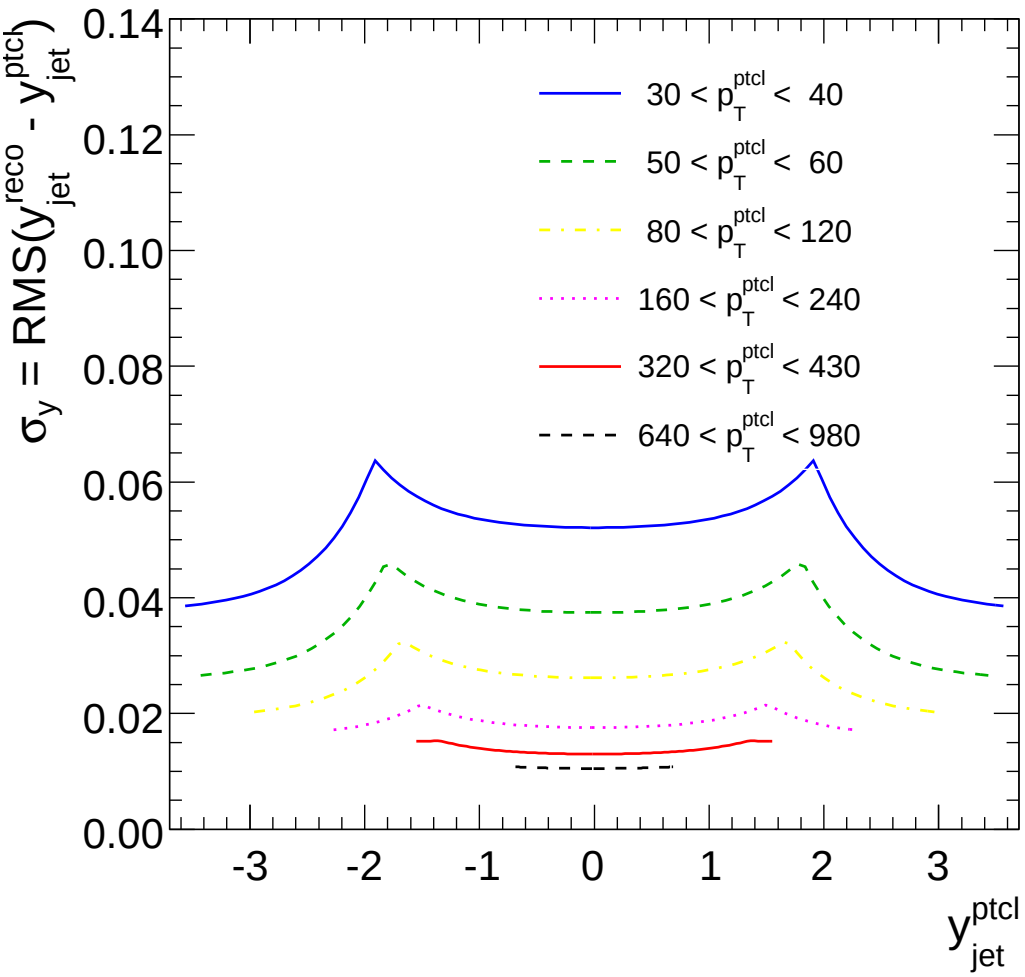

Figure 7.16: Rapidity RMS resolution fits in MC.

Chapter 8

Data analysis

8.1 Overview

This chapter discusses the experimental cuts, efficiency corrections and p_T spectrum unfolding needed to produce a measurement of the inclusive jet cross section. The data-based measurement is compared to the predictions of perturbative QCD, including corrections for non-perturbative effects, and the agreement between data and theory is discussed. The uncertainty correlations are studied in detail and used in a comparison of data and theory.

Sections 8.2 and 8.3 describe the event and jet quality cuts, and the derivation of their efficiencies. These match the event and jet quality definitions used in the jet energy scale determination and the jet p_T resolution derivations to obtain a maximum consistency of the results. The single-jet trigger turn-ons and trigger efficiencies are discussed in Sec. 8.4 along with the other practical issues in combining jet p_T spectra from different trigger samples. The final step in the analysis is the unfolding of the jet cross section, described in Sec. 8.5. The effects of p_T and rapidity resolution are considered separately using an ansatz-based iterative approach. The theoretical predictions for the cross section are discussed in Sec. 8.8. The fully corrected cross section results are presented and compared to theory in Sec. 8.10. A detailed statistical analysis of the consistency between data and theory including uncertainty correlations of both experimental and theoretical uncertainties is given in Sec. 8.11. Finally, the methods used in the analysis are tested for closure with the Monte Carlo simulation in Sec. 8.12.

8.2 Event cuts

The event quality cuts fall into three distinct categories having different goals. The vertex quality cuts are designed to select events with a high quality vertex near the calorimeter center to improve the jet p_T and y measurements and to reduce the number of events with the jets assigned to a wrong vertex. The missing-E_T cut is designed to primarily remove the cosmic ray events at high p_T. About 3% of the events suffer from calorimeter problems such as sparks in the calorimeter, high level coherent electronics noise or detector failures. Such events have been flagged by the data quality group with calorimeter quality flags and are removed from the analysis.

8.2.1 Calorimeter event quality flags

The calorimeter event quality flags in Run IIa include flags for coherent pedestal shifts in the analog-to-digital converter ("coherent noise"), parts of the calorimeter not being read out ("missing crate"), external calorimeter noise often occurring at noon ("noon noise") and external noise often associated with welding and affecting a full ring in ϕ ("ring of fire"). A detailed description of these problems can be found in Ref. [137]. The coherent noise flag is on for 5.5% of the triggered events, and the other flags for 0.9% of the events. Some of the calorimeter event quality flags overlap with the 17.2% of bad events removed by the run or luminosity block number and the fraction of events removed by the flags alone is 4.5%. The noise often causes additional firing of the triggers and creates fake jets that can present a significant background if the real signal is small. As an example, 40% of the events triggered by JT_125TT and having a jet candidate with $p_T > 400$ GeV/c before any quality cuts are bad events with coherent noise.

Unlike bad runs and luminosity blocks, the calorimeter event quality flags do not directly enter the luminosity calculation and need to be considered as an additional inefficiency. The rate at which calorimeter problems occur is independent of physics and can be estimated using an independent sample whose trigger is known to be unaffected by the calorimeter problems. The best estimate for the true inefficiency is provided by the fraction of events removed by the calorimeter quality flags in the zero bias sample. The ZB trigger fires at a constant rate independent of what happens in the calorimeter so the coincidence rate of problematic events in the ZB sample can be used as an estimate of the inefficiency. The calorimeter quality flag inefficiency has been calculated to be 3.2 ± 1.0% for the Run IIa trigger lists v12–v14

using results in [138]. The 1.0% uncertainty covers the time and luminosity variation of the inefficiency between 2–4% that affects different triggers at slightly different amounts. It is believed that there is strong correlation between the L2 accept rate and the rate at which coherent noise occurs in the calorimeter, which causes the strong time dependence observed in [138].

8.2.2 Vertex quality cuts

The vertex selection is based on three simple cuts

- $n_{\text{vtx}} \geq 1$
- $|z_{\text{vtx}}| < 50$ cm
- $n_{\text{tracks}} \geq 3$

The first cut is quite obvious, because a vertex is needed to properly reconstruct jet p_T and y. The vertices are ordered in increasing probability to belong to a MB event, and the first one is selected as the primary vertex for the hard scattering.

The second cut ensures that jets originate reasonably close to the calorimeter center so that the angles of incidence for central and forward calorimeter are fairly direct. Very shallow angles lead to reduced jet response due to increased path length in dead material and reduced performance of the liquid argon calorimeter. In the intercryostat region the high-$|z_{\text{vtx}}|$ jets can hit cracks in the detector and leak energy. These effects degrade the p_T resolution for high-$|z_{\text{vtx}}|$ jets. Cutting at $|z_{\text{vtx}}| < 50$ cm also keeps the vertex in the high efficiency tracking region. The tracking efficiency drops rapidly at $|z_{\text{vtx}}|$ >40–60 cm and the high-$|z_{\text{vtx}}|$ vertices are found with lower efficiency than the central ones.

The third cut is used to select reliably reconstructed vertices. The minimum number of tracks needed to reconstruct a vertex is 2, but such vertices are at risk of being formed from fake high-p_T tracks and could overtake the true primary vertex. This is especially problematic at high instantaneous luminosity, as has been observed in Tevatron Run IIb. For inclusive jet events at $p_T > 50$ GeV/c the track multiplicities are high, averaging 23–30 tracks per vertex as shown in Fig. 8.1, compared to about 5–8 on average for minimum bias interactions. This cut removes about 0.4% of the leading vertices together with $n_{\text{vtx}} \geq 1$.

It is likely that many of the events removed by $n_{\text{tracks}} \geq 3$ and $n_{\text{vtx}} \geq 1$ have the true primary vertex at $|z_{\text{vtx}}| > 40$ cm where it is not reconstructed due to lower tracking efficiency. About 50% of the events in the Run IIa data have minimum bias vertices that can replace the missing primary vertex, but the $n_{\text{vtx}} \geq 3$ cut removes about 30% of these. The observed 0.4% inefficiency in the number of tracks and vertices is consistent with about 0.6% of the primary vertices not being reconstructed, but 0.2% being replaced by a minimum bias vertex with $n_{\text{tracks}} \geq 3$. The efficiency for $n_{\text{tracks}} \geq 3$ and $n_{\text{vtx}} \geq 1$ is estimated as 0.996 ± 0.004, being flat in p_T and rapidity.

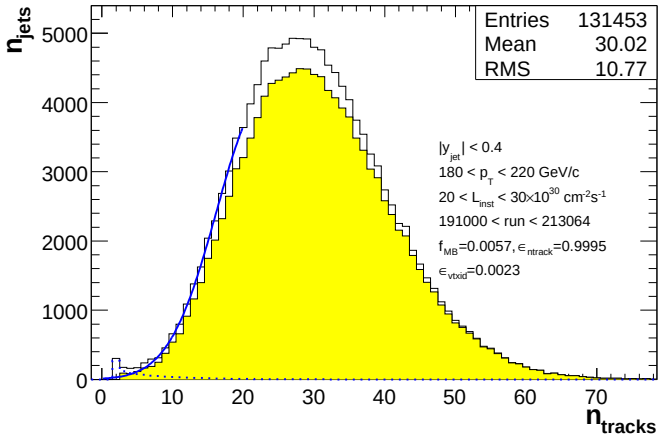

Figure 8.1: Distribution of jets with n_{tracks} tracks associated to the primary vertex. The shaded area shows the fraction of jets passing all vertex ID cuts. The solid line shows Gaussian fit to $8 \leq n_{\text{tracks}} \leq 20$.

The leading inefficiency comes from the $|z_{\text{vtx}}| < 50$ cm cut, which is on average about 7% inefficient compared to the 0.4% inefficiency of the other vertex cuts. The best estimate of the efficiency of the 50 cm cut is provided by a detailed study on the shape of the luminous region provided in Ref. [136]. The longitudinal shape of the luminous region is approximated by the expression

$$\frac{d\mathcal{L}(z)}{dz} = N_p N_{\bar{p}} \frac{1}{\sqrt{2\pi}\sigma_z} \frac{e^{-(z-z_{0z})^2/2/\sigma_z^2}}{4\pi\sigma_x(z)\sigma_y(z)}, \tag{8.1}$$

where the overlap of the proton and antiproton beam bunches having N_p and $N_{\bar{p}}$ particles is described with a Gaussian distribution of width σ_z in the z direction, with a possible offset z_{0z} relative to the nominal interaction point. The $\sigma_x(z)$ and $\sigma_y(z)$ represent the transverse size of the beam spot and vary

as a function of z:

$$\sigma_T^2(z) = \frac{1}{6\pi\gamma}\epsilon_T\beta_T^* \left(1 + \frac{(z - z_{0T})^2}{\beta_T^{*2}}\right). \tag{8.2}$$

Here T is either x or y, γ is the relativity factor of the beam particles, and z_{0T} is the minimum of the β function in the direction T. The emittance ϵ_T and beta parameter β_T^* describe the beam optics near the interaction point.

The provided parametrizations are integrated to yield

$$\epsilon_{|z_{\rm vtx}|<50\ {\rm cm}} = \frac{\int_{-50\ {\rm cm}}^{50\ {\rm cm}} f(z_{\rm vtx}, {\rm run}, \mathcal{L}) dz_{\rm vtx}}{\int_{-100\ {\rm cm}}^{100\ {\rm cm}} f(z_{\rm vtx}, {\rm run}, \mathcal{L}) dz_{\rm vtx}}, \tag{8.3}$$

where the limits of integration in the denominator come from the cuts used in the luminosity determination. The parametrizations have been provided as a function of the instantaneous luminosity for several run ranges, with the efficiency varying by up to 6% as a function of luminosity and up to 5% as a function of the run number. The efficiency correction is applied on a per event basis.

The run number dependence reflects changes in the beam optics that have affected the beam shape such as a change in the β^* [136]. The instantaneous luminosity dependence is primarily caused by the beam heating up during the store. This leads to the beam bunches and the luminous area to be longer at the end of the store (low instantaneous luminosity) than at the injection (high instantaneous luminosity). The results are shown in Fig. 8.2. The average efficiency is 93%, with variation from 89% to 95%.

The 50 cm cut efficiency from the luminous area shape is cross-checked in the analysis by calculating the fraction of jets removed from the inclusive jet sample in each p_T and y bin by the $|z_{\rm vtx}| < 50$ cm cut. The results are generally consistent with the luminous area shape, but show about 1–2% lower efficiency. This is explained by the jet p_T resolution being worse for jets at $|z_{\rm vtx}| > 50$ cm, where a 10% degradation in the resolution is enough to increase the observed number of jets by about 1%. No appreciable p_T or y dependence is observed in the cross-check, which is expected because the true vertex distribution does not depend on the jet rapidity or p_T.

The vertex reconstruction efficiency could be lower for very forward jets, as the tracking efficiency drops with increasing rapidity. The reduced tracking efficiency should also show up as a decrease in the $n_{\rm tracks} \geq 3$ cut efficiency. However, no significant additional inefficiency is observed for the forward region when the fraction of jets cut is broken up in rapidity intervals. The

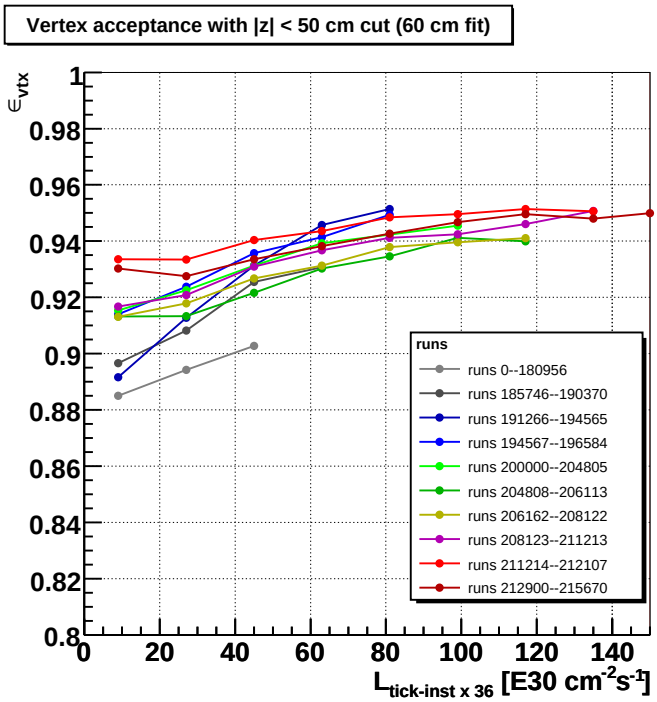

Figure 8.2: Vertex acceptance with $|z_{\rm vtx}| < 50$ cm cut calculated from the parametrized shape of the luminous area in minimum bias events.

average number of tracks for vertices with forward jets is also only slightly decreased compared to central rapidities. These observations are motivated by simple cross section and topology arguments for inclusive jet events: The vertex reconstruction is most likely to fail if all the jets in the event go in the forward direction on the same side of the calorimeter as the vertex ($y \cdot z_{\rm vtx} > 0$) so that they all fall outside the tracking acceptance (see Fig. 4.8 for the SMT fiducial region). The cross section for both leading jets to go to the forward direction is about 10% of central-forward combinations, and half of these are "forward-backward". For the remaining "forward-forward" events, which make roughly 5% of the total, the vertexing efficiency is reduced by less than 10% on average so the expected change in the efficiency is less than 0.5%, consistent with observations. These same arguments may not hold for other more exclusive topologies, of course.

The overall vertex efficiency correction is quite precisely determined using the parametrized vertex distribution discussed earlier, but the shape of this distribution also contains some uncertainty. The uncertainty in this shape is estimated by the full difference between fits to the vertex distribution at $|z_{\rm vtx}| < 60$ cm (default) and $|z_{\rm vtx}| < 40$ cm. Both of these fits are provided

in Ref. [136]. The resulting uncertainty is 0.5%.

The possibility of a lower vertex reconstruction probability and a higher $n_{\text{tracks}} \geq 3$ inefficiency for the forward region is covered by an additional 0.5% uncertainty at $|y| > 1.6$. The size of this uncertainty is dictated by the limited statistical precision of the tests used to constrain these inefficiencies in the forward region.

In conclusion, the vertex quality cut inefficiency is dominated by the cut $|z_{\text{vtx}}| < 50$ cm, which has a time and luminosity dependent efficiency varying between 0.885–0.950. The $n_{\text{vtx}} \geq 1$ and $n_{\text{tracks}} \geq 3$ cut efficiency is 0.996. The average vertex cut efficiency for the full sample is between 0.910–0.924 depending on the trigger, generally lower for low p_T triggers. The total vertex uncertainty is composed of the uncertainty in the luminous region shape (0.5%), uncertainty in the overall $n_{\text{vtx}} \geq 1$ and $n_{\text{tracks}} \geq 3$ efficiency (0.4%) and an additional uncertainty to cover for the possibility of increased inefficiency in the forward region (0.5% at $|y| > 1.6$).

8.2.3 Missing E_T cut

The missing-E_T cut is devised to remove fake jets produced by cosmic ray showers. The cross section for cosmic ray events falls much less steeply versus energy than the inclusive jet cross section, and cosmic ray showers are frequently triggered in the DØ calorimeter at energies well beyond 1 TeV. The cross section for cosmic ray events becomes comparable to or higher than the high-p_T jet cross section at $p_T > 400$ GeV/c. Fortunately, the cosmic ray events have several distinct characteristics that can be used to efficiently remove them from the measurement.

The cosmic ray showers come from the outside and typically deposit most of their energy on one side of the calorimeter, producing high missing-E_T ($\not\!\!E_T$) that peaks at $p_{T,\text{lead}}/\not\!\!E_T \approx 1$ as shown in Fig. 8.3. In event displays the cosmic ray events can be identified by energy deposits in the muon detectors, large, spread-out jets on one side of the calorimeter and often missing tracking information because the cosmic ray events are out of time with the bunch crossings and tracker read-out.

The cosmic ray events can be rejected by requiring tracks to be matched to the jets because the cosmic ray events are rarely in time with the tracking read-out. However, this cut would also remove legitimate jets, particularly in the forward region where the tracking efficiency is lower. The cosmic ray events can also be efficiently removed using calorimeter information only, such as the missing-E_T, so this information is used instead.

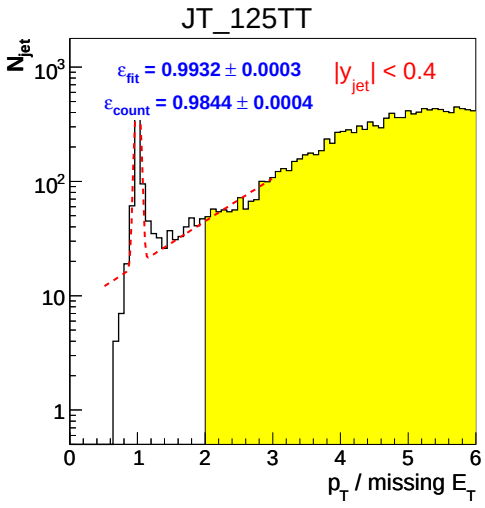

Figure 8.3: Peak in $p_{T,\text{lead}}/\not\!\!E_T$ produced by cosmic ray background. The shaded region shows jets passing the cut on missing-E_T.

The inclusive jet events have normally $\not\!\!E_T \approx 0$. Occasional small amounts of true missing-E_T is generally a product of neutrinos being produced inside jets, especially in decays of heavy flavor jets. The event-by-event fluctuations in the measured energy create significantly larger missing-E_T. The fluctuations in missing-E_T are largest at low p_T where cosmic ray backgrounds are of little concern. At high p_T the jet p_T resolution is good, and cuts can be tightened for better rejection of cosmic ray backgrounds. The following cuts are used in this analysis

$$\frac{\not\!\!E_T}{p_{T,\text{lead}}^{\text{uncorr}}} < 0.7, \quad \text{if} \quad p_{T,\text{lead}}^{\text{uncorr}} < 100 \text{ GeV}/c, \tag{8.4}$$

$$\frac{\not\!\!E_T}{p_{T,\text{lead}}^{\text{uncorr}}} < 0.5, \quad \text{otherwise.} \tag{8.5}$$

The $\not\!\!E_T$ thresholds are several times higher than the RMS of the $\not\!\!E_T$ fluctuations so the efficiency of the missing-E_T cut is expected to be very high. Fitting the observed $p_{T,\text{lead}}/\not\!\!E_T$ distribution with a Gaussian peak and a smooth background gives estimates of the inefficiency at about 0.5% at high p_T and 0.2% at low p_T when the peak is subtracted from data. Estimates using the known jet resolution and energy scale for jet pairs with one jet in CC give inefficiencies of 0.1–0.3% (up to 0.5% in ICR) at $p_T = 50$ GeV/c and at the cut threshold $p_T^{\text{uncorr}} = 100$ GeV/c, with much lower inefficiencies further from the thresholds. The $\not\!\!E_T$ cut inefficiency is considered negligibly small

and is not corrected for, but the two types of estimates of the inefficiency are taken as an uncertainty.

8.3 Jet identification cuts

The Jet identification (JetID) cuts are designed to remove mostly instrumental backgrounds such as jets formed from noisy clusters and hot towers in the calorimeter, but also physical background from electrons and photons. The cuts will also be effective against jets from cosmic ray events, although they are not specifically designed for them.

The primary cuts used in the JetID are listed in [139], and repeated here for convenience

- EMF < 0.95
- EMF > 0.05, or
  EMF ≥ 0 and $0.13 > |(|\eta_{\text{det}}| - 1.25)| + \max(0, 4 \cdot (w_{\text{jet}} - 0.1))$ (narrow jets in no-EM gap), or
  EMF > 0.03 and $|(|\eta_{\text{det}}| - 1.25)| < 0.15$ (wide jets in no-EM gap), or
  EMF > 0.04 and $|\eta_{\text{det}}| > 2.5$ (forward region)
- CHF < 0.4, or
  CHF < 0.6 and $0.85 < |\eta_{\text{det}}| < 1.25$ and $n_{90} < 20$ (CH heavy region), or
  CHF < 0.44 and $|\eta_{\text{det}}| < 0.8$ (CC region), or
  CHF < 0.46 and $1.5 < |\eta_{\text{det}}| < 2.5$ (EC region)
- $E_{\text{L1}} > 80$ GeV, or
  $f_{\text{L1}} > 0.5$, or
  $f_{\text{L1}} > 0.35$ and $p_T^{\text{uncorr}} < 15$ GeV$/c$ and $1.4 < |\eta_{\text{det}}|$, or
  $f_{\text{L1}} > 0.1$ and $p_T^{\text{uncorr}} < 15$ GeV$/c$ and $3.0 < |\eta_{\text{det}}|$, or
  $f_{\text{L1}} > 0.2$ and $p_T^{\text{uncorr}} \geq 15$ GeV$/c$ and $3.0 < |\eta_{\text{det}}|$, where
  $f_{\text{L1}} = p_{T,\text{L1}} / \left(p_T^{\text{uncorr}}(1 - \text{CHF} - \text{CCMG} - \text{ECMG})\right)$.

Here EMF, CHF, CCMG and ECMG are the fractions of jet energy deposited in the electromagnetic calorimeter, coarse hadronic calorimeter, central calorimeter massless gaps and end cap massless gaps, respectively. The w_{jet} is the jet width (a measure of the energy distribution within the jet cone), and E_{L1} and $p_{T,\text{L1}}$ are the jet energy and transverse momentum seen at level 1

in the trigger system. The n_{90} is the minimal number of towers that contain 90% of the jet's energy.

The first cut is devised to remove overlap between jets and electromagnetic objects, *i.e.* electrons and photons. It is also the most inefficient cut in JetID, removing about 1% of jets. Other cuts have been optimized to yield high efficiency ($(1-\epsilon_{\rm JetID}) << 1\%$) for physical jets at all energies and in all directions.

The second cut removes jets with anomalously low EMF that could be due to *e.g.* jets being formed out of noise in the hadron calorimeter. The complicated structure of the cut is devised to keep the inefficiency low in regions of the calorimeter where the EM calorimeter coverage is lacking or is only partial.

The third cut on CHF is devised to remove noisy jets formed from energy in the coarse hadronic calorimeter where the energy resolution is poor and little energy is normally expected. In Run I this cut was also necessary to remove energy clusters produced by halo particles from the Main Ring beam pipe that ran through the upper part of the DØ coarse hadronic calorimeter. The Main Ring was disassembled after Run I and its functions were taken over by the Main Injector in Run II. However, the CHF cut continues to remove jets formed by cosmic-ray showers, which usually deposit most of their energy from outside of the calorimeter.

The last cut, the L1 confirmation, is an important cut for removing jets formed out of noise in the precision readout. The coherent noise in particular creates fake low p_T jets that usually do not pass this cut. The L1 confirmation uses a cut on the ratio of $p_T^{\rm L1}$ measured by the coarse L1 trigger system and the precision read-out energy $p_T^{\rm uncorr}$. Noise in the precision read-out shows up as a low value for $f_{\rm L1}$. To account for the fact that the L1 trigger system does not consider energy from the coarse hadronic calorimeter or the massless gaps, the $p_T^{\rm uncorr}$ is corrected for these fractions. At $E > 80$ GeV/c the L1 read-out saturates so all jets with high enough L1 energy are allowed to pass. The thresholds in ICR and EC are optimized to account for the differing jet p_T resolutions.

Figures 8.4(a)–(c) show typical distributions for the variables used in JetID cuts. The plots also show overlaid the distributions for the jets removed by the other JetID cuts. Jets passing the cut are shown shaded to indicate typical cut regions. Only a small fraction of the jets removed by one of the cuts are removed by another one so the correlations between the cuts are small.

The JetID variables, in particular the EMF, are known to correlate with JES to some extent. However, the study of jet response as a function of EMF did not find strong dependence, except at very high EMF. The average jet response at 100 GeV/c is about 0.72, but EM-like jets are known to have an average response close to 1.00 [119, 128]. Combined with a steeply falling jet cross section this response difference leads to up to a factor of five overestimate for the fraction of jets at EMF > 0.95, unless the correlation with JES is broken by not using the measured jet p_T directly for binning. For γ+jet events the substitute is the photon p_T^γ, for dijet and inclusive jet events it is the sum of recoil momenta, $p_T^{\text{recoil}} = \sum_{j \in \text{recoil}} p_{T,j}$.

8.3.1 Tag-and-probe method

The JetID cuts have been studied by the JetID group using the tag-and-probe method described in [140] that also allows to determine the reconstruction efficiency of the jets. This method uses track jets that are cone jets built using charged particle tracks instead of calorimeter energy clusters. The basic idea is to select a tag object, which in this case is a photon or a track jet associated with a good calorimeter jet, and a probe object, which is another leading track jet back-to-back with the tag at $\Delta\phi > 3.0$. Other track and calorimeter jets outside the search area of $\Delta R < 0.5$ from the probe axis are vetoed. The selection of a restrictive tag-and-probe system ensures that non-physical backgrounds are negligible and the track jet probe must be associated with a good calorimeter jet.

The reconstruction efficiency is determined as the fraction of calorimeter jets found within the search area, and the JetID efficiency is the fraction of reconstructed calorimeter jets passing the JetID cuts. The trigger bias in the dijet tag-and-probe method is avoided by requiring that the tag object can pass all the trigger levels alone[1]. This has been shown to remove all trigger bias by comparing the results from consecutive single-jet triggers, and increases available statistics significantly by making most events in the trigger turn-on region usable for the efficiency calculation. The influence of JES is removed by binning p_T in terms of the p_T^{tag} and then mapping to $\left\langle p_T^{\text{probe}} \right\rangle$.

The tag-and-probe results have been derived on three different samples, dijet, γ+jet and Z+jet, which all give quite consistent results as expected [141]. JetID efficiencies fitted to dijet tag-and-probe results are shown in Fig. 8.5.

[1]When the trigger uses multiple trigger towers at L1, it is important to require that enough of them match the tag object to fire the trigger.

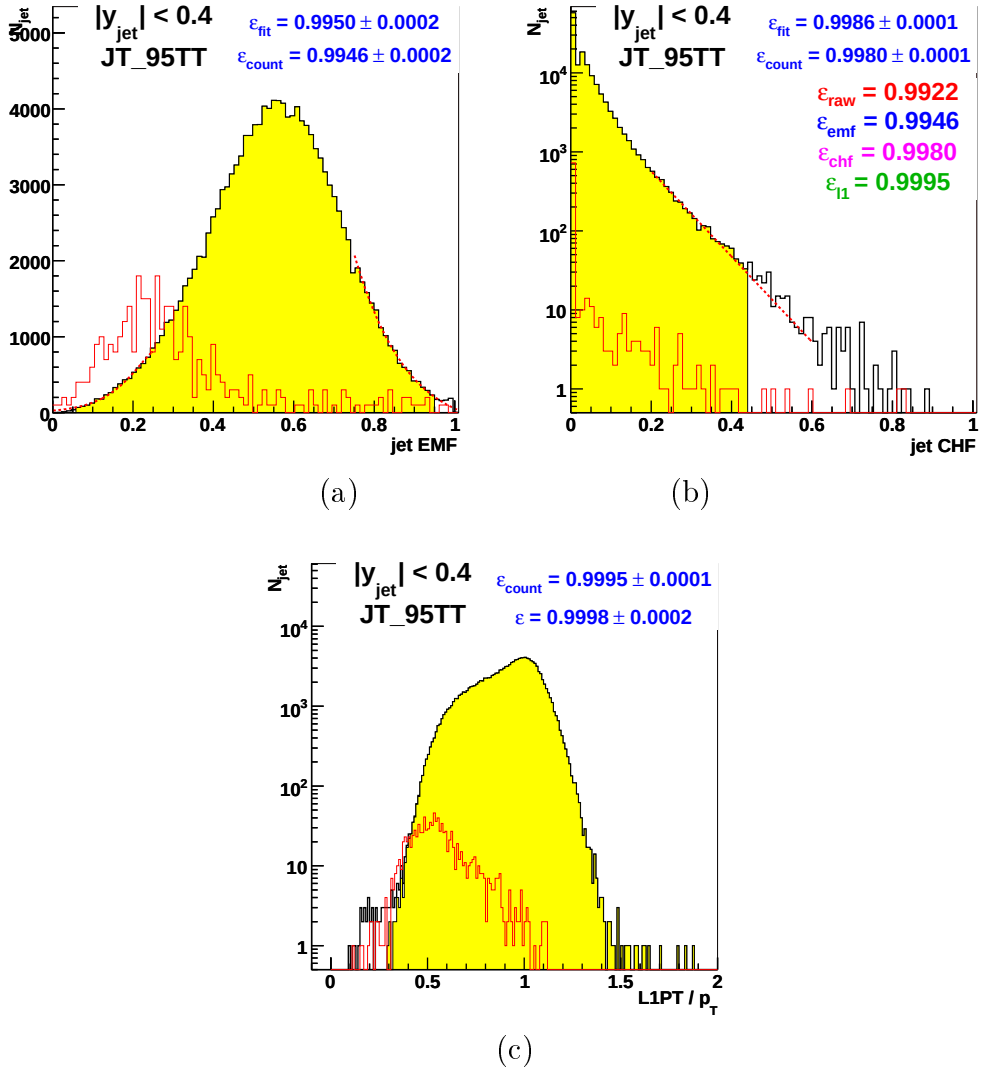

Figure 8.4: Typical distributions of the variables used in JetID cuts (a) EMF, (b) CHF, (c) L1 confirmation, in central calorimeter $|\eta_{\rm det}| < 0.4$ for 180 GeV/c $< p_T^{\rm recoil} <$ 220 GeV/c. The shaded area shows the jets surviving the cut. The dotted line shows the jets removed by the two other variables (jet EMF multiplied by 100 for visibility) to show the distributions for "bad" jets as well as the correlation between cuts. The dashed line shows the extrapolated fit into the cut region for jet EMF and jet CHF.

The fit function used is

$$\epsilon(p_T) = \epsilon_0 + a \cdot \exp(-b \cdot p_T). \tag{8.6}$$

At $p_T > 50$ GeV/c the efficiency is almost flat at 99% for all rapidity regions except $0.8 < |y| < 1.2$, where the efficiency is flat at 98%. The Z+jet results have significantly lower statistics and are not included on the plot.

8.3.2 distribution method

The tag-and-probe results are verified by calculating the fraction of events removed by the JetID cuts in dijet and inclusive jet samples for each JetID variable distribution, also shown in Fig. 8.5. The event selection for the distribution method is similar to the tag-and-probe method, but does not have any track jet requirements. This is an important difference, because the track jet requirement can in principle bias the sample by removing jets that have a high π^0 content. Such jets are expected to have a low number of tracks because π^0's immediately decay to photons, but also show a high EMF. The EM-like jets would often fail the EMF>0.95 cut and removing them could bias the average JetID efficiency up. The influence of JES is removed in the distribution method by binning in terms of p_T^{recoil} and then mapping to $\left\langle p_T^{\text{probe}} \right\rangle$.

The main concerns for the distribution method have been the possible presence of backgrounds in the sample and correlations between the cuts that could lead to an overestimate of the cut inefficiencies. The fraction of jets removed by at least two JetID cuts is very small compared to the total number of jets removed so the correlations are small. The impact of the background is reduced by fitting the distributions in the "good" region for EMF and CHF and using the extrapolation to the "bad" region to estimate the inefficiency, as shown in Figs. 8.4(a)–(b). In the dijet sample the background is also naturally reduced by the requirement to have two back-to-back jets, one of which is good. The extrapolations are in good agreement with the measured distributions, indicating that the backgrounds are small. The average of the direct cut (count) and extrapolation (fit) is taken as the mean value, with the difference taken as a systematic. The L1 confirmation inefficiency is negligibly small compared to EMF and CHF inefficiencies so 50% of the non-confirmed jets are estimated as background, with 50% as a conservative uncertainty.

8.3.3 Summary

The fact the tag-and-probe and distribution methods and different samples agree well has allowed the determination of the JetID inefficiency with sub-

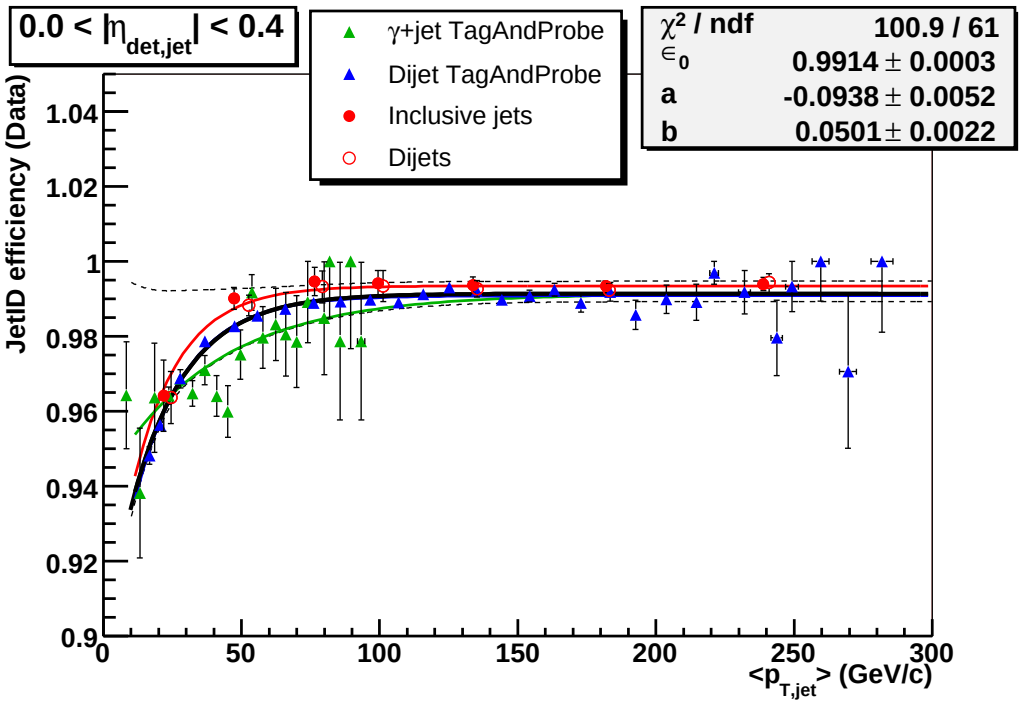

Figure 8.5: JetID efficiency in $|y| < 0.4$. The central fit (black) is done for the dijet tag-and-probe, but fits to distribution method (inclusive jets and dijets) and γ+jet tag-and-probe are shown for comparison and used for estimating the systematics shown by the dashed lines.

percent uncertainty above $p_T > 50$ GeV/c, where the p_T dependence is negligible, as shown in Fig. 8.5 for $|y| < 0.4$. The behavior is similar in other regions of the calorimeter. The efficiency at $p_T > 50$ GeV/c is 99% in all calorimeter regions except in $0.8 < |y| < 1.2$, where it is about 98%. The results have been provided for collaboration-wide use in Ref. [141].

8.4 Trigger efficiency and combined spectra

The trigger turn-ons for Run IIa single-jet triggers are described in detail in Ref. [142] by the author. This section summarizes the main observations and results. The DØ trigger system is composed of three distinct levels, L1, L2 and L3, that are described shortly below. The absolute trigger efficiencies are derived on an independent sample using data collected from muon triggers. The trigger turn-ons and absolute efficiencies are then verified on the analysis

sample using relative trigger efficiencies. Finally, the separate triggers are combined into a continuous jet p_T spectrum.

8.4.1 Level 1, 2 and 3 triggers

The DØ trigger system is composed of three levels, dubbed L1, L2 and L3. The single-jet triggers available in Run IIa are listed in Table 4.1 along with their trigger scripts. This analysis uses trigger lists v12–v14.

The trigger efficiency is generally defined as the efficiency of recording an observable (*e.g.* event or a jet) in the presence of a trigger condition

$$\epsilon(\text{record observable}) = \frac{\#(\text{observables after trigger})}{\#(\text{observables})}. \tag{8.7}$$

For the inclusive jet cross section analysis this observable is a single jet in a bin of p_T and y

$$\epsilon(\text{jet at } p_T, y) = \frac{\#(\text{jets at } p_T, y \text{ after trigger})}{\#(\text{jets at } p_T, y)}, \tag{8.8}$$

which can be equally interpreted as the ratio of jet p_T spectra before and after trigger.

A single event contains several jets that all pass the trigger together so the trigger efficiency is really an event-wide quantity, not a jet quantity. Ideally, any of the jets in the event would fire the trigger independently. The probability of a single-jet trigger firing could then be written approximately[2] as

$$P = 1 - \prod_i (1 - P(p_T^i, y_i)), \tag{8.9}$$

where $P(p_T^i, y_i)$ is the probability of the jet i at (p_T,y) to fire the trigger independently of other jets. However, the assumption of independence from other jets is not met in Run IIa for the single-jet triggers as will be soon discussed. The quantity $P(p_T^i, y_i)$ is referred to as a jet trigger matched efficiency. It is the trigger efficiency for a single jet in the absence of any other jets in the event and can be reconstructed from data by matching all trigger objects to a given jet.

The jet trigger matched efficiencies can be further analyzed by breaking the efficiency into components for different trigger levels

$$P(p_T^i, y_i) = P_{L1}(p_T^i, y_i) P_{L2}(p_T^i, y_i | L1) P(p_T^i, y_i | L1 \& L2). \tag{8.10}$$

[2]The probability of noisy calorimeter towers and other non-jet objects to fire the single-jet triggers is considered very small and is neglected here.

The probabilities for Level 2 and Level 3 are now conditional, *i.e.* the probability of a jet passing higher trigger levels will depend on it having passed the previous looser trigger levels. This break-up is useful because the independent sample used to measure the trigger efficiencies and turn-ons has very few events with Level 3 on-line jet trigger objects stored due to the high prescales applied on jet triggers at Level 1. If the event does not pass the prescale, only the L1 on-line trigger objects are stored for later offline reconstruction of the L1 trigger condition.

The relatively well-behaved Level 3 turn-on can be fitted even with low statistics. The L1 turn-on is much slower and in many cases still slightly inefficient when the Level 3 has already fully turned on. The higher statistics at L1 significantly improve the fit to the turn-on shape and allow the accurate determination of residual inefficiencies near or at the trigger efficiency plateau.

At this point the assumptions underlying Eq. 8.9 need to be revisited: the jets cannot be assumed to independently fire the trigger at Level 1. This is because the Run IIa Level 1 trigger fires on individual trigger towers. Whenever multiple trigger towers are required, these often come from separate jets.

Let us do a simple case study to make the point and look at the trigger term CJT(3,5) that requires three L1 towers with $E_T > 5$ GeV. This term is used *e.g.* in trigger JT_95TT version 17 in v14 trigger lists. The jet trigger matched efficiency for L1 at $p_T^{\text{uncorr}} = 100$ GeV/c is $P_1 = 0.67$, as shown in Fig. 8.6(a). The probability for a typical dijet event with two balanced jets both at $p_T = 100$ GeV/c to fire the trigger, assuming uncorrelated triggers, is then by Eq. 8.9

$$P_{\text{dijet}} = 1 - (1 - P_1) \cdot (1 - P_1) \approx 0.891. \tag{8.11}$$

The fraction of events passing the reconstructed[3] L1 trigger is shown in Fig. 8.6(b). The actual event efficiency is almost 100% at $p_T = 100$ GeV/c.

The Eq. 8.11 above completely ignores the cases where two of the towers comes from one jet and the third one from another jet. The probability for a single jet to fire a looser CJT(2,5) term is shown in Fig. 8.6(c). This probability alone is $P_{(2,5)} = 0.92$, already higher than the event efficiency P_{dijet} obtained above. The single trigger tower condition for the other jet is a very loose CJT(1,5), which has $P_{(1,5)} = 1.00$. Considering the possibility

[3]Only a few events pass the L1 single-jet trigger due to the high prescales, but the full L1 trigger tower information is stored for recorded events and can be used to reconstruct the L1 trigger offline.

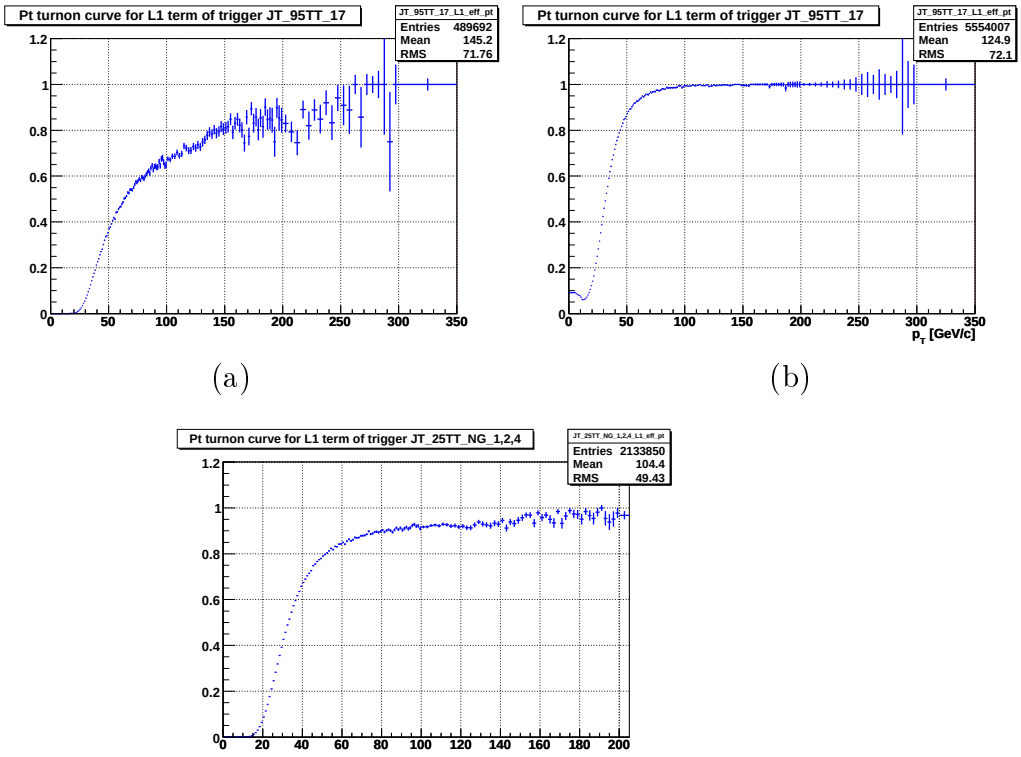

Figure 8.6: Examples of trigger efficiencies at Level-1: (a) CJT(3,5) for a single jet with trigger matching; (b) CJT(3,5) for the whole event; (c) CJT(2,5) for a single jet with trigger matching. The x-axis is uncorrected jet p_T in GeV/c.

of either of the jets to fire CJT(2,5) gives

$$P_{\text{dijet}}^{cross} = 1 - (1 - P_{(1,5)}P_{(2,5)}) \cdot (1 - P_{(2,5)}P_{(1,5)}) = 0.994, \tag{8.12}$$

which agrees with Fig. 8.6(b).

For tighter term CJT(4,5) and more complicated jet topologies with multiple jets the combinatorial calculations get quite heavy. The L1 event efficiency of CJT(m,x) for an arbitrary collection of n jets can be generally expressed as

$$P_{\text{event}}(p_T^1, p_T^2, \ldots, p_T^n; y_1, y_2, \ldots, y_n) = 1 - \prod_{i_j \in [0,m], \sum_j i_j \geq m} (1 - P_{i_1} P_{i_2} \cdots P_{i_n}), \tag{8.13}$$

where the P_{i_j} for $i_j < m$ are exclusive trigger probabilities for exactly i_j trigger towers and P_{i_j} for $i_j = m$ is the inclusive trigger probability for more

than or equal to m trigger towers. These can be calculated using

$$P_k = P_{(k,x)} - P_{(k+1,x)}, \quad k \in [0, m-1], \tag{8.14}$$

$$P_m = P_{(m,x)}, \tag{8.15}$$

$$P_{(0,x)} = 1, \tag{8.16}$$

where $P_{(k,x)}$ are the matched trigger efficiencies for trigger terms CJT(k,x), as used in Eq. 8.12.

Because the Level 1 correlations prohibit the use of Eq. 8.9 to calculate the event trigger efficiency for arbitrary jet topologies, the trigger efficiency for the inclusive jet cross section is calculated as the ratio of jet p_T spectra before and after the trigger requirement using Eq. 8.8 directly. The efficiencies for different levels are still determined separately according to Eq. 8.10 to increase statistics for L1 turn-on fit. The main draw-back is that the derived efficiency curves are not directly applicable to other analyses with different topologies. As will be discussed in the next section, the average topologies of muon triggered events can also differ from those of inclusive jet events.

The trigger efficiency determination is based on analysis machinery implemented in the trigeff_cafe package [143]. The package was modified and updated for use in the QCD group, specifically adapting the calculations to allow efficiency determination without trigger object matching to jets to avoid the aforementioned L1 problems [142].

8.4.2 Absolute efficiency using muon triggers

The absolute trigger efficiencies can only be determined using an unbiased sample. The jet triggers operate entirely on calorimeter quantities, *i.e.* calorimeter towers and measured jet p_T. The unbiased sample can then be any sample that does not use any calorimeter objects for the trigger decision. Two main samples have been used for the trigger efficiency studies, the Minimum Bias sample and a sample collected from muon triggers, the TOP_JET_TRIG skim[4].

The Minimum Bias sample is a collection of events that only require a luminosity monitor hit. As the name suggests, it has minimal trigger bias and is in that sense ideal for trigger studies. The sample has been collected at a constant rate of about 0.5 Hz throughout the Run IIa data taking, and

[4]As the name suggests, the TOP_JET_TRIG skim was primarily collected for use in the Top group.

consists of about 20 million events[5]. Unfortunately, the inclusive jet p_T spectrum of the MB events falls very steeply and the maximum jet p_T with useful statistics is about 70 GeV/c. This limits the sample to be used for only the lowest p_T triggers JT_8TT, JT_15TT and JT_25TT_NG, which all have high prescales and hence very little statistics for L3 turn-on determination.

The TOP_JET_TRIG skim consists of about 28.6 million events collected from various muon triggers with no calorimeter requirements. The skim selection requires at least one jet with an uncorrected p_T>10 GeV/c and an offline prescale of 20 to limit the number of events. To increase statistics at p_T>100 GeV/c, an additional data set was re-skimmed starting from the larger MU_INCLUSIVE skim with the same trigger selection as in the TOP_JET_TRIG skim, but without the offline prescale.

The muons in the TOP_JET_TRIG skim mostly originate from relatively high p_T jets so the jet p_T spectrum is significantly less steep than for the MB sample. Combined with a much higher integrated luminosity this makes the sample useful up to over 200 GeV/c, which is sufficient to determine the L3 plateau efficiencies up to the unprescaled JT_125TT trigger. The best statistical significance for the L3 plateau efficiencies is obtained for JT_65TT and JT_95TT triggers, because lower p_T triggers are heavily prescaled.

The main drawback of the TOP_JET_TRIG skim is that the muon triggers bias the sample heavily toward b-jets that make up only about 2% of the inclusive jet sample [144]. The jet p_T spectrum of muon triggered events is also flatter than for inclusive jets. This may bias the trigger turn-on measurement as has in fact been observed especially at low p_T when comparing the results to the ones obtained from the MB sample, shown in Fig. 8.7. At and near the plateau region both results agree, and there is no obvious reason to expect significant bias when both of the efficiencies are close to 100%.

The main conclusion from the study using muon triggers is that all jet triggers are fully efficient (100%±1% or better) at sufficiently high p_T in all rapidity regions. However, the study also shows that in some cases the L1 trigger is still inefficient at a few percent level up to fairly high p_T, especially in the ICR region, as shown in Fig 8.8 for JT_25TT_NG.

Another major finding from the study was that triggers in the trigger lists v8–v11 turn on much later than the later trigger versions. The difference is tens of GeV/c at worst. However, these trigger lists were used before run 191,000 as shown in Table 5.2 and are not included in the final analysis.

To efficiently combine the triggers and produce a continuous, high statistics

[5]The total Minimum Bias+Zero Bias sample is about 59.2 million events

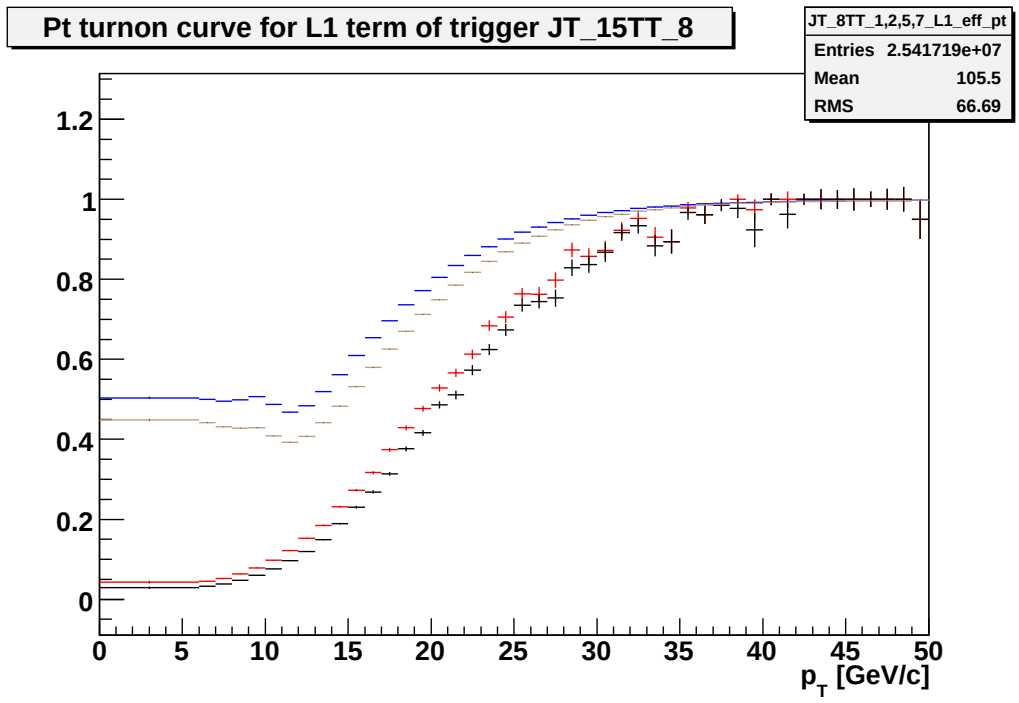

Figure 8.7: Measured L1 trigger efficiency in the Minimum Bias and in the TOP_JET_TRIG skim (curves from top: TOP JT_15TT, TOP JT_8TT, MB JT_15TT, MB JT_8TT). The flat region for TOP_JET_TRIG skim at $p_T < 12$ GeV/c is due to a skimming cut on uncorrected $p_T > 10$ GeV/c for JCCB jets.

p_T spectrum at low p_T, the trigger turn-ons are explicitly corrected using the best available fits to the them. The trigger turn-on is a step function for L3 jet p_T, which is smeared with respect to the offline jet p_T. The analytical result of folding a step function with a Gaussian resolution is the error function. The fit function is an adapted formulation of the standard error function

$$f(p_T) = 0.5 + 0.5 \cdot \mathrm{erf}\left(\frac{p_T - \mu}{1 + |\sigma_0 + \sigma_1 \log(p_T) + \sigma_2 \log(p_T)|}\right). \qquad (8.17)$$

This formulation explicitly allows some additional trailing inefficiency close to the plateau region, and provides a very good fit to the very high statistics L1 turn-ons, as shown *e.g.* in Fig. 8.9(a). For the lower statistics L3 turn-ons fits and for the fits in the forward region some of the extra parameters are set to zero to increase the fit stability. The L3 (and L2, where applicable) turn-on fits, shown *e.g.* in Fig. 8.9(b), are multiplied together with the L1 fits to produce a combined fit, as shown in Fig. 8.9(c).

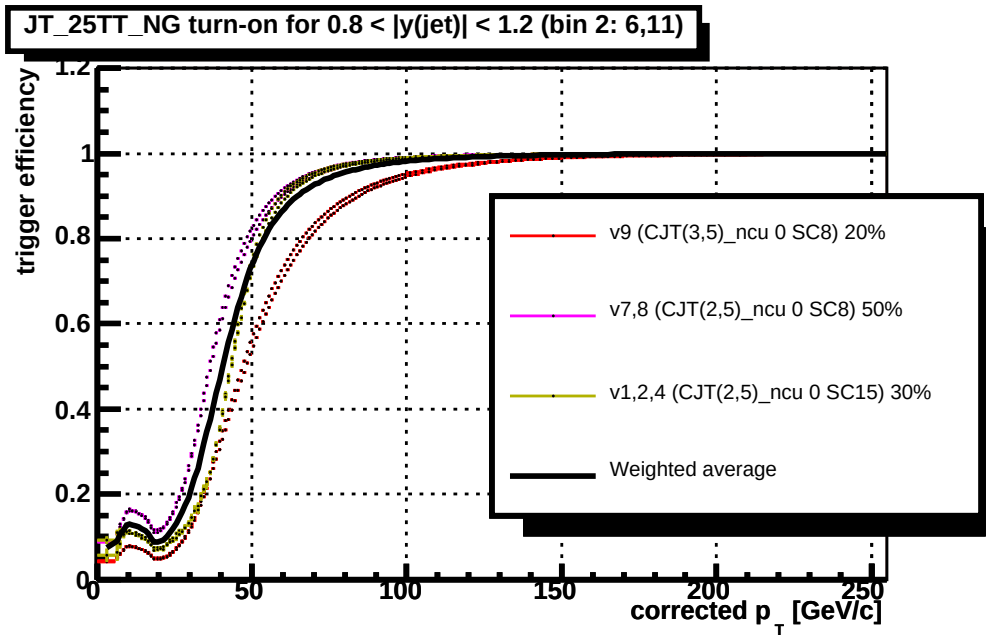

Figure 8.8: Smoothed single jet trigger turn-ons (L1×L2×L3) for the JT_25TT_NG trigger at $0.8 < |y| < 1.2$. The different curves show different versions of the same trigger, with the trigger terms listed in the legend. The percentages in the legend indicate the fraction of the total Run IIa luminosity of 1.1 fb^{-1} collected with each trigger version. The least efficient trigger is the version v9. The black line shows the luminosity weighted trigger efficiency for comparison.

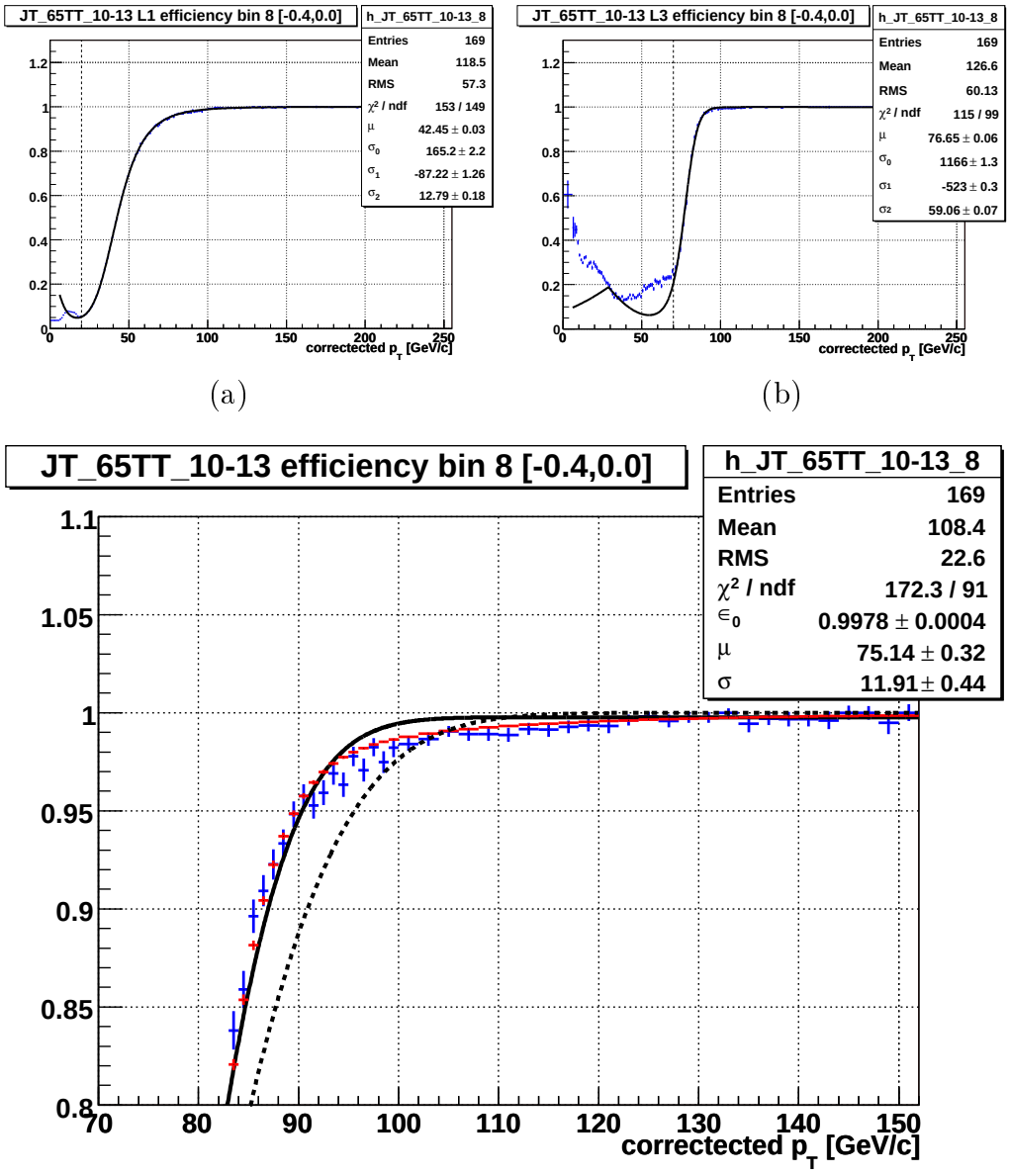

Figure 8.9: Typical turn-on fits for (a) L1 and (b) L3. The points show the original data and black line the turn-on fit. The dashed vertical line indicates the start of the fitted region. (c) Total L1×L2×L3 efficiency. The large points show the combined efficiency and the smaller points the result of separate L1, L2 and L3 fits multiplied together. The dashed line shows an error function fit to the full turn-on and the solid line shows a fit near the plateau region only.

8.4.3 Relative trigger efficiency

As discussed in the previous section, the muon triggered sample differs from the inclusive jet sample due to the enriched b-jet content and flatter p_T spectrum. Both of these may affect the average event topology, biasing the measured trigger efficiency with respect to the inclusive jet sample. Although this is not expected to change the plateau efficiency which is measured to be 100%, the trigger turn-ons may be slightly different in the different samples.

To verify how well the applied trigger efficiency correction works, the relative trigger turn-ons are re-determined from the inclusive jet sample by comparing the p_T spectra from two consecutive triggers after applying the trigger efficiency corrections down to 20% efficiency. To remove differences in the p_T spectra from different triggers due to known luminosity and time dependence effects, the spectra are also fully corrected for JES and vertex efficiency before taking the ratio.

Figure 8.10 shows the ratio of p_T spectra for single-jet triggers in CC. The ratios are in good agreement with 1.0 for all fit procedures: fit to the top of the turn-on using error function (eff0, solid line), constant value fit to the plateau starting at the 99% point of plateau efficiency given by the error function fit (ϵ_{99}, dashed line), and a constant value fit above the final trigger p_T threshold used in the cross section measurement, which is given in Table 8.1 ($\epsilon(X$ GeV), dotted line). The final p_T thresholds for the cross section measurement were selected to be above the 98% point of the absolute trigger efficiency. These p_T thresholds are well into the plateau after correcting for the absolute turn-on, as shown by the dotted line in Fig. 8.10. The plots for other rapidity regions are comparable, with little more fluctuation in ICR. These plots are provided in Appendix D.1.

The relative turn-ons are generally consistent with 100% efficiency for all the triggers in the plateau region, often with a precision better than 1%. This also verifies that the relative luminosities and vertex efficiencies are correctly calculated, as well as the JES and jet energy resolution (JER) being stable with time. It should be noted that such a conclusion is not possible in the ICR when using the full Run IIa sample. The trigger ratios show jumps of tens of percent, which are qualitatively consistent with the instability of the ICR JES in the trigger lists v10–v11 [119]. The ICR problems generally stem from the gain instability of the aging photomultiplier tubes versus time and instantaneous luminosity. The worst of these PMTs were replaced during a shut-down before Run IIb. This problem affects each jet trigger differently because the relative prescales are modified to optimize data-taking with changing luminosity, leading to different luminosity profiles for the trig-

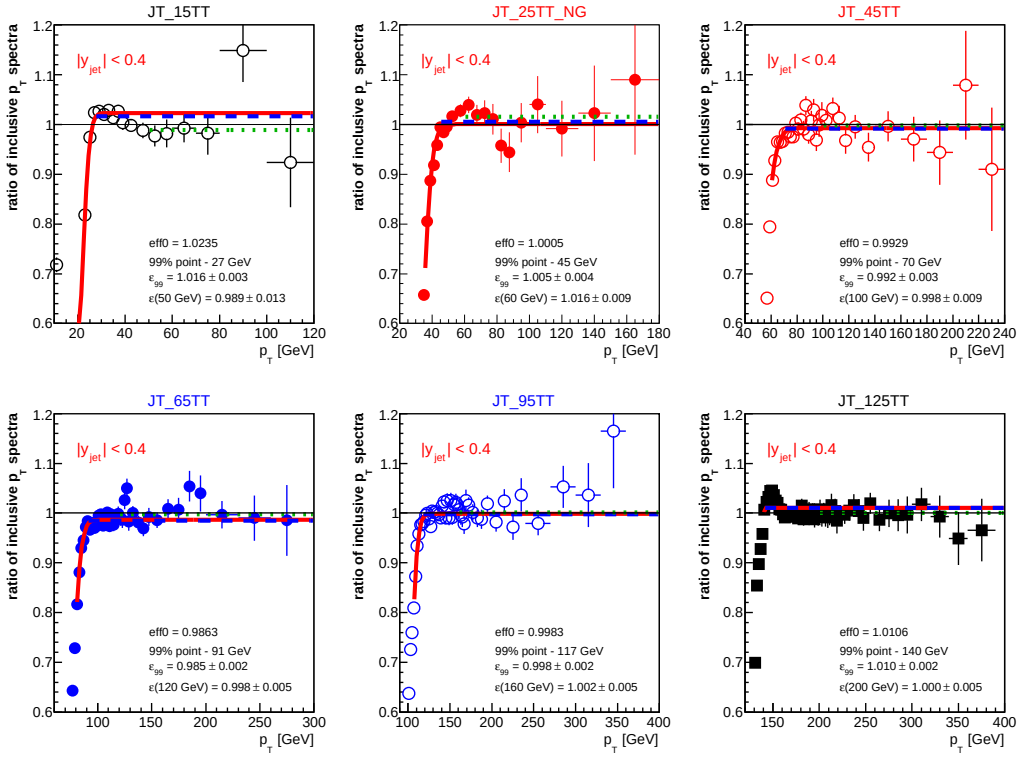

Figure 8.10: Ratio of jet p_T spectra measured from different single-jet triggers. The spectra are corrected for JES and vertex efficiency to cancel known luminosity dependencies, and for trigger efficiency measured from muon triggers down to 20% to test the consistency and to remove L1 trigger efficiency slopes at the plateau region. The curves show the error function fit (solid line), the constant value fit starting from the 99% efficiency (dashed line) and the constant value fit starting from the final trigger p_T threshold (dotted line).

gers. The currently used run range for low p_T triggers, 191,000<run<213,064, covers the trigger lists v12.37–v14, starting after the spring 2004 shut-down and ending at the beginning of the cable swap problem.

Despite having quite consistent trigger p_T spectra, small jumps between the triggers are allowed at the level of the statistical precision of the ratios. The ICR in particular shows possible discontinuities at a couple of percent level, up to 5% in $1.2 < |y| < 1.6$ between triggers JT_65TT and JT_95TT. Such jumps would be consistent with small trigger-to-trigger variations in JES ($< 0.5\%$) and/or JER ($< 4\%$) that are at the limit of the statistical precision. Given the prominence of such jumps in the full Run IIa sample, the fitted

trigger ratios and their statistical uncertainty are taken as a systematic. The size of the systematic is estimated using the three different fit procedures explained earlier.

For later correlations analysis, the trigger ratio uncertainties are assumed to be correlated within CC and EC, and partially correlated in ICR versus rapidity. The uncertainties are treated cumulatively from JT_65TT (which has highest statistics) toward both JT_8TT and JT_125TT so that both of these have several ratio uncertainties stacked together. Although these individual uncertainties are small, mostly 0.5–2.0%, and much smaller than JES or JER uncertainties, they still have a significant impact on the later global fit between data and theory. The small discontinuous jumps between triggers are not accounted for by any other (smooth) theory or experimental uncertainty and result in noticeable increase in χ^2 unless accounted for. This is particularly true in the aforementioned ICR region.

8.4.4 Combining triggers

The jet p_T spectra from single-jet triggers are used starting from the lowest p_T point where the spectrum agrees with the lower p_T trigger after applying the trigger efficiency, JES and vertex efficiency corrections, and where the absolute trigger efficiency is generally higher than 98%. The trigger efficiency correction would in principle allow to go lower than the 98% efficiency, but the measurement is overall not statistics limited. Going lower could also introduce unnecessary biases if the trigger efficiency correction is not perfect. Only one trigger is used for each p_T bin to simplify the luminosity calculations. Figure 8.11 shows the partially corrected p_T spectra from different triggers and their average prescales. The trigger p_T thresholds used in the analysis are listed for all rapidity regions in Table 8.1. These thresholds are applicable for the jet p_T spectra after applying the trigger efficiency corrections for the turn-on region.

Table 8.1: Trigger p_T thresholds used in the final analysis.

Rapidity	15	25	45	65	95	125
$\lvert y\rvert < 0.4$	50	60	100	120	160	200
$0.4 < \lvert y\rvert < 0.8$	50	60	100	120	160	200
$0.8 < \lvert y\rvert < 1.2$	50	90	110	140	190	230
$1.2 < \lvert y\rvert < 1.6$	50	80	90	140	190	240
$1.6 < \lvert y\rvert < 2.0$	50	70	90	110	160	190
$2.0 < \lvert y\rvert < 2.4$	50	70	90	120	160	200

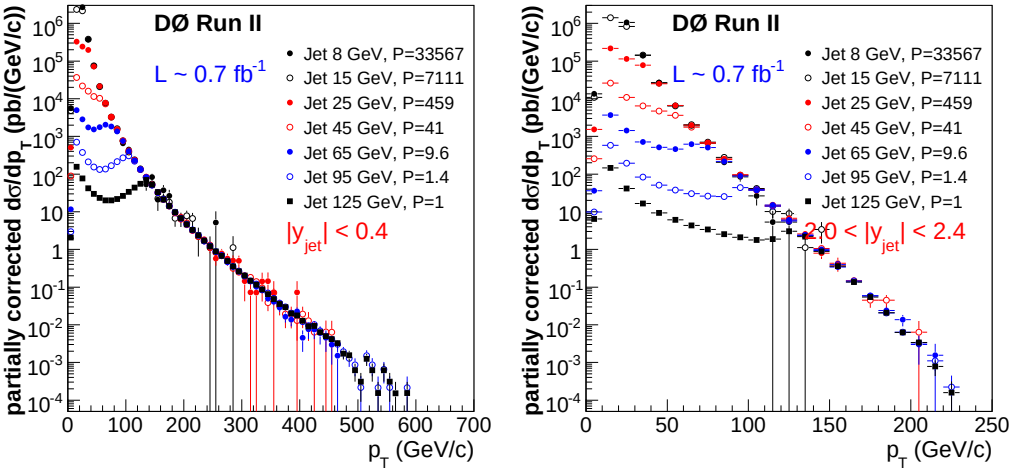

Figure 8.11: Single-jet trigger p_T spectra in central rapidity and forward rapidities and their average prescales. The trigger p_T thresholds used in this analysis are listed in Table 8.1.

8.5 Cross section unfolding

The steeply falling cross section combined with relatively poor jet p_T resolution leads to an increase in the observed cross section relative to the true cross section as a function of the measured jet p_T. An example of this behavior was shown in Fig. 6.14. To appreciate the steepness of the jet p_T spectra, especially at higher rapidities, the partially corrected jet p_T spectra are shown on the same scale in Fig. 8.12. The cross section can fall by up to an order of magnitude in a p_T interval covering just a couple of σ of typical jet resolutions.

The smeared p_T spectrum can be calculated using integration by

$$F(p_T^{\text{meas}}) = \int_{x=0}^{\infty} f(x)g(p_T^{\text{meas}}, x, \sigma)dx, \tag{8.18}$$

where $f(p_T^{\text{ptcl}})$ is the p_T spectrum at particle level and $g(p_T^{\text{mes}}, p_T^{\text{ptcl}}, \sigma)$ is the smearing function with resolution σ. The problem is to invert this relation.

If the p_T spectrum at particle level is assumed exponential $N_0 e^{-\alpha p_T}$ and the smearing function is Gaussian with a constant resolution σ, Eq. 8.18 can be analytically calculated when the integration range is extended from $-\infty$ to $+\infty$. The details are given in Appendix C.1 and the result is

$$F(p_T^{\text{meas}}) \quad = \quad N_0 \exp(-\alpha(p_T^{\text{meas}} - \alpha\sigma^2/2)) \tag{8.19}$$

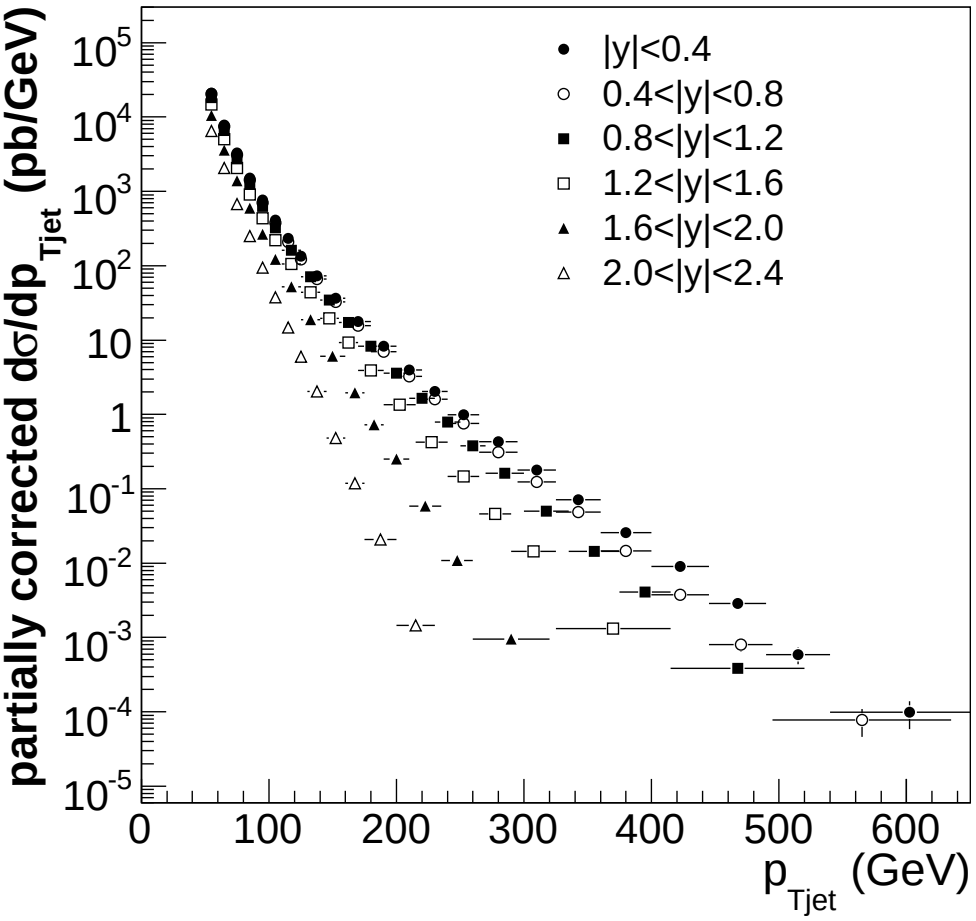

Figure 8.12: Partially corrected jet p_T spectra.

$$= \quad f(p_T^{\rm meas} - \alpha\sigma^2/2) = f(p_T^{\rm meas})\exp(\alpha^2\sigma^2/2).$$

The Eq. 8.19 now tells that the smeared spectrum can be interpreted as either shifted[6] in p_T by $-\alpha\sigma^2/2$ or increased in cross section by $\exp(\alpha^2\sigma^2/2)$.

It is instructive to consider some numerical values for these quantities, taking typical values $\alpha = 0.05$ $(\mathrm{GeV}/c)^{-1}$ and $\sigma = 1.0\sqrt{p_T}$ GeV/c for a $p_T = 100$ GeV/c jet so that $\sigma^2/p_T = 1.0$ GeV/c. The shift interpretation is $\delta p_T/p_T = -\alpha\sigma^2/(2p_T) = -0.025$ and the cross section interpretation $\delta X/X = \exp(\alpha^2\sigma^2/2) - 1 = 0.13$. These rough estimates agree quite well with the unfolding determined more accurately. The primary difference is due to as-

[6]The average true p_T is shifted by a larger amount $\delta p_T = \left\langle p_T^{\rm ptcl} \right\rangle - \langle p_T^{\rm meas} \rangle = -\alpha\sigma^2$.

suming the resolution to be constant for analytical integrability, when the more precise description is $\sigma = \sqrt{N^2 + S^2 p_T + C^2 p_T^2} \approx S\sqrt{p_T}$. In addition, the cross section is not exactly exponential and the Gaussian smearing can be questioned in some regions of the phase space. In any case, the Eq. 8.18 is exactly accurate and can be numerically integrated for arbitrary choices of f and g.

8.5.1 Ansatz method for p_T unfolding

The basic idea of the ansatz method is quite simple: start with a formula for the cross section that has a few free parameters $f(p_T; \alpha_0, \ldots, \alpha_n)$, smear it with the resolution function using Eq. 8.18 and fit the resulting smeared ansatz $F(p_T; \alpha_1, \ldots, \alpha_n)$ to data. The precision of the method is mainly limited by how good the eventual fit to data is, and how well the resolution function describes the real data resolution. The formula for the function f can be arbitrary and have an arbitrary number of parameters as long as the fit to F is good.

The ansatz used in this analysis is a traditional one for inclusive jet cross section [6] with the addition of rapidity dependence and an exponential term

$$f(p_T, \eta) = N_0 \left(\frac{p_T}{100 \text{ GeV/c}} \right)^{-\alpha} \left(1 - \frac{2p_T \cosh(y_{\min})}{\sqrt{s}} \right)^{\beta} \exp\left(-\gamma p_T\right). \quad (8.20)$$

Here $\sqrt{s} = 1960$ GeV is the center-of-mass energy and y_{min} is the lower edge of the bin in absolute rapidity. The ansatz is based on early phenomenological fits and motivated by the parton model [145, 146]. The exponential term represents hydrodynamic production — effectively production by freezing out particles from a quark-gluon sea. The exact exponent γ is a function of the production model, but 0.3–0.6 GeV is typical of the proton size. However, this term is not very well constrained by the high-p_T inclusive jet p_T spectrum. The power term with α represents the scaling violations associated with hard production (power law production). The threshold between hydrodynamic and hard production is ~ 2 GeV and independent of $\sqrt{s}$. The typical exponent for single particle production is about 4–6. This term dominates the fit over most of the kinematic range. The power term with β represents the suppression effect at the edges of the phase space on particle production. The most typical form is $(1 - x_T)^{\beta}$, where $x_T = 2p_T/\sqrt{s}$. This is the threshold term (divergence as $x \to 1$) and it is modified by $\cosh(y_{\min})$ to better relate to x. The threshold term does not typically contribute to the overall ansatz until the spectrum has reached roughly half of the kinematic

range. As mentioned before, none of this is actually required for the ansatz method to work, but a physics-motivated ansatz is still useful to make the parameters understandable.

The fit to the smeared ansatz for central and forward rapidity bins is shown in Figs. 8.13(a)–(b) and Figs. 8.13(c)–(d) show the resulting unfolding correction in CC and EC. The rest of the rapidity bins are shown in Figs. D.6 and D.7 of Appendix D.2. The parameters of the fitted ansatz functions are given in Table 8.2. The unfolding correction is largest where the cross section falls steepest and the jet p_T resolution is worst. The correction is between 10–40% in CC, 20–80% in ICR where the resolution is relatively poor and 15–80% in EC where the cross section falls steepest. The highest p_T bins, where the unfolding correction is largest, are chosen so that the cross section measurement is still meaningful, as discussed in Sec. 8.9. Although in some bins most of the events have migrated from lower p_T, the migrations (p_T resolution) are known well and result in a relatively small uncertainty compared to the JES uncertainty. The ansatz is well constrained by data and the uncertainty in the ansatz shape results in almost negligible uncertainty on the unfolding correction.

Table 8.2: Parameters of the ansatz fits to the unfolded p_T spectra.

N	α	β	γ	$y_{\min}$
868.9e11	5.421	10.83	-0.4914	0.0
781.3e11	5.410	13.53	-0.8625	0.4
426.9e11	5.298	13.59	-1.1409	0.8
743.2e11	5.467	13.35	-1.7358	1.2
117.1e11	4.914	9.316	-0.6546	1.6
24.11e11	4.380	6.974	0.8745	2.0

The bulk of the work in the p_T unfolding has gone to the accurate determination of the shape and of the parameters of the smearing function $g(p_T^{\text{meas}}, p_T^{\text{ptcl}}, \sigma, \alpha_i)$. The relatively simple ansatz function in Eq. 8.20 fits data well when smeared with jet p_T resolution, as shown in Figs. D.7. The smearing function g explicitly accounts for punch-through effects and other non-Gaussian tails. The shape is fitted from MC truth and the parameters are adjusted to match the measured RMS resolutions in data, taking into account some loss of the shape information and resulting biases in the data measurement. The interested reader should refer back to Ch. 7 for more information.

The ansatz unfolding has been shown to be in good agreement with the unfolding using Pythia MC where the cross section is scaled to data and the

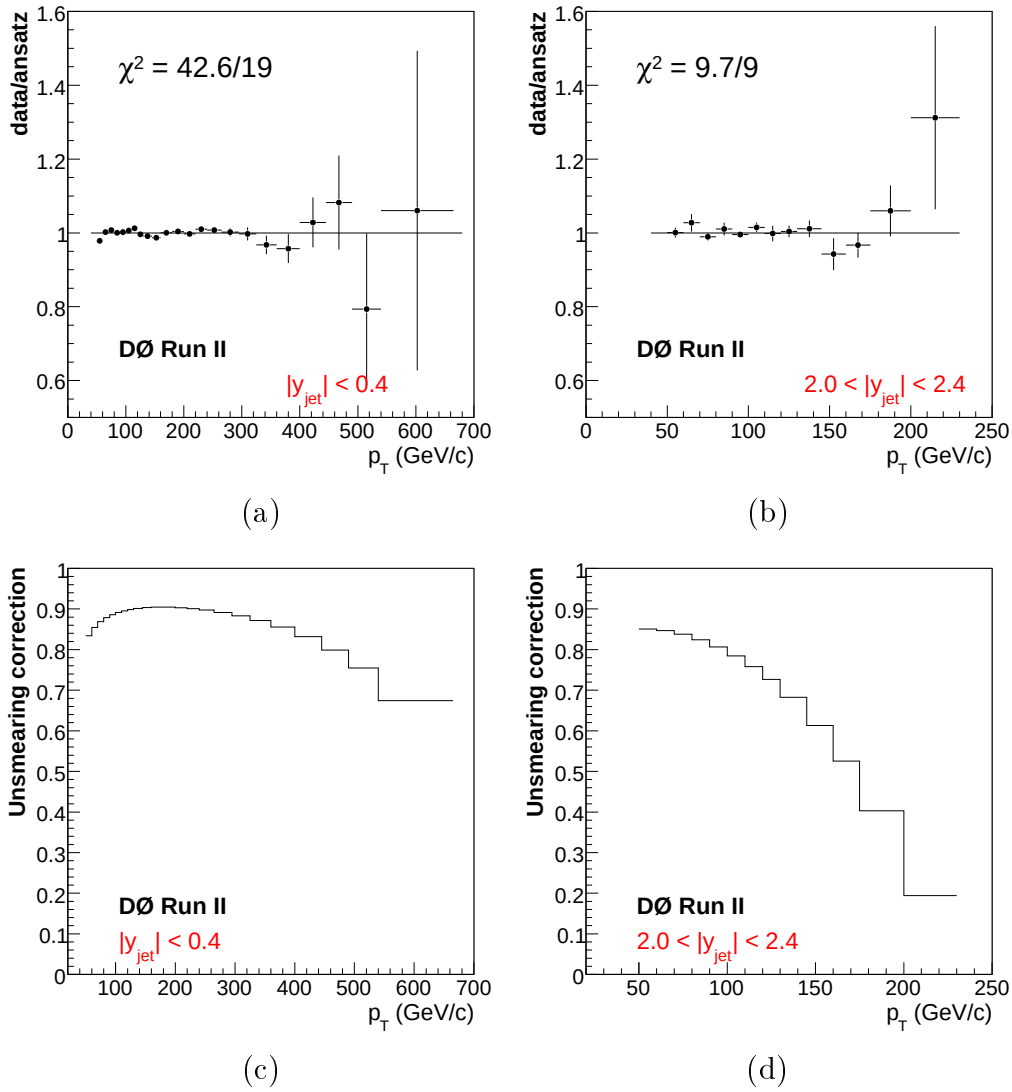

Figure 8.13: (a,b) Data over smeared ansatz fit in CC and EC. (c,d) Resulting unfolding correction, the ratio between smeared and original ansatz.

jets are smeared according to p_T resolutions measured from data [147]. The full Monte Carlo could also be used to derive the unfolding correction if the cross section was scaled to data and the MC resolutions were oversmeared to match data. However, the full MC statistics are too low to derive a precise correction over the full phase space.

8.5.2 Ansatz method for rapidity unfolding

The ansatz method can also be used to unfold the cross section for the rapidity resolution, assuming the p_T and rapidity resolutions are uncorrelated. However, integrating the function in 2D to account for both p_T and rapidity resolution simultaneously is very slow and would require a quite complicated ansatz function. Fortunately, the rapidity resolution is much better than the p_T resolution. Taking advantage of the much smaller size of the rapidity smearing this effect is considered as an additional perturbation on top of the p_T smearing. The ansatz fits to unfolded p_T spectra (unfolded for the p_T resolution only) in neighboring rapidity bins are interpolated versus rapidity to produce a smooth, continuous 2D spectrum in p_T and y

$$\begin{aligned} f_{2D}(p_T, y) &= f^{(1-D)}_{|y|>y_{\min,0}}(p_T; N_0, \alpha_0, \beta_0, \gamma_0, y_{\min,0}) \\ &\quad \cdot f^{D}_{|y|<y_{\min,1}}(p_T; N_1, \alpha_1, \beta_1, \gamma_1, y_{\min,1}), \quad \text{where} \\ D &= \frac{x - x_0}{x_1 - x_0}, \quad x = \log\left(1 - \frac{p_T \cosh(y)}{\sqrt{s}}\right), \\ x_0 &= \log\left(1 - \frac{p_T \cosh(y_{\min,0})}{\sqrt{s}}\right), \quad x_1 = \log\left(1 - \frac{p_T \cosh(y_{\min,1})}{\sqrt{s}}\right). \end{aligned} \tag{8.21}$$

The $f(p_T; N, \alpha, \beta, \gamma, y_{\min})$ are the ansatz functions in Eq. 8.20 whose parameters are determined in the p_T resolution unfolding and provided in Table 8.2. The 1D ansatz functions are interpolated geometrically versus rapidity with a distance parameter D that preserves the properties of the 1D ansatz functions at the kinematic limit $p_T \cosh(y_{\min}) \to \sqrt{s}$.

The rapidity resolution is taken from Monte Carlo truth as

$$\sigma_y = \mathrm{RMS}\left(y_{\mathrm{reco}} - y_{\mathrm{ptcl}}\right) \tag{8.22}$$

in bins of $p_{T,\mathrm{ptcl}}$ and y_{ptcl} by matching particle and calorimeter jets with $\Delta R(\mathrm{ptcl}, \mathrm{reco}) < R_{\mathrm{cone}}/2$. The binned rapidity resolutions are fitted with a 2D function that is provided in Ch. 7.

The smoothed 2D p_T, y spectrum is smeared using rapidity resolution and the ratio between the original and smeared 2D spectra is taken as the unfolding correction. As can be appreciated in Fig. 8.14, the rapidity unfolding is very small except at high p_T in the most forward bins. Even there the effect is small enough that the perturbative approximation can be considered valid.

The rapidity resolution is taken from Monte Carlo, but due to its small size it is difficult to estimate how applicable the MC rapidity resolution is to data. In addition, the MC rapidity resolution is not particularly Gaussian,

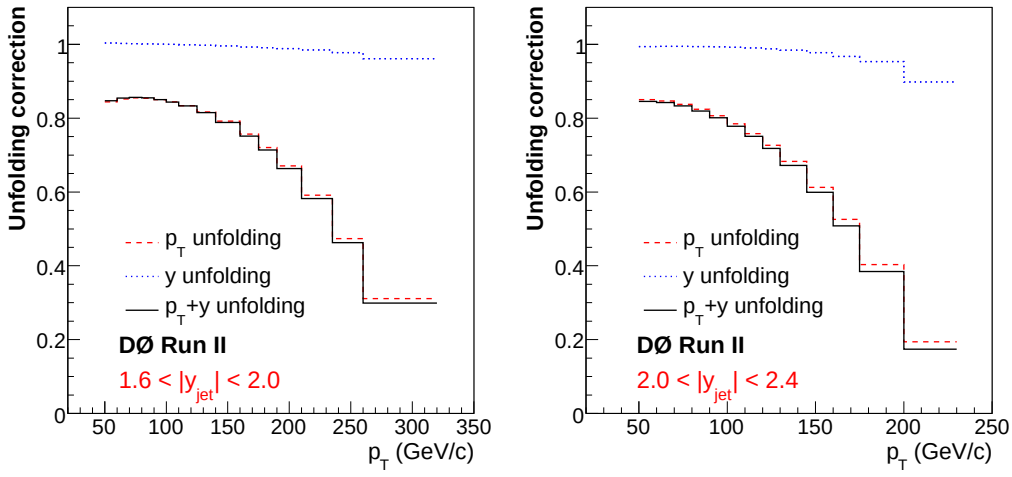

Figure 8.14: Unfolding correction for p_T (dashed line) and rapidity resolution (dotted line). The total unfolding correction is shown by the solid line. The rapidity smearing is very small compared to p_T smearing everywhere.

but has long tails and RMS up to twice as large as the Gaussian σ. To cover the full range of options, the larger RMS is used in rapidity unfolding and the total size of the rapidity unfolding is taken as an uncertainty. This uncertainty is conservative enough to cover a large range of variation in the rapidity resolution between data and MC. It also covers possible correlations between p_T and rapidity resolutions[7], in which case the p_T unfolding may have already accounted for some or all of the rapidity smearing.

8.6 Cross section uncertainties

The uncertainties for jet energy scale, jet p_T resolution, efficiencies *etc.* have been covered in some detail in the previous sections. To estimate the uncertainty on the cross section the different uncertainty sources need to be propagated to the cross section measurement. The simplest approach is to shift each parameter (JES, resolution, efficiency) up and down by its total uncertainty, repeat the whole analysis on data and record the change in the cross section. This approach works well for a few large uncertainties, but is not practical for the tens of small JES uncertainty sources needed for the uncertainty correlations. With JES uncertainties the repeat-everything-on-

[7]In the massless approximation $p_T = E/\cosh(y)$ so $\sigma^2_{p_T} = (\sigma_E/cosh(y))^2 + (p_T \tanh(y)\sigma_y)^2$.

data approach leads to multiple counting of the statistical uncertainty, which is sizable compared to the individual uncertainty sources at the edges of the phase space at high p_T.

To avoid double-counting the statistical uncertainty the uncertainty sources are propagated using a parametrization that describes data. Such a parametrization can be independent of any theory so the data uncertainties are calculated with respect to the best ansatz fit to data. These ansatzes were obtained in Sec. 8.5 during the unfolding procedure and their parameters are provided in Table 8.2. Alternatively, the uncertainties could have been calculated *e.g* using a linear combination of CTEQ PDF eigenvectors that fits data, but this would induce some theory dependence.

A simple analytical model of the analysis chain is used to efficiently implement the error propagation. The raw observable in the inclusive jet cross section analysis is the number of events N_{meas} in a given bin ($[p_{T,\text{min}}, p_{T,\text{max}}]$, $[y_{\text{min}}, y_{\text{max}}]$) that is calculated by

$$N_{\text{meas}} = (f \otimes g) \cdot \epsilon \cdot L, \tag{8.23}$$

where $(f \otimes g)$ is the jet p_T spectrum f folded with the jet p_T and rapidity resolutions g and (implicitly) integrated over the bin in p_T and y, ϵ is the total detection efficiency and L is the luminosity. The measured cross section is given by

$$\frac{d\sigma^2}{dp_T dy} = \frac{N_{\text{meas}}}{\Delta p_T \cdot \Delta y \cdot \epsilon' \cdot L'} \cdot \frac{f'}{f' \otimes g'} = \frac{(f \otimes g)}{\Delta p_T \cdot \Delta y} \cdot \frac{f'}{f' \otimes g'} \cdot \frac{\epsilon L}{\epsilon' L'}, \tag{8.24}$$

where the primed functions and variables are estimates from data for the true functions and variables, with associated uncertainties. The Δp_T and Δy are the bin size in p_T and y, respectively. The analytical model in Eq. 8.24 is sufficient for the error propagation: uncertainty in JES would correspond to a variation in $(f \otimes g)$, uncertainty in ansatz fit to a variation in f', resolution in g', efficiency in ϵ' and the uncertainty in luminosity to a variation in L'. The following subsections outline in more detail how the various uncertainty sources are propagated to cross section uncertainty.

8.6.1 Jet energy scale uncertainty

The uncertainty from jet energy scale for an individual source Δ_sJES is estimated by integrating the smeared ansatz from shifted upper and lower ends of the p_T bin and then comparing to the nominal value

$$p_{T,\text{min}}^{\text{shifted}} = (1 - \Delta_s\text{JES}) p_{T,\text{min}} \tag{8.25}$$

$$p_{T,\max}^{\text{shifted}} = (1 - \Delta_s\text{JES})p_{T,\max} \quad (8.26)$$

$$\Delta_s\left(\frac{d\sigma^2}{dp_T dy}\right) = \frac{\int_{p_{T,\min}^{\text{shifted}}}^{p_{T,\max}^{\text{shifted}}}(f \otimes g)(x)dx}{\int_{p_{T,\min}}^{p_{T,\max}}(f \otimes g)(x)dx} - 1, \quad (8.27)$$

where $f(p_T)$ is the ansatz fit and $p_{T,\max}$ and $p_{T,\min}$ are the p_T bin upper and lower edges, respectively. The up and down variations are treated separately because the non-linear cross section leads to asymmetric uncertainties even when Δ_sJES is symmetric. The result of this approach is shown by the solid line in Fig. 8.15. Note that the integration over the p_T bin that was implicit in Eq. 8.23 is written explicitly in Eq. 8.27. The implicit integration over the y bin is included in the ansatz f and does not need to be repeated, either. Equation 8.27 is then in practice a 2-dimensional integration over particle level p_T^{ptcl} and measured p_T^{meas}.

The simple approach above is complicated by the fact that the jet energy scale depends on a number of parameters such as luminosity, number of vertices, physics η, detector η *etc.* The uncertainties also have some direct η_{det} and p_T dependence. The ansatz approach does not easily facilitate anything else than the p_T dependence. However, the dependence on the other external parameters is small enough that it can be ignored when the average values for these parameters are used in calculating the JES uncertainty.

If the uncertainty correlations do not need to be considered, it is better to shift jets in data directly by the total JES uncertainty. This method automatically encompasses the correct ensemble of values for all the parameters and is used to test the validity of the ansatz approach. The result of this approach is shown by the points in Fig. 8.15. As mentioned earlier, the repeat-everything approach is hindered by the sensitivity to statistical fluctuations at the edges of the phase space. This is clearly indicated by the wildly fluctuating points at high p_T, particularly in CC where the last bins have less than ten jets. To reduce the statistical fluctuations, ansatz fits for the upper and lower JES uncertainty points are used to get a more stable uncertainty estimate, shown by the shaded band in Fig. 8.15.

The different methods for propagating the JES uncertainty into cross section uncertainty are in good agreement in Fig. 8.15 particularly in CC and at low p_T. Some difference is observed at high p_T especially in EC. The difference is explained by the fact that the JES uncertainty propagation in Eq. 8.27 only considers modification to the smeared cross section term $(f \otimes g)$ in Eq. 8.24 and keeps the ansatz f' fixed in the unfolding term $f'/(f' \otimes g')$ in Eq. 8.24. Fully redoing the analysis after shifting the p_T of the jets also modifies f', effectively counting an additional ansatz uncertainty into the total

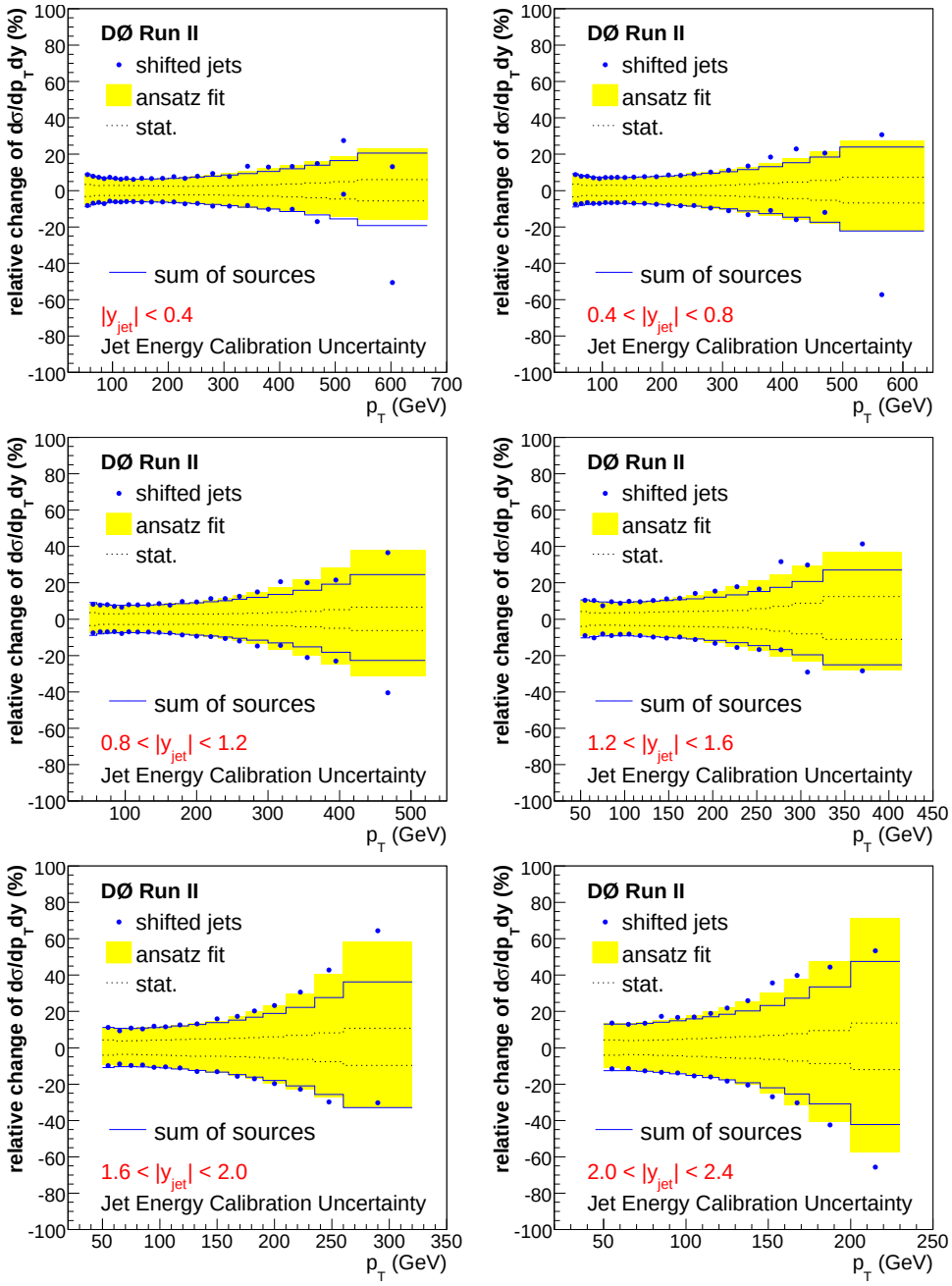

Figure 8.15: The jet energy scale uncertainty derived using three different methods: shifting jet p_T's in data (points), using ansatz fits to the shifted data (shaded band) and taking a quadratic sum of the JES uncertainty sources propagated using the central ansatz (solid line). The dashed line shows the size of the statistical component in the JES uncertainty. The scatter in the points is caused by statistical uncertainty.

JES uncertainty. When all the JES uncertainties are grouped together the total change in f' is relatively large and increasing toward high p_T, causing a change in the unfolding in the same direction as the change in $(f \otimes g)$. The correlation between the JES uncertainty and unfolding is a complex issue for individual uncertainty sources, and the proper statistical treatment could be further pursued in future analyzes.

8.6.2 Unfolding uncertainty

The jet p_T resolution and ansatz fit uncertainties are convolved together in the unfolding correction $f'/(f \otimes g')$ in Eq. 8.24. The jet p_T resolution uncertainty is obtained by varying the resolution function g' while keeping f' fixed

$$\Delta_s \left(\frac{d\sigma^2}{dp_T dy} \right) = \frac{(f' \otimes g')(x)dx}{(f' \otimes g'_s)(x)dx} - 1. \tag{8.28}$$

Note that the f' in the nominator of $f'/(f' \otimes g')$ has canceled out in the ratio. The uncertainty sources g'_s cover uncertainties in the width σ (RMS) of the resolution

$$g'_s(x, y, \sigma) \rightarrow g'(x, y, \sigma + \Delta_s \sigma), \tag{8.29}$$

and in the shape parametrized by $\{\alpha_i\}$, when σ is kept constant

$$g'_s(x, y, \sigma; \{\alpha_i\}) \rightarrow g'(x, y, \sigma; \{\alpha_{i,s}\}). \tag{8.30}$$

Similarly, the statistical uncertainty in the unfolding is propagated using

$$\Delta_s \left(\frac{d\sigma^2}{dp_T dy} \right) = \frac{(f' \otimes g')(x)dx}{(f'_s \otimes g')(x)dx} - 1, \tag{8.31}$$

when g' is kept constant. The eigenfunctions f'_s are obtained by diagonalizing the error matrix obtained from the unfolding step in Sec. 8.5. The diagonalization procedure is detailed in Appendix C.2.

Figure 8.16 shows a summary of the unfolding uncertainties: RMS width, resolution shape and the ansatz fit uncertainty. No uncertainty is assigned to the functional form of the ansatz because it gives good description of data and adding extra parameters would not improve the fit. The resolution uncertainty (dashed line) is the dominant one. The shape uncertainties (triangles) are only assessed in ICR where the double-Gaussian tails in MC truth may not perfectly match those in data. The punch-through tails are based on physics that is expected to be well-modeled by MC. The detailed accounting of the non-Gaussian tails results in significant differences compared to the

simpler Gaussian approach (full circles), but the two are consistent within the larger Gaussian uncertainties (not shown). The ansatz uncertainty (diamonds) is important only at the high p_T region with low statistics.

The propagation of the resolution uncertainties using Eq. 8.29 is verified by redoing the full unfolding with resolution changed by the total resolution uncertainty. The result (open circles) is shown in Fig. 8.16 compared to the results using Eq. 8.29 (dashed line). The two results are generally in good agreement, with small differences at high and low p_T. The propagation of resolution uncertainties using Eq. 8.29 does not change f' and g' simultaneously, while the full unfolding does. As in the case of JES uncertainties, an additional ansatz uncertainty is included in the total resolution uncertainty in the full unfolding, but the sign of the additional change may also be opposite to that of the total resolution uncertainty. The proper statistical treatment of the correlation between resolution uncertainty and unfolding could be further pursued in future analyzes, although it is found to be fairly small.

8.6.3 Efficiency and luminosity uncertainties

The efficiency and luminosity uncertainties are simple to propagate analytically by

$$\Delta_s\left(\frac{d\sigma^2}{dp_T dy}\right) = \frac{\epsilon}{\epsilon + \Delta_s\epsilon}, \tag{8.32}$$

$$\Delta_s\left(\frac{d\sigma^2}{dp_T dy}\right) = \frac{L}{L + \Delta_s L}. \tag{8.33}$$

The uncertainty in the ratio of jet trigger p_T spectra is formally also treated as an efficiency uncertainty, although the underlying cause of offsets in the trigger p_T spectra is likely a combination of time and luminosity dependence in JES, JER, luminosity measurement and calorimeter failure rates. The uncertainty of the trigger efficiency itself is negligible in the plateau region where the single-jet triggers are $> 98\%$ efficient and the residual inefficiency is corrected for. The overall luminosity, efficiency and trigger ratio uncertainties are shown in Fig. 8.17.

The leading inefficiency in Fig. 8.17 is the 6.1% uncertainty in the luminosity measurement [115]. The trigger ratio uncertainties are calculated with respect to the highest statistics trigger JT_65TT and increase toward both low and high p_T up to about 1–2% level. An exception is the ICR region where the jet p_T spectra are relatively poorly aligned for some triggers, and

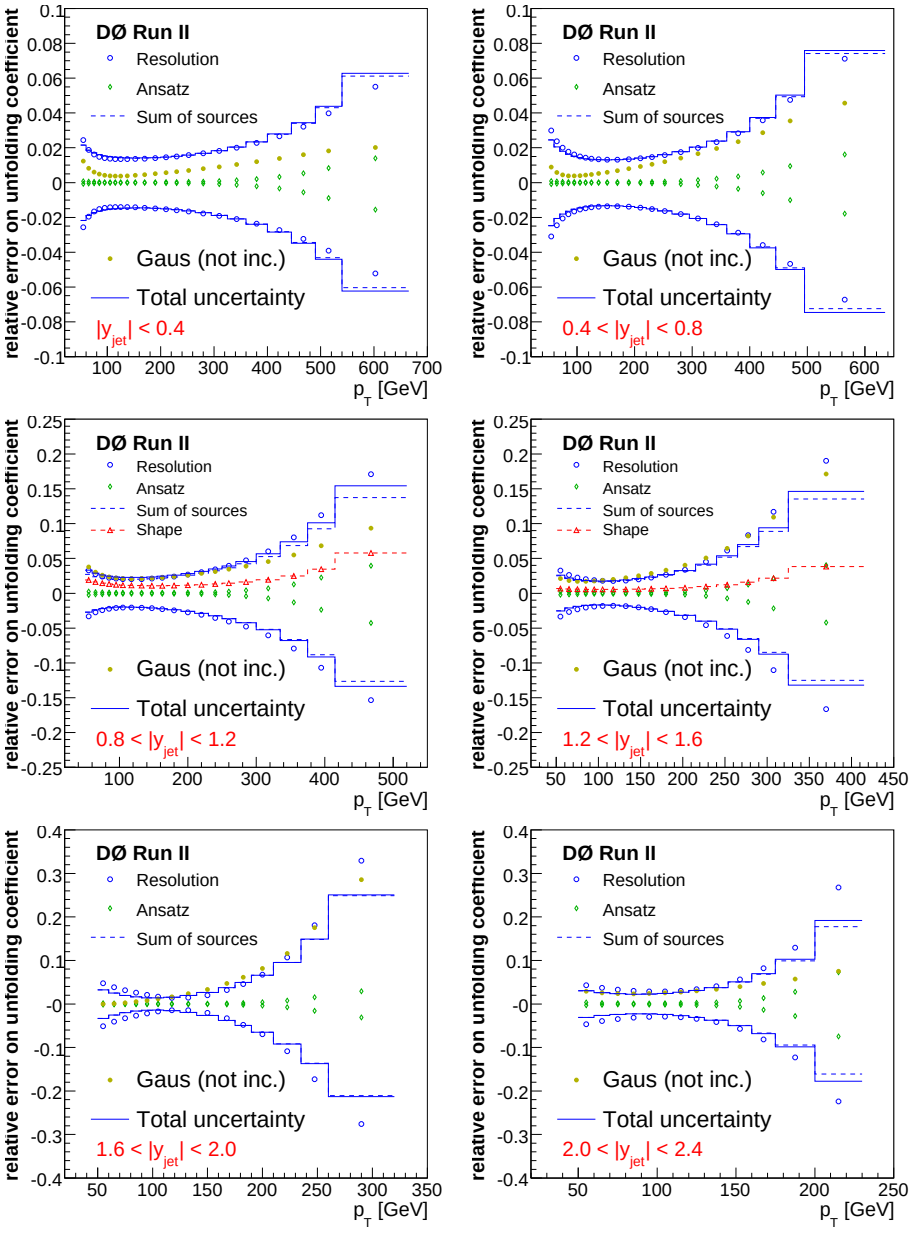

Figure 8.16: Unfolding uncertainty propagated to the cross section. The open circles show the RMS resolution uncertainty obtained by changing resolution by the total uncertainty and repeating unfolding. The same uncertainty is obtained by taking a quadratic sum of the resolution uncertainty sources propagated using the central ansatz (dashed line). The shape uncertainty in ICR is shown by the dashed line with triangles. The open diamonds show the ansatz fit uncertainty. The Gaussian unfolding method (full circles) is shown for comparison, but is not included in the total systematics (solid line).

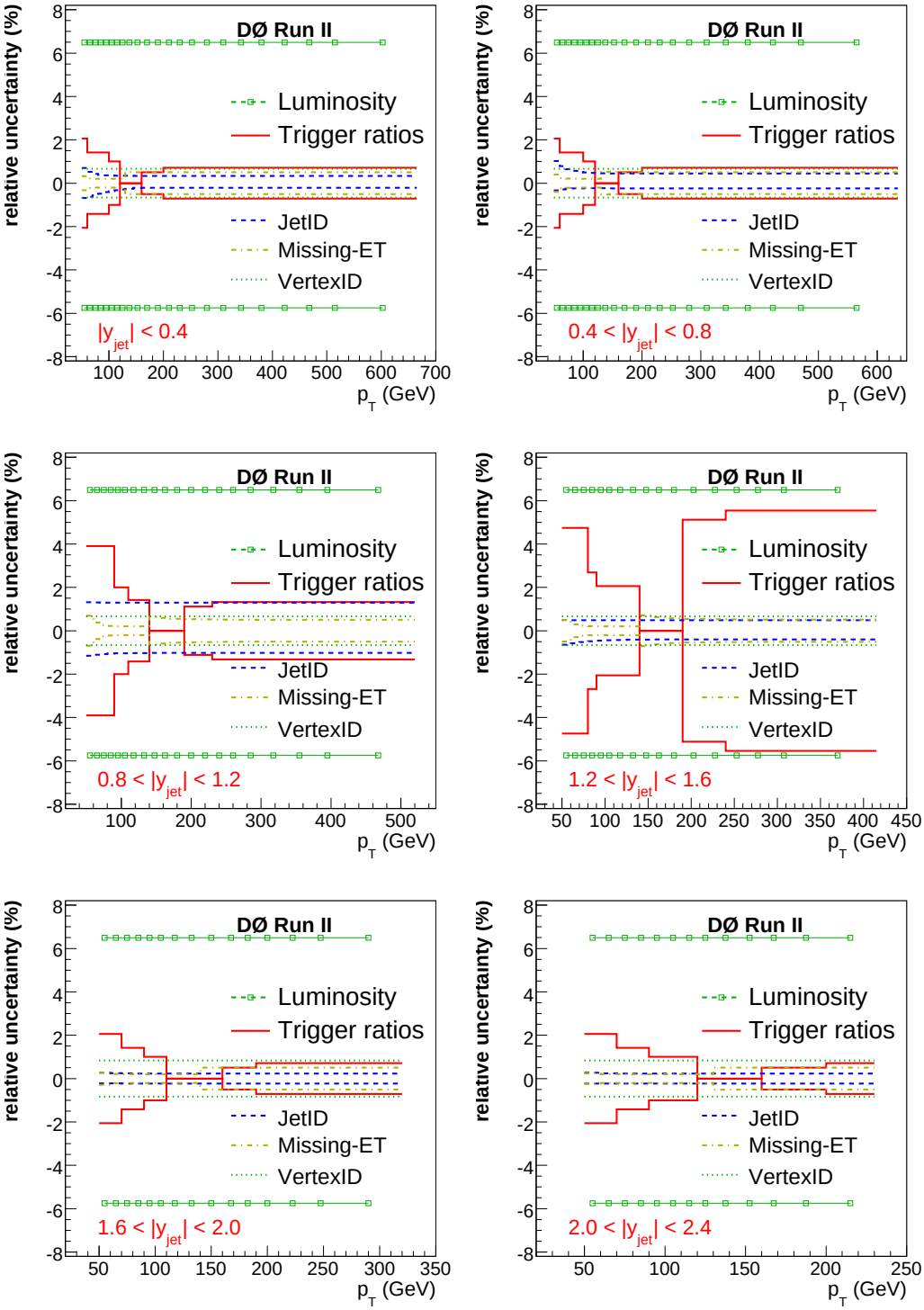

Figure 8.17: Luminosity, trigger ratio and efficiency uncertainties.

the uncertainty grows up to 5%. The JetID, missing-E_T cut and VertexID efficiency uncertainties contribute at a level of about 0.5% or less, except for 1.5% JetID uncertainty in $0.8 < |y| < 1.2$ and about 1% total VertexID uncertainty in EC. These three are overall the smallest uncertainties in the analysis.

8.6.4 Summary of uncertainties

The total uncertainty for the inclusive jet cross section is shown in Fig. 8.18. The dominant uncertainty is JES, but the unfolding (jet p_T resolution) uncertainties are also important particularly at high p_T in EC. The 6.1% luminosity uncertainty is the second most important uncertainty at low p_T, and the third biggest at high p_T. At about $p_T = 150$ GeV/c in CC the luminosity uncertainty is roughly equal to the leading JES uncertainty. The uncertainties associated with the efficiency corrections are small in comparison to the other uncertainties, although the included trigger ratio uncertainty grows sizable for $p_T > 190$ GeV/c at $1.2 < |y| < 1.6$.

8.7 Uncertainty correlations

The correlations between the uncertainties have been studied in detail, and in most cases the individual uncertainties are provided as a single uncertainty source. If the uncertainty has inherent decorrelation between rapidity regions like the residual of the η-dependent corrections, the uncertainty is broken into smaller sources that span each rapidity region. Similarly, if the uncertainty has correlation in p_T like the central response fit uncertainty, the uncertainty is factorized into p_T dependent parts *e.g.* by diagonalizing the error matrix (see Appendix C.2 for details).

The uncertainty sources are considered uncorrelated, and each source describes how all the points in the measurement move in a fully correlated fashion for a 1 σ uncertainty. The sign of the source can be both positive and negative. They are essentially "shapes" whose sign tells the direction a point should move, and the size tells by how much. The total uncertainty of the measurement in any point is given simply by the quadratic sum of all the uncertainty sources at that point.

The number of uncertainty sources provided is 48 for JES, 19 for unfolding with p_T resolution (13), rapidity resolution (1), non-Gaussian tails (1) and ansatz fit (4) uncertainty and 23 for efficiency with trigger ratio (15), JetID

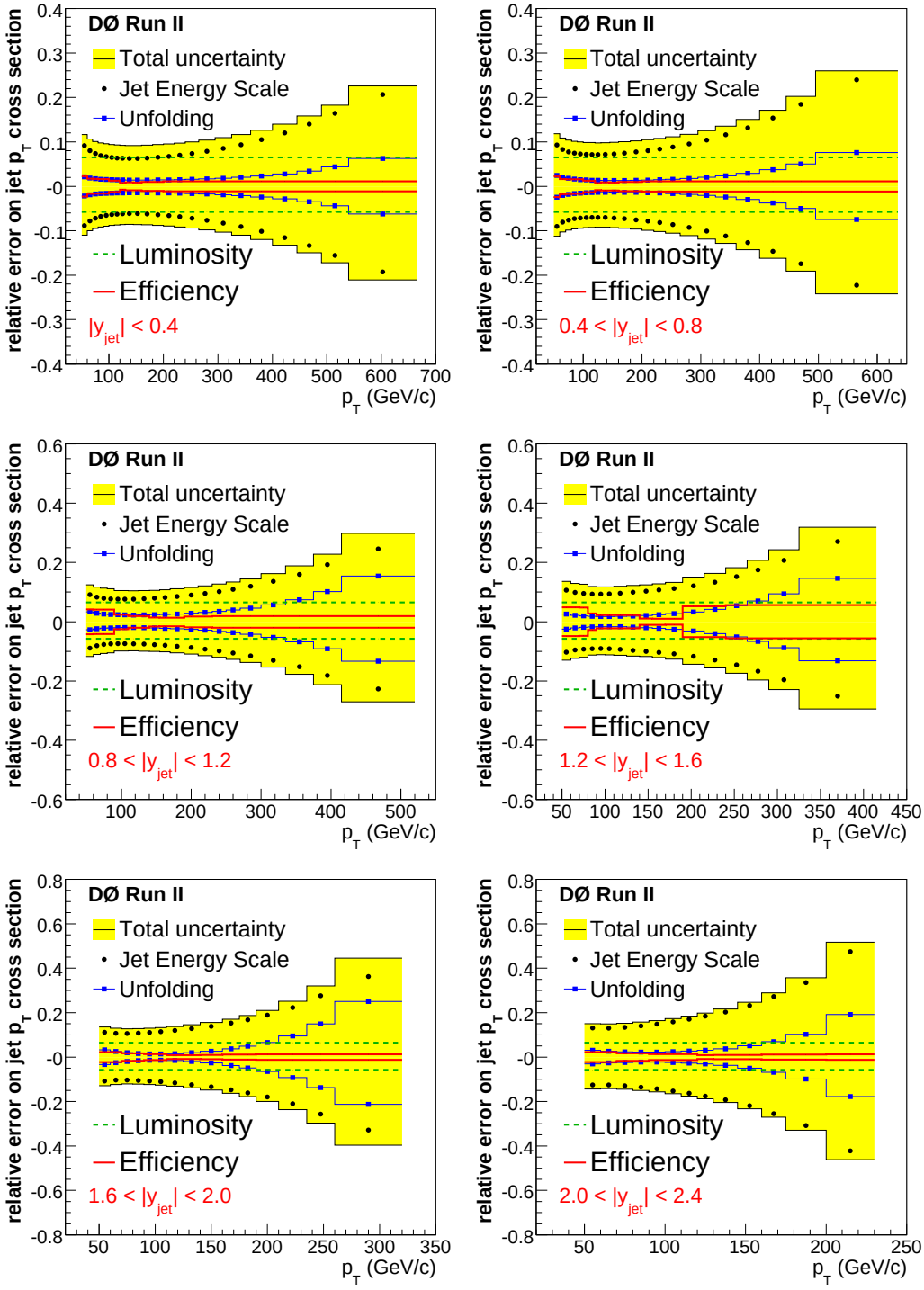

Figure 8.18: The total systematic uncertainty broken down to its primary components.

efficiency (3), vertex efficiency (3) and missing-E_T efficiency (2) uncertainties. The luminosity uncertainty is a single fully correlated source as it only affects the overall normalization. The total number of uncertainty sources is 91, many which are combined by shape similarities and size to an effective set of 24 in Sec. 8.11.3. These combined sources are listed in Table 8.9 and their original components in Tables 8.10–8.12.

8.8 Theory predictions

The theory predictions for inclusive jet cross section are calculated with perturbative QCD in next-to-leading-order (NLO) precision with the CTEQ 6.5 [150] and MRST2004 [22] PDF sets. The practical calculations are done with NLOJET++ [148, 149] and fastNLO [53].

The central CTEQ6.5M prediction uses the factorization and renormalization scales $\mu_F = \mu_R = p_T$. The alternative scale choices $\mu_F = \mu_R = 0.5p_T$ and $\mu_F = \mu_R = 2p_T$ are used to estimate the theory uncertainty on the higher order corrections. In an all-orders calculation the result does not depend on the choice of scale, but the dependence enters for a fixed scale when the higher order terms are omitted. The scales $0.5p_T$ and $2p_T$ are somewhat arbitrary, but commonly used choices to estimate the theory uncertainty.

The PDF uncertainties are calculated using the set of 20 up and down eigenvectors provided by the CTEQ collaboration for the CTEQ6.5M PDF fits. The MRST2004 PDF set [22] is used as an alternative for CTEQ6.5M for comparison.

8.8.1 Non-perturbative corrections

The NLO pQCD predictions are corrected for non-perturbative effects to connect the parton level jets predicted by theory to the measured particle level jets. The leading non-perturbative corrections are hadronization and underlying event that, however, cancel to a large extent. Their primary impact is at low p_T. Another small correction is the exclusion of parton shower muons and neutrinos from the definition of DØ particle jets. This leads on average to a small additional energy loss in going from parton to particle level. The muon/neutrino energy loss is in principle accounted for by the MPF method in γ+jet events, but the additional topology (MPF) bias corrections calibrate the JES to the DØ particle level. Other particle jet definitions usually include the muons and neutrinos in the particle jet.

Replacing the standard DØ cone algorithm with a seedless infrared-safe cone algorithm, SIScone [151], affects the cross section by 2–8%. The SIScone correction plots are provided for reference only, because neither DØ or CDF currently implement this algorithm in their standard jet reconstruction. However, there has been discussion on including this algorithm for future measurements at the Tevatron and LHC. The benefits are a smaller hadronization correction that improves the cancellation of non-perturbative corrections and a more sensible comparison between data and theory due to improved infrared safety.

The MC corrections have been obtained using Pythia v6.412 with parameters for tune QW [56]. The tune QW was obtained by tuning Pythia to reproduce CDF Run II data with CTEQ6.1M PDF set, whose central prediction is almost identical to that of CTEQ6.5M, but with almost twice as large uncertainties for the inclusive jet cross section measurement. The new CTEQ6.5M uncertainties became available in the beginning of 2007 and reduced the previous CTEQ6.1M PDF uncertainties by almost a factor of two primarily because the definition of the uncertainty changed[8]. The strong coupling "constant" is fixed to $\alpha_s(M_Z) = 0.118$ at the Z boson mass and uses 2-loop formula for the Q^2 evolution of α_s. The Pythia cross section is re-weighted in $\hat{s}$ so that the Pythia parton shower prediction agrees with NLO pQCD, which again agrees with data.

The correction factors for the theory prediction for hadronization and underlying event are shown in Fig. 8.19, along with their product to show the level of cancellation. The numerical values of these corrections are also listed in Tables 8.3–8.8. The energy loss correction to data for parton shower muons and neutrinos is shown in Fig. 8.20 together with the SIScone correction, which is provided for reference only. The energy loss correction is almost flat at 1–2%. There is no uncertainty assigned for the small energy loss correction, but the non-perturbative correction can be estimated as 50% of the individual corrections added in quadrature.

8.9 Choice of p_T binning

The theory predictions and measured jet p_T resolution have been used as a guide to set the bin limits particularly for the high p_T region: the highest bin is required to have $N_{\text{theory}}/\sqrt{N_{\text{smeared}}} \geq 1.645$, where N_{theory} is the lowest

[8]CTEQ6.1M uses $\Delta\chi^2 = 100$ that is interpreted as 90% confidence level, whereas MRST2004 and CTEQ6.5M have $\Delta\chi^2 = 50$ for the same purpose [152].

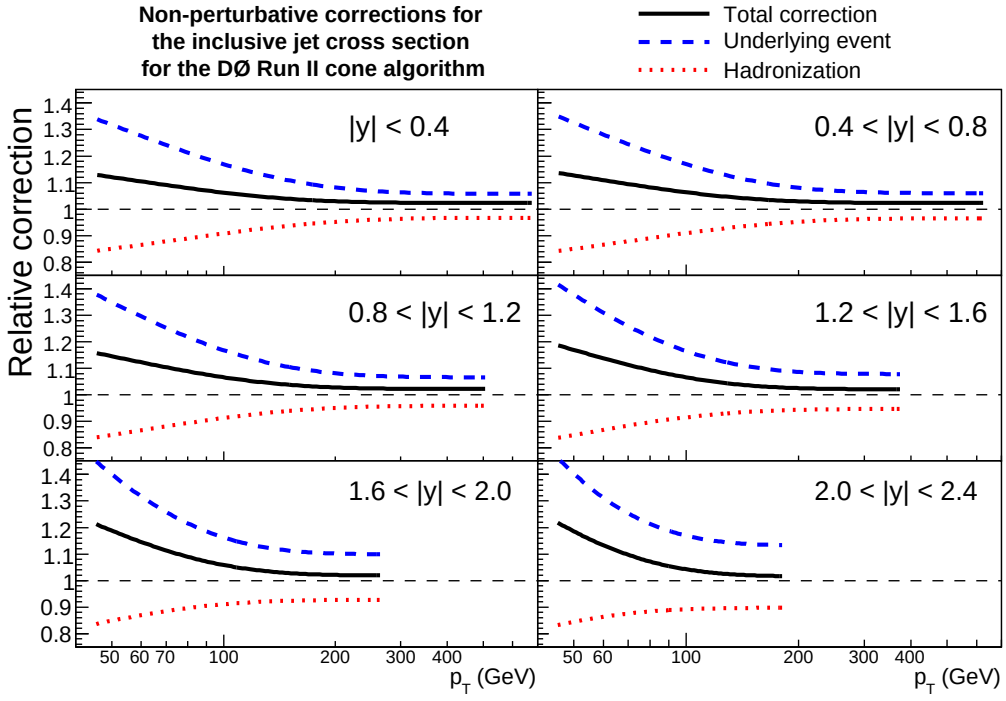

Figure 8.19: Hadronization and underlying event corrections for inclusive jet cross section theory prediction and their product. The uncertainty is estimated as 50% of the individual corrections added in quadrature.

expected number of jets from theory for $L = 700$ pb^{-1} and assuming an average efficiency of 0.85, N_{smeared} is the corresponding expected number of jets after p_T smearing, and 1.645 gives the one-sided 95% confidence level. This requirement gives the optimal p_T reach and sensitivity in CC for compositeness searches, but limits the maximum unfolding correction in the forward rapidity so that the measurement is sensitive to the true cross section.

The upper bin edge is chosen such that $N_{\text{smeared}} \leq 0.05$ for the overflow bin, except in ICR where 0.5 and 2.0 events are allowed at $p_T > 520$ GeV/c and $p_T > 415$ GeV/c for $0.8 < |y| < 1.2$ and $1.2 < |y| < 1.6$, respectively, to avoid excessively wide last bin. No jets are observed in the overflow bins, except at $1.2 < |y| < 1.6$ where two isolated jets are observed close to $p_T = 455$ GeV/c ($E > 800$ GeV). This is in agreement with the predicted 1.7 jets after smearing in this region.

The p_T bins are required to be multiples of 5 GeV/c and a minimum of 10 GeV/c, RMS(p_T) or $0.1 \cdot p_T$ wide, whichever is highest. The bin widths are then adjusted to match the trigger p_T thresholds so that only one trigger

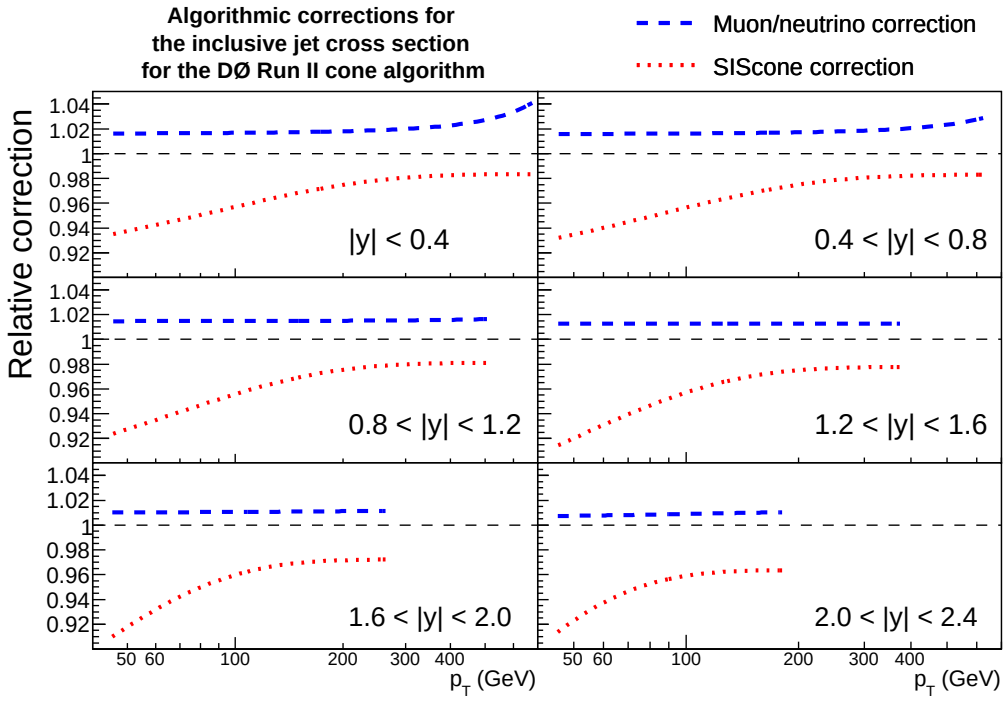

Figure 8.20: Correction to data for parton shower muons and neutrinos and for the seedless cone algorithm, SIScone. The latter is provided for reference only.

contributes to each p_T bin. The minimum width requirement of RMS(p_T) is loosened in ICR so that the final bin widths are comparable to CC and EC.

8.10 Final cross section results

The final cross section corrected for JES (specifically for p_T in the inclusive jet sample), rapidity bias, known inefficiencies and p_T and y smearing is shown in Fig. 8.21 in double logarithmic scale for all the rapidity regions. The choice of logarithmic x-axis emphasizes the relatively precise low p_T measurement. Overlaid on the plot are the theory predictions using CTEQ 6.5M NLO PDFs with the theory calculated using $\mu_F = \mu_R = p_T$ and corrected for underlying event and hadronization effects. The different rapidity regions are offset by powers of two to separate the curves. On logarithmic scale the agreement between data and theory is good over the full kinematic range. The tabulated cross sections for data and theory are provided in Tables 8.3–8.8.

Table 8.3: Jet cross section measurement for $0.0 < |y| < 0.4$

p_T bin	p_T^{plot}	data	systematic uncertainty	statistical uncertainty	theory	Non-perturbative corrections		
						hadroniz-	underlying	total
GeV	GeV	pb/GeV	%	%	pb/GeV	ation (%)	event (%)	%
50–60	54.5	2.310×10^{4}	+10.1,−9.5	0.7	2.085×10^{4}	-14.3	+29.9	+11.3
60–70	64.6	8.807×10^{3}	+9.5,−9.0	0.3	7.965×10^{3}	-12.9	+26.0	+9.8
70–80	74.6	3.769×10^{3}	+9.3,−8.7	0.5	3.439×10^{3}	-11.6	+22.8	+8.5
80–90	84.7	1.758×10^{3}	+9.1,−8.6	0.7	1.629×10^{3}	-10.6	+20.2	+7.5
90–100	94.7	8.926×10^{2}	+9.1,−8.5	1.0	8.301×10^{2}	-9.6	+18.0	+6.6
100–110	104.7	4.826×10^{2}	+8.9,−8.4	0.4	4.488×10^{2}	-8.8	+16.1	+5.9
110–120	114.7	2.744×10^{2}	+8.9,−8.3	0.5	2.543×10^{2}	-8.1	+14.6	+5.3
120–130	124.8	1.588×10^{2}	+8.9,−8.3	0.3	1.500×10^{2}	-7.5	+13.3	+4.8
130–145	137.0	8.645×10^{1}	+8.9,−8.3	0.4	8.232×10^{1}	-6.9	+12.0	+4.3
145–160	152.0	4.339×10^{1}	+9.0,−8.4	0.5	4.169×10^{1}	-6.2	+10.7	+3.8
160–180	169.3	2.132×10^{1}	+9.1,−8.5	0.3	2.033×10^{1}	-5.6	+9.6	+3.4
180–200	189.3	9.813×10^{0}	+9.3,−8.7	0.4	9.433×10^{0}	-5.0	+8.6	+3.1
200–220	209.4	4.720×10^{0}	+9.5,−8.9	0.5	4.603×10^{0}	-4.6	+7.8	+2.9
220–240	229.4	2.417×10^{0}	+9.8,−9.2	0.6	2.355×10^{0}	-4.3	+7.3	+2.7
240–265	251.6	1.177×10^{0}	+10.1,−9.5	0.8	1.163×10^{0}	-4.0	+6.9	+2.6
265–295	278.8	5.084×10^{-1}	+10.6,−10.0	1.1	5.142×10^{-1}	-3.8	+6.5	+2.5
295–325	308.9	2.095×10^{-1}	+11.2,−10.6	1.8	2.165×10^{-1}	-3.6	+6.3	+2.4
325–360	341.0	8.178×10^{-2}	+12.0,−11.3	2.6	8.880×10^{-2}	-3.5	+6.1	+2.4
360–400	378.2	2.901×10^{-2}	+13.0,−12.4	4.1	3.238×10^{-2}	-3.4	+6.0	+2.4
400–445	420.2	9.866×10^{-3}	+14.5,−13.7	6.6	1.046×10^{-2}	-3.3	+5.9	+2.3
445–490	465.2	3.006×10^{-3}	+16.5,−15.6	11.8	3.090×10^{-3}	-3.3	+5.8	+2.3
490–540	512.1	5.841×10^{-4}	+19.1,−18.0	25.8	8.347×10^{-4}	-3.3	+5.8	+2.3
540–665	584.3	8.693×10^{-5}	+23.8,−22.1	40.8	9.616×10^{-5}	-3.3	+5.8	+2.3

Table 8.4: Jet cross section measurement for $0.4 < |y| < 0.8$

p_T bin	p_T^{plot}	data	systematic uncertainty	statistical uncertainty	theory	Non-perturbative corrections		
						hadroniz-	underlying	total
GeV	GeV	pb/GeV	%	%	pb/GeV	ation (%)	event (%)	%
50–60	54.5	2.151×10^{4}	+10.4,−9.9	0.8	1.976×10^{4}	-14.3	+30.6	+11.9
60–70	64.6	8.092×10^{3}	+9.9,−9.4	0.3	7.510×10^{3}	-12.8	+26.4	+10.2
70–80	74.6	3.466×10^{3}	+9.7,−9.2	0.5	3.219×10^{3}	-11.6	+23.1	+8.9
80–90	84.7	1.610×10^{3}	+9.6,−9.1	0.7	1.517×10^{3}	-10.5	+20.3	+7.7
90–100	94.7	7.994×10^{2}	+9.6,−9.0	1.0	7.710×10^{2}	-9.5	+18.0	+6.8
100–110	104.7	4.352×10^{2}	+9.5,−8.9	0.4	4.128×10^{2}	-8.7	+16.1	+6.0
110–120	114.7	2.415×10^{2}	+9.5,−8.9	0.6	2.334×10^{2}	-8.0	+14.5	+5.4
120–130	124.8	1.409×10^{2}	+9.5,−8.9	0.4	1.365×10^{2}	-7.4	+13.2	+4.8
130–145	137.0	7.639×10^{1}	+9.6,−9.0	0.4	7.422×10^{1}	-6.8	+11.9	+4.3
145–160	152.0	3.806×10^{1}	+9.7,−9.1	0.6	3.721×10^{1}	-6.1	+10.6	+3.8
160–180	169.2	1.812×10^{1}	+9.9,−9.3	0.3	1.785×10^{1}	-5.5	+9.5	+3.4
180–200	189.3	8.108×10^{0}	+10.2,−9.6	0.4	8.116×10^{0}	-5.0	+8.5	+3.1
200–220	209.4	3.780×10^{0}	+10.5,−9.9	0.5	3.868×10^{0}	-4.6	+7.8	+2.8
220–240	229.4	1.853×10^{0}	+10.8,−10.2	0.7	1.931×10^{0}	-4.3	+7.3	+2.7
240–265	251.6	8.716×10^{-1}	+11.3,−10.7	0.9	9.243×10^{-1}	-4.1	+6.9	+2.5
265–295	278.8	3.529×10^{-1}	+12.0,−11.4	1.3	3.891×10^{-1}	-3.9	+6.6	+2.5
295–325	308.8	1.379×10^{-1}	+12.9,−12.3	2.1	1.546×10^{-1}	-3.7	+6.4	+2.4
325–360	340.9	5.253×10^{-2}	+14.1,−13.4	3.1	5.903×10^{-2}	-3.6	+6.2	+2.4
360–400	377.9	1.530×10^{-2}	+15.8,−15.0	5.3	1.956×10^{-2}	-3.6	+6.1	+2.3
400–445	419.9	3.702×10^{-3}	+18.1,−17.1	9.8	5.531×10^{-3}	-3.5	+6.1	+2.3
445–495	466.6	7.247×10^{-4}	+21.5,−20.2	20.4	1.298×10^{-3}	-3.5	+6.0	+2.3
495–635	539.3	5.830×10^{-5}	+27.9,−25.8	40.8	1.081×10^{-4}	-3.5	+6.0	+2.3

Table 8.5: Jet cross section measurement for $0.8 < |y| < 1.2$

p_T bin	p_T^{plot}	data	systematic uncertainty	statistical uncertainty	theory	Non-perturbative corrections		
						hadroniz-	underlying	total
GeV	GeV	pb/GeV	%	%	pb/GeV	ation (%)	event (%)	%
50–60	54.5	1.754×10^{4}	+11.2,−10.6	0.8	1.778×10^{4}	-14.3	+32.4	+13.5
60–70	64.6	6.575×10^{3}	+10.9,−10.3	1.3	6.648×10^{3}	-12.7	+27.5	+11.4
70–80	74.6	2.785×10^{3}	+10.8,−10.2	2.0	2.828×10^{3}	-11.3	+23.6	+9.7
80–90	84.7	1.283×10^{3}	+10.7,−10.1	3.0	1.310×10^{3}	-10.1	+20.5	+8.3
90–100	94.7	6.540×10^{2}	+10.2,−9.6	1.1	6.549×10^{2}	-9.2	+18.0	+7.1
100–110	104.7	3.380×10^{2}	+10.2,−9.6	1.5	3.459×10^{2}	-8.4	+15.9	+6.2
110–125	116.9	1.690×10^{2}	+10.2,−9.6	0.5	1.697×10^{2}	-7.6	+14.0	+5.4
125–140	132.0	7.455×10^{1}	+10.3,−9.7	0.8	7.587×10^{1}	-6.8	+12.1	+4.5
140–155	147.0	3.614×10^{1}	+10.5,−9.9	0.5	3.600×10^{1}	-6.2	+10.8	+3.9
155–170	162.0	1.795×10^{1}	+10.7,−10.1	0.8	1.802×10^{1}	-5.7	+9.7	+3.5
170–190	179.2	8.459×10^{0}	+11.0,−10.4	1.0	8.522×10^{0}	-5.3	+8.9	+3.1
190–210	199.3	3.641×10^{0}	+11.6,−11.0	0.6	3.741×10^{0}	-5.0	+8.2	+2.8
210–230	219.3	1.633×10^{0}	+12.2,−11.5	0.8	1.701×10^{0}	-4.7	+7.7	+2.6
230–250	239.4	7.565×10^{-1}	+12.9,−12.3	1.0	7.996×10^{-1}	-4.5	+7.4	+2.5
250–270	259.4	3.547×10^{-1}	+13.8,−13.1	1.4	3.820×10^{-1}	-4.4	+7.1	+2.4
270–300	283.6	1.427×10^{-1}	+15.0,−14.2	1.8	1.575×10^{-1}	-4.3	+6.9	+2.3
300–335	315.6	4.088×10^{-2}	+17.0,−16.0	3.0	4.929×10^{-2}	-4.2	+6.8	+2.3
335–375	352.5	1.023×10^{-2}	+19.9,−18.7	5.2	1.266×10^{-2}	-4.2	+6.7	+2.3
375–415	392.4	2.357×10^{-3}	+24.3,−22.6	9.9	2.782×10^{-3}	-4.1	+6.7	+2.2
415–520	449.4	1.529×10^{-4}	+32.0,−28.8	19.6	2.529×10^{-4}	-4.1	+6.6	+2.2

Table 8.6: Jet cross section measurement for $1.2 < |y| < 1.6$

p_T bin	p_T^{plot}	data	systematic uncertainty	statistical uncertainty	theory	Non-perturbative corrections		
						hadroniz-	underlying	total
GeV	GeV	pb/GeV	%	%	pb/GeV	ation (%)	event (%)	%
50–60	54.5	1.501×10^{4}	+12.3,−11.7	0.9	1.509×10^{4}	-14.2	+34.7	+15.5
60–70	64.5	5.200×10^{3}	+12.0,−11.5	1.5	5.468×10^{3}	-12.4	+28.6	+12.6
70–80	74.6	2.171×10^{3}	+11.9,−11.4	2.3	2.258×10^{3}	-11.0	+24.0	+10.4
80–90	84.6	9.542×10^{2}	+11.2,−10.7	0.9	1.019×10^{3}	-9.8	+20.5	+8.6
90–100	94.7	4.594×10^{2}	+11.1,−10.6	0.4	4.933×10^{2}	-8.9	+17.7	+7.2
100–110	104.7	2.329×10^{2}	+11.3,−10.7	0.5	2.523×10^{2}	-8.2	+15.6	+6.2
110–125	116.9	1.099×10^{2}	+11.5,−10.9	0.6	1.179×10^{2}	-7.5	+13.7	+5.2
125–140	131.9	4.551×10^{1}	+11.9,−11.3	1.0	4.928×10^{1}	-6.9	+11.9	+4.2
140–155	147.0	1.986×10^{1}	+12.2,−11.5	0.7	2.165×10^{1}	-6.4	+10.7	+3.6
155–170	162.0	9.150×10^{0}	+12.6,−12.0	1.1	9.967×10^{0}	-6.1	+9.9	+3.1
170–190	179.2	3.740×10^{0}	+13.3,−12.6	1.4	4.232×10^{0}	-5.9	+9.2	+2.8
190–215	201.2	1.231×10^{0}	+15.3,−14.6	0.8	1.453×10^{0}	-5.6	+8.7	+2.5
215–240	226.2	3.522×10^{-1}	+16.9,−16.1	1.4	4.405×10^{-1}	-5.5	+8.3	+2.3
240–265	251.2	1.073×10^{-1}	+19.3,−18.4	2.1	1.337×10^{-1}	-5.4	+8.1	+2.2
265–290	276.2	2.855×10^{-2}	+22.3,−21.1	3.7	3.988×10^{-2}	-5.4	+8.0	+2.2
290–325	304.8	6.826×10^{-3}	+26.7,−25.0	5.6	9.291×10^{-3}	-5.3	+7.9	+2.1
325–415	351.9	3.464×10^{-4}	+35.5,−32.5	11.5	6.317×10^{-4}	-5.3	+7.9	+2.1

Table 8.7: Jet cross section measurement for $1.6 < |y| < 2.0$

p_T bin	p_T^{plot}	data	systematic uncertainty	statistical uncertainty	theory	Non-perturbative corrections		
						hadroniz-	underlying	total
GeV	GeV	pb/GeV	%	%	pb/GeV	ation (%)	event (%)	%
50–60	54.5	1.145×10^{4}	+12.2,−11.6	1.0	1.165×10^{4}	-14.2	+36.1	+16.9
60–70	64.5	3.985×10^{3}	+12.0,−11.4	1.8	4.031×10^{3}	-12.3	+29.0	+13.1
70–80	74.6	1.546×10^{3}	+12.0,−11.4	0.7	1.566×10^{3}	-11.0	+23.8	+10.2
80–90	84.6	6.622×10^{2}	+12.2,−11.6	1.1	6.649×10^{2}	-10.0	+20.1	+8.1
90–100	94.7	2.930×10^{2}	+12.4,−11.8	0.5	2.990×10^{2}	-9.2	+17.4	+6.6
100–110	104.7	1.351×10^{2}	+12.8,−12.2	0.7	1.414×10^{2}	-8.7	+15.4	+5.4
110–125	116.8	5.651×10^{1}	+13.3,−12.7	0.4	5.923×10^{1}	-8.3	+13.8	+4.4
125–140	131.9	2.019×10^{1}	+14.2,−13.5	0.7	2.130×10^{1}	-7.9	+12.4	+3.5
140–160	148.9	6.296×10^{0}	+15.4,−14.7	1.1	6.885×10^{0}	-7.6	+11.4	+2.9
160–175	166.9	1.910×10^{0}	+17.2,−16.4	0.9	2.103×10^{0}	-7.5	+10.7	+2.5
175–190	181.9	6.777×10^{-1}	+19.2,−18.3	1.4	7.917×10^{-1}	-7.4	+10.4	+2.3
190–210	198.9	2.148×10^{-1}	+22.1,−20.9	1.8	2.534×10^{-1}	-7.3	+10.2	+2.1
210–235	220.7	4.317×10^{-2}	+27.2,−25.5	3.3	5.526×10^{-2}	-7.3	+10.0	+2.0
235–260	245.4	6.053×10^{-3}	+35.7,−32.7	7.6	8.876×10^{-3}	-7.3	+9.9	+2.0
260–320	277.7	3.195×10^{-4}	+50.8,−44.3	16.4	5.054×10^{-4}	-7.3	+9.9	+1.9

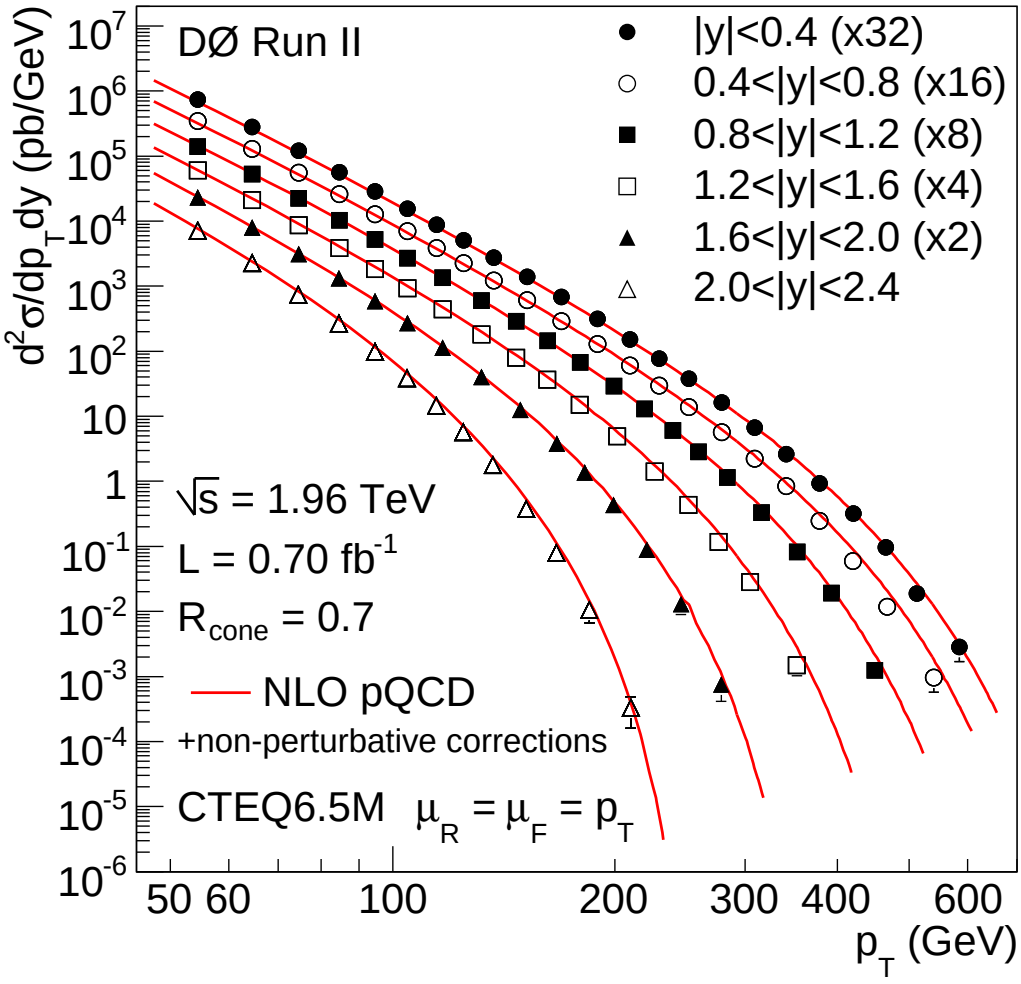

Figure 8.21: The final cross section measurement in double logarithmic scale.

The ratio of data and theory is plotted in Fig. 8.22. The logarithmic x-axis scale spreads the points evenly and emphasizes the precise low p_T data. The interesting region for both PDF constraints and new physics searches is at high p_T, but the low p_T data is useful for shape constraints. The shaded error band covers the total systematic uncertainty due to JES, unfolding, luminosity and efficiencies and is centered around the ansatz fit to the measured data. The dashed lines outline the PDF uncertainty, which is the leading theoretical uncertainty at about $p_T > 100\text{GeV}/c$.

Data and theory agree within experimental and theoretical uncertainties, but data would seem to favor the lower end of the CTEQ6.5M PDF uncertainty band. The shape agreement with the MRST2004 PDFs is generally better.

Table 8.8: Jet cross section measurement for $2.0 < |y| < 2.4$

p_T bin	p_T^{plot}	data	systematic uncertainty	statistical uncertainty	theory	Non-perturbative corrections		
GeV	GeV	pb/GeV	%	%	pb/GeV	hadronization (%)	underlying event (%)	total %
50–60	54.4	7.075×10^{3}	+13.5,–12.9	1.3	7.602×10^{3}	-14.6	+36.1	+16.2
60–70	64.5	2.248×10^{3}	+13.8,–13.2	2.3	2.364×10^{3}	-13.1	+28.4	+11.6
70–80	74.5	7.326×10^{2}	+14.3,–13.6	1.0	8.193×10^{2}	-12.1	+23.4	+8.5
80–90	84.6	2.685×10^{2}	+15.0,–14.3	1.7	3.013×10^{2}	-11.4	+20.1	+6.4
90–100	94.6	9.869×10^{1}	+15.8,–15.0	0.8	1.151×10^{2}	-11.0	+17.8	+4.9
100–110	104.6	3.845×10^{1}	+16.8,–16.0	1.3	4.547×10^{1}	-10.7	+16.3	+3.9
110–120	114.6	1.460×10^{1}	+18.0,–17.2	2.1	1.810×10^{1}	-10.6	+15.3	+3.2
120–130	124.6	5.665×10^{0}	+19.7,–18.7	1.6	7.105×10^{0}	-10.5	+14.6	+2.7
130–145	136.6	1.788×10^{0}	+22.2,–21.0	2.2	2.291×10^{0}	-10.4	+14.1	+2.3
145–160	151.6	3.722×10^{-1}	+26.6,–24.9	4.6	5.269×10^{-1}	-10.3	+13.7	+2.0
160–175	166.5	7.711×10^{-2}	+32.6,–30.2	3.5	1.120×10^{-1}	-10.3	+13.5	+1.8
175–200	184.6	9.782×10^{-3}	+42.4,–38.2	6.5	1.400×10^{-2}	-10.3	+13.3	+1.7
200–230	209.7	2.689×10^{-4}	+65.2,–55.4	18.9	3.864×10^{-4}	-10.3	+13.2	+1.6

As can be appreciated, the experimental uncertainties have been reduced overall to the same level as the current best CTEQ6.5M PDF uncertainties. The experimental uncertainties are highly correlated, with an average bin-to-bin correlation of 0.79 and RMS of 0.11, both calculated from the 110×110 elements of the correlation matrix shown in Fig. 8.24 excluding the 110 diagonal elements. The measured shape of the data over theory then also provides strong constraints on the PDFs, as discussed in the next section.

8.11 Statistical comparison with theory

The experimental uncertainties contain a significant amount of correlation between p_T and rapidity bins that can be used in constraining the theory PDF uncertainties. The luminosity uncertainty is naturally fully correlated across all p_T and rapidity bins, but the new methods of deriving the JES uncertainties have also increased bin-to-bin correlations. Some of the largest JES uncertainties in CC, the electron and photon energy scales, are fully correlated across rapidity at fixed p_T due to the central-to-forward η-dependent corrections. The correlation across p_T is also strong due to the calibrated Monte Carlo models used to extrapolate the response to higher p_T in CC. Using dijet events together with γ+jets in a combined fit for the JES calibration has reduced high p_T statistical uncertainties also at more forward rapidities, with the constraints coming directly from data. The new global fit procedure that is used in most sub-corrections has produced smooth parametrizations that have low statistical uncertainty and high level of bin-to-bin correlation.

Together all the new improvements have increased the overall bin-to-bin correlations shown in Fig. 8.24 to an average level of 0.79, with RMS of 0.11. The

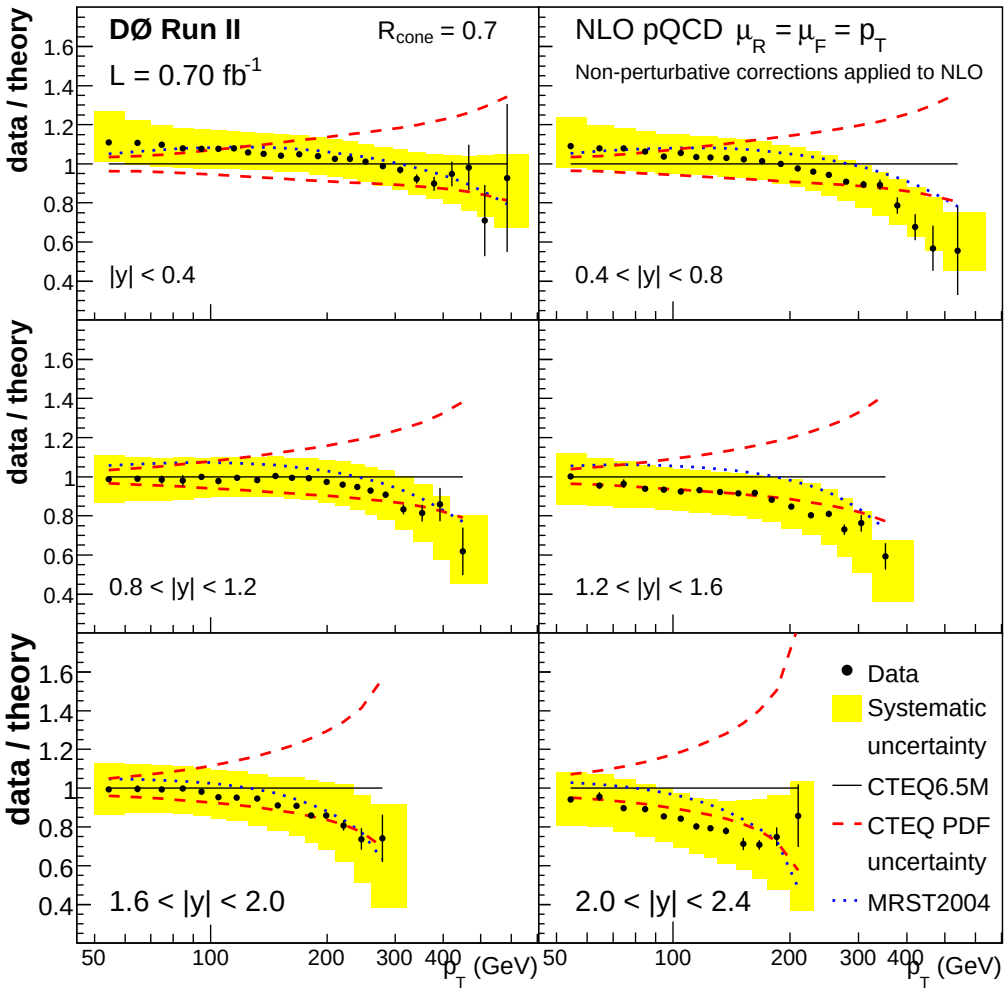

Figure 8.22: The final cross section measurement compared to next-to-leading order perturbative QCD theory with CTEQ6.5M PDF set and additional corrections to theory for hadronization and underlying event. The shaded error band covers the systematic experimental uncertainties, while the error bars show the statistical uncertainty of the measurement. The dashed lines outline the theoretical uncertainty in the CTEQ parton distribution functions. The dotted line shows the alternative MRST2004 PDF parametrization for comparison.

correlation information for the experimental uncertainties is broken down to 91 uncertainty sources that are combined to 24 effective sources listed in Tables 8.13–8.36. The correlation information can be used in a global fit to the theory with the theory uncertainties represented as a set of sources

for the PDF, scale, underlying event and hadronization correction uncertainties. This allows the shape of the measured cross section to be used to provide additional constraints for the theory (PDFs). The most significant PDF uncertainty correlation information is readily available from the CTEQ collaboration as a set of 20 eigenvector pairs representing independent up and down variations of the PDFs [150]. These eigenvectors estimate a confidence range such that, within this range, the fit to every data set used in the global fit is within its 90% confidence level. The cross section uncertainties corresponding to these PDF eigenvector pairs are shown in Fig. 8.23. The uncertainty over most of the kinematic range is dominated by a single pair of eigenvectors, the pair #13. This corresponds to the uncertainty in the high-x gluon PDF.

The correlation information encoded in the uncertainty sources s_k can be visualized by calculating the correlation ρ between bins x_i and x_j using

$$\sigma_{x_i} = \sqrt{\sum_k s_k^2(x_i)}, \tag{8.34}$$

$$\sigma_{x_j} = \sqrt{\sum_k s_k^2(x_j)}, \tag{8.35}$$

$$\rho(x_i, x_j) = \frac{\sum_k s_k(x_i) s_k(x_j)}{\sigma_{x_i}\sigma_{x_j}}. \tag{8.36}$$

The bins are ordered first by p_T, then by rapidity such that the index i of point $x_i = (p_{T,y}, y_i)$ is $i(x_i) = 6 \times i(p_{T,i}) + i(y_i)$. The full 110×110 matrix of correlation information is shown in Fig. 8.24. The correlation is clearly strongest for the bins close to each other in the (p_T, y) space.

8.11.1 The χ^2 minimization procedure

The first step in determining the statistical agreement between data and theory is to define a χ^2 function for the comparison. Such a function is obtained by allowing the data x_i or the central theory prediction t_i to be shifted by an amount $\delta_{i,k}(\epsilon_k)$ for each bin i and source k and then adding the shifts ϵ_k to the χ^2

$$\begin{aligned}\chi^2 &= \sum_i \left[\frac{x_i + \sum_k \delta_{i,k}(\epsilon_k) - (t_i + \sum_{k'} \delta_{i,k'}(\epsilon_{k'}))}{\Delta^2_{i,\text{uncorr}}}\right]^2 + \sum_k \epsilon_k^2 + \sum_{k'} \epsilon_{k'}^2 \\ &= \sum_i \left[\frac{x_i + \sum_k \delta_{i,k}(\epsilon_k) - t_i}{\Delta^2_{i,\text{uncorr}}}\right]^2 + \sum_k \epsilon_k^2, \end{aligned} \tag{8.37}$$

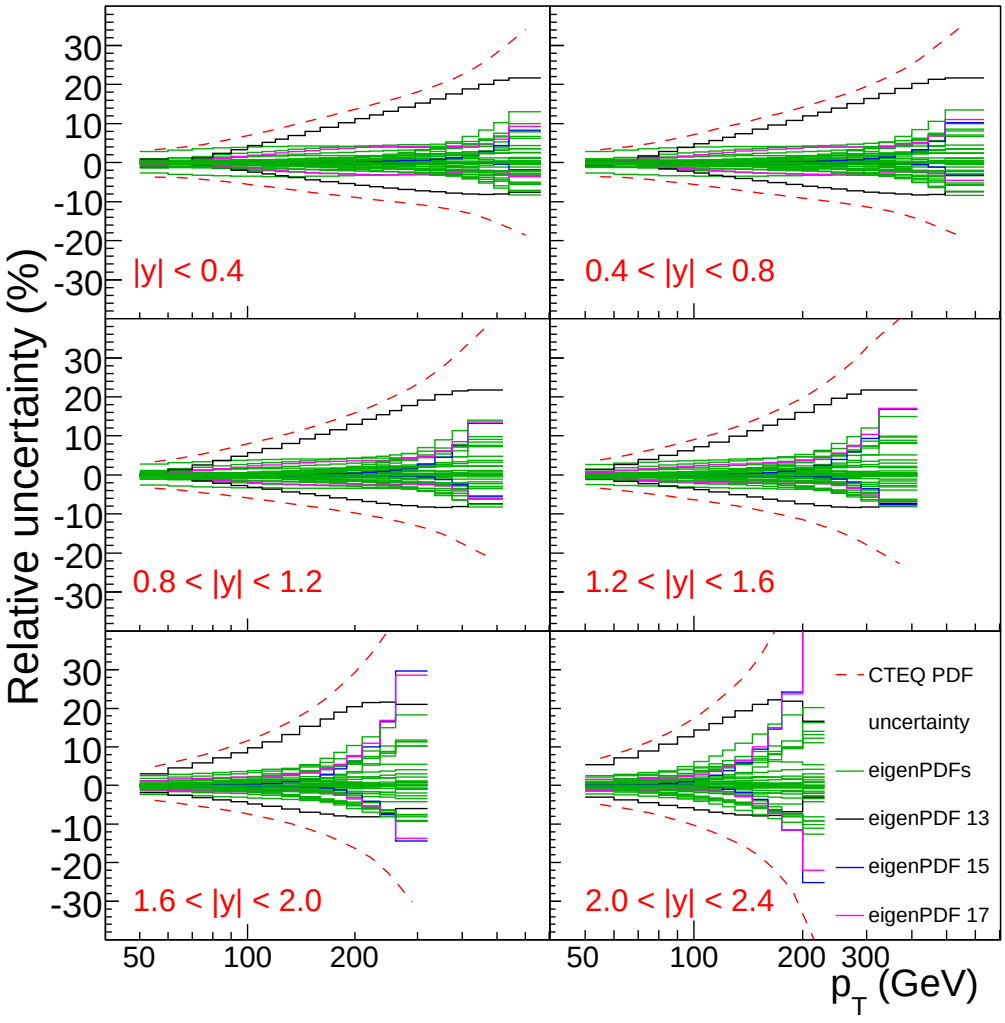

Figure 8.23: The 20 PDF eigenvector pairs from CTEQ6.5M fit propagated to the inclusive jet cross section. The dashed line shows the total PDF uncertainty, and solid lines show individual eigenvectors. The dominant eigenvector pair #13 is singled out, as well as pairs #15 and #17 that are dominant at high p_T in the forward region.

where the special case $\epsilon_k = \pm 1$ corresponds to a $\pm 1\ \sigma$ shift for the uncertainty source k and $\Delta_{i,\mathrm{uncorr}}$ gives the total uncorrelated uncertainty for each bin i. The former summations with k and k' are taken over data and theory sources, respectively. The latter summations over sources include both data and theory uncertainties, but with theory shifts getting an implicit minus sign. The χ^2 function is adapted from Ref. [153] and the method is generally

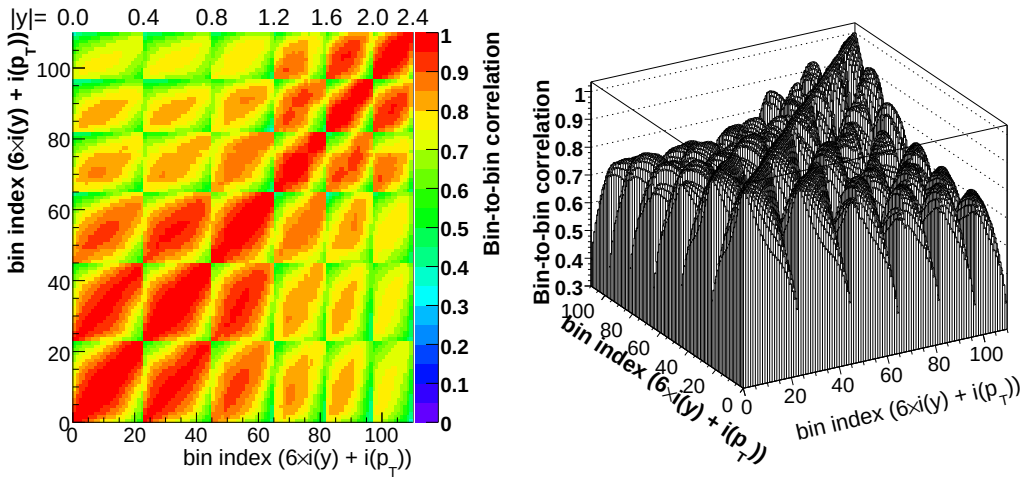

Figure 8.24: Bin-to-bin correlation for the cross section measurement uncertainties. The bins are ordered first in p_T, then in rapidity, such that each large "box" is a single rapidity bin. The same correlations are shown as (a) a color map, and (b) a lego plot.

the same as used by the CTEQ collaboration.

The number of degrees of freedom (NDF) for the χ^2 in Eq. 8.37 is the same as the number of data points x_i, 110. Although there are 91 sources $\delta_{i,k}(\epsilon_k)$ for data and 20 sources $\delta_{i,k'}(\epsilon'_k)$ for PDFs and a corresponding number of parameters ϵ_k and ϵ'_k, these do not affect the overall NDF because they are constrained by the additional penalty points. *A priori* the ϵ_k and ϵ'_k are expected to be Gaussian distributed with mean 0 and RMS of 1.

The simplest choice for the shift $\delta_{i,k}(\epsilon_k)$ is to make it a linear function of ϵ_k [153]

$$\delta_{i,k}(\epsilon_k) = \epsilon_k \sigma_i^k, \tag{8.38}$$

where σ_i^k is the one standard deviation uncertainty for source k. The minimum χ^2 of Eq. 8.37 can be obtained by fitting the parameters ϵ_k that describe both the data and theory systematics to get a good agreement between data and theory. However, with $\delta_{i,k}(\epsilon_k)$ set as in Eq. 8.38, the partial derivatives of Eq. 8.37 result in linear set of equations for ϵ_k

$$\frac{\partial \chi^2}{\partial \epsilon_i} = \sum_k 2 \left[\frac{x_k + \sum_j \epsilon_j \sigma_k^j - t_k}{\Delta^2_{k,\text{uncorr}}} \right] \sigma_k^i + 2\epsilon_i = 0, \tag{8.39}$$

which is solved directly to find the minimum χ^2. The summation indexes in Eq. 8.39 have been renamed in anticipation of the next step. Equation 8.39

can be reordered and written in linear algebra notation

$$Ax = c, \quad \text{where} \tag{8.40}$$

$$A_{ij} = 2 \cdot (i \neq j) + \sum_k \frac{2\sigma_k^i \sigma_k^j}{\Delta_{k,\text{uncorr}}^2}, \tag{8.41}$$

$$x_j = \epsilon_j, \tag{8.42}$$

$$c_i = \sum_k \frac{2(t_k - x_k)\sigma_k^i}{\Delta_{k,\text{uncorr}}^2}. \tag{8.43}$$

The matrix equation Eq. 8.40 is solved using standard linear algebra packages (ROOT [94] TMatrixD) for matrix inversion

$$x = A^{-1}c, \tag{8.44}$$

where A^{-1} denotes the inverse of the matrix A.

As a practical detail, the σ_k^i are in general not symmetric so the A_{ij} and c_i do actually depend on the signs of ϵ_i. This is solved by iterating the matrix inversion a few times (up to a maximum of 100) and selecting the σ_k^i according to the sign of ϵ_i. In normal cases 2–3 iterations are enough to find a stable solution, but if some parameters are very close to zero the iteration can end up flipping their sign back and forth. However, in these cases all the allowed solutions would be practically identical.

A more elegant solution to deal with the σ_k^i being asymmetric and Eq. 8.38 being non-derivative at $\epsilon_k = 0$ is to choose a quadratic formulation for the shifts [153]

$$\delta_{i,k}(\epsilon_k) = \epsilon_k \frac{\sigma_i^{+,k} - \sigma_i^{-,k}}{2} + \epsilon_k^2 \frac{\sigma_i^{+,k} - \sigma_i^{-,k}}{2}, \tag{8.45}$$

where the positive and negative uncertainties are explicitly written in the same equation, and the choice does not implicitly depend on ϵ_k anymore. Equation 8.45 agrees with Eq. 8.38 at $\epsilon_k = \pm 1$ and is derivative at $\epsilon_k = 0$.

The draw-back of using the quadratic Eq. 8.45 is that substitution back to Eq. 8.37 and taking partial derivatives does not result in a system of linear equations anymore and an analytical solution for the minimum χ^2 is not easy (if even possible) to come by. The minimum of Eq. 8.37 is therefore solved using standard χ^2 minimization techniques implemented in the Minuit package [154]. The solution for the linear problem is used as an initial guess for the quadratic case, and the minimization quickly converges to a minimum close to the linear case. The minimization procedure automatically returns the error matrix and estimates of the ϵ_k uncertainties.

8.11.2 Global fit results

Figure 8.25 shows the level of constraint the current data set can impose on the PDF uncertainties (shaded band) if the overall scale and non-perturbative correction uncertainties in the theory can be ignored in the context of the global fit. The error band and the data uncertainties represent a 68% confidence level, whereas the CTEQ6.5M PDF fit uncertainties are quoted to represent a 90% confidence level agreement with all data sets. To account for this difference in the choice of confidence levels, the theory shifts in Eq. 8.37 are weighted by a factor of 1.645, which scales the theory uncertainty to 68% confidence level. The resulting change in the fit is quite small as the theory shifts represent a minimal contribution to the overall χ^2 compared to the experimental shifts: $\chi^2_{\rm th} = 4.1$ compared to experimental $\chi^2_{\rm exp} = 37.0$.

The minimum χ^2 for the Eq. 8.37 modified with theory scale of 1.645 is 135.2, when fitted with the CTEQ6.5M set of PDF uncertainties shown in Fig. 8.23. The number of degrees of freedom in the fit is equal to the number of data points, 110. This gives $\chi^2/NDF = 1.23$, which is reasonable compared to the expectation of 1.00, but not perfect. The χ^2/NDF has an expected variation proportional to the number of degrees of freedom, $\Delta\chi^2/NDF = \sqrt{2/N}$, which in this case is 0.13. The corresponding χ^2 probability[9] for the fluctuation of +0.23 is 5.2%, which is improbable, but not impossible. The data and theory have possibly some shape disagreement, which, however, is not obvious by eye, or the degree of freedom for the uncertainty sources has been slightly underestimated. The latter option is favored by the observations with the effective set of sources, as discussed in Sec. 8.11.3.

The present global fit does not include the theory scale uncertainty or non-perturbative correction uncertainty to avoid issues with the overall scaling between data and theory. The CTEQ6.5M set of PDFs has been fitted to different data sets with a fixed choice of factorization and renormalization scales and a fixed description non-perturbative corrections. Using only the PDF uncertainties then provides a stringent test of consistency against all the other data sets used for the PDF fits, and of the validity of pQCD itself. The agreement between data and theory is good even when limiting the overall scale and low p_T freedom of the theory. Comparing Fig. 8.25 to the set of PDF eigenvectors in Fig. 8.23, the data seems to favor the lower high-x gluon PDF (PDF #13). Taking the correlation matrix of the fit at face value, the PDF eigenvector #13 has a favored value of -0.30 ± 0.09, which is among the highest shift to fit uncertainty ratios for the theory parameters.

[9] See *e.g.* http://www.fourmilab.ch/rpkp/experiments/analysis/chiCalc.html

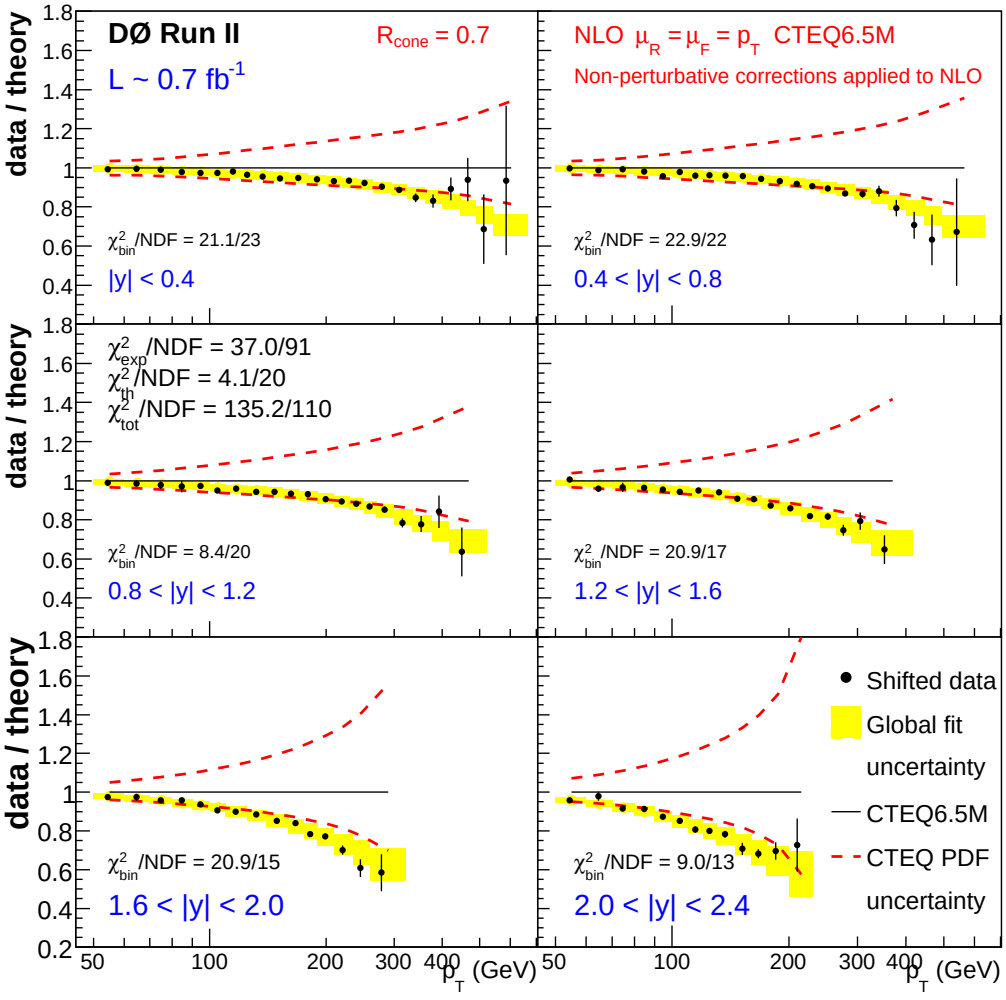

Figure 8.25: Data shifted by the amount favored by the global fit over the original theory in the central rapidity. The PDF uncertainty from the global fit (shaded band) is drawn around the shifted theory (center of the band). Also shown on the plot are the χ^2 for points in the bins (bin) against the shifted theory, experimental (exp) and theoretical (th) uncertainty shifts, and the global fit total for all bins $\chi^2_{\rm tot} = \chi^2_{\rm exp} + \chi^2_{\rm th} + \sum_k \chi^2_{{\rm bin},k}$. The NDF for the experimental and theoretical shifts equals the number of sources, the NDF for the bins and the global fit total equals the number of measurements.

8.11.3 Effective correlations

The detailed global fit results in Sec. 8.11.2 were obtained using a relatively large number (91) of systematic sources for data, listed in Tables 8.10–8.11.

This number is comparable to the total number of experimental systematic sources used *e.g.* by the CTEQ collaboration in their global PDF fits for more than twenty data sets [20], where the typical number of systematic sources is less than ten per data set. Many other groups rely on even less elaborate approaches to statistical analysis in their global fits. As a purely practical matter, the reduction in number and regrouping of the systematic sources benefits the communication of the results across the high-energy physics community. The current set of 91 systematic sources for 110 data points represents a fairly large table with about 10,000 entries. From a physics point of view the re-analysis of uncertainty correlations provides insight to their reliability and highlights the most important contributions.

Many of the systematic sources are small in magnitude and/or highly correlated in shape with other sources. Some of the sources are statistical in nature and could be reasonably assigned as uncorrelated in the analysis. This subsection describes a systematic approach to regroup and reduce the number of sources, without significantly impacting the overall quality of the fits or complicating the physical interpretation of the largest and most significant systematic sources.

The traditional interpretation of sources as independent uncertainties requires that the sum of all sources in quadrature must equal the total systematic uncertainty. When combining sources in pairs, they must consequently be added in quadrature. The second observation is that the set of all linear combinations of sources represents the overall freedom the global fit has. Unless the sources are linearly dependent (*i.e.* paired sources have the same shape), adding sources in quadrature will lose some of this freedom. Excessive loss of fit freedom can be avoided by pairing only sources with similar shapes whose orthogonal components (defined later) are small. Finally, adding a source to the statistical uncertainty will generally reduce correlations unless the source exhibits large anticorrelation between bins. This can be used to compensate the increase in correlation from source pairings.

To turn the above observations into a robust systematic approach for regrouping the sources it is necessary to define the notions of source size, shape similarity and orthogonality analytically. The natural measure for the size of a source is the impact it has on the overall χ^2 when shifted by 1 σ around the minimum. To aid in writing the definitions let us first define an inner product for sources h and g as

$$\langle h \cdot g \rangle = \sum_{i \in \text{bins}} \frac{h_i \cdot g_i}{\sigma^2_{\text{stat},i}}. \tag{8.46}$$

The size, or norm, of a source h can be written using this notation as

$$||h|| = \sqrt{\langle h \cdot h \rangle}. \tag{8.47}$$

The shape similarity of two sources h and g can be quantified by calculating their correlation, which is written in the notation of Eq. 8.46 as

$$\rho = \frac{\langle h \cdot g \rangle}{||h|| \cdot ||g||}. \tag{8.48}$$

This definitions yields 1.0 if the sources are fully correlated, -1.0 if fully anti-correlated and 0.0 if completely uncorrelated. The allowed values for ρ fall between these extrema. The source g can be broken into a component that is fully correlated with source h and another component that is fully uncorrelated by considering a linear transformation

$$g' = g - \alpha h. \tag{8.49}$$

When the orthogonality of h and g' is defined in terms of the inner product,

$$h \perp g' \Rightarrow \langle h \cdot g' \rangle = 0, \tag{8.50}$$

the Eq. 8.49 and Eq. 8.50 yield together

$$\alpha = \frac{\langle h \cdot g \rangle}{\langle h \cdot h \rangle}. \tag{8.51}$$

The g' is now the orthogonal component that is fully uncorrelated with source h. It is easy to show that $\langle g' \cdot g' \rangle \leq \langle g \cdot g \rangle$ and $\langle g' \cdot g' \rangle = \langle g \cdot g \rangle \Leftrightarrow h||g, \quad \langle g' \cdot g' \rangle = 0 \Leftrightarrow h \perp g$. Small values of $||g'||$ indicate that the sources can be combined with little impact on the freedom of the global fit.

In the practical regrouping procedure, the sources coming from statistical uncertainties in fits are first assigned as uncorrelated to compensate later artificial increase in correlations. This is particularly well-motivated for combined sources from resolution fits, because these are not broken into a large number of eigenvectors and as such overestimate the correlations across p_T. The same is true for the sources coming from η-dependence and ansatz fits. These sources are also fairly small in size. In contrast, the CC response fit sources are not assigned uncorrelated because the η-dependent JES corrections cause these sources to be fully correlated across rapidity for given p_T. They are also fairly large in magnitude and are provided as proper eigenvector factorizations to describe the correlation in p_T.

The remaining statistical and non-statistical sources are sorted in their size and are then iteratively recombined with other sources most similar in shape

and having smallest orthogonal components. As a practical rule of thumb, the sources are combined when their correlation is more than 80–90% and the orthogonal components have a norm smaller than 0.1. In comparison, the largest individual source, luminosity, has a norm of 0.7 and the total uncorrelated uncertainty has a norm of 0.45, which would rank as the 9^{th} largest source.

A few exceptions to the above general rules have been made. The trigger ratio sources are small and are mostly expected to deviate in the same direction above and below JT_65TT trigger[10] for consecutive triggers so these are regrouped even when the correlation between sources is relatively small. The EM scale and detector showering sources are very similar in shape and have a fairly small orthogonal component, but they are also some of the largest sources and represent distinct physical sources and are kept separate.

At the end of the iterative procedure the remaining set of sources no longer has any pairings with an orthogonal component less than 0.1 for the five most similar sources (with the exception of EM scale and detector showering). The smallest of the remaining sources has a norm of 0.10. The final reduced set has 23 correlated sources and one fully uncorrelated one, which is a significant reduction compared to the original 91 sources. It should be noted that the minimal set should have at least twelve sources to describe the decorrelations between six rapidity regions and low and high p_T ends for each region. The reduced set of 23 correlated sources and the total uncorrelated uncertainty are provided in Tables 8.13–8.36. The components of these sources (from the original set of 91) are listed in Table 8.9.

The global fit with CTEQ6.5 PDF uncertainties for the reduced set of 24 sources is shown in Fig. 8.26. The horizontal bars indicate the uncorrelated systematic uncertainty, whereas the lines show the statistical uncertainty. The shaded band shows the uncertainty for the shifted theory calculated using the correlation matrix of the fit. The fit is statistically compatible with the result for the full set of 91 sources shown in Fig. 8.25. The fit χ^2/NDF of 97.4/110 for the reduced set is also comparable to the $\chi^2/NDF = 135.2/110$ for the full set. The reduction in the χ^2 is due to assigning several fit uncertainty sources as fully uncorrelated. Most of these sources have not been factorized to eigenvectors and as such overestimate the correlations across p_T, yielding larger χ^2.

The distribution of shifts of data uncertainties in the global fit with the

[10]The most likely candidate for the small deviations of trigger ratios from 1.0 is the instantaneous luminosity dependence of PMT response in ICR. The average instantaneous luminosity increases almost monotonically with trigger p_T.

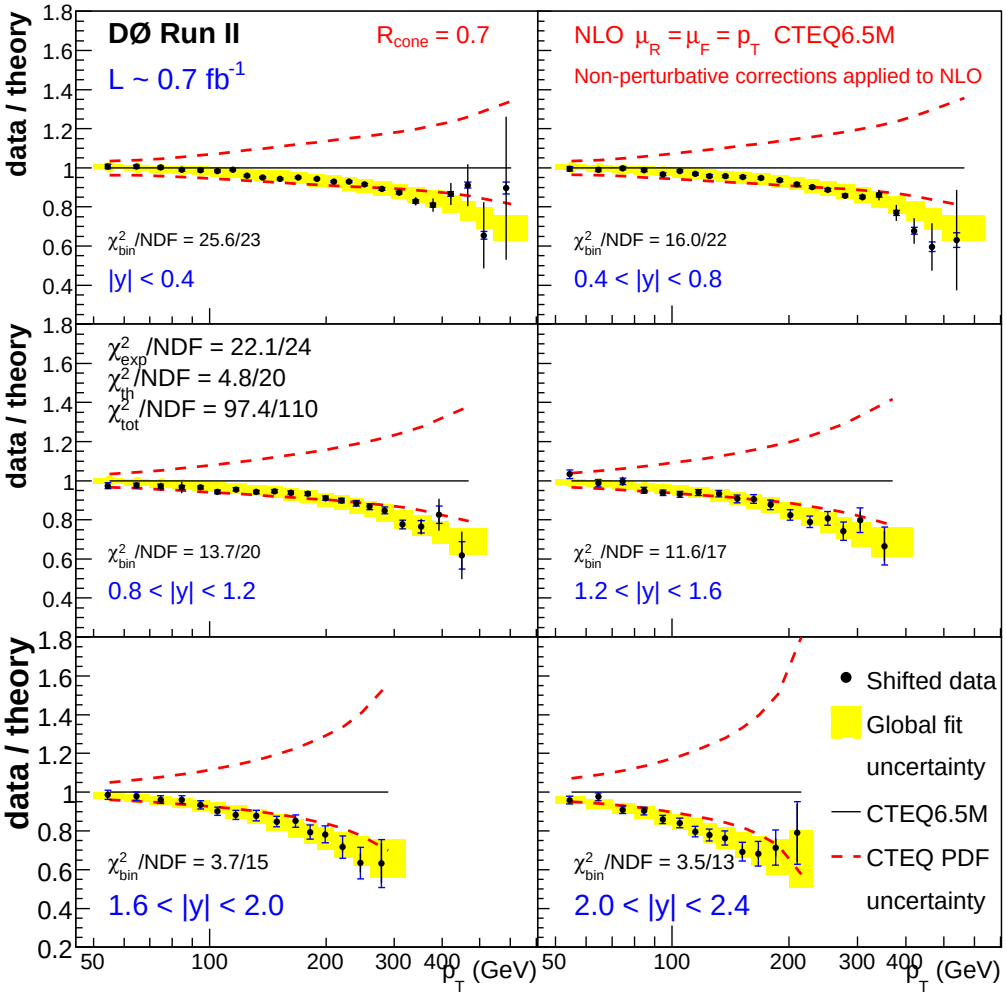

Figure 8.26: Data shifted by the amount favored by the global fit over the original theory in the central rapidity for a reduced set of experimental uncertainty sources. The PDF uncertainty from the global fit (shaded band) is drawn around the shifted theory (center of the band).

reduced set has an RMS of 0.91 and is compatible with a Gaussian distribution, as shown in Fig. 8.27(a). The χ^2 for the data shifts is 22.1 for the 23 sources, and the total χ^2/NDF is 97.4/110. This follows the *a priori* statistical assumptions for data uncertainties: RMS of 1.0, Gaussian distribution, $\chi^2_{\rm exp} = n_{\rm sources} = 23$ and $\chi^2_{\rm tot} = n_{\rm points} = 110$.

In contrast, the full set has RMS of 0.64 and a large number of sources with near-zero shifts, as shown in Fig. 8.27(b). The total χ^2 for data shifts is 37.0 for the 91 sources and the total χ^2/NDF is 135.2/110. This deviates slightly

from the *a priori* statistical assumptions and may be a consequence of having some systematic sources with non-physical shapes on the other hand, and some non-factorized fit uncertainty sources with too little p_T decorrelation on the other. Visually and by looking at the χ^2_{bin} for different bins the full set behaves slightly more as expected: $\chi^2_{\text{bin}}/NDF(\text{bin}) \sim 1.0$, point-by-point fluctuations proportional to the statistical and uncorrelated uncertainties. In conclusion, both the reduced and full set can be estimated to be equally physical, albeit slightly different descriptions of the uncertainty correlation information.

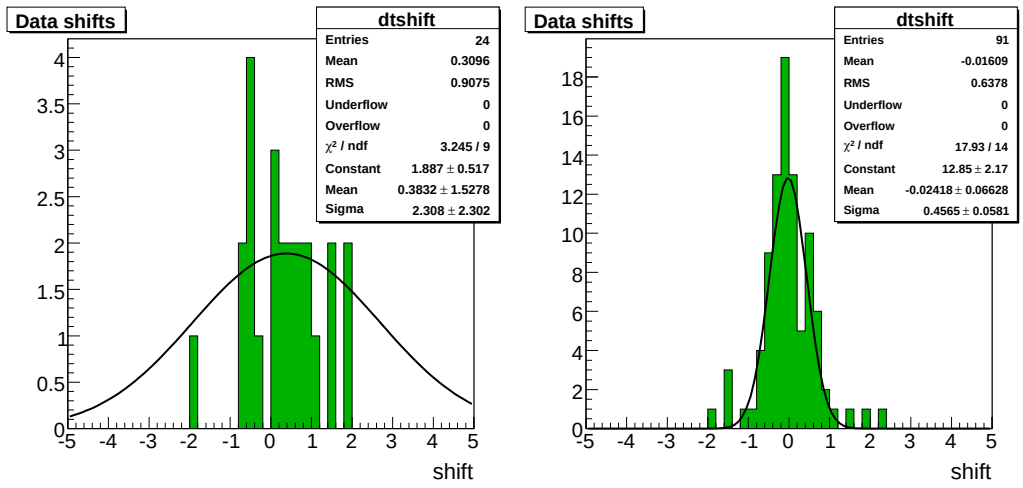

(a) (b)

Figure 8.27: Observed shifts of the data uncertainties in the global fit of the CTEQ6.5 PDF eigenvector set to data in the case of (a) reduced set of 23 correlated and one fully uncorrelated uncertainty, and of (b) full set of 91 correlated uncertainties.

Five representative leading sources of the reduced set, the total uncorrelated uncertainty and the total uncertainty are shown in Fig. 8.28 for CC and EC. These sources summarize nicely the leading systematics for the measurement: the EM scale uncertainty comes from the calibration of the EM calorimeter using $Z \rightarrow e^+e^-$ events, which is the first step in the JES calibration. The photon energy scale includes the uncertainty in the MC description of the difference in the electron and photon responses and the uncertainty in the amount of dead material in front of the calorimeter, which affects the response difference as a function of p_T. The high p_T uncertainty is due to differences in the fragmentation models of Pythia and Herwig, which leads to additional uncertainty in the high p_T extrapolation of the central response. The rapidity decorrelation uncertainty summarizes the uncertainty in the relative

response calibration between calorimeter regions and the detector showering uncertainty is primarily the uncertainty in the goodness-of-fit to showering templates in data. The detector showering uncertainty also includes significant contributions from other uncertainties in the showering measurement, such as sample purity, choice of ΔR matching between particle jets and reconstructed jets and the difference between tunes A and QW of Pythia. The source with the largest norm is the fully correlated luminosity uncertainty of 6.1%, which is not shown on the plot.

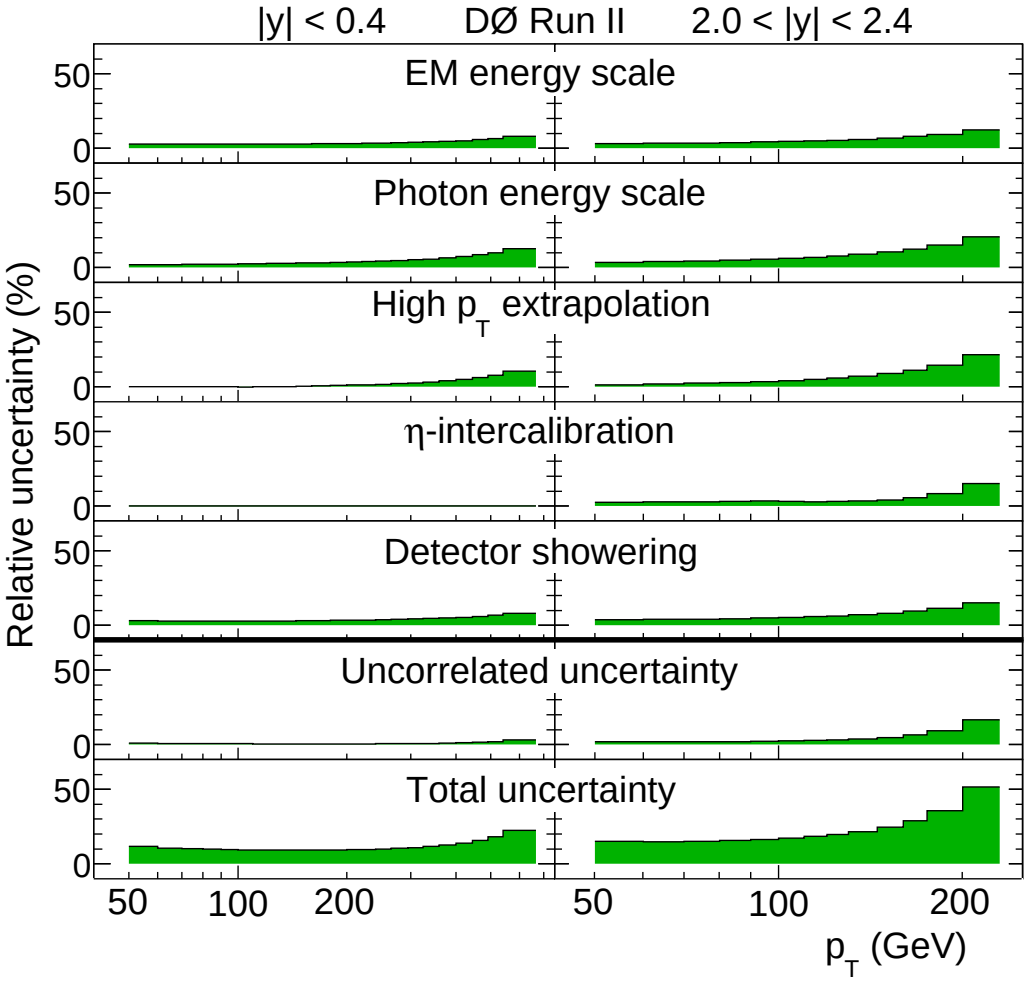

Figure 8.28: Five leading uncertainty sources, the total uncorrelated uncertainty and the total correlated uncertainty in CC and EC. The fully correlated luminosity uncertainty of 6.1% is not shown on the plot.

Overall it is evident that the leading sources of uncertainty in the measurement are due to the absolute response calibration in the central calorimeter and the overall normalization (luminosity). This leads to partially correlated uncertainty across p_T and full correlation across rapidity. The rapidity decorrelation uncertainties are sizable, but significantly smaller in comparison. By exploiting the change in shape across rapidity for different sources the global fit can further constrain the PDFs, as indicated by the significantly reduced uncertainty band in Fig. 8.26 and Fig. 8.25 compared to the original experimental uncertainty in Fig. 8.22.

8.12 MC closure of methods

The full analysis chain has been repeated on Monte Carlo and compared to the truth level answer to test the validity of the methods used in this analysis. This testing has been particularly useful to verify that the JES and resolution corrections are applied consistently, that no correction factors are applied twice and that the final result is indeed given at the DØ particle jet level. Not less important is it to test that the analysis programs are free of programming errors, "bugs", that could affect the results.

Figure 8.29 shows the MC cross section measurement versus particle level jet p_T spectrum that has been smoothed[11] with a fifth order logarithmic polynomial. The JES and jet p_T resolutions are both corrected back to MC truth level to avoid the large uncertainties otherwise coming from these sources. The uncertainty band reflects the statistical uncertainty in the JES and p_T resolution fits in MC truth, and the uncertainty of the ansatz fit in reconstructed MC. The JES and jet p_T resolutions were individually tested for MC closure in Chapters 6 and 7.

The MC efficiencies differ slightly from data so these have been redetermined from MC. The vertex acceptance has no luminosity dependence and the vertex distribution is Gaussian with $\sigma = 25$ cm. This gives a flat vertex acceptance of 95.5%. The calorimeter failure rate in MC (due to ZB overlay including bad events) is 2.8%. The Monte Carlo weights are normalized to a luminosity of 1.0 fb^{-1} before the bad LBN removal (4.4%) and event quality cuts, but after removing duplicate events. The JetID efficiency is about 99.0%. The muon/neutrino correction is applied to both reco and particle jets (2% on the cross section).

The reconstructed jets have been matched to particle jets within $\Delta R < 0.35$ at $p_T < 100$ GeV/c to avoid contamination by minimum bias (non-hard scatter) jets from the ZB overlay. In data the contribution from MB jets is automatically normalized by luminosity and does not affect the result. In MC the low $\hat{p_T}$ bins, *e.g.* the 5–10 GeV/c bin, get occasional hard scatter jets from the ZB overlay, which can end up in bins at $p_T > 50$ GeV/c. Because the lowest $\hat{p}_T$ bins have very large relative weights (thousands), a single jet or two can significantly impact the overall cross-section. In practice this is seen by the MC cross section going up by tens of percent, with an equally large error bar for the affected bins. The matching step stabilizes the low p_T measurement, but does not otherwise affect the result.

[11] The measured cross section is the local average of the particle level spectrum due to smearing so the smoothing removes some extra jumpiness from the particle level spectrum.

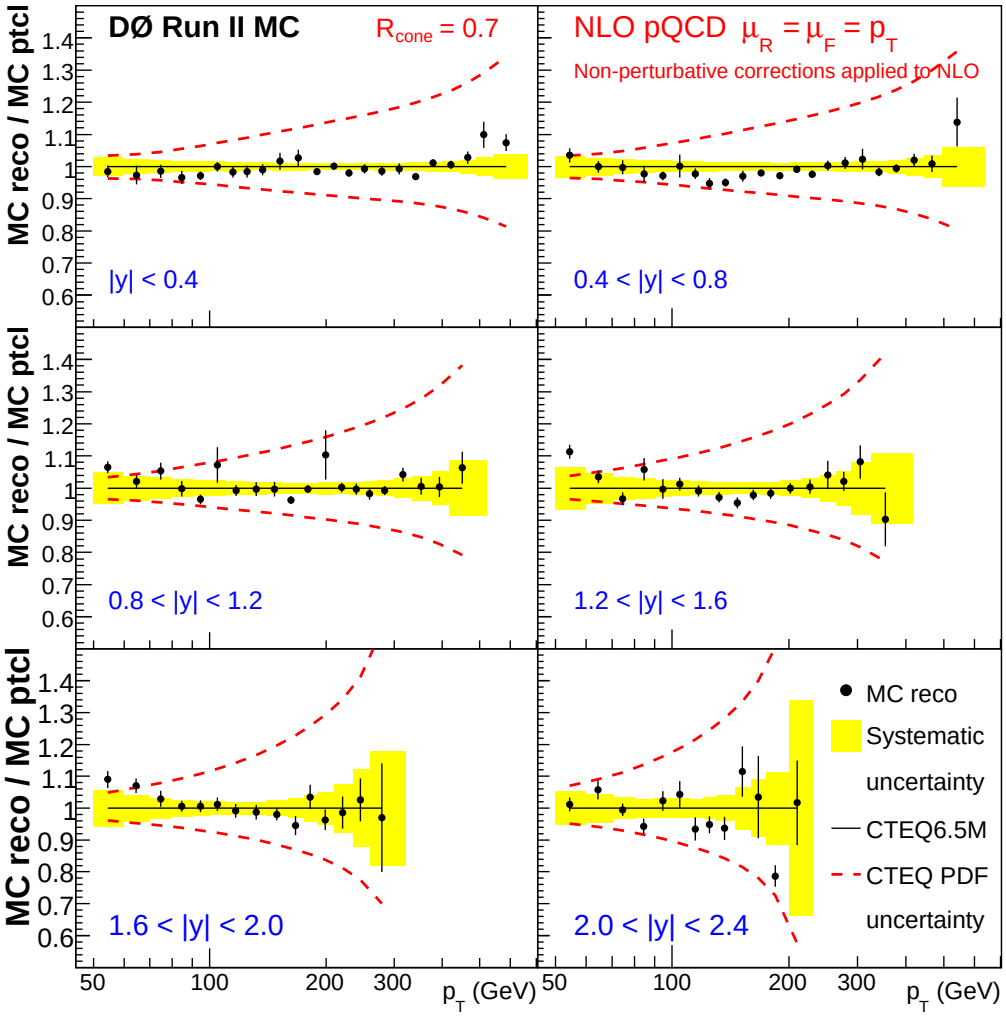

Figure 8.29: Monte Carlo closure of the methods used in this analysis. Both JES and jet p_T resolutions are taken directly from MC truth, as are the various efficiencies. The error band indicates the uncertainty in the truth level fits for JES and JER and the uncertainty in the ansatz fit.

As can be appreciated in Fig. 8.29, the analysis methods close well within the closure uncertainty, which is primarily coming from the truth level fits to the JES and resolution. The ansatz fit in reconstructed MC also contributes a little in the forward region. The closure uncertainty is dominated by the MC statistics, but it is significantly smaller than the measurement systematic uncertainty in data.

Table 8.9: Description and components of the uncertainty sources listed in Tables 8.13–8.36. The components are described in Tables 8.10–8.11.

Source	Description	Components
duncorr	Uncorrelated uncertainty	jes_049, jes_021, jes_020, jes_023, jes_022, jes_025, jes_024, jes_026, jes_029, jes_033, jes_047, jer_000, jer_001, jer_002, jer_003, jer_004, jer_005, jeu_000, jeu_001, jeu_002, jeu_003
dsys001	EM energy scale	jes_000, jes_010
dsys002	Photon energy scale	jes_002, jes_001, jes_006, jes_009
dsys003	High p_T extrapolation	jes_005
dsys004	η-intercalibration	jes_016, jes_017
dsys005	Detector showering	jes_037, jes_034, jes_036, jes_038, jes_044
dsys006	Luminosity	lum_000, vtx_000, vtx_001
dsys007	η-intercalibration	jes_011
dsys008	η-intercalibration	jes_012, jes_013
dsys009	η-intercalibration	jes_014, jes_015
dsys010	JES resolution bias	jes_018, jes_031, jes_030
dsys011	Resolution method	jer_012
dsys012	Non-Gaussian tails	jus_000, jid_002, jid_001, met_000
dsys013	Zero-suppression	jes_028, jes_027, jes_035, jes_048
dsys014	Resolution	jer_006, jer_007
dsys015	η-intercalibration fit	jes_019
dsys016	JES MPF bias	jes_040, jid_000, jer_008
dsys017	JES MPF bias	jes_041
dsys018	Rapidity unfolding	jrr_000
dsys019	Trigger matching	trg_013, trg_014, trg_008, trg_009, trg_003, trg_004, met_001
dsys020	Dijet response fit	jes_042
dsys021	Dijet response fit	jes_043, jes_046, jes_004, jes_003, jes_032, jes_045, jer_009, jer_010, jer_011, vtx_002
dsys022	Trigger matching	trg_005, trg_006, trg_000, trg_010, trg_007, trg_011, trg_002, trg_001, trg_012
dsys023	CC response fit	jes_008

Table 8.10: Description of the source components. The enumerators, if provided, are used in jetcorr/JESErrors and qcd_jet_caf/JERErrors classes.

Component	Description	Enumerator
Jet energy scale (JES)		
jes_000	EM energy scale	kEmScale
jes_001	Dead material	kRjetMaterial
jes_002	Photon energy scale	kPhShower
jes_003	Photon sample purity	kRjetPurity
jes_004	EM-jet background	kRjetBkgrShift
jes_005	High-p_T extrapolation	RjetHighPTFrag
jes_006	PDF uncertainty at high p_T	kRjetHighPTPDF
jes_008	Fit in CC	kRjetCCStat0
jes_009	Fit in CC	kRjetCCStat1
jes_010	Fit in CC	kRjetCCStat2
jes_011	η-intercalibration in CC	kEtaAvgResEta0
jes_012	η-intercalibration in IC	kEtaAvgResEta1
jes_013	η-intercalibration in IC	kEtaAvgResEta_1
jes_014	η-intercalibration in EC	kEtaAvgResEta2
jes_015	η-intercalibration in EC	kEtaAvgResEta_2
jes_016	η-intercalibration in EC	kEtaAvgResEta3
jes_017	η-intercalibration in EC	kEtaAvgResEta_3
jes_018	JES resolution bias	kEtaDijetResBiasEta
jes_019	η fit in CC	kEtaStatEta0
jes_020	η fit in IC	kEtaStatEta1
jes_021	η fit in IC	kEtaStatEta_1
jes_022	η fit in EC	kEtaStatEta2
jes_023	η fit in EC	kEtaStatEta_2
jes_024	η fit in EC	kEtaStatEta3
jes_025	η fit in EC	kEtaStatEta_3
jes_026	Zero suppression bias (ZSb)	kZSStat
jes_027	ZSb number of vertexes	kZSSysNPV
jes_028	ZSb jet matching	kZSSysDR
jes_029	MPF method bias (MPFb)	kMPFStat
jes_030	MPFb Pythia vs. Herwig	kMPFPhysics
jes_031	MPFb scaling	kMPFScaling
jes_032	MPF jet matching	kMPFdR
jes_033	Detector showering (Shw)	kShwStat
jes_034	Shw sample purity	kShwPurity
jes_035	Shw scaling	kShwScaling
jes_036	Shw jet mathing	kShwdR
jes_037	Shw template fits	kShwGOF
jes_038	Shw Tune A vs. Tune DW	kShwTune
jes_040	MPFb for dijets	kMPFDijetEta0
jes_041	MPFb for dijets	kMPFDijetEta1

Table 8.11: Description of the source components. The enumerators, if provided, are used in jetcorr/JESErrors and qcd_jet_caf/JERErrors classes.

Component	Description	Enumerator
Jet energy scale (JES)		
jes_042	Dijet CC response	kRdijetCCStat0
jes_043	Dijet CC response	kRdijetCCStat1
jes_044	Dijet CC response	kRdijetCCStat2
jes_045	Dijet CC response	kRdijetCCStat3
jes_046	Inclusive jet response	kRincljetSys
jes_047	Offset	kOffsetStat
jes_048	Offset systematics	kOffsetSys
jes_049	Empty placeholder	kRemainder
Jet p_T resolution		
jer_000	Fit in CC	kStatCC1
jer_001	Fit in CC	kStatCC2
jer_002	Fit in ICR	kStatIC1
jer_003	Fit in ICR	kStatIC2
jer_004	Fit in EC	kStatEC1
jer_005	Fit in EC	kStatEC2
jer_006	Fit residual	kFitSys
jer_007	Soft radiation correction	kKsoftSys
jer_008	Particle level imbalance	kPtclSys
jer_009	Noise in CC	kNoiseSysCC
jer_010	Noise in IC	kNoiseSysIC
jer_011	Noise in EC	kNoiseSysEC
jer_012	Method closure	kClosureSys
Jet p_T unfolding		
jeu_000	Unfolding	
jeu_001	Unfolding	
jeu_002	Unfolding	
jeu_003	Unfolding	
Jet identification (JetID)		
jid_000	JetID in CC	
jid_001	JetID in IC	
jid_002	JetID in EC	
Rapidity unfolding		
jrr_000	Rapidity unfolding	
Jet p_T resolution shape in unfolding		
jus_000	Unfolding shape	
Luminosity		
lum_000	Luminosity	
Missing-E_T (MET) cut		
met_000	MET	
met_001	MET	

Table 8.12: Description of the source components. The enumerators, if provided, are used in jetcorr/JESErrors and qcd_jet_caf/JERErrors classes.

Component	Description	Enumerator
Trigger matching		
trg_000	JT_15TT / JT_25TT	
trg_001	JT_25TT / JT_45TT	
trg_002	JT_45TT / JT_65TT	
trg_003	JT_95TT / JT_65TT	
trg_004	JT_125TT / JT_95TT	
trg_005	JT_15TT / JT_25TT in IC	
trg_006	JT_25TT / JT_45TT in IC	
trg_007	JT_45TT / JT_65TT in IC	
trg_008	JT_95TT / JT_65TT in IC	
trg_009	JT_125TT / JT_95TT in IC	
trg_010	JT_15TT / JT_25TT in IC	
trg_011	JT_25TT / JT_45TT in IC	
trg_012	JT_45TT / JT_65TT in IC	
trg_013	JT_95TT / JT_65TT in IC	
trg_014	JT_125TT / JT_95TT in IC	
Vertex acceptance and identification		
vtx_000	Vertex	
vtx_001	Vertex	
vtx_002	Vertex	

Table 8.13: Uncertainty sources for $|y| < 0.4$.

x1	x2	duncorr(%)	dsys001(%)	dsys002(%)	dsys003(%)	dsys004(%)	dsys005(%)
50	60	+1.0,-1.0	+2.6,-2.6	+2.1,-2.0	+0.0,+0.0	+0.0,+0.0	+2.7,-2.6
60	70	+0.8,-0.8	+2.6,-2.6	+2.2,-2.2	+0.0,+0.0	+0.0,+0.0	+2.7,-2.6
70	80	+0.7,-0.7	+2.6,-2.6	+2.4,-2.3	-0.1,+0.1	+0.0,+0.0	+2.7,-2.6
80	90	+0.6,-0.6	+2.7,-2.6	+2.5,-2.4	-0.1,+0.1	+0.0,+0.0	+2.7,-2.7
90	100	+0.6,-0.6	+2.7,-2.6	+2.6,-2.6	+0.1,-0.1	+0.0,+0.0	+2.8,-2.7
100	110	+0.5,-0.5	+2.7,-2.6	+2.7,-2.7	+0.2,-0.2	+0.0,+0.0	+2.8,-2.8
110	120	+0.5,-0.5	+2.7,-2.7	+2.8,-2.8	+0.4,-0.4	+0.0,+0.0	+2.9,-2.8
120	130	+0.5,-0.5	+2.8,-2.7	+3.0,-2.9	+0.5,-0.5	+0.0,+0.0	+2.9,-2.9
130	145	+0.5,-0.5	+2.8,-2.7	+3.1,-3.0	+0.7,-0.7	+0.0,+0.0	+3.0,-3.0
145	160	+0.5,-0.5	+2.9,-2.8	+3.3,-3.2	+0.9,-0.9	+0.0,+0.0	+3.1,-3.0
160	180	+0.5,-0.5	+3.0,-2.9	+3.5,-3.4	+1.1,-1.1	+0.0,+0.0	+3.2,-3.2
180	200	+0.5,-0.5	+3.1,-3.0	+3.7,-3.6	+1.4,-1.4	+0.0,+0.0	+3.4,-3.3
200	220	+0.5,-0.5	+3.2,-3.1	+4.0,-3.9	+1.7,-1.7	+0.0,+0.0	+3.5,-3.4
220	240	+0.5,-0.5	+3.3,-3.2	+4.3,-4.1	+2.0,-2.0	+0.0,+0.0	+3.6,-3.6
240	265	+0.6,-0.6	+3.5,-3.4	+4.6,-4.4	+2.4,-2.3	+0.0,+0.0	+3.8,-3.7
265	295	+0.6,-0.6	+3.7,-3.5	+5.0,-4.8	+2.8,-2.7	+0.0,+0.0	+4.0,-3.9
295	325	+0.7,-0.7	+3.9,-3.8	+5.5,-5.3	+3.4,-3.3	+0.0,+0.0	+4.2,-4.1
325	360	+0.8,-0.8	+4.2,-4.1	+6.0,-5.8	+4.0,-3.9	+0.0,+0.0	+4.5,-4.4
360	400	+1.0,-1.0	+4.6,-4.4	+6.8,-6.5	+4.8,-4.6	+0.0,+0.0	+4.9,-4.7
400	445	+1.2,-1.2	+5.1,-4.9	+7.8,-7.4	+5.9,-5.6	+0.0,+0.0	+5.3,-5.2
445	490	+1.5,-1.5	+5.8,-5.5	+9.0,-8.5	+7.4,-6.9	+0.0,+0.0	+5.9,-5.7
490	540	+2.0,-2.1	+6.6,-6.2	+10.5,-9.9	+9.1,-8.4	+0.0,+0.0	+6.6,-6.3
540	665	+3.0,-3.1	+8.0,-7.5	+13.1,-12.2	+12.2,-10.9	+0.0,+0.0	+7.9,-7.5

Table 8.14: Uncertainty sources for $|y| < 0.4$.

x1	x2	dsys006(%)	dsys007(%)	dsys008(%)	dsys009(%)	dsys010(%)	dsys011(%)
50	60	+6.5,-5.8	+0.5,-0.5	+0.0,+0.0	+0.0,+0.0	+1.0,-1.0	+0.4,-0.4
60	70	+6.5,-5.8	+0.5,-0.5	+0.0,+0.0	+0.0,+0.0	+0.9,-0.8	+0.3,-0.3
70	80	+6.5,-5.8	+0.5,-0.5	+0.0,+0.0	+0.0,+0.0	+0.8,-0.8	+0.3,-0.3
80	90	+6.5,-5.8	+0.5,-0.5	+0.0,+0.0	+0.0,+0.0	+0.7,-0.7	+0.2,-0.2
90	100	+6.5,-5.8	+0.5,-0.5	+0.0,+0.0	+0.0,+0.0	+0.6,-0.6	+0.2,-0.2
100	110	+6.5,-5.8	+0.5,-0.5	+0.0,+0.0	+0.0,+0.0	+0.6,-0.6	+0.2,-0.2
110	120	+6.5,-5.8	+0.5,-0.5	+0.0,+0.0	+0.0,+0.0	+0.6,-0.6	+0.2,-0.2
120	130	+6.5,-5.8	+0.5,-0.5	+0.0,+0.0	+0.0,+0.0	+0.6,-0.6	+0.2,-0.2
130	145	+6.5,-5.8	+0.6,-0.6	+0.0,+0.0	+0.0,+0.0	+0.5,-0.5	+0.2,-0.2
145	160	+6.5,-5.8	+0.6,-0.6	+0.0,+0.0	+0.0,+0.0	+0.5,-0.5	+0.2,-0.2
160	180	+6.5,-5.8	+0.6,-0.6	+0.0,+0.0	+0.0,+0.0	+0.5,-0.5	+0.2,-0.2
180	200	+6.5,-5.8	+0.6,-0.6	+0.0,+0.0	+0.0,+0.0	+0.5,-0.5	+0.1,-0.1
200	220	+6.5,-5.8	+0.6,-0.6	+0.0,+0.0	+0.0,+0.0	+0.5,-0.5	+0.1,-0.1
220	240	+6.5,-5.8	+0.5,-0.5	+0.0,+0.0	+0.0,+0.0	+0.5,-0.5	+0.1,-0.1
240	265	+6.5,-5.8	+0.5,-0.5	+0.0,+0.0	+0.0,+0.0	+0.5,-0.5	+0.1,-0.1
265	295	+6.5,-5.8	+0.4,-0.4	+0.0,+0.0	+0.0,+0.0	+0.5,-0.5	+0.1,-0.1
295	325	+6.5,-5.8	+0.4,-0.4	+0.0,+0.0	+0.0,+0.0	+0.6,-0.6	+0.1,-0.1
325	360	+6.5,-5.8	+0.4,-0.4	+0.0,+0.0	+0.0,+0.0	+0.6,-0.6	+0.1,-0.1
360	400	+6.5,-5.8	+0.4,-0.4	+0.0,+0.0	+0.0,+0.0	+0.6,-0.6	+0.1,-0.1
400	445	+6.5,-5.8	+0.6,-0.6	+0.0,+0.0	+0.0,+0.0	+0.7,-0.7	+0.2,-0.2
445	490	+6.5,-5.8	+0.8,-0.8	+0.0,+0.0	+0.0,+0.0	+0.8,-0.8	+0.2,-0.2
490	540	+6.5,-5.8	+1.3,-1.3	+0.0,+0.0	+0.0,+0.0	+0.9,-0.9	+0.2,-0.2
540	665	+6.5,-5.8	+1.5,-1.5	+0.0,+0.0	+0.0,+0.0	+1.0,-1.0	+0.2,-0.2

Table 8.15: Uncertainty sources for $|y| < 0.4$.

x1	x2	dsys012(%)	dsys013(%)	dsys014(%)	dsys015(%)	dsys016(%)	dsys017(%)
50	60	+0.3,-0.3	+3.2,-3.2	+1.1,-1.1	+0.0,+0.0	+2.3,-2.3	+0.0,+0.0
60	70	+0.2,-0.2	+2.9,-2.9	+0.9,-0.9	+0.0,+0.0	+2.1,-2.1	+0.0,+0.0
70	80	+0.1,-0.2	+2.7,-2.7	+0.8,-0.8	+0.0,+0.0	+1.9,-1.9	+0.0,+0.0
80	90	+0.1,-0.2	+2.5,-2.5	+0.8,-0.8	+0.0,+0.0	+1.8,-1.8	+0.0,+0.0
90	100	+0.1,-0.1	+2.3,-2.3	+0.7,-0.7	+0.0,+0.0	+1.7,-1.7	+0.0,+0.0
100	110	+0.1,-0.1	+2.2,-2.2	+0.7,-0.7	+0.0,+0.0	+1.6,-1.6	+0.0,+0.0
110	120	+0.1,-0.1	+2.1,-2.0	+0.6,-0.6	+0.0,+0.0	+1.5,-1.5	+0.0,+0.0
120	130	+0.1,-0.1	+2.0,-1.9	+0.6,-0.6	+0.0,+0.0	+1.5,-1.6	+0.0,+0.0
130	145	+0.2,-0.1	+1.8,-1.8	+0.6,-0.6	+0.0,+0.0	+1.6,-1.6	+0.0,+0.0
145	160	+0.1,-0.1	+1.7,-1.7	+0.6,-0.6	+0.0,+0.0	+1.6,-1.6	+0.0,+0.0
160	180	+0.1,-0.1	+1.6,-1.6	+0.6,-0.6	+0.0,+0.0	+1.6,-1.6	+0.0,+0.0
180	200	+0.1,-0.1	+1.5,-1.4	+0.6,-0.6	+0.0,+0.0	+1.7,-1.7	+0.0,+0.0
200	220	+0.1,-0.1	+1.4,-1.3	+0.6,-0.6	+0.0,+0.0	+1.7,-1.7	+0.0,+0.0
220	240	+0.1,-0.1	+1.3,-1.3	+0.6,-0.6	+0.0,+0.0	+1.8,-1.8	+0.0,+0.0
240	265	+0.1,-0.1	+1.2,-1.2	+0.6,-0.6	+0.0,+0.0	+1.9,-1.9	+0.0,+0.0
265	295	+0.1,-0.1	+1.1,-1.1	+0.7,-0.7	+0.0,+0.0	+2.0,-2.0	+0.0,+0.0
295	325	+0.1,-0.1	+1.1,-1.1	+0.7,-0.7	+0.0,+0.0	+2.1,-2.1	+0.0,+0.0
325	360	+0.1,-0.1	+1.0,-1.0	+0.8,-0.8	+0.0,+0.0	+2.3,-2.3	+0.0,+0.0
360	400	+0.1,-0.1	+1.0,-1.0	+0.9,-0.9	+0.0,+0.0	+2.6,-2.6	+0.0,+0.0
400	445	+0.1,-0.1	+1.0,-1.0	+1.1,-1.1	+0.0,+0.0	+3.0,-3.0	+0.0,+0.0
445	490	+0.1,-0.1	+1.1,-1.1	+1.3,-1.3	+0.0,+0.0	+3.5,-3.5	+0.0,+0.0
490	540	+0.1,-0.1	+1.2,-1.2	+1.7,-1.7	+0.0,+0.0	+4.2,-4.1	+0.0,+0.0
540	665	+0.1,-0.1	+1.4,-1.3	+2.4,-2.4	+0.0,+0.0	+5.5,-5.4	+0.0,+0.0

Table 8.16: Uncertainty sources for $|y| < 0.4$.

x1	x2	dsys018(%)	dsys019(%)	dsys020(%)	dsys021(%)	dsys022(%)	dsys023(%)
50	60	+0.1,-0.1	+0.2,-0.2	-1.2,+1.2	+3.9,-3.8	+2.1,-2.1	-0.3,+0.3
60	70	+0.1,-0.1	+0.2,-0.2	-1.7,+1.7	+3.0,-3.0	+1.4,-1.4	-0.3,+0.3
70	80	+0.0,-0.0	+0.2,-0.2	-1.9,+2.0	+2.4,-2.3	+1.4,-1.4	-0.4,+0.4
80	90	+0.0,-0.0	+0.2,-0.2	-2.0,+2.1	+1.9,-1.8	+1.4,-1.4	-0.4,+0.4
90	100	+0.0,-0.0	+0.2,-0.2	-2.0,+2.1	+1.5,-1.5	+1.4,-1.4	-0.4,+0.4
100	110	+0.0,-0.0	+0.2,-0.2	-2.0,+2.0	+1.2,-1.2	+1.0,-1.0	-0.4,+0.4
110	120	+0.0,-0.0	+0.2,-0.2	-1.9,+2.0	+0.9,-0.9	+1.0,-1.0	-0.4,+0.4
120	130	+0.0,-0.0	+0.2,-0.2	-1.8,+1.9	+0.7,-0.7	+0.0,+0.0	-0.4,+0.4
130	145	+0.0,-0.0	+0.5,-0.5	-1.7,+1.7	+0.6,-0.6	+0.0,+0.0	-0.4,+0.4
145	160	+0.0,-0.0	+0.5,-0.5	-1.5,+1.5	+0.4,-0.4	+0.0,+0.0	-0.3,+0.3
160	180	+0.0,-0.0	+0.7,-0.7	-1.3,+1.3	+0.3,-0.3	+0.0,+0.0	-0.3,+0.3
180	200	+0.0,-0.0	+0.7,-0.7	-1.0,+1.0	+0.3,-0.3	+0.0,+0.0	-0.2,+0.2
200	220	+0.0,-0.0	+0.9,-0.9	-0.7,+0.7	+0.4,-0.4	+0.0,+0.0	-0.2,+0.2
220	240	+0.0,-0.0	+0.9,-0.9	-0.5,+0.5	+0.4,-0.4	+0.0,+0.0	-0.1,+0.1
240	265	+0.0,-0.0	+0.9,-0.9	-0.2,+0.2	+0.5,-0.5	+0.0,+0.0	+0.1,-0.1
265	295	+0.0,-0.0	+0.9,-0.9	+0.1,-0.1	+0.6,-0.6	+0.0,+0.0	+0.2,-0.2
295	325	+0.0,-0.0	+0.9,-0.9	+0.4,-0.4	+0.7,-0.7	+0.0,+0.0	+0.4,-0.4
325	360	+0.0,-0.0	+0.9,-0.9	+0.7,-0.7	+0.7,-0.7	+0.0,+0.0	+0.7,-0.7
360	400	+0.0,-0.0	+0.9,-0.9	+1.0,-0.9	+0.8,-0.8	+0.0,+0.0	+1.0,-1.0
400	445	+0.0,-0.0	+0.9,-0.9	+1.1,-1.1	+0.9,-0.9	+0.0,+0.0	+1.5,-1.5
445	490	+0.0,-0.0	+0.9,-0.9	+1.2,-1.2	+0.9,-0.9	+0.0,+0.0	+2.2,-2.1
490	540	+0.0,-0.0	+0.9,-0.9	+1.1,-1.1	+1.0,-1.0	+0.0,+0.0	+3.0,-2.9
540	665	+0.0,-0.0	+0.9,-0.9	+0.5,-0.5	+1.2,-1.2	+0.0,+0.0	+4.5,-4.3

Table 8.17: Uncertainty sources for $0.4 < |y| < 0.8$.

x1	x2	duncorr(%)	dsys001(%)	dsys002(%)	dsys003(%)	dsys004(%)	dsys005(%)
50	60	+1.1,-1.1	+2.7,-2.6	+2.2,-2.2	+0.0,+0.0	+0.0,+0.0	+2.8,-2.7
60	70	+0.9,-0.9	+2.7,-2.6	+2.4,-2.3	-0.2,+0.2	+0.0,+0.0	+2.8,-2.7
70	80	+0.8,-0.8	+2.7,-2.6	+2.5,-2.5	-0.0,+0.0	+0.0,+0.0	+2.8,-2.7
80	90	+0.7,-0.7	+2.7,-2.6	+2.6,-2.6	+0.2,-0.2	+0.0,+0.0	+2.8,-2.8
90	100	+0.6,-0.6	+2.7,-2.6	+2.8,-2.7	+0.3,-0.3	+0.0,+0.0	+2.9,-2.8
100	110	+0.6,-0.6	+2.8,-2.7	+2.9,-2.9	+0.5,-0.5	+0.0,+0.0	+3.0,-2.9
110	120	+0.6,-0.6	+2.8,-2.7	+3.0,-3.0	+0.7,-0.7	+0.0,+0.0	+3.0,-3.0
120	130	+0.6,-0.6	+2.8,-2.8	+3.2,-3.1	+0.8,-0.8	+0.0,+0.0	+3.1,-3.0
130	145	+0.6,-0.6	+2.9,-2.8	+3.3,-3.3	+1.0,-1.0	+0.0,+0.0	+3.2,-3.1
145	160	+0.5,-0.6	+3.0,-2.9	+3.5,-3.5	+1.3,-1.2	+0.0,+0.0	+3.3,-3.2
160	180	+0.6,-0.6	+3.1,-3.0	+3.8,-3.7	+1.5,-1.5	+0.0,+0.0	+3.4,-3.4
180	200	+0.6,-0.6	+3.2,-3.1	+4.1,-4.0	+1.9,-1.8	+0.0,+0.0	+3.6,-3.5
200	220	+0.6,-0.6	+3.4,-3.3	+4.4,-4.2	+2.2,-2.2	+0.0,+0.0	+3.8,-3.7
220	240	+0.7,-0.7	+3.5,-3.4	+4.7,-4.6	+2.6,-2.5	+0.0,+0.0	+4.0,-3.9
240	265	+0.7,-0.7	+3.7,-3.6	+5.1,-4.9	+3.0,-2.9	+0.0,+0.0	+4.2,-4.1
265	295	+0.8,-0.8	+4.0,-3.8	+5.6,-5.4	+3.5,-3.4	+0.0,+0.0	+4.5,-4.3
295	325	+0.9,-0.9	+4.3,-4.2	+6.2,-6.0	+4.2,-4.0	+0.0,+0.0	+4.8,-4.7
325	360	+1.1,-1.1	+4.7,-4.5	+7.0,-6.7	+5.0,-4.8	+0.0,+0.0	+5.2,-5.0
360	400	+1.3,-1.3	+5.3,-5.0	+7.9,-7.6	+6.1,-5.8	+0.0,+0.0	+5.7,-5.5
400	445	+1.8,-1.8	+6.0,-5.7	+9.3,-8.8	+7.6,-7.0	+0.0,+0.0	+6.4,-6.1
445	495	+2.4,-2.4	+7.0,-6.6	+11.1,-10.4	+9.6,-8.8	+0.0,+0.0	+7.3,-7.0
495	635	+3.7,-3.8	+8.6,-8.0	+14.1,-13.0	+13.1,-11.7	+0.0,+0.0	+8.8,-8.3

Table 8.18: Uncertainty sources for $0.4 < |y| < 0.8$.

x1	x2	dsys006(%)	dsys007(%)	dsys008(%)	dsys009(%)	dsys010(%)	dsys011(%)
50	60	+6.5,-5.8	+2.6,-2.5	+0.0,+0.0	+0.0,+0.0	+1.3,-1.3	-1.2,+1.2
60	70	+6.5,-5.8	+2.6,-2.5	+0.0,+0.0	+0.0,+0.0	+1.2,-1.2	-1.0,+1.0
70	80	+6.5,-5.8	+2.6,-2.5	+0.0,+0.0	+0.0,+0.0	+1.1,-1.1	-0.8,+0.8
80	90	+6.5,-5.8	+2.6,-2.6	+0.0,+0.0	+0.0,+0.0	+1.1,-1.0	-0.7,+0.6
90	100	+6.5,-5.8	+2.7,-2.6	+0.0,+0.0	+0.0,+0.0	+1.0,-1.0	-0.5,+0.5
100	110	+6.5,-5.8	+2.7,-2.6	+0.0,+0.0	+0.0,+0.0	+1.0,-1.0	-0.5,+0.4
110	120	+6.5,-5.8	+2.8,-2.7	+0.0,+0.0	+0.0,+0.0	+1.0,-1.0	-0.4,+0.4
120	130	+6.5,-5.8	+2.8,-2.7	+0.0,+0.0	+0.0,+0.0	+1.0,-1.0	-0.3,+0.3
130	145	+6.5,-5.8	+2.9,-2.8	+0.0,+0.0	+0.0,+0.0	+1.0,-1.0	-0.3,+0.3
145	160	+6.5,-5.8	+3.0,-2.9	+0.0,+0.0	+0.0,+0.0	+1.0,-1.0	-0.2,+0.2
160	180	+6.5,-5.8	+3.1,-3.0	+0.0,+0.0	+0.0,+0.0	+1.0,-1.0	-0.1,+0.1
180	200	+6.5,-5.8	+3.2,-3.0	+0.0,+0.0	+0.0,+0.0	+1.0,-1.0	-0.0,+0.0
200	220	+6.5,-5.8	+3.2,-3.1	+0.0,+0.0	+0.0,+0.0	+1.1,-1.1	+0.0,-0.0
220	240	+6.5,-5.8	+3.2,-3.1	+0.0,+0.0	+0.0,+0.0	+1.1,-1.1	+0.1,-0.1
240	265	+6.5,-5.8	+3.3,-3.2	+0.0,+0.0	+0.0,+0.0	+1.2,-1.1	+0.2,-0.2
265	295	+6.5,-5.8	+3.5,-3.4	+0.0,+0.0	+0.0,+0.0	+1.2,-1.2	+0.3,-0.3
295	325	+6.5,-5.8	+3.8,-3.7	+0.0,+0.0	+0.0,+0.0	+1.3,-1.3	+0.4,-0.4
325	360	+6.5,-5.8	+4.2,-4.0	+0.0,+0.0	+0.0,+0.0	+1.4,-1.4	+0.5,-0.5
360	400	+6.5,-5.8	+4.8,-4.6	+0.0,+0.0	+0.0,+0.0	+1.5,-1.5	+0.8,-0.8
400	445	+6.5,-5.8	+5.5,-5.2	+0.0,+0.0	+0.0,+0.0	+1.7,-1.7	+1.1,-1.1
445	495	+6.5,-5.8	+6.8,-6.4	+0.0,+0.0	+0.0,+0.0	+2.0,-1.9	+1.6,-1.6
495	635	+6.5,-5.8	+9.8,-9.0	+0.0,+0.0	+0.0,+0.0	+2.4,-2.4	+2.6,-2.6

Table 8.19: Uncertainty sources for $0.4 < |y| < 0.8$.

x1	x2	dsys012(%)	dsys013(%)	dsys014(%)	dsys015(%)	dsys016(%)	dsys017(%)
50	60	+0.5,-0.4	+3.4,-3.3	+1.2,-1.2	+0.4,-0.4	+2.4,-2.2	+0.0,+0.0
60	70	+0.3,-0.2	+3.1,-3.0	+1.1,-1.1	+0.4,-0.4	+2.1,-1.9	+0.0,+0.0
70	80	+0.2,-0.1	+2.8,-2.8	+1.0,-1.0	+0.4,-0.4	+1.9,-1.7	+0.0,+0.0
80	90	+0.2,-0.1	+2.6,-2.6	+0.9,-0.9	+0.4,-0.4	+1.7,-1.6	+0.0,+0.0
90	100	+0.2,-0.1	+2.4,-2.4	+0.8,-0.8	+0.4,-0.4	+1.6,-1.5	+0.0,+0.0
100	110	+0.2,-0.1	+2.3,-2.3	+0.8,-0.8	+0.4,-0.4	+1.5,-1.4	+0.0,+0.0
110	120	+0.2,-0.1	+2.2,-2.1	+0.8,-0.8	+0.4,-0.4	+1.4,-1.4	+0.0,+0.0
120	130	+0.2,-0.1	+2.0,-2.0	+0.7,-0.7	+0.4,-0.4	+1.4,-1.4	+0.0,+0.0
130	145	+0.2,-0.2	+1.9,-1.9	+0.7,-0.7	+0.4,-0.4	+1.5,-1.4	+0.0,+0.0
145	160	+0.2,-0.1	+1.8,-1.8	+0.7,-0.7	+0.4,-0.4	+1.5,-1.5	+0.0,+0.0
160	180	+0.2,-0.1	+1.7,-1.7	+0.7,-0.7	+0.4,-0.4	+1.6,-1.5	+0.0,+0.0
180	200	+0.2,-0.1	+1.6,-1.5	+0.7,-0.7	+0.5,-0.5	+1.6,-1.6	+0.0,+0.0
200	220	+0.2,-0.1	+1.5,-1.5	+0.7,-0.7	+0.5,-0.5	+1.7,-1.7	+0.0,+0.0
220	240	+0.1,-0.1	+1.4,-1.4	+0.8,-0.8	+0.5,-0.5	+1.8,-1.8	+0.0,+0.0
240	265	+0.1,-0.1	+1.3,-1.3	+0.8,-0.8	+0.6,-0.6	+1.9,-1.9	+0.0,+0.0
265	295	+0.1,-0.1	+1.3,-1.3	+0.9,-0.9	+0.8,-0.8	+2.1,-2.0	+0.0,+0.0
295	325	+0.1,-0.1	+1.2,-1.2	+1.0,-1.0	+1.0,-1.0	+2.3,-2.3	+0.0,+0.0
325	360	+0.1,-0.1	+1.2,-1.2	+1.1,-1.1	+1.3,-1.3	+2.6,-2.5	+0.0,+0.0
360	400	+0.1,-0.1	+1.2,-1.2	+1.3,-1.3	+1.8,-1.8	+3.0,-2.9	+0.0,+0.0
400	445	+0.1,-0.1	+1.3,-1.2	+1.6,-1.6	+2.3,-2.2	+3.5,-3.5	+0.0,+0.0
445	495	+0.1,-0.1	+1.3,-1.3	+2.1,-2.1	+3.0,-2.9	+4.4,-4.3	+0.0,+0.0
495	635	+0.1,-0.1	+1.6,-1.5	+3.1,-3.1	+4.3,-4.1	+6.1,-5.9	+0.0,+0.0

Table 8.20: Uncertainty sources for $0.4 < |y| < 0.8$.

x1	x2	dsys018(%)	dsys019(%)	dsys020(%)	dsys021(%)	dsys022(%)	dsys023(%)
50	60	+0.0,-0.0	+0.2,-0.2	-1.2,+1.2	+3.4,-3.3	+2.1,-2.1	-0.3,+0.3
60	70	+0.0,-0.0	+0.2,-0.2	-1.7,+1.7	+2.6,-2.5	+1.4,-1.4	-0.3,+0.3
70	80	+0.0,-0.0	+0.2,-0.2	-1.9,+2.0	+2.0,-2.0	+1.4,-1.4	-0.4,+0.4
80	90	+0.0,-0.0	+0.2,-0.2	-2.0,+2.1	+1.6,-1.6	+1.4,-1.4	-0.4,+0.4
90	100	+0.0,-0.0	+0.2,-0.2	-2.1,+2.1	+1.3,-1.2	+1.4,-1.4	-0.4,+0.4
100	110	+0.0,-0.0	+0.2,-0.2	-2.0,+2.1	+1.0,-1.0	+1.0,-1.0	-0.4,+0.4
110	120	+0.0,-0.0	+0.2,-0.2	-1.9,+2.0	+0.8,-0.8	+1.0,-1.0	-0.4,+0.4
120	130	+0.0,-0.0	+0.2,-0.2	-1.8,+1.9	+0.6,-0.6	+0.0,+0.0	-0.4,+0.4
130	145	+0.0,-0.0	+0.5,-0.5	-1.7,+1.7	+0.5,-0.5	+0.0,+0.0	-0.4,+0.4
145	160	+0.0,-0.0	+0.5,-0.5	-1.5,+1.5	+0.4,-0.4	+0.0,+0.0	-0.3,+0.4
160	180	+0.0,-0.0	+0.7,-0.7	-1.3,+1.3	+0.3,-0.3	+0.0,+0.0	-0.3,+0.3
180	200	+0.0,-0.0	+0.7,-0.7	-1.0,+1.0	+0.3,-0.3	+0.0,+0.0	-0.2,+0.2
200	220	+0.0,-0.0	+0.9,-0.9	-0.7,+0.7	+0.4,-0.4	+0.0,+0.0	-0.1,+0.1
220	240	+0.0,-0.0	+0.9,-0.9	-0.5,+0.5	+0.4,-0.4	+0.0,+0.0	-0.0,+0.0
240	265	+0.0,-0.0	+0.9,-0.9	-0.2,+0.2	+0.5,-0.5	+0.0,+0.0	+0.1,-0.1
265	295	+0.0,-0.0	+0.9,-0.9	+0.2,-0.2	+0.6,-0.6	+0.0,+0.0	+0.3,-0.3
295	325	+0.0,-0.0	+0.9,-0.9	+0.5,-0.5	+0.7,-0.7	+0.0,+0.0	+0.5,-0.5
325	360	+0.0,-0.0	+0.9,-0.9	+0.8,-0.8	+0.8,-0.8	+0.0,+0.0	+0.8,-0.8
360	400	+0.0,-0.0	+0.9,-0.9	+1.1,-1.1	+0.9,-0.9	+0.0,+0.0	+1.2,-1.2
400	445	+0.1,-0.1	+0.9,-0.9	+1.3,-1.3	+1.0,-1.0	+0.0,+0.0	+1.8,-1.8
445	495	+0.1,-0.1	+0.9,-0.9	+1.4,-1.4	+1.1,-1.1	+0.0,+0.0	+2.7,-2.6
495	635	+0.3,-0.3	+0.9,-0.9	+1.1,-1.1	+1.2,-1.2	+0.0,+0.0	+4.2,-4.1

Table 8.21: Uncertainty sources for $0.8 < |y| < 1.2$.

x1	x2	duncorr(%)	dsys001(%)	dsys002(%)	dsys003(%)	dsys004(%)	dsys005(%)
50	60	+1.5,-1.5	+2.7,-2.6	+2.4,-2.4	-0.0,+0.0	+0.0,+0.0	+2.9,-2.8
60	70	+1.2,-1.3	+2.7,-2.6	+2.6,-2.6	+0.2,-0.2	+0.0,+0.0	+2.9,-2.8
70	80	+1.1,-1.1	+2.7,-2.6	+2.8,-2.7	+0.4,-0.4	+0.0,+0.0	+2.9,-2.8
80	90	+1.0,-1.0	+2.7,-2.6	+2.9,-2.8	+0.6,-0.6	+0.0,+0.0	+3.0,-2.9
90	100	+0.9,-0.9	+2.8,-2.7	+3.1,-3.0	+0.8,-0.8	+0.0,+0.0	+3.0,-3.0
100	110	+0.9,-0.9	+2.8,-2.7	+3.2,-3.1	+1.0,-1.0	+0.0,+0.0	+3.1,-3.0
110	125	+0.8,-0.8	+2.9,-2.8	+3.4,-3.3	+1.3,-1.2	+0.0,+0.0	+3.2,-3.1
125	140	+0.8,-0.8	+3.0,-2.9	+3.6,-3.5	+1.6,-1.5	+0.0,+0.0	+3.3,-3.3
140	155	+0.8,-0.8	+3.1,-3.0	+3.9,-3.8	+1.8,-1.8	+0.0,+0.0	+3.5,-3.4
155	170	+0.9,-0.9	+3.2,-3.1	+4.1,-4.0	+2.1,-2.1	+0.0,+0.0	+3.6,-3.5
170	190	+1.0,-1.0	+3.3,-3.2	+4.4,-4.3	+2.5,-2.4	+0.0,+0.0	+3.8,-3.7
190	210	+1.1,-1.1	+3.5,-3.4	+4.8,-4.6	+2.9,-2.8	+0.0,+0.0	+4.0,-3.9
210	230	+1.2,-1.2	+3.7,-3.6	+5.2,-5.0	+3.3,-3.2	+0.0,+0.0	+4.3,-4.2
230	250	+1.3,-1.3	+4.0,-3.8	+5.6,-5.4	+3.8,-3.6	+0.0,+0.0	+4.6,-4.4
250	270	+1.5,-1.5	+4.2,-4.1	+6.1,-5.9	+4.3,-4.1	+0.0,+0.0	+4.8,-4.7
270	300	+1.8,-1.8	+4.6,-4.4	+6.7,-6.5	+5.0,-4.8	+0.0,+0.0	+5.2,-5.1
300	335	+2.3,-2.3	+5.1,-4.9	+7.7,-7.3	+6.0,-5.7	+0.0,+0.0	+5.7,-5.6
335	375	+3.1,-3.1	+5.8,-5.5	+9.0,-8.5	+7.4,-6.9	+0.0,+0.0	+6.5,-6.2
375	415	+4.5,-4.5	+6.7,-6.3	+10.7,-10.0	+9.4,-8.6	+0.0,+0.0	+7.4,-7.0
415	520	+7.1,-7.0	+8.0,-7.5	+13.2,-12.2	+12.5,-11.1	+0.0,+0.0	+8.7,-8.2

Table 8.22: Uncertainty sources for $0.8 < |y| < 1.2$.

x1	x2	dsys006(%)	dsys007(%)	dsys008(%)	dsys009(%)	dsys010(%)	dsys011(%)
50	60	+6.5,-5.8	+2.6,-2.5	+0.0,+0.0	+0.0,+0.0	+2.0,-1.9	-0.9,+0.9
60	70	+6.5,-5.8	+2.6,-2.5	+0.0,+0.0	+0.0,+0.0	+1.8,-1.8	-0.9,+0.9
70	80	+6.5,-5.8	+2.6,-2.5	+0.0,+0.0	+0.0,+0.0	+1.7,-1.7	-1.0,+1.0
80	90	+6.5,-5.8	+2.7,-2.6	+0.0,+0.0	+0.0,+0.0	+1.7,-1.7	-1.0,+1.0
90	100	+6.5,-5.8	+2.7,-2.6	+0.0,+0.0	+0.0,+0.0	+1.7,-1.7	-1.1,+1.1
100	110	+6.5,-5.8	+2.8,-2.7	+0.0,+0.0	+0.0,+0.0	+1.7,-1.7	-1.1,+1.1
110	125	+6.5,-5.8	+2.8,-2.8	+0.0,+0.0	+0.0,+0.0	+1.7,-1.7	-1.2,+1.2
125	140	+6.5,-5.8	+2.9,-2.8	+0.0,+0.0	+0.0,+0.0	+1.7,-1.7	-1.3,+1.3
140	155	+6.5,-5.8	+3.1,-3.0	+0.0,+0.0	+0.0,+0.0	+1.8,-1.8	-1.4,+1.4
155	170	+6.5,-5.8	+3.2,-3.1	+0.0,+0.0	+0.0,+0.0	+1.8,-1.8	-1.5,+1.5
170	190	+6.5,-5.8	+3.3,-3.2	+0.0,+0.0	+0.0,+0.0	+1.9,-1.9	-1.7,+1.7
190	210	+6.5,-5.8	+3.5,-3.3	+0.0,+0.0	+0.0,+0.0	+2.0,-2.0	-1.9,+1.9
210	230	+6.5,-5.8	+3.7,-3.6	+0.0,+0.0	+0.0,+0.0	+2.1,-2.1	-2.2,+2.2
230	250	+6.5,-5.8	+4.0,-3.9	+0.0,+0.0	+0.0,+0.0	+2.2,-2.2	-2.4,+2.4
250	270	+6.5,-5.8	+4.4,-4.3	+0.0,+0.0	+0.0,+0.0	+2.3,-2.3	-2.8,+2.8
270	300	+6.5,-5.8	+5.1,-4.8	+0.0,+0.0	+0.0,+0.0	+2.5,-2.4	-3.3,+3.3
300	335	+6.5,-5.8	+6.1,-5.8	+0.0,+0.0	+0.0,+0.0	+2.7,-2.7	-4.0,+4.1
335	375	+6.5,-5.8	+7.8,-7.2	+0.0,+0.0	+0.0,+0.0	+3.1,-3.0	-5.2,+5.4
375	415	+6.5,-5.8	+10.3,-9.4	+0.0,+0.0	+0.0,+0.0	+3.6,-3.5	-6.9,+7.3
415	520	+6.5,-5.8	+14.6,-12.8	+0.0,+0.0	+0.0,+0.0	+4.3,-4.2	-9.9,+11.0

Table 8.23: Uncertainty sources for $0.8 < |y| < 1.2$.

x1	x2	dsys012(%)	dsys013(%)	dsys014(%)	dsys015(%)	dsys016(%)	dsys017(%)
50	60	+2.4,-1.6	+3.4,-3.4	+1.6,-1.6	+0.6,-0.6	+2.2,-2.2	+0.0,+0.0
60	70	+2.1,-1.4	+3.1,-3.1	+1.5,-1.5	+0.6,-0.6	+1.9,-1.9	+0.0,+0.0
70	80	+1.9,-1.3	+2.9,-2.9	+1.4,-1.4	+0.6,-0.6	+1.7,-1.7	+0.0,+0.0
80	90	+1.8,-1.2	+2.7,-2.7	+1.3,-1.3	+0.6,-0.5	+1.6,-1.5	+0.0,+0.0
90	100	+1.8,-1.2	+2.5,-2.5	+1.3,-1.3	+0.5,-0.5	+1.4,-1.4	+0.0,+0.0
100	110	+1.7,-1.2	+2.4,-2.4	+1.2,-1.2	+0.6,-0.6	+1.3,-1.3	+0.0,+0.0
110	125	+1.7,-1.1	+2.3,-2.2	+1.2,-1.2	+0.6,-0.6	+1.3,-1.3	+0.0,+0.0
125	140	+1.7,-1.1	+2.1,-2.1	+1.2,-1.2	+0.6,-0.6	+1.3,-1.3	+0.0,+0.0
140	155	+1.7,-1.2	+2.0,-2.0	+1.2,-1.2	+0.6,-0.6	+1.3,-1.3	+0.0,+0.0
155	170	+1.7,-1.2	+1.9,-1.9	+1.3,-1.3	+0.6,-0.6	+1.4,-1.3	+0.0,+0.0
170	190	+1.7,-1.2	+1.8,-1.8	+1.3,-1.3	+0.6,-0.6	+1.4,-1.4	+0.0,+0.0
190	210	+1.7,-1.2	+1.7,-1.7	+1.4,-1.4	+0.7,-0.7	+1.5,-1.5	+0.0,+0.0
210	230	+1.8,-1.2	+1.6,-1.6	+1.5,-1.5	+0.9,-0.8	+1.6,-1.6	+0.0,+0.0
230	250	+1.8,-1.2	+1.6,-1.6	+1.7,-1.7	+1.0,-1.0	+1.7,-1.6	+0.0,+0.0
250	270	+1.9,-1.2	+1.6,-1.5	+1.8,-1.8	+1.2,-1.2	+1.8,-1.7	+0.0,+0.0
270	300	+2.1,-1.3	+1.5,-1.5	+2.1,-2.1	+1.4,-1.4	+1.9,-1.9	+0.0,+0.0
300	335	+2.3,-1.4	+1.5,-1.5	+2.5,-2.5	+1.7,-1.7	+2.1,-2.1	+0.0,+0.0
335	375	+2.8,-1.6	+1.5,-1.5	+3.2,-3.1	+2.1,-2.0	+2.4,-2.3	+0.0,+0.0
375	415	+3.7,-2.0	+1.6,-1.6	+4.2,-4.0	+2.7,-2.7	+2.8,-2.7	+0.0,+0.0
415	520	+6.0,-3.1	+1.7,-1.7	+6.0,-5.7	+3.8,-3.6	+3.3,-3.2	+0.0,+0.0

Table 8.24: Uncertainty sources for $0.8 < |y| < 1.2$.

x1	x2	dsys018(%)	dsys019(%)	dsys020(%)	dsys021(%)	dsys022(%)	dsys023(%)
50	60	+0.0,-0.0	+0.2,-0.2	-1.3,+1.3	+2.7,-2.6	+3.9,-3.9	-0.3,+0.3
60	70	+0.0,-0.0	+0.2,-0.2	-1.8,+1.8	+2.1,-2.0	+3.9,-3.9	-0.3,+0.3
70	80	+0.0,-0.0	+0.2,-0.2	-2.0,+2.0	+1.6,-1.6	+3.9,-3.9	-0.4,+0.4
80	90	+0.0,-0.0	+0.2,-0.2	-2.1,+2.1	+1.3,-1.3	+3.9,-3.9	-0.4,+0.4
90	100	+0.0,-0.0	+0.2,-0.2	-2.1,+2.1	+1.1,-1.1	+2.0,-2.0	-0.4,+0.4
100	110	+0.0,-0.0	+0.2,-0.2	-2.0,+2.1	+0.9,-0.9	+2.0,-2.0	-0.4,+0.4
110	125	+0.0,-0.0	+0.2,-0.2	-1.9,+2.0	+0.7,-0.7	+1.4,-1.4	-0.4,+0.4
125	140	+0.0,-0.0	+0.2,-0.2	-1.8,+1.8	+0.5,-0.5	+1.4,-1.4	-0.4,+0.4
140	155	+0.0,-0.0	+0.5,-0.5	-1.6,+1.6	+0.4,-0.4	+0.0,+0.0	-0.4,+0.4
155	170	+0.0,-0.0	+0.5,-0.5	-1.4,+1.4	+0.2,-0.2	+0.0,+0.0	-0.3,+0.3
170	190	+0.0,-0.0	+0.5,-0.5	-1.2,+1.2	+0.2,-0.2	+0.0,+0.0	-0.3,+0.3
190	210	+0.0,-0.0	+1.2,-1.2	-0.9,+0.9	+0.3,-0.3	+0.0,+0.0	-0.2,+0.2
210	230	+0.0,-0.0	+1.2,-1.2	-0.6,+0.6	+0.4,-0.4	+0.0,+0.0	-0.1,+0.1
230	250	+0.0,-0.0	+1.4,-1.4	-0.3,+0.3	+0.5,-0.5	+0.0,+0.0	+0.0,-0.0
250	270	+0.1,-0.1	+1.4,-1.4	-0.1,+0.1	+0.6,-0.6	+0.0,+0.0	+0.2,-0.2
270	300	+0.1,-0.1	+1.4,-1.4	+0.2,-0.2	+0.7,-0.7	+0.0,+0.0	+0.4,-0.3
300	335	+0.2,-0.2	+1.4,-1.4	+0.6,-0.6	+0.9,-0.9	+0.0,+0.0	+0.7,-0.7
335	375	+0.3,-0.3	+1.4,-1.4	+1.1,-1.0	+1.0,-1.0	+0.0,+0.0	+1.1,-1.1
375	415	+0.5,-0.5	+1.4,-1.4	+1.4,-1.4	+1.1,-1.1	+0.0,+0.0	+1.8,-1.7
415	520	+0.8,-0.8	+1.4,-1.4	+1.7,-1.6	+1.3,-1.2	+0.0,+0.0	+2.8,-2.7

Table 8.25: Uncertainty sources for $1.2 < |y| < 1.6$.

x1	x2	duncorr(%)	dsys001(%)	dsys002(%)	dsys003(%)	dsys004(%)	dsys005(%)
50	60	+1.9,-1.9	+2.8,-2.7	+2.9,-2.8	+0.6,-0.6	+0.0,+0.0	+3.1,-3.0
60	70	+1.7,-1.7	+2.8,-2.7	+3.1,-3.0	+0.9,-0.8	+0.0,+0.0	+3.1,-3.1
70	80	+1.5,-1.5	+2.9,-2.8	+3.3,-3.2	+1.1,-1.1	+0.0,+0.0	+3.2,-3.1
80	90	+1.5,-1.5	+2.9,-2.8	+3.5,-3.4	+1.4,-1.4	+0.0,+0.0	+3.3,-3.2
90	100	+1.4,-1.4	+3.0,-2.9	+3.7,-3.6	+1.7,-1.7	+0.0,+0.0	+3.4,-3.3
100	110	+1.4,-1.4	+3.1,-3.0	+3.9,-3.8	+2.0,-1.9	+0.0,+0.0	+3.5,-3.4
110	125	+1.5,-1.5	+3.2,-3.1	+4.1,-4.0	+2.3,-2.3	+0.0,+0.0	+3.6,-3.6
125	140	+1.7,-1.7	+3.3,-3.2	+4.5,-4.3	+2.7,-2.7	+0.0,+0.0	+3.8,-3.7
140	155	+2.0,-2.0	+3.5,-3.4	+4.8,-4.7	+3.2,-3.1	+0.0,+0.0	+4.1,-4.0
155	170	+2.3,-2.3	+3.7,-3.5	+5.2,-5.1	+3.6,-3.5	+0.0,+0.0	+4.3,-4.2
170	190	+2.6,-2.6	+3.9,-3.8	+5.7,-5.5	+4.2,-4.0	+0.0,+0.0	+4.6,-4.5
190	215	+3.0,-2.9	+4.3,-4.1	+6.4,-6.1	+4.9,-4.7	+0.0,+0.0	+5.0,-4.9
215	240	+3.3,-3.2	+4.8,-4.6	+7.2,-6.9	+5.8,-5.5	+0.0,+0.0	+5.6,-5.4
240	265	+4.1,-4.0	+5.3,-5.1	+8.2,-7.8	+6.9,-6.4	+0.0,+0.0	+6.2,-6.0
265	290	+5.4,-5.2	+6.0,-5.7	+9.4,-8.9	+8.3,-7.7	+0.0,+0.0	+6.9,-6.7
290	325	+7.2,-6.9	+6.8,-6.4	+11.0,-10.3	+10.3,-9.4	+0.0,+0.0	+7.8,-7.5
325	415	+10.9,-10.3	+8.3,-7.7	+13.8,-12.8	+13.9,-12.2	+0.0,+0.0	+9.4,-8.9

Table 8.26: Uncertainty sources for $1.2 < |y| < 1.6$.

x1	x2	dsys006(%)	dsys007(%)	dsys008(%)	dsys009(%)	dsys010(%)	dsys011(%)
50	60	+6.5,-5.8	+0.0,+0.0	+1.9,-1.8	+0.0,+0.0	+2.9,-2.9	+0.2,-0.2
60	70	+6.5,-5.8	+0.0,+0.0	+1.9,-1.9	+0.0,+0.0	+2.8,-2.7	-0.0,+0.0
70	80	+6.5,-5.8	+0.0,+0.0	+2.0,-1.9	+0.0,+0.0	+2.7,-2.6	-0.2,+0.2
80	90	+6.5,-5.8	+0.0,+0.0	+2.0,-2.0	+0.0,+0.0	+2.7,-2.6	-0.3,+0.3
90	100	+6.5,-5.8	+0.0,+0.0	+2.1,-2.0	+0.0,+0.0	+2.7,-2.6	-0.4,+0.4
100	110	+6.5,-5.8	+0.0,+0.0	+2.1,-2.1	+0.0,+0.0	+2.7,-2.7	-0.5,+0.5
110	125	+6.5,-5.8	+0.0,+0.0	+2.2,-2.1	+0.0,+0.0	+2.8,-2.7	-0.7,+0.7
125	140	+6.5,-5.8	+0.0,+0.0	+2.3,-2.2	+0.0,+0.0	+2.9,-2.8	-0.8,+0.8
140	155	+6.5,-5.8	+0.0,+0.0	+2.4,-2.3	+0.0,+0.0	+3.0,-2.9	-1.0,+1.0
155	170	+6.5,-5.8	+0.0,+0.0	+2.5,-2.4	+0.0,+0.0	+3.1,-3.1	-1.3,+1.3
170	190	+6.5,-5.8	+0.3,-0.3	+2.8,-2.7	+0.0,+0.0	+3.3,-3.2	-1.6,+1.6
190	215	+6.5,-5.8	+1.3,-1.3	+3.1,-3.0	+0.0,+0.0	+3.6,-3.5	-2.0,+2.0
215	240	+6.5,-5.8	+3.0,-2.9	+3.3,-3.1	+0.0,+0.0	+3.9,-3.8	-2.6,+2.7
240	265	+6.5,-5.8	+4.6,-4.4	+3.3,-3.2	+0.0,+0.0	+4.3,-4.2	-3.4,+3.5
265	290	+6.5,-5.8	+5.9,-5.6	+4.2,-4.0	+0.0,+0.0	+4.9,-4.7	-4.5,+4.6
290	325	+6.5,-5.8	+7.8,-7.2	+5.6,-5.2	+0.0,+0.0	+5.6,-5.4	-5.9,+6.3
325	415	+6.5,-5.8	+11.6,-10.5	+8.4,-7.5	+0.0,+0.0	+6.9,-6.6	-8.8,+9.7

Table 8.27: Uncertainty sources for $1.2 < |y| < 1.6$.

x1	x2	dsys012(%)	dsys013(%)	dsys014(%)	dsys015(%)	dsys016(%)	dsys017(%)
50	60	+0.9,-0.8	+4.9,-4.7	+1.4,-1.4	+0.0,+0.0	+0.8,-0.8	+2.9,-2.8
60	70	+0.8,-0.7	+4.5,-4.4	+1.3,-1.3	+0.0,+0.0	+0.7,-0.7	+2.7,-2.6
70	80	+0.8,-0.6	+4.2,-4.0	+1.2,-1.2	+0.0,+0.0	+0.6,-0.6	+2.6,-2.5
80	90	+0.7,-0.6	+3.9,-3.8	+1.2,-1.2	+0.0,+0.0	+0.5,-0.5	+2.5,-2.4
90	100	+0.7,-0.5	+3.6,-3.5	+1.2,-1.2	+0.0,+0.0	+0.5,-0.5	+2.5,-2.4
100	110	+0.7,-0.5	+3.4,-3.3	+1.2,-1.2	+0.0,+0.0	+0.5,-0.5	+2.6,-2.5
110	125	+0.7,-0.5	+3.2,-3.1	+1.2,-1.2	+0.0,+0.0	+0.5,-0.5	+2.8,-2.8
125	140	+0.7,-0.5	+3.0,-2.9	+1.3,-1.3	+0.0,+0.0	+0.4,-0.4	+3.3,-3.2
140	155	+0.9,-0.7	+2.8,-2.7	+1.4,-1.4	+0.0,+0.0	+0.4,-0.4	+3.3,-3.2
155	170	+0.9,-0.6	+2.7,-2.6	+1.5,-1.5	+0.0,+0.0	+0.4,-0.4	+3.2,-3.1
170	190	+0.9,-0.6	+2.6,-2.5	+1.7,-1.7	+0.2,-0.2	+0.5,-0.5	+3.0,-2.9
190	215	+1.0,-0.6	+2.5,-2.4	+1.9,-1.9	+1.0,-1.0	+0.9,-0.9	+2.7,-2.6
215	240	+1.1,-0.7	+2.5,-2.4	+2.3,-2.3	+2.2,-2.2	+1.4,-1.4	+2.0,-2.0
240	265	+1.3,-0.7	+2.5,-2.4	+2.9,-2.8	+4.2,-4.0	+1.6,-1.6	+1.5,-1.5
265	290	+1.7,-0.9	+2.4,-2.4	+3.5,-3.4	+5.3,-5.1	+1.8,-1.8	+1.7,-1.7
290	325	+2.3,-1.2	+2.4,-2.4	+4.5,-4.3	+6.9,-6.5	+2.0,-2.0	+1.9,-1.9
325	415	+4.0,-2.0	+2.5,-2.5	+6.5,-6.2	+9.8,-9.0	+2.5,-2.5	+2.3,-2.3

Table 8.28: Uncertainty sources for $1.2 < |y| < 1.6$.

x1	x2	dsys018(%)	dsys019(%)	dsys020(%)	dsys021(%)	dsys022(%)	dsys023(%)
50	60	+0.0,-0.0	+0.2,-0.2	-1.4,+1.5	+2.5,-2.5	+4.7,-4.7	-0.3,+0.3
60	70	+0.0,-0.0	+0.2,-0.2	-1.9,+1.9	+2.0,-2.0	+4.7,-4.7	-0.4,+0.4
70	80	+0.0,-0.0	+0.2,-0.2	-2.1,+2.2	+1.6,-1.6	+4.7,-4.7	-0.4,+0.4
80	90	+0.0,-0.0	+0.2,-0.2	-2.2,+2.3	+1.3,-1.3	+2.7,-2.7	-0.4,+0.4
90	100	+0.0,-0.0	+0.2,-0.2	-2.2,+2.3	+1.1,-1.1	+2.1,-2.1	-0.4,+0.5
100	110	+0.0,-0.0	+0.2,-0.2	-2.2,+2.2	+0.8,-0.8	+2.1,-2.1	-0.5,+0.5
110	125	+0.0,-0.0	+0.2,-0.2	-2.0,+2.1	+0.6,-0.6	+2.1,-2.1	-0.4,+0.4
125	140	+0.0,-0.0	+0.2,-0.2	-1.8,+1.8	+0.4,-0.4	+2.1,-2.1	-0.4,+0.4
140	155	+0.0,-0.0	+0.5,-0.5	-1.6,+1.6	+0.3,-0.3	+0.0,+0.0	-0.4,+0.4
155	170	+0.0,-0.0	+0.5,-0.5	-1.3,+1.3	+0.2,-0.2	+0.0,+0.0	-0.3,+0.3
170	190	+0.0,-0.0	+0.5,-0.5	-1.0,+1.1	+0.3,-0.3	+0.0,+0.0	-0.2,+0.2
190	215	+0.1,-0.1	+5.1,-5.1	-0.7,+0.7	+0.5,-0.5	+0.0,+0.0	-0.1,+0.1
215	240	+0.2,-0.2	+5.1,-5.1	-0.3,+0.4	+0.6,-0.6	+0.0,+0.0	+0.1,-0.1
240	265	+0.4,-0.4	+5.6,-5.6	-0.0,+0.0	+0.8,-0.8	+0.0,+0.0	+0.3,-0.3
265	290	+0.6,-0.6	+5.6,-5.6	+0.4,-0.4	+1.0,-1.0	+0.0,+0.0	+0.5,-0.5
290	325	+0.9,-0.9	+5.6,-5.6	+0.9,-0.9	+1.2,-1.2	+0.0,+0.0	+1.0,-1.0
325	415	+1.7,-1.7	+5.6,-5.6	+1.5,-1.5	+1.4,-1.4	+0.0,+0.0	+1.8,-1.8

Table 8.29: Uncertainty sources for $1.6 < |y| < 2.0$.

x1	x2	duncorr(%)	dsys001(%)	dsys002(%)	dsys003(%)	dsys004(%)	dsys005(%)
50	60	+2.1,-2.1	+2.8,-2.7	+3.2,-3.1	+1.2,-1.2	+0.0,+0.0	+3.2,-3.1
60	70	+1.9,-1.9	+2.9,-2.8	+3.5,-3.4	+1.6,-1.6	+0.0,+0.0	+3.3,-3.2
70	80	+1.9,-1.9	+3.0,-2.9	+3.8,-3.7	+2.0,-1.9	+0.0,+0.0	+3.5,-3.4
80	90	+2.0,-2.0	+3.2,-3.1	+4.1,-4.0	+2.3,-2.3	+0.0,+0.0	+3.6,-3.6
90	100	+2.0,-2.0	+3.3,-3.2	+4.4,-4.3	+2.7,-2.7	+0.0,+0.0	+3.8,-3.8
100	110	+2.1,-2.1	+3.5,-3.4	+4.8,-4.6	+3.1,-3.0	+0.0,+0.0	+4.1,-4.0
110	125	+2.3,-2.3	+3.7,-3.6	+5.2,-5.1	+3.6,-3.5	+0.0,+0.0	+4.4,-4.2
125	140	+2.7,-2.7	+4.1,-3.9	+5.9,-5.6	+4.3,-4.2	+0.0,+0.0	+4.8,-4.6
140	160	+2.8,-2.8	+4.5,-4.3	+6.6,-6.4	+5.2,-5.0	+0.0,+0.0	+5.3,-5.1
160	175	+3.2,-3.2	+5.0,-4.8	+7.6,-7.3	+6.3,-5.9	+0.0,+0.0	+6.0,-5.8
175	190	+3.9,-3.8	+5.5,-5.3	+8.6,-8.2	+7.5,-7.0	+0.0,+0.0	+6.6,-6.4
190	210	+4.8,-4.7	+6.2,-5.9	+9.9,-9.3	+9.0,-8.3	+0.0,+0.0	+7.4,-7.1
210	235	+6.3,-6.2	+7.2,-6.8	+11.8,-11.0	+11.5,-10.3	+0.0,+0.0	+8.6,-8.2
235	260	+9.1,-8.7	+8.7,-8.0	+14.6,-13.4	+15.1,-13.2	+0.0,+0.0	+10.3,-9.8
260	320	+14.2,-13.1	+10.9,-9.9	+18.8,-16.9	+20.8,-17.4	+0.0,+0.0	+12.8,-11.9

Table 8.30: Uncertainty sources for $1.6 < |y| < 2.0$.

x1	x2	dsys006(%)	dsys007(%)	dsys008(%)	dsys009(%)	dsys010(%)	dsys011(%)
50	60	+6.5,-5.8	+0.0,+0.0	+0.0,+0.0	+2.3,-2.3	+3.9,-3.8	+2.4,-2.5
60	70	+6.5,-5.8	+0.0,+0.0	+0.0,+0.0	+2.4,-2.4	+3.8,-3.7	+1.8,-1.8
70	80	+6.5,-5.8	+0.0,+0.0	+0.0,+0.0	+2.6,-2.5	+3.8,-3.7	+1.2,-1.3
80	90	+6.5,-5.8	+0.0,+0.0	+0.0,+0.0	+2.7,-2.6	+3.9,-3.8	+0.8,-0.8
90	100	+6.5,-5.8	+0.0,+0.0	+0.0,+0.0	+2.8,-2.7	+4.0,-3.9	+0.4,-0.4
100	110	+6.5,-5.8	+0.0,+0.0	+0.0,+0.0	+3.0,-2.9	+4.1,-4.0	+0.0,-0.0
110	125	+6.5,-5.8	+0.0,+0.0	+0.0,+0.0	+3.2,-3.1	+4.3,-4.2	-0.4,+0.4
125	140	+6.5,-5.8	+0.0,+0.0	+0.5,-0.5	+3.3,-3.2	+4.6,-4.5	-1.0,+1.0
140	160	+6.5,-5.8	+0.0,+0.0	+1.3,-1.3	+3.4,-3.3	+5.1,-4.9	-1.7,+1.7
160	175	+6.5,-5.8	+0.0,+0.0	+2.6,-2.5	+3.3,-3.2	+5.6,-5.4	-2.8,+2.8
175	190	+6.5,-5.8	+0.0,+0.0	+3.3,-3.2	+4.1,-3.9	+6.2,-5.9	-3.9,+3.9
190	210	+6.5,-5.8	+0.0,+0.0	+4.3,-4.1	+5.3,-5.1	+6.9,-6.6	-5.3,+5.4
210	235	+6.5,-5.8	+0.0,+0.0	+6.1,-5.7	+7.6,-7.1	+8.1,-7.7	-7.8,+8.1
235	260	+6.5,-5.8	+0.0,+0.0	+9.2,-8.2	+11.3,-10.3	+9.9,-9.3	-11.8,+13.1
260	320	+6.5,-5.8	+0.0,+0.0	+14.6,-12.2	+17.8,-15.4	+12.5,-11.6	-18.4,+22.6

Table 8.31: Uncertainty sources for $1.6 < |y| < 2.0$.

x1	x2	dsys012(%)	dsys013(%)	dsys014(%)	dsys015(%)	dsys016(%)	dsys017(%)
50	60	+0.3,-0.3	+5.1,-4.9	+1.0,-1.1	+0.0,+0.0	+0.4,-0.4	+2.3,-2.2
60	70	+0.3,-0.2	+4.8,-4.6	+1.0,-1.0	+0.0,+0.0	+0.3,-0.3	+2.0,-2.0
70	80	+0.2,-0.2	+4.6,-4.5	+0.9,-0.9	+0.0,+0.0	+0.2,-0.2	+1.8,-1.8
80	90	+0.2,-0.2	+4.5,-4.3	+0.9,-0.9	+0.0,+0.0	+0.2,-0.2	+1.7,-1.6
90	100	+0.2,-0.2	+4.3,-4.2	+0.9,-0.9	+0.0,+0.0	+0.1,-0.1	+1.5,-1.5
100	110	+0.2,-0.2	+4.3,-4.1	+1.0,-1.0	+0.0,+0.0	+0.1,-0.1	+1.5,-1.5
110	125	+0.2,-0.2	+4.2,-4.1	+1.0,-1.0	+0.0,+0.0	+0.1,-0.1	+1.5,-1.5
125	140	+0.2,-0.2	+4.1,-4.0	+1.1,-1.1	+0.0,+0.0	+0.1,-0.1	+1.6,-1.6
140	160	+0.2,-0.2	+4.1,-4.0	+1.3,-1.3	+0.0,+0.0	+0.1,-0.1	+1.8,-1.8
160	175	+0.2,-0.2	+4.1,-4.0	+1.5,-1.5	+0.0,+0.0	+0.1,-0.1	+2.0,-2.0
175	190	+0.2,-0.2	+4.0,-3.9	+1.7,-1.7	+0.0,+0.0	+0.1,-0.1	+2.2,-2.2
190	210	+0.2,-0.2	+4.0,-3.9	+2.1,-2.1	+0.0,+0.0	+0.1,-0.1	+2.5,-2.4
210	235	+0.2,-0.2	+4.0,-3.9	+2.7,-2.6	+0.0,+0.0	+0.1,-0.1	+2.9,-2.8
235	260	+0.2,-0.2	+4.1,-4.0	+3.7,-3.6	+0.0,+0.0	+0.1,-0.1	+3.5,-3.3
260	320	+0.2,-0.2	+4.4,-4.3	+5.5,-5.2	+0.0,+0.0	+0.1,-0.1	+4.3,-4.1

Table 8.32: Uncertainty sources for $1.6 < |y| < 2.0$.

x1	x2	dsys018(%)	dsys019(%)	dsys020(%)	dsys021(%)	dsys022(%)	dsys023(%)
50	60	+0.4,-0.4	+0.2,-0.2	-1.3,+1.4	+2.6,-2.6	+2.1,-2.1	-0.3,+0.3
60	70	+0.3,-0.3	+0.2,-0.2	-1.9,+1.9	+2.2,-2.2	+2.1,-2.1	-0.4,+0.4
70	80	+0.2,-0.2	+0.2,-0.2	-2.2,+2.3	+1.9,-1.8	+1.4,-1.4	-0.4,+0.4
80	90	+0.1,-0.1	+0.2,-0.2	-2.4,+2.4	+1.6,-1.6	+1.4,-1.4	-0.5,+0.5
90	100	+0.0,-0.0	+0.2,-0.2	-2.5,+2.5	+1.3,-1.3	+1.0,-1.0	-0.5,+0.5
100	110	+0.0,-0.0	+0.2,-0.2	-2.5,+2.5	+1.2,-1.2	+1.0,-1.0	-0.5,+0.5
110	125	+0.1,-0.1	+0.2,-0.2	-2.4,+2.5	+1.0,-1.0	+0.0,+0.0	-0.5,+0.5
125	140	+0.2,-0.2	+0.2,-0.2	-2.3,+2.3	+0.8,-0.8	+0.0,+0.0	-0.5,+0.5
140	160	+0.4,-0.4	+0.5,-0.5	-2.1,+2.1	+0.7,-0.7	+0.0,+0.0	-0.5,+0.5
160	175	+0.7,-0.7	+0.7,-0.7	-1.8,+1.8	+0.7,-0.7	+0.0,+0.0	-0.4,+0.4
175	190	+0.9,-0.9	+0.7,-0.7	-1.5,+1.5	+0.7,-0.7	+0.0,+0.0	-0.3,+0.3
190	210	+1.2,-1.2	+0.9,-0.9	-1.1,+1.1	+0.9,-0.9	+0.0,+0.0	-0.2,+0.2
210	235	+1.7,-1.7	+0.9,-0.9	-0.6,+0.6	+1.2,-1.1	+0.0,+0.0	+0.1,-0.1
235	260	+2.6,-2.6	+0.9,-0.9	+0.2,-0.2	+1.5,-1.5	+0.0,+0.0	+0.5,-0.5
260	320	+4.4,-4.4	+0.9,-0.9	+1.1,-1.1	+2.0,-2.0	+0.0,+0.0	+1.3,-1.3

Table 8.33: Uncertainty sources for $2.0 < |y| < 2.4$.

x1	x2	duncorr(%)	dsys001(%)	dsys002(%)	dsys003(%)	dsys004(%)	dsys005(%)
50	60	+1.9,-1.9	+3.0,-2.9	+3.8,-3.7	+2.2,-2.2	+2.5,-2.5	+3.5,-3.5
60	70	+1.8,-1.8	+3.3,-3.2	+4.3,-4.2	+2.8,-2.7	+2.7,-2.7	+3.8,-3.7
70	80	+1.8,-1.8	+3.5,-3.4	+4.9,-4.7	+3.4,-3.3	+3.0,-2.9	+4.1,-4.0
80	90	+1.9,-1.9	+3.8,-3.7	+5.4,-5.2	+4.0,-3.9	+3.2,-3.1	+4.5,-4.4
90	100	+2.1,-2.1	+4.1,-4.0	+6.0,-5.8	+4.7,-4.5	+3.2,-3.1	+4.9,-4.8
100	110	+2.4,-2.4	+4.5,-4.3	+6.7,-6.4	+5.5,-5.2	+3.1,-3.0	+5.4,-5.2
110	120	+2.8,-2.8	+4.9,-4.7	+7.5,-7.1	+6.3,-6.0	+2.9,-2.9	+5.9,-5.7
120	130	+3.4,-3.4	+5.4,-5.1	+8.3,-7.9	+7.4,-6.9	+3.6,-3.5	+6.4,-6.2
130	145	+4.2,-4.2	+6.0,-5.6	+9.5,-9.0	+8.9,-8.2	+4.9,-4.7	+7.2,-6.9
145	160	+5.8,-5.7	+6.9,-6.4	+11.2,-10.5	+11.1,-10.1	+7.2,-6.8	+8.3,-7.9
160	175	+8.1,-7.8	+7.9,-7.4	+13.3,-12.3	+14.0,-12.3	+10.6,-9.7	+9.7,-9.2
175	200	+11.7,-11.1	+9.5,-8.7	+16.3,-14.8	+18.1,-15.4	+16.0,-14.0	+11.5,-10.9
200	230	+19.8,-18.4	+12.6,-11.3	+22.2,-19.6	+26.7,-21.3	+28.7,-22.9	+15.3,-14.1

Table 8.34: Uncertainty sources for $2.0 < |y| < 2.4$.

x1	x2	dsys006(%)	dsys007(%)	dsys008(%)	dsys009(%)	dsys010(%)	dsys011(%)
50	60	+6.5,-5.8	+0.0,+0.0	+0.0,+0.0	+0.0,+0.0	+5.4,-5.2	+2.1,-2.2
60	70	+6.5,-5.8	+0.0,+0.0	+0.0,+0.0	+0.0,+0.0	+5.3,-5.2	+1.7,-1.8
70	80	+6.5,-5.8	+0.0,+0.0	+0.0,+0.0	+0.0,+0.0	+5.5,-5.3	+1.4,-1.4
80	90	+6.5,-5.8	+0.0,+0.0	+0.0,+0.0	+0.2,-0.2	+5.7,-5.5	+1.1,-1.1
90	100	+6.5,-5.8	+0.0,+0.0	+0.0,+0.0	+1.0,-1.0	+6.1,-5.9	+0.9,-0.9
100	110	+6.5,-5.8	+0.0,+0.0	+0.0,+0.0	+1.9,-1.8	+6.5,-6.3	+0.6,-0.6
110	120	+6.5,-5.8	+0.0,+0.0	+0.0,+0.0	+2.9,-2.8	+7.0,-6.7	+0.3,-0.3
120	130	+6.5,-5.8	+0.0,+0.0	+0.0,+0.0	+3.6,-3.5	+7.7,-7.3	-0.1,+0.1
130	145	+6.5,-5.8	+0.0,+0.0	+0.0,+0.0	+4.8,-4.6	+8.5,-8.1	-0.5,+0.5
145	160	+6.5,-5.8	+0.0,+0.0	+0.0,+0.0	+7.1,-6.7	+9.8,-9.2	-1.4,+1.4
160	175	+6.5,-5.8	+0.0,+0.0	+0.0,+0.0	+10.4,-9.5	+11.4,-10.6	-2.5,+2.6
175	200	+6.5,-5.8	+0.0,+0.0	+0.0,+0.0	+15.7,-13.8	+13.7,-12.6	-4.3,+4.4
200	230	+6.5,-5.8	+0.0,+0.0	+0.0,+0.0	+28.2,-22.6	+18.3,-16.5	-8.7,+9.6

Table 8.35: Uncertainty sources for $2.0 < |y| < 2.4$.

x1	x2	dsys012(%)	dsys013(%)	dsys014(%)	dsys015(%)	dsys016(%)	dsys017(%)
50	60	+0.3,-0.3	+5.6,-5.4	+1.0,-1.0	+0.0,+0.0	+0.4,-0.4	+3.2,-3.1
60	70	+0.2,-0.2	+5.5,-5.3	+1.0,-1.0	+0.0,+0.0	+0.3,-0.3	+3.0,-2.9
70	80	+0.2,-0.2	+5.6,-5.4	+1.1,-1.1	+0.0,+0.0	+0.2,-0.2	+2.8,-2.7
80	90	+0.2,-0.2	+5.6,-5.4	+1.2,-1.2	+0.0,+0.0	+0.1,-0.1	+2.6,-2.5
90	100	+0.2,-0.2	+5.7,-5.5	+1.3,-1.3	+0.0,+0.0	+0.1,-0.1	+2.4,-2.3
100	110	+0.2,-0.2	+5.8,-5.6	+1.5,-1.5	+0.0,+0.0	+0.2,-0.2	+2.1,-2.1
110	120	+0.2,-0.2	+5.9,-5.7	+1.7,-1.7	+0.0,+0.0	+0.3,-0.3	+2.0,-1.9
120	130	+0.2,-0.2	+6.0,-5.8	+1.9,-1.9	+0.0,+0.0	+0.4,-0.4	+2.1,-2.1
130	145	+0.2,-0.2	+6.0,-5.8	+2.3,-2.3	+0.0,+0.0	+0.6,-0.6	+2.4,-2.3
145	160	+0.2,-0.2	+6.1,-5.9	+2.9,-2.9	+0.0,+0.0	+0.9,-0.9	+2.7,-2.7
160	175	+0.2,-0.2	+6.3,-6.1	+3.7,-3.7	+0.0,+0.0	+1.3,-1.3	+3.2,-3.1
175	200	+0.2,-0.2	+6.6,-6.4	+5.1,-5.0	+0.0,+0.0	+1.9,-1.9	+3.8,-3.6
200	230	+0.2,-0.2	+7.3,-7.0	+8.5,-7.9	+0.0,+0.0	+3.5,-3.4	+5.0,-4.7

Table 8.36: Uncertainty sources for $2.0 < |y| < 2.4$.

x1	x2	dsys018(%)	dsys019(%)	dsys020(%)	dsys021(%)	dsys022(%)	dsys023(%)
50	60	+0.6,-0.6	+0.2,-0.2	-1.5,+1.5	+2.9,-2.8	+2.1,-2.1	-0.3,+0.3
60	70	+0.5,-0.5	+0.2,-0.2	-2.2,+2.2	+2.4,-2.4	+2.1,-2.1	-0.4,+0.4
70	80	+0.5,-0.5	+0.2,-0.2	-2.6,+2.7	+2.1,-2.1	+1.4,-1.4	-0.5,+0.5
80	90	+0.6,-0.6	+0.2,-0.2	-2.8,+2.9	+1.8,-1.8	+1.4,-1.4	-0.6,+0.6
90	100	+0.7,-0.7	+0.2,-0.2	-3.0,+3.1	+1.6,-1.6	+1.0,-1.0	-0.6,+0.6
100	110	+0.8,-0.8	+0.2,-0.2	-3.1,+3.2	+1.4,-1.4	+1.0,-1.0	-0.6,+0.6
110	120	+1.0,-1.0	+0.2,-0.2	-3.1,+3.2	+1.2,-1.2	+1.0,-1.0	-0.7,+0.7
120	130	+1.2,-1.2	+0.2,-0.2	-3.0,+3.1	+1.1,-1.1	+0.0,+0.0	-0.7,+0.7
130	145	+1.6,-1.6	+0.5,-0.5	-2.9,+3.0	+1.0,-1.0	+0.0,+0.0	-0.7,+0.7
145	160	+2.2,-2.2	+0.5,-0.5	-2.7,+2.7	+1.0,-1.0	+0.0,+0.0	-0.6,+0.6
160	175	+3.3,-3.3	+0.7,-0.7	-2.3,+2.4	+1.2,-1.1	+0.0,+0.0	-0.5,+0.5
175	200	+4.9,-4.9	+0.7,-0.7	-1.8,+1.9	+1.5,-1.5	+0.0,+0.0	-0.3,+0.3
200	230	+11.0,-11.0	+0.9,-0.9	-0.8,+0.8	+2.2,-2.2	+0.0,+0.0	+0.2,-0.2

Chapter 9

Conclusions and outlook

In this thesis, the inclusive jet cross section has been measured in proton-antiproton collisions at the center-of-mass energy $\sqrt{s} = 1.96$ TeV with luminosity $\mathcal{L} = 0.70$ fb^{-1}. The measurement is presented as a function of p_T in six bins of jet rapidity extending out to $|y| = 2.4$. The kinematic range covers jet p_T 50–600 GeV and the proton momentum fraction $x = 0.05$–0.6. This provides the largest data set of the inclusive jet spectra at the Fermilab Tevatron Collider with the smallest experimental uncertainties to date.

The measured spectra have been compared to theory and found to be in good agreement with perturbative quantum chromodynamics predictions with the CTEQ6.5 and MRST sets of parton distribution functions. Correlations for the systematic uncertainties have been calculated in detail and a global fit to data and theory including correlated systematic uncertainties and the CTEQ6.5 PDF uncertainties is performed. The global fit is found to favor the lower end of CTEQ6.5 PDF uncertainty band, with reduced high x gluon PDF. The results have been published in Ref. [155] and will be included in the global PDF fits by the CTEQ and MRST collaborations. Figure 9.1 summarizes the comparison to theory.

This thesis has aimed to provide the best possible measurement of the inclusive jet cross section and a more thorough physical interpretation is left for future work. However, it should be noted that the CTEQ6.5M and MRST2004 predictions at high p_T are mainly constrained by the Tevatron Run I jet data. The new Run II data set is larger and has improved understanding of the JES systematic uncertainties. The PDF fits for the HERA data alone extrapolate to a lower high x gluon content than the Tevatron Run I jet data so the new data has significant impact in resolving the high x gluon PDF behavior.

The current measurement provides strong constraints for the high x gluon

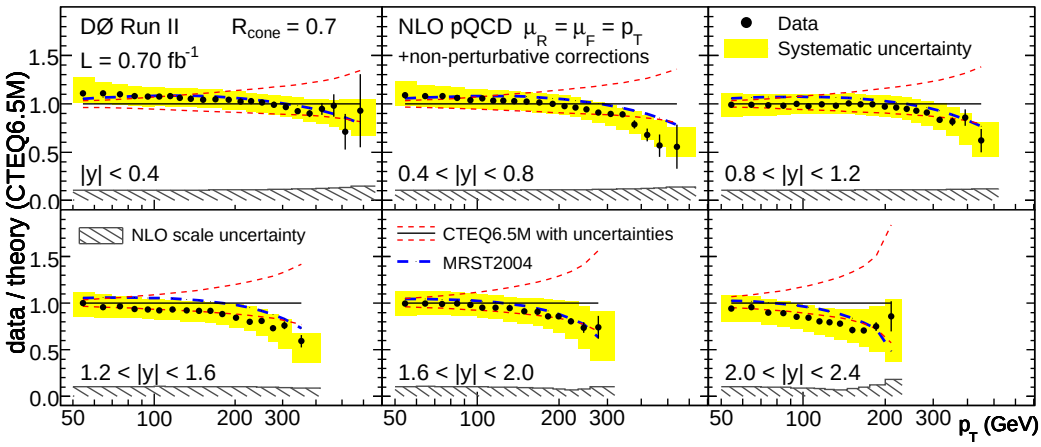

Figure 9.1: Summary of comparison to theory for inclusive jet cross section.

PDF, which is the leading uncertainty in new physics searches at the LHC [18]. The integrated luminosity is almost ten times higher than in the Run I measurements at $\sqrt{s} = 1.8$ TeV [6, 7, 13] and leads to about a factor three improvement for the high x gluon PDF constraints. The impact is further increased by the lower systematic uncertainties and high correlation between rapidity bins.

The 10% increase in center-of-mass energy between Run I and Run II leads to a factor three increase in the cross section at $p_T = 550$ GeV/c, and with increased luminosity to an effective improvement of about a factor of five in the sensitivity to quark substructure at the few TeV scale compared to Run I. The wide rapidity coverage of the measurement allows both PDFs and quark substructure to be studied simultaneously, with new physics mostly contributing at central rapidity and all regions sensitive to PDFs. The high correlation between measurements in different rapidity regions and the detailed understanding of correlations between systematic uncertainties provided in this thesis are essential for the dual interpretation of the data.

The quark substructure sensitivity is much higher in the 14 TeV proton-proton collisions at the LHC due to start in 2008, but the sensitivity to PDFs is conversely lower, as shown in Fig. 9.2. It will take years for the LHC to improve their systematics and to accumulate enough statistics (200 fb^{-1}) to achieve comparable sensitivity for the high x gluon PDF.

Much of the work in this thesis is dedicated to improving the understanding of the jet energy scale and the jet p_T resolutions. The JES uncertainty has reached an all-time low of 1.2% in the central calorimeter at $p_T \sim 150$ GeV/c, and the η-dependent corrections keep the uncertainty between 1.5–2.5% else-

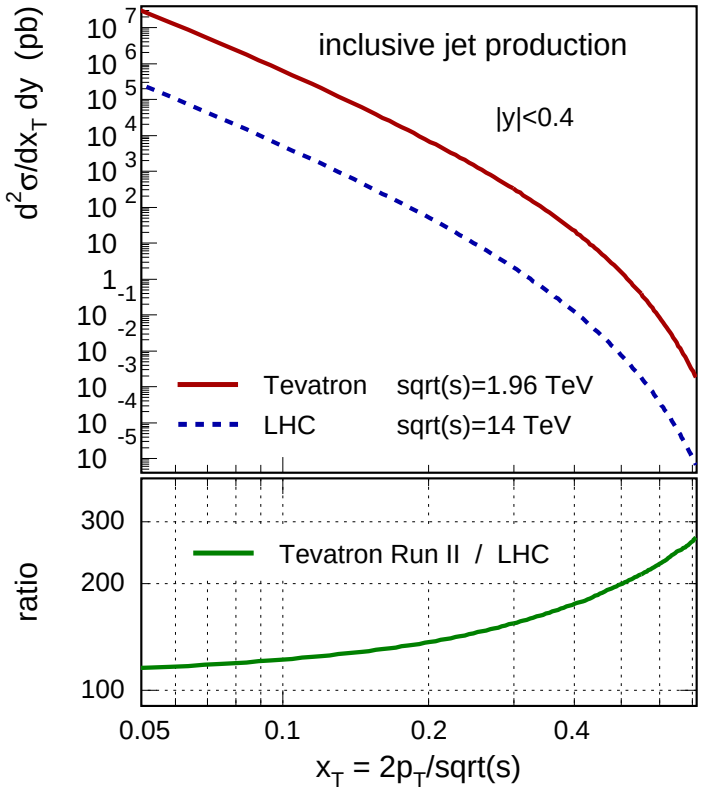

Figure 9.2: Comparison of the inclusive jet production at the Tevatron Run II and at the LHC as a function of transverse momentum fraction x_T.

where in the calorimeter at $|y| < 2.4$ and $p_T > 50$ GeV/c. The method for the η-dependence resolution bias correction and the explicit handling of γ+jet and dijet JES differences, attributed to quark and gluon jet differences, are innovations produced in this thesis. The explicit dijet four-vector corrections in JES, the full analytical treatment of non-Gaussian tails in the jet p_T resolutions and the η-dependence closure test with explicit accounting of several biases are also results of this thesis.

The JES and jet p_T resolutions are not only used in this thesis, but affect all the other measurement using jets at DØ also. In particular, other jet analyses (*e.g.* dijet mass, three jet mass, dijet angular distributions) benefit from the work done for the inclusive jet analysis. The inclusive jet cross section is only the second[1] QCD jet analysis to be published from DØ in Run II and paves the way for many others.

[1]First is the dijet azimuthal decorrelations [44] that is not very sensitive to JES.

Bibliography

[1] J. P. Ostriker, P. J. Steinhardt, arXiv:astro-ph/9505066v1 (1995).

[2] WMAP collaboration, D. N. Spergel *et al.*, ApJS 170 (2007) 377 [arXiv:astro-ph/0603449v2].

[3] A. Belyaev, J. Pumplin, W. K. Tung, C. P. Yuan, JHEP **0601**, 069 (2006);
S. Ferrag, proceedings of 39$^{\text{th}}$ Rencontres de Moriond on QCD and High-Energy Hadronic Interactions, La Thuile, Italy, 28 Mar – 4 Apr 2004.

[4] DØ collaboration, B. Abbot *et al.*, Phys. Rev. D64 (2001) 032003 [arXiv:hep-ex/0012046v2].

[5] G. C. Blazey, B. L. Flaugher, Annu. Rev. Nucl. Part. Sci. 49 (1999) 633 [arXiv:hep-ex/9903058].

[6] DØ collaboration, B. Abbot *et al.*, Phys. Rev. Lett. 82 (1999) 2451 [arXiv:hep-ex/9807018v1].

[7] DØ collaboration, B. Abbot *et al.*, Phys. Rev. Lett. 86 (2001) 1707 [arXiv:hep-ex/0011036v2];
L. Babukhadia, Ph.D. dissertation, University of Arizona, Tucson, FERMILAB-THESIS-1999-03 (1999).

[8] DØ collaboration, V. M. Abazov, Phys. Lett. B525 (2002) 211 [arXiv:hep-ex/0109041].

[9] H. L. Lai *et al.*, Phys. Rev. D 51, 4763 (1995).

[10] H. L. Lai *et al.*, Phys. Rev. D 55, 1280 (1997).

[11] A. D. Martin, R. G. Roberts, W. J. Stirling, and R. S. Thorne, Eur. Phys. J. C4 (1998) 463-496 [arXiv:hep-ph/9803445].

[12] DØ collaboration, B. Abbot *et al.*, Phys. Rev. Lett. 86 (2001) 2523 [arXiv:hep-ex/0008072v3];
J. Krane, Ph.D. dissertation, University of Nebraska, FERMILAB-THESIS-1998-16 (1998).

[13] CDF collaboration, F. Abe *et al.*, Phys. Rev. Lett. 77 (1996) 438.

[14] CDF collaboration, F. Abe *et al.*, NIM Res., Sect. A271, 387 (1988) and references therein;
CDF collaboration, F. Abe *et al.*, Phys. Rev. D50 2966 (1994).

[15] CDF collaboration, T. Affolder *et al.*, Phys. Rev. D64 (2001) 032001.

[16] J. Huston *et al.*, Phys. Rev. Lett. 77, 444 (1996).

[17] CDF collaboration, T. Affolder *et al.*, Phys. Rev. D64 (2001) 012001.

[18] A. Belyaev *et al.*, JHEP **0601**, 069 (2006);
S. Ferrag, proceedings of Rencontres de Moriond QCD, March 2003 [arXiv:hep-ph/0407303].

[19] CDF collaboration, A. Abulencia *et al.*, Phys. Rev. D74, (2006) 071103(R);
G. Flanagan, Ph.D. dissertation, Michigan State University, FERMILAB-THESIS-2005-58 (2005).

[20] J. Pumplin *et al.*, J. High Energy Phys. 0207, 012 (2002) [arXiv:hep-ph/0201195].

[21] D. Stump *et al.*, J. High Energy Phys. 0310, 046 (2003) [arXiv:hep-ph/0303013].

[22] A. D. Martin *et al.*, Phys. Lett. B 604, 61 (2004) [arXiv:hep-ph/0410230].

[23] CDF collaboration, A. Abulencia *et al.*, Phys. Rev. Lett. 96 (2006) 122001.

[24] M. Voutilainen, in "Deep Inelastic Scattering, Proceedings of the 14th International Workshop", ed. by M. Kuze, K. Nagano and K. Tokushuku, World Scientific (2006) [arXiv:hep-ex/0609026].

[25] CDF collaboration, A. Abulencia *et al.*, Phys. Rev. D75 (2007) 092006 [arXiv:hep-ex/0701051].

[26] BCDMS collaboration, A. C. Benvenuti *et al.*, Phys. Lett. B223 (1989) 485.

[27] BCDMS collaboration, A. C. Benvenuti *et al.*, Phys.Lett. B236 (1989) 592.

[28] New Muon Collaboration, M. Arneodo *et al.*, Nucl. Phys. B483 (1997) 3 [arXiv:hep-ph/9610231]; Nucl. Phys. B487 (1997) 3 [arXiv:hep-ex/9611022].

[29] CCFR collaboration, W. G. Seligman *et al.*, Phys. Rev. Lett. 79 (1997) 1213 [arXiv:hep-ex/970107].

[30] H1 collaboration, C. Adloff *et al.*, Eur. Phys. J. C13 (2000) 609 [arXiv:hep-ex/9908059]; Eur. Phys. J. C19 (2001) 269 [arXiv:hep-ex/0012052]; Eur. Phys. J C21 (2001) 33 [arXiv:hep-ex/0012053];

[31] ZEUS collaboration, S. Chekanov *et al.*, Eur. Phys. J. C21 (2001) 443 [arXiv:hep-ex/0105090];
A. M. Cooper-Sarkar, *Proceedings of International Europhysics Conference on HEP 2001*, Budapest [arXiv:hep-ph/0110386].

[32] C. Glasman, arXiv:hep-ex/0506035 (2005).

[33] CDF collaboration, F. Abe *et al.*, Phys. Rev. Lett. 81 (1998) 5754 [arXiv:hep-ex/9809001].

[34] CDF collaboration, D. Acosta *et al.*, Phys. Rev. D71 (2005) 051104 [arXiv:hep-ex/0501023].

[35] DØ collaboration, V. M. Abazov *et al.*, Phys. Rev. D77 (2007) 011106(R) [arXiv:0709.4254v1];
S. Sengupta, Ph.D. dissertation, Florida State University, UMI-32-32446, FERMILAB-THESIS-2006-54 (2006).

[36] CDF collaboration, B. Han, A. Bodek, Y. Chung, K. McFarland, E. Halkiadakis, CDF public note 8942 (2006).

[37] R. K. Ellis, J. C. Sexton, Nucl. Phys. B269 (1986) 445.

[38] DØ collaboration, B. Abbot *et al.*, Phys. Rev. Lett. 82 (1999) 2457 [arXiv:hep-ex/9807014].

[39] I. Bertram, E. H. Simmons, Phys. Lett. B443 (1998) 347 [arXiv:hep-ph/9809472].

[40] CDF collaboration, T. Affolder *et al.*, Phys. Rev. D61 (2000) 091101 [arXiv:hep-ex/9912022].

[41] A. Kupco, Ph.D. dissertation, Charles University, Prague, FERMILAB-THESIS-2004-08 (2003);
A. Kupco, P. Demine, C. Royon, M. Zielinski, "Measurement of the dijet mass cross section", DØ note 4145 (2003).

[42] DØ collaboration, B. Abbot *et al.*, FERMILAB-Conf-98/279-E (1998) [arXiv:hep-ex/9809009].

[43] N. Parua, M. Wobisch, "First Measurement of Dijet Angular Distributions in the TeV Regime", DØ Note 5616 (2008).

[44] DØ collaboration, V. M. Abazov *et al.*, Phys. Rev. Lett. 94 (2005) 221801 [arXiv:hep-ex/0409040].

[45] A. Kupco, M. Begel, P. Demine, C. Royon, M. Wobisch, M. Zielinski, "Measurement of dijet azimuthal angle distribution in ppbar collisions at $\sqrt{s} = 1.96$ TeV", DØ note 4384 (2004).

[46] W. B. Kilgore, W .T. Giele, arXiv:hep-ph/0009193 (2000).

[47] M. Toennesmann (for the CDF collaboration), Eur. Phys. J. C33 (2004) S422 [arXiv:hep-ex/0310055].

[48] S. Glashow, Nucl. Phys. 22, 579 (1961).
S. Weinberg, Phys. Rev. Lett. 19, 1264 (1967).
A. Salam in *Elementary Particle Theory*, ed. by N. Svartholm, Aspenäsgården, 367 (1968).

[49] F. Halzen, A. D. Martin, *Quarks & Leptons: An Introductory Course in Modern Particle Physics*, John Wiley & Sons (1984).

[50] P. W. Higgs, Phys. Letters 12 (1964) 132;
P. W. Higgs, Phys. Rev. Lett. 13 (1964) 508;
P. W. Higgs, Phys. Rev. 145 (1966) 1156.

[51] N. Kidonakis, J .F Owens, Phys. Rev. D63 (2001) 054019 [arXiv:hep-ph/0007268].

[52] Z. Nagy, Phys. Rev. D68 (2003) 094002;
Z. Nagy, Phys. Rev. Lett. 88 (2002) 122003;
Z. Nagy, Z. Trocsanyi, Phys. Rev. Lett. 87 (2001) 082001.

[53] T. Kluge, K. Rabbertz, M. Wobisch, DESY 06-186, FERMILAB-CONF-06-352-E (2006) [arXiV:hep-ph/0609285].

[54] On-line plotting and calculations of PDFs,
`http://durpdg.dur.ac.uk/hepdata/pdf3.html`

[55] S. Alekhin, Phys. Rev. D68 (2003) 014002 [arXiv:hep-ph/0211096].

[56] R. Field in: M. G. Albrow *et al.* [TeV4LHC QCD Working Group], arXiv:hep-ph/0610012 (2006).

[57] T. Sjöstrand, P. Edén, C. Friberg, L. Lönnblad, G. Miu, S. Mrenna, E. Norrbin, Computer Physics Commun. 135 (2001) 238;
T. Sjöstrand, L. Lönnblad, S. Mrenna, P. Skands, arXiv:hep-ph/0308153 (2003).

[58] H.-U. Bengtsson, T. Sjöstrand, Computer Physics Commun. 46 (1987).

[59] B. Andersson, G. Gustafson, G. Ingelman, T. Sjöstrand, Phys. Rep. 97 (1983) 31.

[60] B. Andersson, "The Lund Model", Cambridge University Press (1998).

[61] G. Corcella *et al.*, JHEP 0101 (2001) 010 [arXiv:hep-ph/0011363]; arXiv:hep-ph/0210213 (2002).

[62] R. Brun, F. Carminati, CERN Program Library, Long Writeup W5013 (1993).

[63] CDF Collaboration, F. Abe *et al.*, Phys. Rev. D50 (1994) 5562.

[64] A. D. Martin, W. J. Stirling, R. S. Thorne and G. Watt, Phys. Lett. B652 (2007) 292–299 [arXiv:0706.0459].

[65] M. C. Gonzalez-Garcia, Y. Nir, Rev. Mod. Phys. 75 (2003) 345 [arXiv:hep-ph/0202058v3].

[66] Kamiokande collaboration, Y. Fukuda *et al.*, Phys. Rev. Lett. 77 (1996) 1683.

[67] Soudan collaboration, W. W. M. Allison *et al.*, Phys. Lett. B 449 (1999) 137 [arXiv:hep-ex/9901024v1].

[68] CDF Collaboration, D. Acosta *et al.*, Phys. Rev. D **71**, 1112002 (2005).

[69] DØ collaboration, S. Abachi *et al.*, Phys. Rev. Lett. 74 (1995) 2632.

[70] DØ collaboration, S. Abachi *et al.*, Phys. Rev. Lett. 79 (1997) 1997.

[71] DØ collaboration, B. Abbot *et al.*, Phys. Rev. Lett. 80 (1998) 2063.

[72] DØ collaboration, B. Abbot *et al.*, Phys. Rev. D58 (1999) 052001.

[73] DØ collaboration, B. Abbot *et al.*, Phys. Rev. D60 (1998) 052001.

[74] DØ collaboration, V. M. Abazov *et al.*, Nature 429 (2004) 638.

[75] DØ collaboration, S. Abachi *et al.*, Phys. Rev. Lett. 77 (1996) 3309.

[76] DØ collaboration, B. Abbot *et al.*, Phys. Rev. D58 (1998) 12002.

[77] DØ collaboration, B. Abbot *et al.*, Phys. Rev. Lett. 80 (1998) 3008.

[78] DØ collaboration, B. Abbot *et al.*, Phys. Rev. D58 (1998) 092003.

[79] DØ collaboration, B. Abbot *et al.*, Phys. Rev. D62 (2000) 092006.

[80] DØ collaboration, B. Abbot *et al.*, Phys. Rev. Lett. 84 (2000) 222.

[81] DØ collaboration, V. M. Abazov *et al.*, Phys. Rev. D66 (2002) 012001.

[82] See `www-d0.fnal.gov/www_buffer/pub/Run1_publications.html` for a complete list of DØ Run I publications.

[83] DØ collaboration, S. Abachi *et al.*, Nucl. Instrum. Methods Phys. Res. A338 (1994) 185.

[84] DØ collaboration, V. M. Abazov *et al.*, Nucl. Instrum. Meth. A565 (2006) 463-537 [arXiv:physics/0507191].

[85] C. Fabjan, "Calorimetry in High Energy Physics", Experimental Techniques in High-Energy Nuclear and Particle Physics, World Scientific Publishing Co. Pte. Ltd., 1991, pp. 257–324, and R. Wigmans, "High Resolution Hadron Calorimetry", Nucl. Instrum. Methods, **A265**, pp. 273–290 (1988).

[86] C. W. Fabjan, F. Gianotti, Rev. Mod. Phys. 75 (2003) 1243–1286.

[87] A. Besson, Ph.D. dissertation, Universite de Grenoble 1, ISN 02-50, FERMILAB-THESIS-2002-51 (2002).

[88] Y. Peters, A. Schwartzman, M. Strauss, "Certification of the adaptive primary vertex in p17", DØ note 5192 (2006).

[89] B. E. Bonner, J. B. Roberts, Jr., Rice university progress report to the Department of Energy, DOE/ER/41031-59 (2006).

[90] C. Miao, Nucl. Phys. B (Proc. Suppl.) 78 (1999) 342.

[91] A. Pla-Dalmau, A. Bross, C. Hurlbut, Fermilab-Conf-94/096 (1994).

[92] Hamamatsu Corporation.
URL `www.hamamatsu.com`

[93] A. Baranovski *et al.*, Fermilab-TM-2175 (2002).

[94] R. Brun, F. Rademakers, "ROOT - An Object Oriented Data Analysis Framework", Proceedings AIHENP (1997);
URL `http://root.cern.ch`

[95] F. Deliot, H. Greenlee, S. Kulik, A. Lyon, S. Protopopescu, G. Watts, "Report of the D0 Data Format Working Group", DØ Note 4473 (2004).

[96] T. Sjostrand, Comp. Phys. Comm. 82 (1994) 74.

[97] G. Marchesini *et al.*, Comp. Phys. Comm. 67 (1992) 465.

[98] A. Schwartzman, C. Tully, "Primary Vertex Reconstruction by Means of Adaptive Vertex Fitting", DØ note 4918 (2005).

[99] H1 Collaboration, arXiv:hep-ex/0411046v1 (2004).

[100] A. Schwartzman, M. Narain, "Vertex Fitting by means of the Kalman Filter technique", DØ note 3907 (2001).

[101] A. Garcıa-Bellido, S. Lager, F. Rizatdinova, A. Schwartzman, G. Watts, "Primary vertex certification in p14", DØ note 4320 (2004).

[102] A. Schwartzman, M. Narain, "Probabilistic Primary Vertex Selection", DØ note 4042 (2002).

[103] G. C. Blazey *et al.*, "Run II Jet Physics: Proceedings of the Run II QCD and Weak Boson Physics Workshop", arXiv:hep-ex/0005012 (2000).

[104] J. Huth *et al.*, "Proceedings 1990 Summer Study on High Energy Physics", ed. E. Berger, Singapore: World Scientific, 134 (1992).

[105] DØ collaboration, B. Abbott *et al.*, Fermilab-Pub-97-242-E (1997).

[106] S. Ellis, D. Soper, Phys. Rev. D48 (1993) 3160;
S. Catani *et al.*, Nucl. Phys. B406 (1993) 187.

[107] A. Baranovski *et al.*, Nuclear Inst. and Methods in Physics Research A502/2-3 (2003) 423.

[108] P. A. Delsart, J. Donini, P. Lebrun, "Phi-intercalibration of the DØ calorimeter in Run II", DØ note 4299 (2003).

[109] M. Wetstein, J. Stark, M. Verzocchi, "Gain Calibration for the EM calorimeter in Run II", DØ note 5004 (2006).

[110] J. Kvita, K. Peters, "Run II Phi-Intercalibration of the Fine Hadronic Calorimeter", DØ note 5005 (2006).

[111] M. Cwiok, A. Haas, "Run II Eta-Intercalibration of the Hadronic Calorimeter", DØ note 5006 (2006).

[112] M. Voutilainen, "Jet p_T resolution for Run IIa final JES (v7.2) with dijet J4S jet corrections", DØ Note 5499 (2007).

[113] M. Agelou, J. L. Agram, C. Royon, "Jet Pt Resolution with jetcorr 5.3", DØ Note 4775 (2005).

[114] S. Eidelman *et al.*, "Review of Particle Physics", Phys. Lett. B592, 1 (2004).

[115] T. Andeen *et al.*, FERMILAB-TM-2365 (2007).

[116] C-C. Miao, FERMILAB-Conf-98/395-E (1998).

[117] S. Klimenko, J. Konigsberg, T.M Liss, FERMILAB-FN-0741 (2003).

[118] B. Casey *et al.*, "Cross-Section for the D0 Luminosity Measurement Using Upgraded Readout Electronics", DØ Note 4958 (2005).

[119] JES Group, "Jet Energy Scale Determination at DØ Run II (final p17 version)", DØ Note 5382 (2007). *version 1.3, October 9, 2007*; *Results to be published as a NIM paper.*

[120] M. Voutilainen, JES Group, "Jet Four-vector Scale Determination for Dijets in DØ Run IIa (final p17 version)", DØ Note 5550 (2007).

[121] OPAL Collaboration, G. Abbiendi *et al.*, Eur. Phys. J. C19 (2001) 587–651 [arXiv:hep-ex/0012018v1];
DELPHI collaboration, P. Abreu *et al.*, Eur. Phys. J. C16 (2000) 371;
L3 collaboration, M. Acciarri *et al.*, Eur. Phys. J. C16 (2000) 1;
ALEPH collaboration, R. Barate *et al.*, Eur. Phys. J. C14 (2000) 1.

[122] D. E. Groom, Nucl. Instrum. Meth. A572 (2007) 633–653 [arXiv:physics/0605164v4];
T. A. Gabriel, D. E. Groom, P. K. Job, N. V. Mokhov, G. R. Stevenson, Nucl. Instrum. Meth. A338 (1994) 336–347.

[123] J. Stark, presentation at the "All DØ Meeting", June 9, 2006:
`http://www-d0.hef.kun.nl//fullAgenda.php?ida=a061060&fid=51`

[124] J. Stark, presentation at the "MC Summit", June 20, 2006:
`http://www-d0.hef.kun.nl//fullAgenda.php?ida=a061101&fid=47`

[125] J. Stark, presentation at the "W Mass Meeting", January 24, 2007:
`http://www-d0.hef.kun.nl//fullAgenda.php?ida=a07120&fid=75`

[126] DØ collaboration, "Measurement of Triple Differential Photon Plus Jet Cross Section in $p\bar{p}$ Collisions at 1.96 TeV in DØ", DØ Note 5369-CONF (2007);
DØ collaboration, V. M. Abazov *et al.*, Phys. Lett. B639 (2006) 151–158 [arXiv:hep-ex/0511054v1].

[127] O. Atramentov, A. Askew, D. Bandurin, D. Duggan, A. Ferapontov, Y. Gershtein, Y. Maravin, G. Pavlovski, "Photon Identification in P17 Data", DØ Note 4976 (2005).

[128] O. Atramentov, D. Bandurin, Y. Maravin, "Photon energy scale for jet energy scale setting", DØ Note 4974 (2005).

[129] DØ collaboration, B. Abbott *et al.*, Nucl. Instrum. Meth. A424 (1999) 352-394.

[130] OPAL Collaboration, K. Ackerstaff *et al.*, Eur. Phys. J. C1 (1998) 479–494 [arXiv:hep-ex/9708029v1].

[131] CDF Collaboration, D. Acosta *et al.*, Phys. Rev. Lett. 94 (2005) 171802.

[132] K. Peters, presentation a the "CALGO meeting", February 13, 2007:
`http://www-d0.hef.kun.nl//fullAgenda.php?ida=a07250&fid=64`

[133] A. Bhatti *et al.*, Nucl. Instrum. Meth. A566 (2006) 375–412 [arXiv:hep-ex/0510047v1].

[134] D. Lincoln, Y. Galyaev, N. Cason, "b Jet Fraction as a Function of Jet p_T and Dijet Mass", *DØ Note draft v0.1, 12 July 2006.*

[135] Jan Stark, private communication.

[136] H. Schellman, "The longitudinal shape of the luminous region at DØ", DØ Note 5142 (2006).

[137] L. Duflot, V. Shary, I. Torchiani, R. Zitoun, "cal_event_quality package", DØ Note 4614 (2004).

[138] J. Hays, H. Schellman, J. Steele, "Calorimeter Event Quality Flag Rates for W/Z Production Cross-section Measurement (second pass)", DØ Note 5412 (2007).

[139] A. Harel, "Jet ID Optimization", DØ Note 4919, v1.1 (2005).

[140] B. Andrieu, A. Harel, H. Nogima, M. Rangel, M. Voutilainen, "Measuring Reconstruction*Jet-ID efficiencies using the tag and probe method in p17", DØ Note 5250 (2006).

[141] A. Harel, H. Nogima, M. Rangel, M. Voutilainen, "Combined JetID efficiency for p17", DØ Note 5218 (2006).

[142] M. Voutilainen, "Single jet trigger efficiencies in Run IIa", DØ Note 5549 (2007).

[143] C. Belanger-Champagne, "trigeff_cafe: Single Object Efficiency Calculation in the CAFe Environment", DØ Note 5093 (2006).

[144] C. Belanger-Champagne, B. Vachon, "Observation of Biases in Jet Trigger Efficiency Measurements", DØ Note 5217 (2006).

[145] S. M. Berman, J. D. Bjorken, J. B. Kogut, Phys. Rev. D4 (1971) 3388.

[146] R. P. Feynman, R. D. Field, G. C. Fox, Phys. Rev. D18 (1978) 3320.

[147] A. Kupco, C. Royon, M. Voutilainen, "Measurement of the Inclusive Jet Cross Section in $p\bar{p}$ Collisions at sqrt(s)=1.96 TeV", DØ Note 5087 (2006).

[148] Z. Nagy, Phys. Rev. D68, 094002 (2003) [arXiv:hep-ph/0307268].

[149] Z. Nagy, Phys. Rev. Lett. 88, 122003 (2002) [arXiv:hep-ph/0110315].

[150] W. K. Tung, H. L. Lai, A. Belyaev, J. Pumplin, D. Stump, C.-P. Yuan, JHEP 0702 (2007) 053 [arXiv:hep-ph/0611254v3].

[151] G. P. Salam, G. Soyez, arXiv:0704.0292v2 (2007).

[152] H. Schellman, private communication.

[153] M. Wobisch, Ph.D. dissertation, Technischen Hochschule Aachen (2000) [http://www-h1.desy.de/psfiles/theses/h1th-201.ps].

[154] F. James, "MINUIT - Function Minimization and Error analysis", Minuit Reference Manual, v94.1, CERN Program Library Long Writeup D506 (1998) [http://root.cern.ch/root/html/TMinuit.html].

[155] V. M. Abazov *et al.*, FERMILAB-PUB-08-034-E, submitted to Phys. Rev. Lett (2008) [arXiv:0802.2400].

Appendix A

LO Feynman diagrams

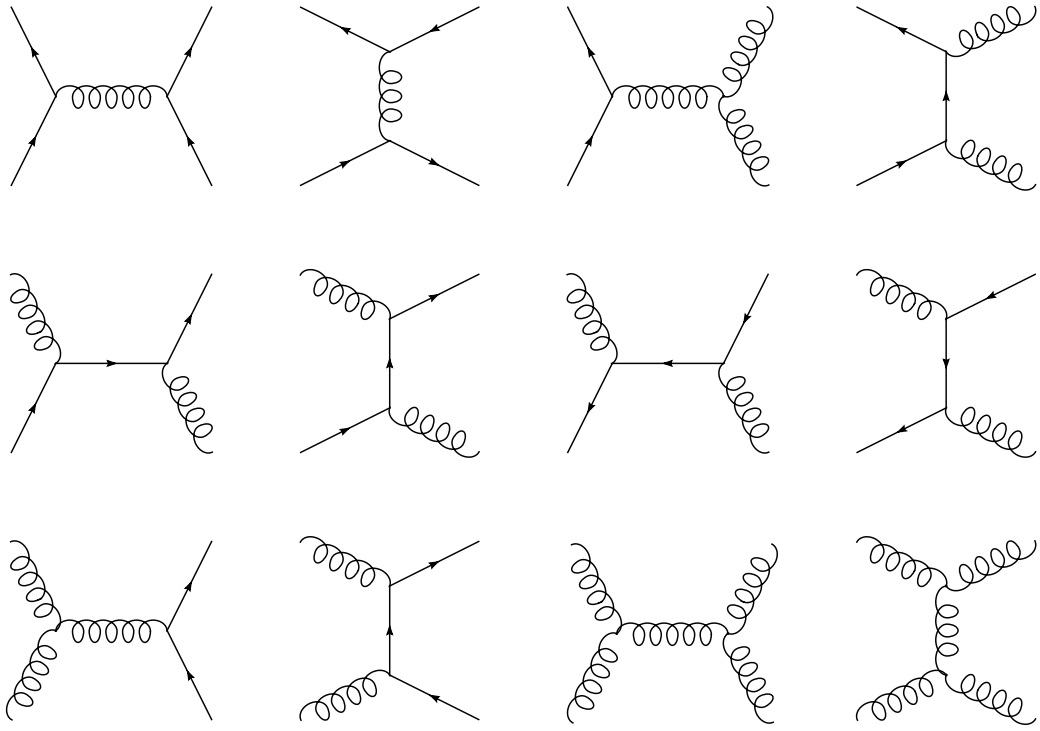

Figure A.1: Leading order Feynman diagrams for dijet production in pQCD. Top row: $q_i\bar{q}_i \to q_k\bar{q}_k$, $q_i\bar{q}_i \to gg$, Middle row: $q_i g \to q_i g$, $\bar{q}_i g \to \bar{q}_i g$, Bottom row: $gg \to q_k\bar{q}_k$, $gg \to gg$.

Appendix B

Gluon-jet fractions in MC

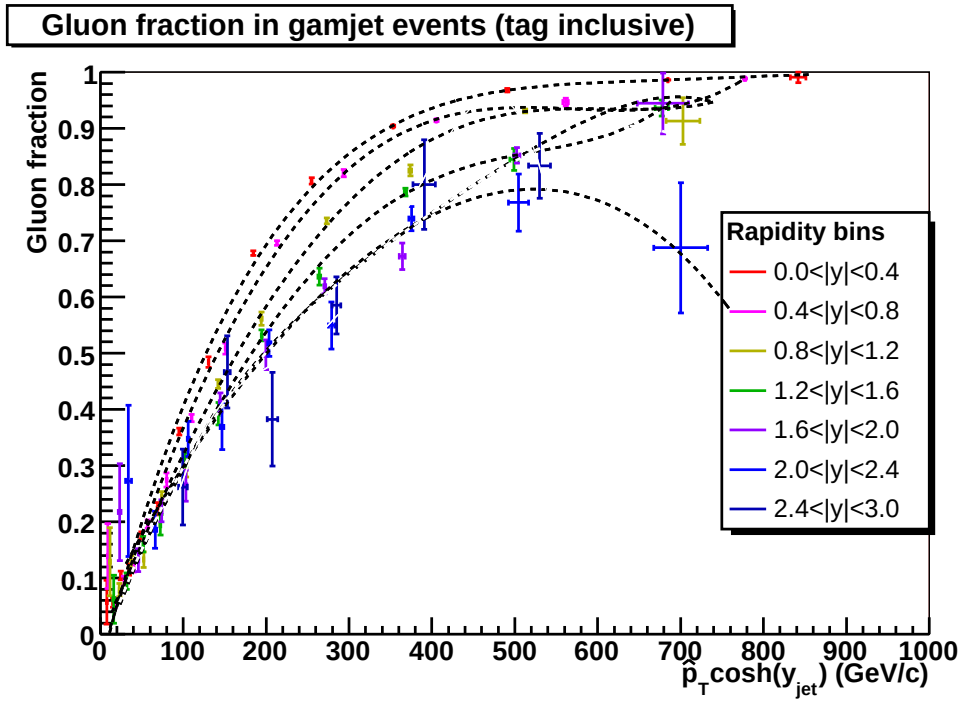

Figure B.1: Gluon fraction for γ+jets with $|y^{\gamma}_{\text{parton}}| < 0.5$, $\Delta R > 3.0$.

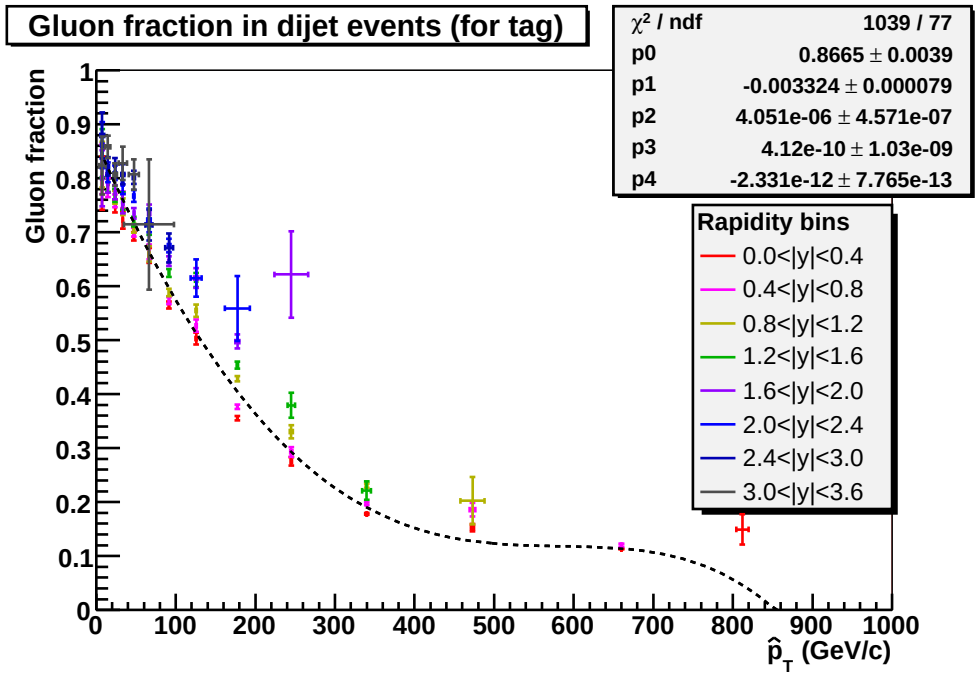

Figure B.2: Tag jet gluon fraction f_g^{tag} in dijets with $|\eta^{\text{tag}}_{\text{parton}}| < 0.5$, $\Delta R > 3.0$.

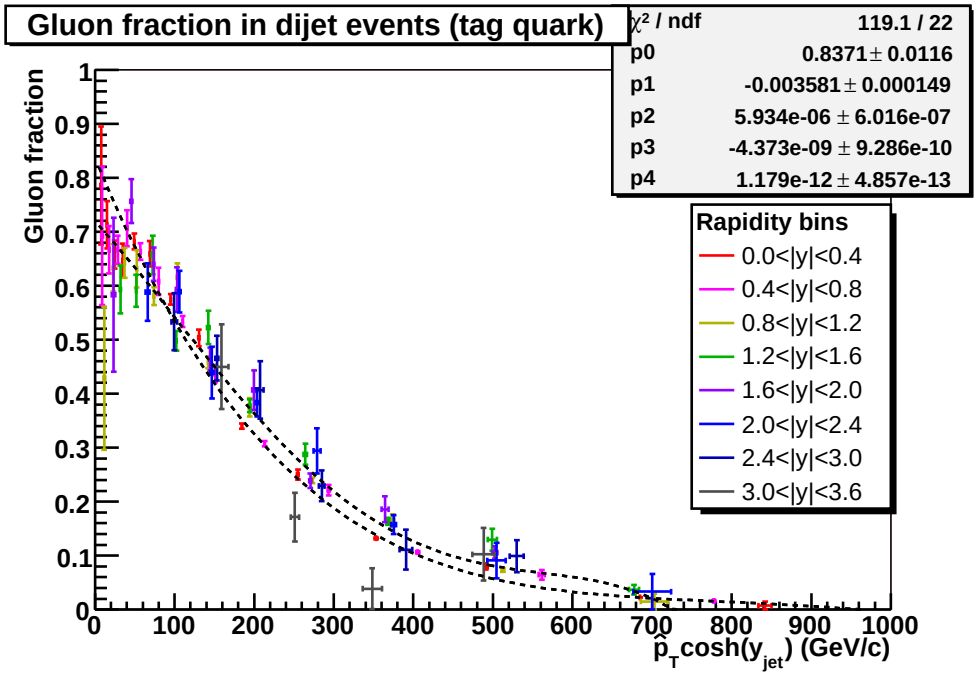

Figure B.3: Probe jet gluon fraction f_g^q in dijets with $|\eta^{\text{tag}}_{\text{parton}}| < 0.5$, $\Delta R > 3.0$ when the tag jet is a quark jet.

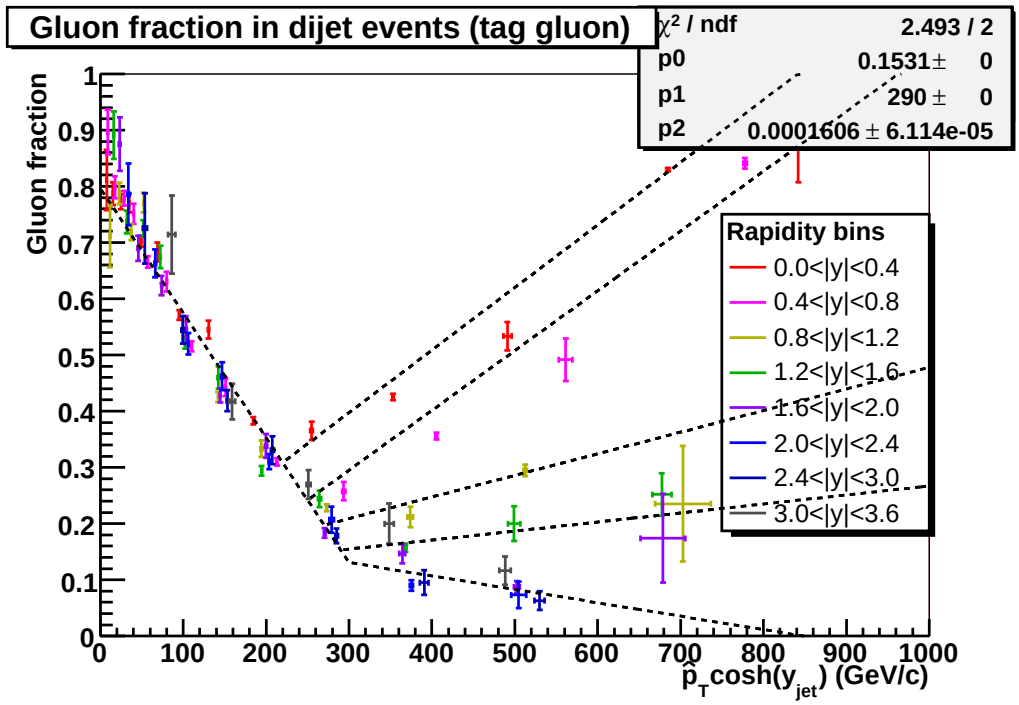

Figure B.4: Probe jet gluon fraction f_g^q in dijets with $|\eta^{\text{tag}}_{\text{parton}}| < 0.5$, $\Delta R > 3.0$ when the tag jet is a gluon jet.

Appendix C

Integrals and eigenfunctions

C.1 Selected integrals

The smeared cross section can be analytically calculated assuming an exponentialy falling p_T spectrum $N_0 e^{-\alpha x}$ and Gaussian smearing $e^{\frac{(p_T-x)^2}{2\sigma^2}}/(\sqrt{2\pi}\sigma)$ with constant resolution σ. In this equation p_T^{meas} is abbreviated as p_T for clarity:

$$
\begin{aligned}
F(p_T) &= \int_{-\infty}^{\infty} N_0 e^{-\alpha x} \frac{1}{\sqrt{2\pi}\sigma} e^{-\frac{(p_T-x)^2}{2\sigma^2}} dx && \text{(C.1)}\\
&= \int_{-\infty}^{\infty} \frac{N_0}{\sqrt{2\pi}\sigma} e^{-\frac{1}{2\sigma^2}\left(x^2-2(p_T-\alpha\sigma^2)x+p_T^2\right)} dx && \text{(C.2)}\\
&= \int_{-\infty}^{\infty} \frac{N_0}{\sqrt{2\pi}\sigma} e^{-\frac{1}{2\sigma^2}\left(x^2-2(p_T-\alpha\sigma^2)x+(p_T-\alpha\sigma^2)^2+\alpha\sigma^2(2p_T-\alpha\sigma^2)\right)} dx && \text{(C.3)}\\
&= \int_{-\infty}^{\infty} \frac{N_0}{\sqrt{2\pi}\sigma} e^{-\frac{1}{2\sigma^2}\left(x-(p_T-\alpha\sigma^2)\right)^2} e^{-\alpha\left(p_T-\alpha\sigma^2/2\right)} dx && \text{(C.4)}\\
&= N_0 e^{-\alpha\left(p_T-\alpha\sigma^2/2\right)} \int_{-\infty}^{\infty} \frac{1}{\sqrt{2\pi}\sigma} e^{-\frac{1}{2\sigma^2}\left(x-(p_T-\alpha\sigma^2)\right)^2} dx && \text{(C.5)}\\
&= N_0 e^{-\alpha\left(p_T-\alpha\sigma^2/2\right)}. && \text{(C.6)}
\end{aligned}
$$

Above calculation uses the method of completing a square and the fact that the integral of a normalized Gaussian is equal to 1, regardless of the mean.

Following this same practice of completing a square the true p_T can be analytically integrated (the denominator is written as $F(p_T)$ for brevity):

$$\begin{aligned} < p_T^{ptcl} > &= \frac{\int_{-\infty}^{\infty} N_0 e^{-\alpha x} \frac{1}{\sqrt{2\pi}\sigma} e^{-\frac{(p_T-x)^2}{2\sigma^2}} x dx}{F(p_T)} \qquad \text{(C.7)} \\ &= \dots \\ &= \int_{-\infty}^{\infty} \frac{1}{\sqrt{2\pi}\sigma} e^{-\frac{1}{2\sigma^2}\left(x-(p_T-\alpha\sigma^2)\right)^2} x dx \\ &= p_T - \alpha\sigma^2 \qquad \text{(C.8)} \end{aligned}$$

The steps marked with ... are identical to the ones in Eqs. C.2–C.5, with only an additional x inside the integral and $F(p_T)$ in the denominator. The last step integrates the mean value of a gaussian centered at $\mu = (p_T - \alpha\sigma^2)$, which is naturally μ.

Finally, let us also calculate the mean of the squared p_T^{ptcl}:

$$\begin{aligned} < (p_T^{ptcl})^2 > &= \frac{\int_{-\infty}^{\infty} N_0 e^{\alpha x} \frac{1}{\sqrt{2\pi}\sigma} e^{-\frac{(p_T-x)^2}{2\sigma^2}} x^2 dx}{F(p_T)} \qquad \text{(C.9)} \\ &= \dots \\ &= \int_{-\infty}^{\infty} \frac{1}{\sqrt{2\pi}\sigma} e^{-\frac{1}{2\sigma^2}\left(x-(p_T-\alpha\sigma^2)\right)^2} x^2 dx \\ &= \int_{-\infty}^{\infty} \frac{1}{\sqrt{2\pi}\sigma} e^{-\frac{1}{2\sigma^2}(x')^2} \left(x' + (p_T - \alpha\sigma^2)\right)^2 dx' \\ &= \int_{-\infty}^{\infty} \frac{1}{\sqrt{2\pi}\sigma} e^{-\frac{1}{2\sigma^2}(x')^2} \\ &\quad \cdot \left((x')^2 + 2x'(p_T - \alpha\sigma^2) + (p_T - \alpha\sigma^2)\right)^2 dx' \\ &= \int_{-\infty}^{\infty} \frac{1}{\sqrt{2\pi}\sigma} e^{-\frac{1}{2\sigma^2}(x')^2} x'^2 dx' \\ &\quad + (p_T - \alpha\sigma^2) \int_{-\infty}^{\infty} \frac{1}{\sqrt{2\pi}\sigma} e^{-\frac{1}{2\sigma^2}(x')^2} x' dx \\ &\quad + (p_T - \alpha\sigma^2)^2 \int_{-\infty}^{\infty} \frac{1}{\sqrt{2\pi}\sigma} e^{-\frac{1}{2\sigma^2}(x')^2} dx \\ &= \sigma^2 + (p_T - \alpha\sigma^2) \cdot 0 + (p_T - \alpha\sigma^2)^2 \cdot 1 \\ &= \sigma^2 + (p_T - \alpha\sigma^2)^2. \qquad \text{(C.10)} \end{aligned}$$

The RMS for the $p_T^{\rm ptcl}$ distribution in a bin of $p_T^{\rm meas}$ is now

$$RMS = \sqrt{< (p_T^{ptcl})^2 > - < p_T^{ptcl} >^2} = \sigma. \qquad \text{(C.11)}$$

This matches with the resolution of p_T^{meas} in a bin of p_T^{ptcl}, a useful result.

C.2 Uncertainty eigenfunctions

The inclusive jet cross section measurement involves fits of physical parametrizations in many stages of the analysis. The fitting algorithm (TMinuit) provides the fit uncertainty and uncertainty correlation information coded in the error matrix M. The uncertainty correlation information contained in the error matrix can then be extracted as a set of functions, the uncertainty sources f_s, by diagonalizing the error matrix. This section outlines the general diagonalization procedure and extraction of the uncertainty sources.

The fit uncertainty can be calculated using the error matrix as

$$\epsilon(x) = \sqrt{\sum_{i,j} m_{ij} \partial f_i(x) \partial f_j(x)}, \tag{C.12}$$

$$\partial f_i(x) \equiv \frac{\partial f(x;\{\alpha_i\})}{\partial \alpha_i}, \tag{C.13}$$

where m_{ij} is an element of the error matrix M and $f(x;\{\alpha_i\})$ is the fit function with a set of parameters $\{\alpha_i\}$. The above equation can be represented in matrix form as

$$\epsilon^2 = v^T M v, \tag{C.14}$$

where v is the column vector of partial derivatives of f, $v_i = \partial f_i$, and v^T is its transpose. The error matrix M can be diagonalized using standard linear algebra and Eq. C.14 rewritten

$$\epsilon^2 = v^T X^T D X v = (Xv)^T D (Xv) = v'^T D v', \tag{C.15}$$

where D is the diagonal matrix and X the matrix of eigenvectors produced by the diagonalization procedure. The vector v' is now the uncertainty eigenvector in the new diagonal basis. Its representation in the original basis ∂f_i is given by $v'_i = \sum_j x_{ij} \partial f_j$.

Equation C.15 is written element-wise as

$$\epsilon^2 = \sum_i v'_i \lambda_i^2 v'_i = \sum_i (\lambda_i v'_i)^2 = \sum_i s_i^2, \tag{C.16}$$

where λ_i^2 are the diagonal (non-negative) elements of D and $s_i = \lambda_i v'_i$ are the uncertainty sources. This procedure gives a number of uncertainty sources that is equal to the rank (number of non-zero elements in D) of matrix M. In the special case that $f(x;\{\alpha_j\})$ is linear in the parameters $\{\alpha_j\}$, the uncertainty sources s_i can be represented by the original function $f(x;\{\alpha_j\})$ with each α_j replaced by $\alpha_j = x_{ij}$.

The uncertainty sources obtained this way have a very intuitive interpretation: they give a set of independent variations around the central fit that each represent a 1 standard deviation shift from the central value. The total uncertainty at any point is simply the sum of the sources in quadrature, as shown in Eq. C.16, and the correlation ρ between any two points x_i and x_j is given by the sum of the products of each of the sources at the two points divided by the product of the total uncertainties σ

$$\sigma_(x_i) = \sqrt{\sum_k s_k^2(x_i)}, \tag{C.17}$$

$$\sigma_{x_j} = \sqrt{\sum_k s_k^2(x_j)}, \tag{C.18}$$

$$\rho(x_i, x_j) = \frac{\sum_k s_k(x_i) s_k(x_j)}{\sigma_{x_i}\sigma_{x_j}}. \tag{C.19}$$

This approach is directly generalizable to an arbitrary number of dimensions, as the point x_i can represent a multidimensional point $x_i = \{x_j\}_k$. Figure C.1 shows a representative 1-D example of the central calorimeter response uncertainty (without contraints from scaled MC) broken down to individual sources.

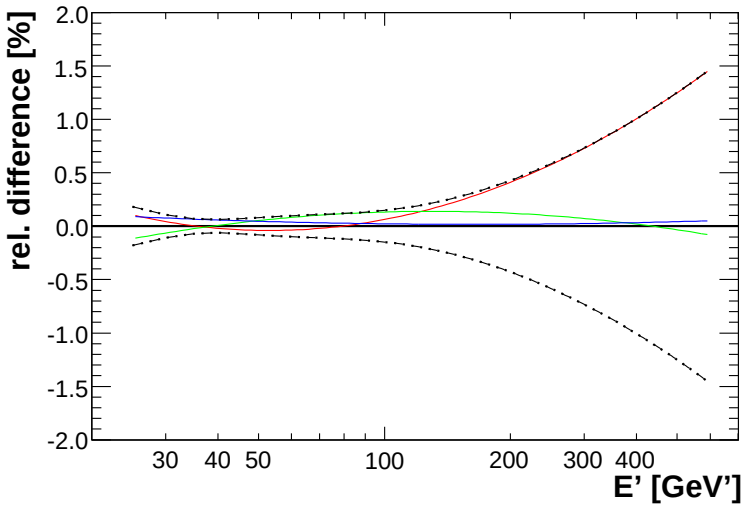

Figure C.1: Uncertainty in the quadratic logarithmic fit the central calorimeter response without constraints from scaled single pion response MC. The solid lines show the break up of the total fit uncertainty (dashed line) into independent uncertainty sources.

Appendix D

Additional analysis plots

D.1 Relative trigger ratio

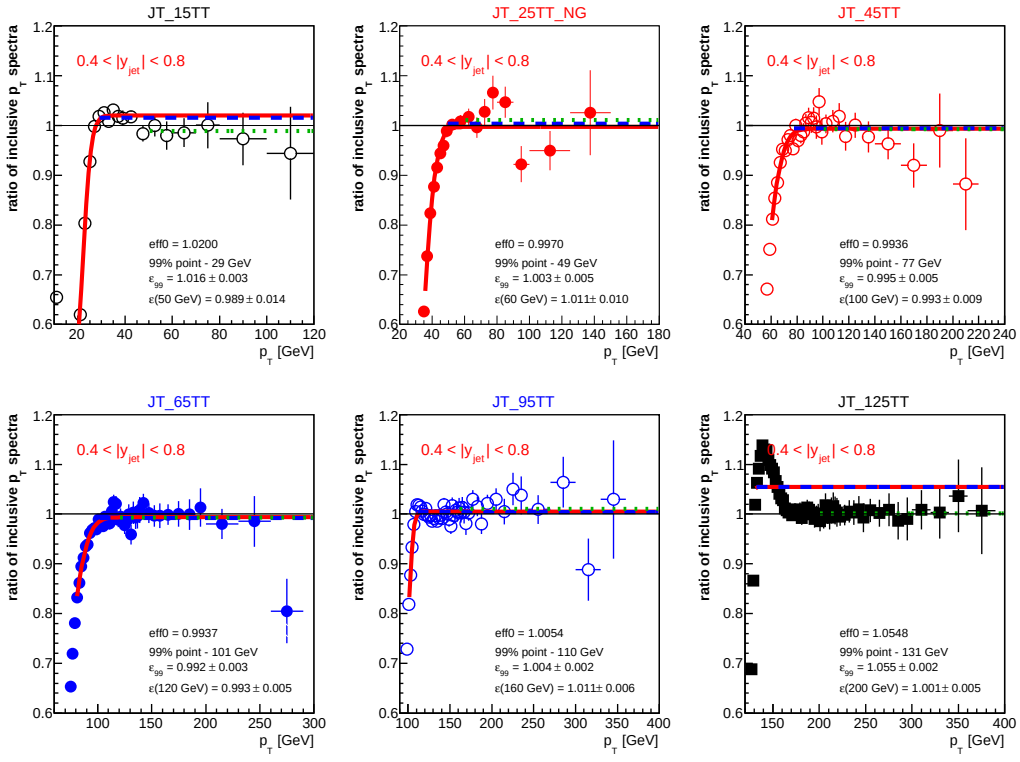

Figure D.1: Ratio of partially corrected jet p_T spectra.

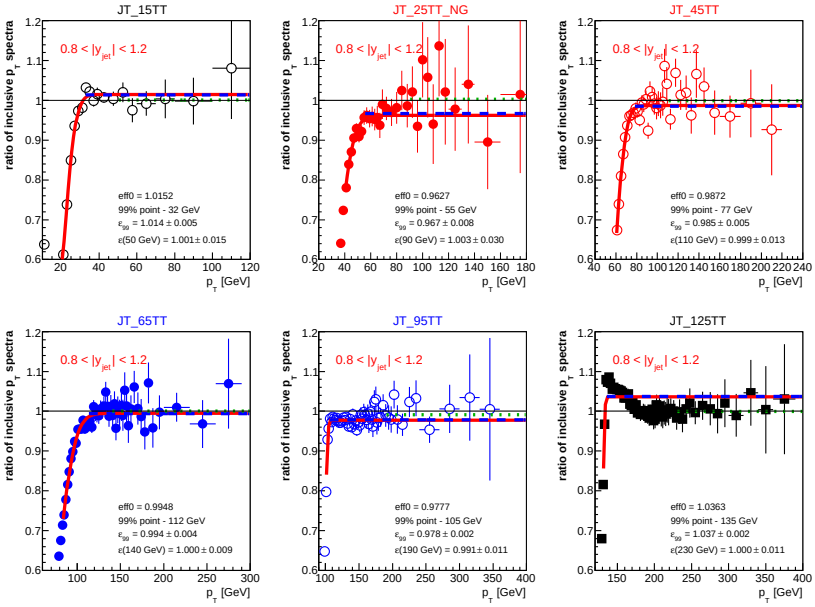

Figure D.2: Ratio of partially corrected jet p_T spectra.

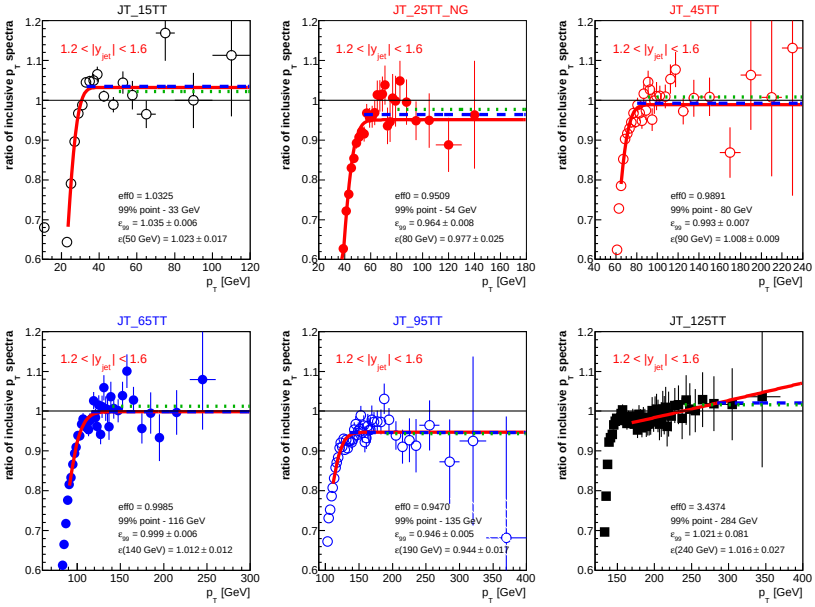

Figure D.3: Ratio of partially corrected jet p_T spectra.

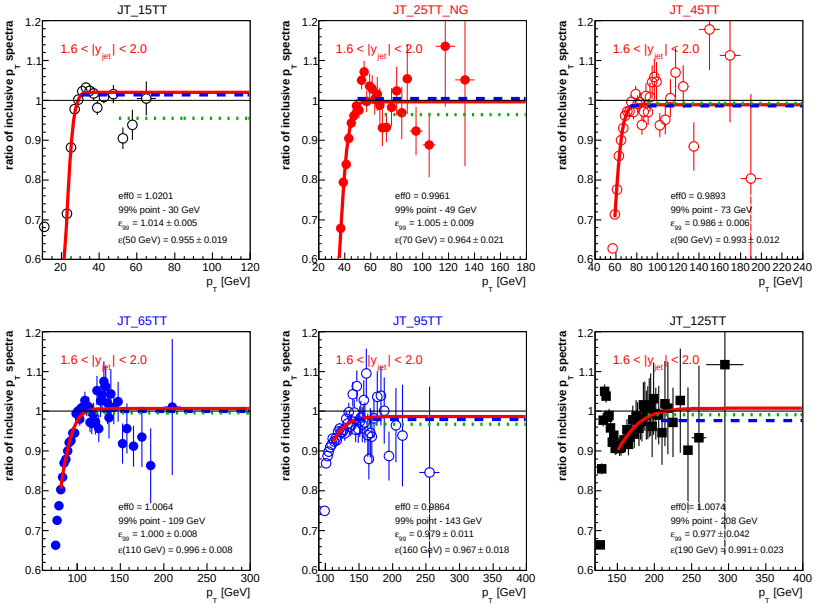

Figure D.4: Ratio of partially corrected jet p_T spectra.

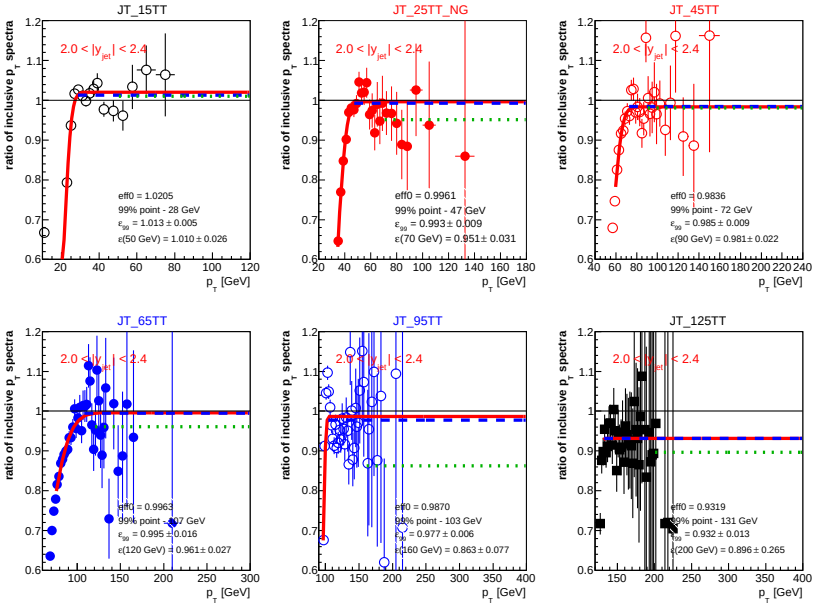

Figure D.5: Ratio of partially corrected jet p_T spectra.

D.2 Unfolding

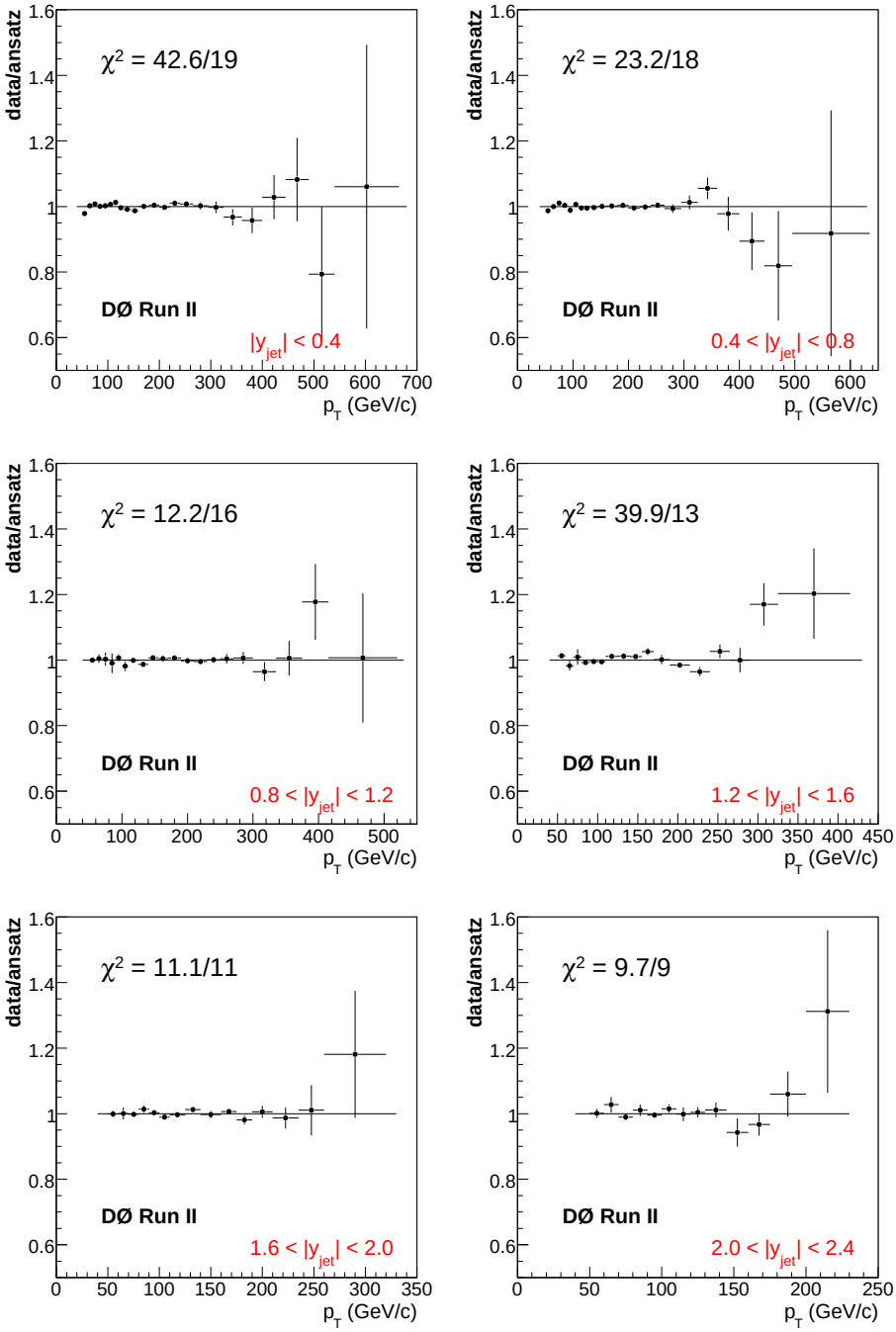

Figure D.6: Ratio of smeared ansatz to data.

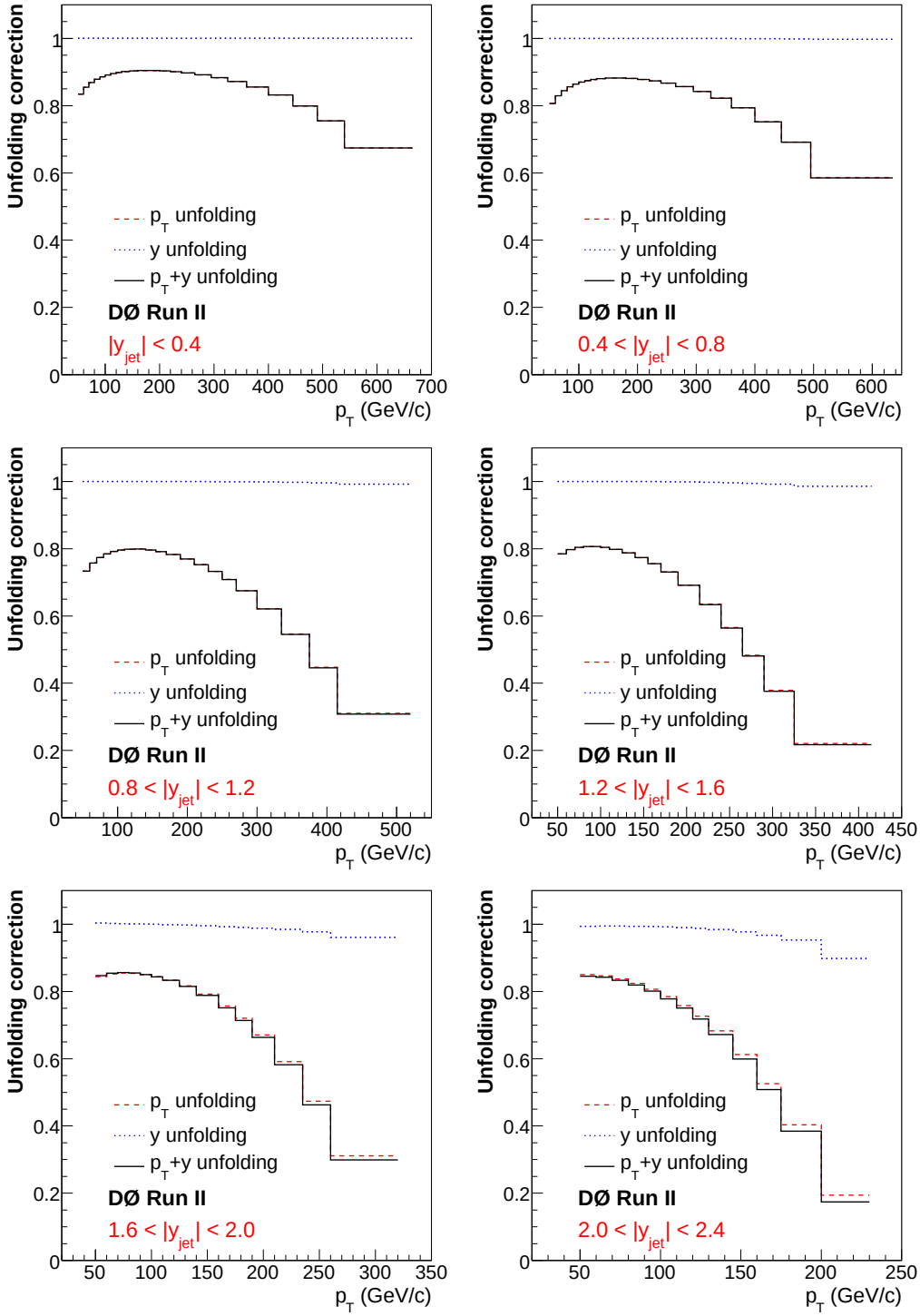

Figure D.7: Unfolding correction for p_T (dashed line), rapidity y (dotted line) and both (solid line).